Modeling Oxidation-induced Degradation and Environment-induced Damage of Thermal Barrier Coatings

Bochun Zhang

Thesis submitted to the University of Ottawa
in partial fulfillment of the requirements for the
Doctorate in Philosophy Mechanical Engineering

The Ottawa-Carleton Institute for Mechanical and Aerospace Engineering
Faculty of Engineering
University of Ottawa

Abstract

Thermal Barrier Coating systems (TBCs) serve as a key component in gas turbines in aerospace engines, isolating the metallic substrate from severe heat flux of the environment. The durability of TBCs has been considered to be a critical issue to determine the service lifespan of hot section components. Comprehensive studies of failure mechanisms benefit the gas turbine industry to develop TBCs with better material properties and stable microstructures, thus potentially enhancing their durability.

To date, many failure mechanism analyses have been conducted based on the understanding of critical residual stress developed under different thermal tests. For the present study, using the Finite Element (FE) method with temperature-process-dependent model parameters, the maximum residual stress is calculated with evolution of the localized/global interfacial roughness profile based on Electron Beam-Physical Vapour Deposition Thermal Barrier Coating system (EB-PVD TBCs). With studies of cracking routes from past research, qualitative failure mechanism analysis is conducted for EB-PVD TBCs. In addition, the estimated energy release rates are compared to reveal the effect of different thermal profiles on the crack driving forces for Atmospheric Plasma Sprayed Thermal Barrier Coating systems (APS-TBCs). Using previously observed cracking routes from different thermal cycling experiments, a quantitative failure mechanism analysis is conducted for APS-TBCs with modified analytical expressions.

In addition, literature works revealed that physics and mechanics-based models were proposed to evaluate environment induced damage. For the last part of my research, erosion of EB-PVD TBCs is estimated using a modified solid particle erosion model. A stochastic approach is applied to study the erosion of EB-PVD topcoat (TC) under real engine service conditions. The durability of TBCs is affected by both oxidation-induced degradation and environment-induced damage. The combination of “internal” crack driving forces (generated from residual stresses developed upon different stages of thermal cycles) and “external” erosion damage (from temperature-process dependent brittle/ductile erosion) lead to complexity of evaluating durability under different service conditions.

Key Words: Thermal Barrier Coating, stress models, failure mechanism analysis, crack driving forces, solid particle erosion

Acknowledgement

First of all, I have been very grateful to be advised under my supervisor, prof. Natalie Baddour and my co-supervisor, Prof. Kuiying Chen since I was a master student. Prof. Baddour has been very patient on guiding me to identify the research objectives based on my field of study, she also helped me a lot with my outline and scientific English writing of my thesis/journal papers. The financial support she offered was a great help when I was struggling during the end of my Ph.D. study. Prof. Chen has been playing as a major role in my academic contributions. He kept enlightening me with his insight on research fields. I'm really glad to learn from him and develop my method to deal with technical challenges under his proper guidance. I would thank for prof. Baddour and Prof. Chen for offering me the opportunity to work with them which benefits me for a lifetime.

I appreciate the work done from my thesis committee. Their comments and suggestions are valuable for my Ph.D. dissertation. Their advice means a lot to me and I feel really confident to develop my future career with their encouragement.

I want to thank my family, my motherland and the University of Ottawa. The care from my parents and other family members never stopped since the first day I arrived in Canada. The contract between the China scholarship council and University of Ottawa provides me with funding for daily expense during the first four-years Ph.D. study. These kept motivating me during the time I spent in Ottawa. I kept asking myself to make more academic contributions during my Ph.D. study and I'm looking forward to fulfill my two-years service after graduation and returning back to China.

I would like to thank all professors, my colleagues and friends who helped me during my Ph.D. study. To Prof. Mihaita Matei, Prof. Tao Jin and Prof. Fabio Variola, it is significant for your help with technical challenges in my researches. To Mr. Junqi Hong and Mr. yujie Hu, thanks for inspiration to my research modelling. To Mr. Yang Du, Dr. Yang li, Mr. Wentian Wang, Ms. Shuhong Dong, all your suggestions affect me in a positive way during my studies.

I would like to give special thanks to people and groups who live in Ottawa. I really enjoyed the time I spent in Futuro soccer academy where head coach Mr. Sanjeev Parmar, former goalkeeper coach Mr. Francesco Leuzzi and the rest of coaches were willing to help me improve with my coaching skills. It was my favorite to play with my friends in Team Atletico Bronson and Team Falcon soccer club. The warmth from Canadian people kept encouraging me for this long journey.

Table of Contents

List of Figures

List of Tables

List of Abbreviations

To simplify the description of key concepts in the context, abbreviation is used for terminologies including

Abbreviations	Full name
TBCs	Thermal Barrier Coating system
APS-TBC	Atmospheric Plasma Sprayed-Thermal Barrier Coating
EB-PVD TBC	Electron Beam-Physical Vapour Deposition Thermal Barrier Coating
TC	topcoat
YSZ	Yttria (partially) Stabilized Zirconia
BC	bondcoat
TGO	Thermally grown oxide
Pt-Al	Platinum-modified-Aluminium (Coating)

MCrAlY	Nickel-Cobalt-Chromium-Aluminum-Yttrium (overlay)
FEA	Finite Element Analysis
CTE	Coefficient of thermal expansion
ERR	Energy Release Rate
TMF	Thermal Mechanical Fatigue (test)
SEM	Scanning Electron Microscopy
RMS	Root Mean Square
RT	Room Temperature

Nomenclature

Symbols used to define the physical implication of parameters in either analytical and numerical solutions are significant and are clearly stated below. It should be noted that a parameter can be defined with superscript (subscript) in specific conditions, e.g., considering the effect of thermal gradient and sintering on TC layer, the temperature-process-position dependent elastic modulus of TC is indicated by $E_{TC}\left(T_{TC}\big|_{y},t\right)$. For simplicity, the definition of generalized symbols are presented and tabulated below. Fitting parameters for each chapters are not demonstrated here.

Symbols	Physical implication
Mechanical/Thermal properties of different layers	
E	Elastic modulus
κ	Bulk modulus for EB-PVD TBC
G (μ)	Shear modulus for EB-PVD TBC (APS-TBC)
ρ	Density
p	Porosity
ν	Poisson's ratio

α	Coefficient of thermal expansion
K_{IC}	Mode I Fracture toughness
σ_Y	Yielding strength
H_V	Vickers Hardness
K	Critical impact velocity from particle erosion
r	Radius of the contact point between erodent and target materials
$\phi(T,t), \varepsilon(T,t)$	Temperature-process-dependent cutting wear kinetic energy and deformation wear kinetic energy
Π	Pilling-Bedworth ratio for BC oxidation
Geometrical parameters in TBCs	
H	TC thickness
d_{TGO}	TGO thickness

$S(x)$	Roughness curve undulations
$\beta(x)$	Angle between the tangent to the roughness curve
A	Roughness amplitude
W	Roughness Width
T_L (L/L_0)	Tortuosity
D	Spacing parameter
b (a)	Sintering crack length developed parallel (perpendicular) to interface under isothermal high temperature dwell time
y ($g(y)$)	Positions for residual stress evaluations for EB-PVD TBC (APS-TBC)
Y	Cracking tip geometrical parameter
N_r	Number of noticeable imperfections at interface
Parameters controlling "external" environments (thermal cycling environments/Erosion particles)	

T	Temperature profile
ΔT	Difference between instantaneous temperature to elevated temperature during dwell time
t	Time
N	Number of thermal cycles
C_O	Oxygen concentration
Rt	The ratio of high temperature dwell time over total time in thermal cycles
R	Radius of spherical erosion particles
V	Velocity of erosion particles
P	Total number of impacts
m_i	Individual mass of erosion particles
α_i	Impact angle of erosion particles
Calculated intermediate/final results	

σ (σ_{ij})	Residual stress (Cauchy stress tensor)
ε_{ij}	Strain tensor
F	Force per length
M	Moment per length
K_I (K_{II})	Mode I (Mode II) Stress intensity factor
$\tilde{G}_i^k$	Equivalent Energy Flux
ψ	Mode mixture
$\dot{\varepsilon}^{er}$	Creep strain rate
D^{tr}	Inelastic stretching tensor
f	Normalized fraction of the oxidizing phase
σ^V	Equivalent Von Mises stress
s_{ij}	Deviatoric stress tensor
S	Fourth-order elastic compliance tensor

e_V^T	Mean local dilatational strain
W_t, (W_r)	Erosion damage (Erosion rate)

1. Introduction

1.1. Background of Thermal Barrier Coating system

Thermal barrier coating systems (TBCs) have been used in the gas turbine engine industry as thermal isolators to protect substrate blades from severe service environments. For example, a massive thermal shock can be generated within a short period since the engine works at extremely high dwell temperatures during service. The TBCs are used to sustain high thermal gradients and provide adequate backside cooling that prolongs the lifetime of components [1]–[8]. Since the invention and introduction of TBCs to the turbine engine industry, many attempts have been made to fabricate coating constituent layers using a variety of deposition methods. Atmospheric Plasma Spraying (APS) and Electron Beam-Physical Vapor Deposition (EB-PVD) are the most common approaches for TBC fabrication [9]–[14]. Although TBCs can be fabricated by other methods, such as Suspension Plasma-Spraying (SPS) [15]–[21], Detonation-Spraying (DS)[22]–[26] and even High-Velocity Oxygen-Fuel (HVOF) [27], these other methods generate similar coating microstructures compared to those of APS and EB-PVD TBCs. The industrial sector still prefers TBCs fabricated by APS and EB-PVD since they typically display better performance and durability during service conditions.

Typically, the TBCs are comprised of a ceramic topcoat (TC), a metallic bond coat (BC) and a substrate that needs to be protected by the coating. The TC layer consists of an 7-8% Yttria partially Stabilized Zirconia (YSZ) with low thermal conductivity, intermediate thermal expansion coefficient and high thermal shock resistance. Based on the difference of deposition methods, the capability of the

TC to sustain a high thermal gradient can vary [17], [28]–[34]. Meanwhile, the concept of strain-tolerance is also integrated into the design of the TC to avoid instantaneous delamination of the topcoat. This might occur as large residual stresses could be generated on the topcoat/bond coat interface under thermal cyclic conditions [35]–[42]. The bond coat (BC) of TBCs is applied onto the substrate before topcoat deposition. The materials of the bond coat are preferably selected as either diffusion aluminide (Platinum-modified-Aluminium coating) or Nickel-Cobalt-Chromium-Aluminum-Yttrium overlay (MCrAlY). The bond coat serves as a layer of "glue" that holds the TC and substrate together. It is important to recognize that the degree of surface finish of the BC and the interfacial adhesion between TC and BC layers are significant to the durability of TBCs. Therefore, to strengthen interfacial adhesion, the bond coat is deliberately designed to be able to provide sufficient chemical and mechanical bonding [43]–[48] through post-processing such as heavy or light surface grit-blasting. The selection of such post-processing treatment depends on the topcoat deposition methods [49]–[55].

The fabrication methods of the BC, such as by HVOF, APS, cold gas dynamic spraying (CGDS) and chemical vapor deposition, have a strong effect on its mechanical behavior and the oxidation of the TBCs. This is illustrated by the difference in TBC performance reflected by specific failure mechanisms and lifetime records, or characteristics of damage behavior during various thermal-mechanical tests [56]. Another important feature of the bond coat is its ability to prevent further progressive oxidation of the substrate under extremely high temperature service conditions. This is achieved by the formation of a thin protective dense oxide scale known as thermally grown oxide (TGO) [57]–[62]. The preferred continuous α-alumina scale is mainly formed at the BC surface due to the oxidation of the BC governed mostly by the inward diffusion of anions (oxygen ions or oxygen), where the BC acts as a sufficient aluminide reservoir to facilitate oxidation. However, this oxidation of the BC also results in a large residual stress as the TGO layer continuously thickens [63]–[68].

One possible failure mechanism suggests that at the initial oxidation stage, the transient oxides such as spinel nucleate first and grow fast, leading to crack formation and reduction of fracture toughness [69]–[77]. The spallation of the topcoat from the substrate signals the failure of the TBC, which could lead to severe damage of hot section components and failure of the turbine engine. Therefore, to better serve gas turbine engines, there is a need to understand failure mechanisms and to develop a reliable lifetime prediction model to estimate the average lifetime corresponding to various service conditions [4], [78]–[86]. Systematic studies need to be conducted on specific TBCs degradation since the failure mechanism and associated lifetime model critically depend on the TBC fabrication method.

1.2. Identified gaps in the literature

1.2.1. Stress models

From a review of the literature (Chapter 2), the shortcomings of past analytical or numerical stress models are the way the parameters are implemented into the models. Either temperature-dependent or thermal process-dependent parameters were used in the stress analysis for previous studies. For example, the elastic modulus of the TC is implemented as temperature dependent behavior in a temperature variation from holding temperature to ambient temperature [82], [87], [87]–[91]. However, to the best of the candidate's knowledge, no proposed model combines the effects of both temperature and thermal processes on the description of material properties of the TC. Similar shortcomings exist for description of BC and TGO materials involving the phase transformation, and the material properties for the

transitional layer (from pure metallic BC with oxidation-prone β phase to oxidation-resistant γ' phase + oxide). These combined effects have not been found in previous studies, and thus there could be a discrepancy for calculated stress from previous studies compared to the actual stress generated during phase transformation under thermal cyclic loading, especially with a long period of high temperature holding time.

The effect of the evolution of interfacial roughness was investigated in many articles [18], [52], [53], [92], [93]. Nevertheless, the effect of the variation of interfacial roughness on the stress distribution has hardly been investigated. For EB-PVD TBCs, the evolution of interfacial roughness for a grit-blasting-smoothed interface between TGO/BC would increase the out-of-plane stress level at the peak within the BC. In extreme cases, the sharp tip can cause an abnormal stress level.

Although some attempts have been made in previous research, it is difficult to establish analytical models by incorporating inelastic properties of materials into stress models. For example, creep and yielding behavior of TBCs, inelastic strain generated because of phase transformation due to BC oxidation, and swelling behavior due to unit cell expansion from metallic matrix to oxide matrix are not usually incorporated. This makes it difficult to accurately evaluate the lifetime of TBCs through stress-based lifetime prediction models.

Previous analytical stress models focused on evaluating the residual stresses close to the interface at designated positions, i.e., the trough or peak close to the interface. However, through-thickness cracks were identified from APS systems and hence the maximum stress was also identified at flanks of imperfections for both APS and EB-PVD TBCs via FE results [94], [95]. Therefore, it is necessary to evaluate the energy release rate at positions other than peaks and valleys of imperfections for potential

crack nucleation. However, to date no analytical solutions have been proposed to describe the stress at an arbitrary position within the TC of a 2D TBC model.

1.2.2. Failure mechanism analysis

Much research has been performed to identify the failure crack routes observed from cross-sectional areas of failed specimens. However, no clear evidence has been presented for crack initiation, nor crack propagation accompanied with stress variations related to the evolution of interfacial roughness. In other words, previous research has not established a clear connection between the residual stress that results from temperature process-dependent interfacial roughness models and failure mechanisms.

The failure mechanism in previous research focused on the effect of localized imperfection-triggered crack initiation and propagation but neglected the effect of global interfacial roughness variation at relatively large scale. The rumpling effect of the BC surface was considered to be a typical global failure mechanism of EB-PVD TBCs. However, there has been no consideration of the effect of global spacing parameters on the residual stress for void generation. That is, existing failure mechanism analysis neglects the effect of the evolution of global interfacial roughness.

Past studies have focused on the failure mechanisms triggered by stress induced by CTE mismatch upon cooling and TGO growth during isothermal holding time. With interest in real service conditions, the effects of (i) thermal gradient generated during high temperature holding time and (ii) thermal shock resulting from rapid temperature variation on the durability of TBCs were gradually studied. However, there is a lack of studies that compare the two different types of experiments with the quantitative

evaluation of energy release rate (ERR) using existing analytical models. Are the failure mechanisms and crack routes from the two types of experiments identical? Is the same type of ERR responsible for crack initiation for experiments with and without thermal gradients? What is the influence of different high temperature holding time on the durability of TBCs for isothermal furnace cycling tests vs burner cycling tests? In other words, it is necessary to investigate the main factor that leads to failure under each type of experimental conditions.

In addition, based on the results from failure mechanism analysis, further work can be expected where life of TBCs can be estimated through analytical or numerical methods. Past studies revealed the research challenges regarding development of lifetime prediction models. The accuracy of semi-empirical lifetime prediction models still needs to be improved by incorporating temperature-process dependent parameters and developing methods to evaluate the lifetime based on specific failure mechanisms of TBCs.

It is a challenge for either analytical or numerical lifetime models to predict the failure time under multiple failure mechanisms. For example, as will be described in section 2.2.2, the failure mechanism of APS-TBCs was considered to be experimentally-determined and can be described as the coalescence of multi-layer cracks at the valley of the TC, where out-of-plane tensile stress develops as the TGO thickens. The major driving forces of such TC spallation includes the ERR generated from CTE mismatch between layers upon cooling, as well as dilatational TGO growth stress developed during high temperature holding time. The type of crack driving forces, as well as crack routes were considered under isothermal cycling experiments, where thermal cycles consist of a relative long high temperature holding time with a relative slow heating and cooling rate during temperature variation. For a burner-rig test with a short-duration high temperature holding time and rapid heating and cooling rate during temperature variation, additional through-thickness cracks were identified within the TC layer. The

effect of thermal gradient and thermal shock were introduced, and different crack routes were observed due to the interaction of multiple crack driving forces. This increased the difficulty of lifetime modelling. For EB-PVD TBCs, it was evident that spallation of the TC might be triggered by cracks either in the same layer (described as failure mode A in [96]) or penetrating through different layers (described as failure mode B in [96]). Speculation could be found in different publications claiming that these failure mechanisms were identified at different stages of life cycles [52], but none mentioned whether there was an interaction of crack propagation driven by different failure mechanisms. Thus, the functionality of lifetime models is still limited as the mode of crack propagation under multiple failure mechanisms is not well understood.

To date, many different damage models have been developed for TBCs based on experimental data (isothermal/ thermal cyclic conditions). The damage model which will be described in section 2.2.2-2.2.3 evaluated the proportionality of damage area over total damage. The damage can be estimated through internal factors like stress generated from CTE mismatch or TGO growth under thermal cyclic experiments. It also includes factors such as external forces applied to the TBCs as mechanical strains measured under thermal mechanical fatigue (TMF) tests. In real service conditions, there is inevitable intrusion or impacting of external particles and many studies have been done experimentally to determine the damage of CMAS intrusion and deposition at the surface of the TC [97]–[99]. However, there is a lack of analytical lifetime models that evaluate the effect of both internal and external factors on durability and lifetime. In addition, the analytical models that estimate progressive damage under real service thermal environments, or related work on the effect of thermal environment on damage progression are rarely found.

1.3. Research objectives

Stress models:

Research on stress models is separated based on different TBCs. Due to the complexity of estimating the stress distribution in EB-PVD TBCs, numerical FEA approaches are used to reveal the relationship between stress and different interfacial roughness profiles. The stress analysis will also be conducted for APS-TBCs. The development of analytical models is required to explicitly describe the relationship between each model parameter and their interactions.

Objective 1: By using either analytical or numerical methods, the goal is to investigate the effect of the evolution of localized/global interfacial roughness on the residual stress distribution and on the failure mechanism/durability of TBCs during service conditions.

Failure Mechanism Analysis

The failure mechanism analysis also depends on different TBCs. The research work of identifying possible crack routes and failure mechanisms for EB-PVD TBCs takes advantage of FE results from stress analysis. The failure mechanism analysis based on APS-TBCs involves quantitative estimation of different crack driving forces under either isothermal furnace tests or burner cycling test with existence of thermal gradient.

Objective 2: By using either analytical or numerical methods, the goal is to identify the crack driving forces and possible cracking routes that might be affected by the variation of interfacial roughness and different service conditions.

Solid Particle erosion model

The damage model estimates the degree of damage of components in thermal environment based on specific damage sources which also reveals the stage of TBCs during the entire life cycle. Specifically, for solid particle erosion where parameters characterizing the erosion process are randomly distributed, the development of an erosion model combines the stochastic approach with the analytical expressions, where the amount of erosion is evaluated statistically following a probability distribution.

Objective 3: Development of solid particle erosion model under a thermal environment simulating real service conditions with the assistance of a stochastic approach.

1.4. Thesis outline

Chapter 2 contains the literature review regarding the stress analysis and failure mechanism analysis based on APS and EB-PVD TBCs. Chapter 3 focuses on numerical finite element modelling to estimate the variation of residual stresses with evolution of localized interfacial roughness profile in EB-PVD TBCs under thermal cycling environment. Chapter 4 describes failure mechanism analysis via parametric study based on the numerical FE model developed in chapter 3 for EB-PVD TBCs under thermal cycling environment. Chapter 5 concentrates on estimating the energy release rates through analytical solutions for APS-TBCs under different thermal cycling environments. Chapter 6 evaluates

the damage generated by erosion of EB-PVD TC through analytical solutions under thermal cycling environments. Chapter 7 gives the summary and conclusions of the Ph.D. research work.

1.5. Contributions of the thesis

The contributions of the Ph.D. are demonstrated in chapter 3-6. A numerical FE model was developed based on EB-PVD TBCs, as described in chapters 3-4. The effect of evolution of localized/global interfacial roughness profile on residual stresses was found. Based on the results provided from stress analysis, a failure mechanism analysis was conducted based on EB-PVD TBCs. With a modified analytical model and experimental data, a failure mechanism analysis based on APS-TBCs was conducted and described in chapter 5. The discrepancy of energy release rates for TBCs under different thermal cycling experiments was revealed. The crack driving forces for TBCs under different working environments were suggested. The analytical approach was developed to evaluate the damage caused by solid particle erosion based on EB-PVD TBCs, as described in chapter 6. The effect of material properties and thermal environments on the erosion rates was identified. The damage caused by both "internal" and "external" factors were discussed based on different stages of various of thermal cycling experiments.

2. Literature review of TBCs

2.1. Microstructural characteristics of TBCs from APS and EB-PVD deposition methods

Typical microstructure from a cross-section of an APS-TBC specimen is observed by scanning electron microscopy (SEM) and shown in Figure 1.

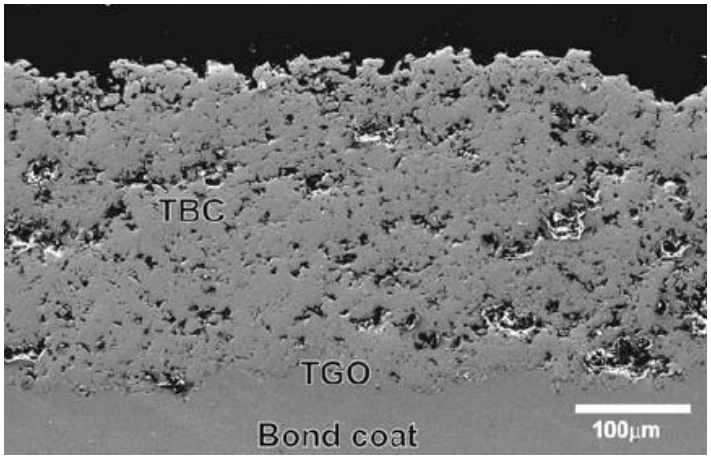

Figure 1 Typical microstructure of APS-TBCs, the intra/intersplat voids could be observed within topcoat that lower the conductivity of topcoat [32]

The deposits consist of a multitude of pancake-like 'splats' called lamellae, formed by flattening of the liquid droplets. As the feedstock powders typically have sizes from micrometers to above 100 micrometers, the lamellae have thickness in the micrometer range and lateral dimension from several to hundreds of micrometers. The geometrical parameters of lamellae (size and deposit position) are

determined by the impact of high speed YSZ particles bombarding the bond coat surface. These lamellae together with the small voids, such as pores, cracks and regions of incomplete bonding between lamellae, are the most significant factors that determine the microstructure of the topcoat, which in turn play a major role in chemical and mechanical properties of the topcoat. For example, the intersplat pores and voids formed by overlapping splats provide high strain tolerance. However, the high porosity of the topcoat due to the existence of intrasplat pores lowers strength; although it is through its low thermal conductivity that effective thermal isolation is achieved. In addition, the overall cost of APS-TBCs fabrication is much lower than TBCs deposited by EB-PVD. Thus, APS-TBCs have usually been used as an alternative land-based thermal isolator in land-based turbine applications.

The bond coat of APS-TBCs is based on Nickel-Cobalt-Chromium-Aluminium-Yttrium coating (MCrAlY system), where the element "Y" stands for the yttrium that is used to improve the adhesion between the TGO and bond coat. The surface of the bond coat from APS-TBCs is typically rough compared to that of EB-PVD TBCs, where this roughness is designed to provide sufficient mechanical bonding between the topcoat and substrate.

The TGO scale forms as a result of progressive oxidation of the bond coat. Apart from α-alumina grown between the topcoat and bond coat, it is observed that a heterogeneous TGO for the MCrAlY system is partially related to the oxidation of yttrium, which is easier to oxidize than other elements. Thus, the yttrium aluminum garnet or namely, peg observed from the cross-section of an SEM image usually indicates an area with high concentration of yttria. Typical microstructure from the cross-section of an EB-PVD TBC specimen is shown in Figure 2. The most attractive characteristic is the columnar grain structure, which grows normal to the ceramic-bond coat interface. This, along with segmentation vertical cracks could provide sufficient in-plane strain tolerance [100]–[105]. It is also found that a reduced thermal conductivity could be achieved in the presence of the columnar gaps and pores.

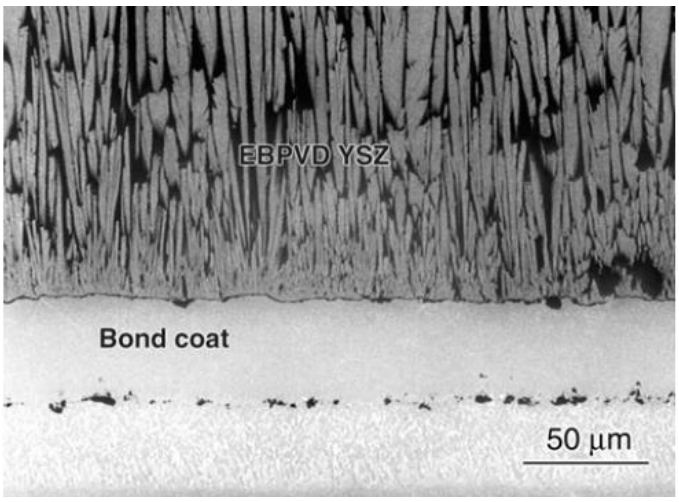

Figure 2 Typical microstructure of EB-PVD TBCs, topcoat shows the columnar structure with vertical cracks [32].

There are two different types of bond coats for EB-PVD TBCs, diffusion aluminide coating and MCrAlY overlay coating. The latter type of bond coat was discussed in the preceding section, as for the previous one, the bond coat usually consists of platinum modified diffusion aluminide (Pt-Al). The Pt is adopted into BC materials to provide better adhesion between the topcoat and substrate [106]–[108]. The surface of the bond coat, unlike the undulated interfacial profile of APS-TBCs, is smoothed by sand-blasting before further topcoat deposition. A smoother interface has been shown to reduce the effect of large imperfections on stress concentration at the interface between TC/BC layers, which could be one of reasons for EB-PVD coatings exhibiting longer lifetimes than PS YSZ coatings [109]. The type of TGO layer formed between the topcoat and bond coat depends on the selection of bond coat. As described in the preceding section, apart from typical α-alumina, the yttrium aluminum garnet is often observed for MCrAlY BC [32], [110]–[113]. However, it is seldomly reported to be found in the Pt-Al BC TBCs.

It is shown that different microstructural features of TBCs result from their specific fabrication

process such as by APS and EB-PVD, and it is reported that improved performance could be achieved from TBCs fabricated by EB-PVD [17], [29], [34], [34]. For EB-PVD TBCs, the external porosity and vertical growth-segmentation cracks between feather-like columnar structures provide more strain-tolerance compared to APS-TBCs. The smoother surface at the interface between the TC and BC layer is capable of inhibiting out-of-plane residual stress at early stages of TBC lifetime, thus preventing the initiation of early horizontal cracks within the TC. Moreover, by incorporating Pt into BC materials, a better adhesion between topcoat and TGO could be achieved [114]–[116]. For solid particle erosion tests, EB-PVD-TBCs show better erosion resistance for the majority of angles (30^{o}-90^{o}) of impact compared to APS-TBCs [17]. However, the designed microstructure from APS-TBCs also have some advantages on specific aspects. Due to a higher void content and a reduction in size of porosity within the TC, typically an APS structure exhibits lower thermal conductivity compared to EB-PVD [29]. Moreover, the relative rough interface observed between TC/TGO(BC) is believed to inhibit crack propagation since roughness causes crack propagation along the interface under mixed mode conditions, thereby increasing the energy dissipated during coating decohesion [117]. Therefore, both APS-TBCs and EB-PVD TBCs are still currently applied as high temperature protective coating systems on turbine blades in the aerospace industry.

2.2. The state-of-art durability analysis of two coating systems

Based on the fundamental knowledge of microstructure observations many attempts have been made on improving the durability of TBCs and their fabrication with longer life expectation [118]–[123]. Consequently, it becomes an essential issue to understand the failure mechanism with respective to

TBCs fabricated by different methods. On the one hand, one of the typical ways to conduct failure mechanism analysis is by obtaining the critical stress level at positions where either a crack is identified according to experimental results, or there is high possibility that crack might nucleate (e.g., the interfacial roughness with high radius of curvature). On the other hands, by modelling the stress generated under simulated thermal experiments, it is possible to quantitatively evaluate the damage progression, which in turn facilitates the development of life model for TBCs. The following sections describe the results of current work based on stress modeling, failure mechanism analysis and life model.

2.2.1. Stress analysis

Stress model: theoretical analysis

Although there are many advantages to using numerical models for stress analysis, one disadvantage is that unlike analytical methods, FE modelling processes do not reveal the correlation between the estimated residual stress and material properties and geometrical parameters explicitly with mathematical expressions. Instead, implicit models are established, where the model parameters are varied and the stresses are evaluated in an iterative manner, thus requiring much computational effort. This problem could be partially addressed by using analytical solutions with integrated process-dependent model parameters. In addition, analytical solutions offer a better understanding of the importance and connections of the roles played by combination of parameters in the model, which will be elaborated in the following.

Clarke et al [117] described the situation where a stress film was formed on a rough rather than a flat surface. To quantitatively evaluate the maximum tensile stress state at the peak of roughness, an idealized roughness model was applied by a sinusoidal variation in height and wavelength.

Mao et al [124] proposed an analytical model describing the in-plane thermal residual stress behavior under thermal cyclic conditions with non-linear couple effects of temperature gradient, thermal fatigue, initial residual stress, elasto-plastic deformation and creep deformation. Evans [125] presented the preliminary results for stresses estimated from critical positions where a crack might initiate within the TC, TGO and BC, respectively. For the residual stresses caused by the coefficient of thermal expansion mismatch (CTE mismatch) between layers, the classical approach of the "Eshelby" protocol [126] was applied by allowing the strains to occur unconstrained and imposing the tractions to assure displacement and traction continuity [125]. Stress inversion was expected when the TGO thickness reached a critical value, which is identified at a valley of the TC in APS-TBCs [67], [81], [127]. Different from thermal residual stresses that are generated uniformly throughout the layer, the TGO growth stresses occurs predominately at one of the interfaces. Evan's model focused on describing the residual stresses within different layers as a consequence of TGO growth with BC oxidation as indicated by the phase transformation from metallic BC to oxide TGO.

Similar but different from the residual stress generated due to CTE mismatch between layers, stress is also generated due to the non-uniformity of temperature distribution within TBCs (thermal gradient). Hutchinson el at[128] suggested that the existence of a sufficiently large thermal gradient was one of the driving forces that triggered crack propagation at delamination planes of the TC, which led to spallation of the TC and failure of the TBCs. Two different crack modes were categorized, where analytical expressions for stress were developed with respect to each case: (Category I) thermal stress generated with existence of an isolated crack and thermal gradient or cracks extended to the free edges

or throughout the thickness, Figure 3 (top); (Category II) in-plane tensile thermal stress generated due to the sintering of the top layer of TC, where through-thickness cracks reoriented into delamination cracks propagating parallel to the interface, Figure 3 (bottom).

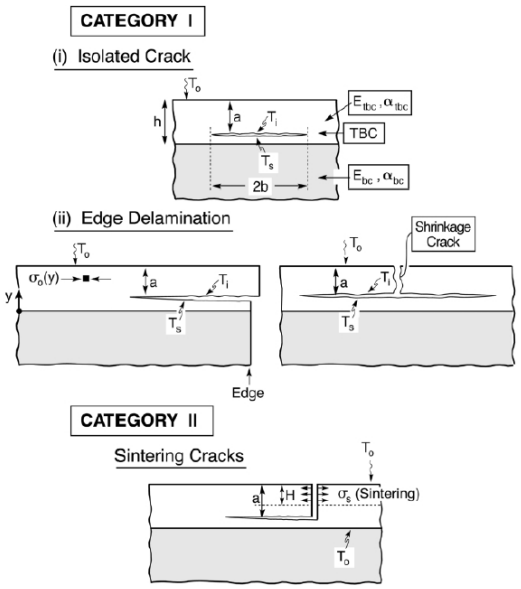

Figure 3 Schematic of the three potential modes of delamination of a TBC in the presence of a thermal gradient [128]

Choi et at[129] investigated the mechanisms of different scale buckling for EB-PVD TBCs. A critical buckling stress was developed for single layer films by considering the straight-sided blisters. For multi-layer system, there existed a critical buckling stress resultant which could initiate the large-sized buckling (LSB) process. For each case described above, once either the stress or the stress resultant was greater than the critical stress or critical stress resultant, the associated energy release rate was applied for calculating the corresponding energy consumed for crack propagation.

Semi-empirical stress model: APS-TBC

Ahrens et al [67]investigated the out-of-plane thermal residual stress generated as a consequence of the coefficient of thermal expansion mismatch between layers in APS-TBCs. The work focused on the stress distribution close to the interface where the interfacial roughness exerted a strong influence on stress level. Assuming the sinusoidal interfacial roughness profile characterized by roughness parameters, it is possible to establish an approximate relationship between the radial stress and the geometrical parameters of the bond-coat roughness.

Zhang et al [130] proposed a stress model for the top coat at the valley location for the wave-like TGO/top coat interface, which reflected a combined contribution of stresses from the bond coat and the TGO. The combination of the geometrical parameters was used to evaluate the influence of BC roughness on the thermal residual stress level at valley of TC.

Schlichting et al [127] conducted an analysis based on failure modes in APS-TBCs where an analytical stress model was used to evaluate the radial stress at the interface between TGO/BC. Assuming the TGO becomes substantially thick relative to the BC radius where the BC itself was treated as a sphere according to Eshelby's model, the radial stress governed by the thermal-expansion coefficient mismatch between the top-coat and a composite of the BC and TGO was developed, which provides a way to evaluate the thermal stress at the interface between TC/TGO and BC composite without considering the residual stress distribution within TGO/BC layer.

Beck et al [131] proposed two analytical stress functions to estimate the thermal stress within the TC and TGO as a consequence of lateral strain generated due to phase transformation from metallic BC to TGO oxide. These equations were integrated into life models at a secondary stage during cracking as crack propagation following linear elastic fracture mechanics. The function of the thermal residual

stress within the TC was proposed only considering pure elastic conditions where thermal strain was generated due to CTE mismatch between the TC and substrate during temperature drop from high temperature (Ductile Brittle transition temperature DBTT) to room temperature. The stress within the TGO layer induced by TGO growth was calculated by considering the volume change during metal-oxide phase transformation, as well as additional strain induced by oxide formed at grain boundaries within the oxide layer.

Semi-empirical stress model: EB-PVD TBC

Busso et al [132] proposed a constitutive model that accounts for the phase transformation associated with the oxidizing phase and incorporated the effect of local volumetric expansion of the newly formed oxide in the generation of inelastic volumetric strains and stresses. A hypoelastic formulation for the oxidizing metal, which could account for non-isothermal effects, was expressed in terms of the Jaumann derivative of the overall aggregate stress. Balint et al [133] proposed a set of equations to evaluate the in-plane and out-of-plane stress rate of the BC, as well as the TGO layer generated under thermomechanical fatigue test (TMF). By integrating the material parameters and thermal history, as well as the applied external loading condition, the in-plane cyclic oxide stress was calculated. The stress demonstrated anisotropy parallel or perpendicular to the loading directions, Figure 4.

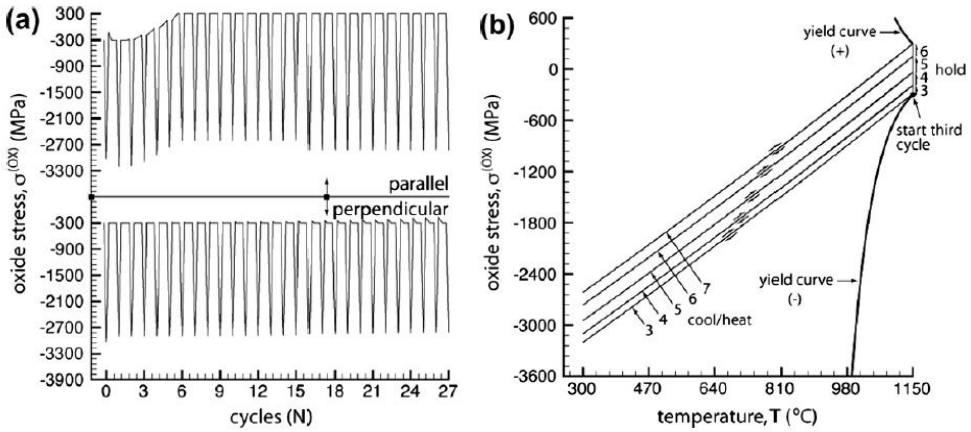

Figure 4 Stress in the oxide (a) parallel to the direction of loading and (b) perpendicular to the direction of loading [133]

This introduced undulations in different directions where the roughness amplitude was inhibited by the in-plane tensile stress parallel to the loading direction (Figure 4(a)), but facilitated by the in-plane compressive stress perpendicular to the loading direction (Figure 4(b)).

Zhao et al[134] investigated the residual stress generated as a consequence of CTE mismatch by using photoluminescence piezospectroscopy (PLPS). In their article, analytical expressions for evaluating the macro-stress, as well as the elastic modulus as a function of distance away from the TC/TGO layer were proposed. The equation for macro-stress was proposed using a peak-shifting parameter during PLPS measurement. It was concluded that both macro-stress and elastic modulus decreased from the interface to the TC surface. The same trend was observed comparing the stresses at different positions of the stressed TBC estimated by an indentation method that was determined by PLPS measurements.

Numerical models

The challenge of stress estimation with analytical models is increased with complicated interfacial roughness, non-predictable evolution of mechanical/thermal properties, and difficulties estimating strain continuity at interfaces between layers. Numerical methods, especially the finite element method (FEM), could address those problems. Various software are used for TBC FE analysis including Ansys, ABAQUS, COMSOL etc., each with its own advantages although the coding process is similar.

Typically, the difference between FE models is illustrated by different "modules" incorporated into FE calculations, for example different analytical expressions are used to describe the sintering process of the TC. There is a difference between stresses resulting from FE models that consider perfect elastic behavior vs elasto-viscoplastic behavior of the TC layer. Meanwhile, various methods of coupling the diffusion–constitutive framework for the bond coat oxidation process can be found in different publications [87], [88], [94], [135], [136]. More importantly, it is the type of TBCs that plays an essential role in determining the "module" incorporated into the FE model. For example, it is necessary to assume anisotropic material behavior for the TC deposited by EB-PVD, while isotropic material behaviors are assumed for the TC material in APS-TBCs. The factors frequently encountered in FE models are described in the following sections.

APS

Sfar et al [94] used Finite Element Analysis to numerically evaluated the thermal residual stress generated due to CTE mismatch between different layers of APS-TBCs, specifically, the stress generated close to the interface between TC/TGO and TGO/BC layers where horizontal cracks might nucleate and propagate parallel to the interface. The qualitative residual stress distribution was illustrated by FEA where the maximum tensile stress was presented at the tip of the TC close to the

interface, specifically upon heating. Sfar et al found that the valley position of the TC is always in a compression state, such that it was not considered as a critical cracking and crack propagation region. This was contradictory to conclusions obtained by others [87], [89], [90], [136]–[138] and explained further herein. Kyaw et al [137] improved the FE model by using the temperature dependent material properties and constitutive material model for the BC. The constitutive model was used for calculating the properties of aggregate BC from intermetallic phases while taking into account of temperature dependency of the MCrAlY creep. Kyaw et al found that the magnitude of stresses at the end of the cooling cycle were much greater than those at the end of steady state, and were much more significantly affected by geometry. In contrast to the conclusions drawn by Sfar et al [94], Kyaw et al considered that failure was not expected to be found at a peak of the BC, although higher tensile stresses can be found.

Nayebpashaee et al [89] applied the actual microstructures of the TBC taken by a scanning electron microscope (SEM) into a computational model that was utilized as the representative volume elements (RVEs) in the FE analysis. The purpose of the study was to predict the temperature distribution and induced residual stress in TBCs due to a) blasting stresses b) stresses due to phase transformation in ceramic top-coat c) stresses due to rapid contraction of sprayed droplets of coating materials from spraying temperature to the underlying materials named “quenching stresses” d) stresses due to differences in thermal expansion coefficients in different layers of coating called “thermal stress”. In contrast to the conclusions drawn by Sfar et al [94], Nayebpashaee et al showed that the vertical cracks initiate at the valley of TC and propagate throughout the thickness of TC which is validated by vertical distributed tensile region calculated according to his FE results. Rösler el al[87] conducted a parametric analysis where the stress was obtained at the valley of the TC with integration of different creep parameters of TC and TGO layer, as well as various geometrical parameters where a sinusoidal

interfacial roughness was assumed. Despite cooling stress generated as a consequence of the CTE mismatch, the paper focused on stress generated due to TGO growth while relaxed by TC and TGO creep behavior during high temperature holding time.

Rösler el al[138] described the factors that determine the cooling stress under thermal cylic conditions. The thermal stress induced by the coefficient of thermal expansion mismatch (CTE mismatch) was shown to increase the cooling stress within the TC, while the BC and TGO creep had oppositve behavior, which played an essential role in prolonging the lifetime of TBCs. However, the creep in BC during high temperature holding time was revealed to increase the stress level at the valley of TC layer, thus it was difficult to evaluate whether it was a beneficial or detrimental factor for TBC durability. This same conclusion was also reached from the candidate's current ph.D. research work, as described in a journal paper attached in Appendix A. Another important conlusion drawn by Rösler el al [138] was the characteristic of strain-rate independent plasticity of the BC, which facilitates the TC cooling stress, leading to a larger value of residual stress at the end of cooling process. This was also in accordance with results obatained by current Ph.D. FE model and published in a journal paper given in chapter 4. The effect of BC oxidation on thermal stress within the TC layer was also revealed by Freborg [136] by considering the creep of the TC and BC layers, as well as interfacial geometrical roughness. The results should be understood at different time scales, as well as measured positions.

Busso et al[135] established a method to describe the FE model for oxidation-induced degradation in PS-TBCs, along with the work in [139]. The oxidation of the BC was modelled by two parts, given by

i. The fraction of progressive oxide over the total amount of aluminum reservoir, evaluated by internal variable based on nucleation kinetics and

ii. The accompanying volumetric strain represented by the non-recoverable deformation rate induced by the oxidation of one of the metallic phases.

The results of the FE model then estimate the critical stress at either the peak of the BC or the valley of the TC, using elastic-perfect plastic assumption described above.

EB-PVD

In general, the methodology used for FEA for EV-PVD TBCs is similar compared to that applied to APS-TBCs. However, there are still some considerations in modelling EB-PVD TBCs which are revealed by the anisotropic behavior of materials including the following:

i. The difference in anisotropic material properties are presented compared to that of APS-TBCs, such as the elastic modulus of the TC and related anisotropic sintering and creep rate for the in and out-of-plane directions. Busso et al [139] explained the theory of transversely isotropic elastic moduli based on the 2D EB-PVD TBC FE model and calculated the fourth order elastic compliance tensor. The sintering model was given by considering the effect of internal porosity and external porosity on the TC modulus during the sintering of the TC during high temperature dwell time. This also leads to time-dependent inelastic deformation, introduced by Coble creep [140].

ii. The issues related to different progressive oxidation mechanisms of different BC layer materials was addressed including platinum-modified-aluminum (Pt-Al) overlays compared to the MCrAlY applied as traditional APS BC materials [32], [95]. These result in differences in oxidation rate, creep rate of the BC layer and swelling rate of the TGO layer. Busso et al [135], [139] described the chemical reaction of the oxidation process based on the aforementioned BC materials, which

yields different values of true mean volumetric strain with respect to different TBCs. In addition, the anisotropic phase transformation from metallic BC to TGO oxide leads to the different phase transformation rate components normal and parallel to TGO interface [135], [139].

iii. The irregular interfacial roughness profile can be profiled in the form of a sinusoidal curve as there are less "large roughness imperfections". Cheng et al [62] applied the image of metallographic sections into the FE model, which generates the FE meshes based on actual interface geometries observed from cross-sectional SEM images. Zhang et al [115], [116] developed triangular-shaped interfacial roughness profiles into FE mapping in order to characterize the critical effect of stress concentration that could be raised due to the sharp tip at the peak/valley of imperfections.

Measured stress

Residual stresses within TBCs can be measured indirectly through non-destructive methods, for example the abovementioned PLPS [134] was used to estimate the residual stress through wavelength shifts of luminescence spectra. Xie et al [53] described a evolutional PLPS method and applied it to measuring the residual stress within the TGO layer. The effect of grit-blasting on the evolution of TGO stress under thermal cyclic experiments was summarized and it was demonstrated that the lifetime of the TBC with BC surface grit-blasted varies in a narrower range which was more "engineering-preferred". Liu et al [115] measured the residual stresses within TC and TGO layers using a non-destructive approach via Raman spectroscopy (RS) and photo-stimulated luminescence piezo-spectroscopy (PLPS), respectively. It was found that the substrate curvature had a strong effect on the TGO stress distribution where the sintering of the TC for EB-PVD TBCs (intra-columnar or inter-columnar) were recorded by RS, which demonstrated two different types of Raman shifts. Tanaka et al [141] recorded the thermal stress measured within the TC along the through-the-thickness direction

using micro-Raman spectroscopy. By applying uniaxial compressive stress with specific Raman piezo-spectroscopic coefficient, the residual stresses were found to be compressive and increased in magnitude, measured from close to the surface of the TC to deeper positions. According to the Tanaka et al, the method is promising due to its ability to measure stress inside columnar grain within the TC. This could make it possible to identify the potential failure mechanism by obtaining the inhomogeneous stress distribution by mapping Raman stress throughout the TC layer.

2.2.2. Failure Mechanism analysis

Typically, failure mechanism analysis is conducted based on experimental results with further assistance of analytical/numerical models which qualitatively and quantitatively evaluate the energy release rate (ERR) generated through cracking process [1], [52], [82], [96], [125], [127], [130], [142], [143]. The cross-sectional images of failed TBC specimens are observed by SEM where crack routes can be identified. Possible failure mechanisms are then proposed using analytical solutions, where failure of the TBCs is assumed when the calculated ERR is larger than the critical fracture toughness measured experimentally. Numerical methods are developed due to the complexity of the failure process where final failure of the TBC system might be due to interactions of several factors. With assistance of numerical methods such as finite element analysis (FEA) and with powerful computing abilities, it is possible to demonstrate failure mechanisms that cannot be predicted through traditional analytical methods. Therefore, failure mechanism analysis should be conducted combining the above-mentioned methodologies together. Some failure mechanism analyses with classical theories are described below.

An early attempt was made by Clarke et al [117] based on the analysis of failure mechanisms for bi-layer film analysis, based on the mechanics of failure of thin, highly-stressed film on rough surfaces. With the analytical expressions proposed to describe the maximum out-of-plane stresses at the crest between the substrate and film layer, the elastic strain energy was developed and converted to the surface energy when a separation between film and substrate forms and extends at the interface. The classical theories for failure mechanism of tri-layer TBCs are based on several assumptions and geometrical approximations. Evans et al [125] described a general cracking route for TBCs considering a spherical imperfections as BC roughness profile, as shown in Figure 5.

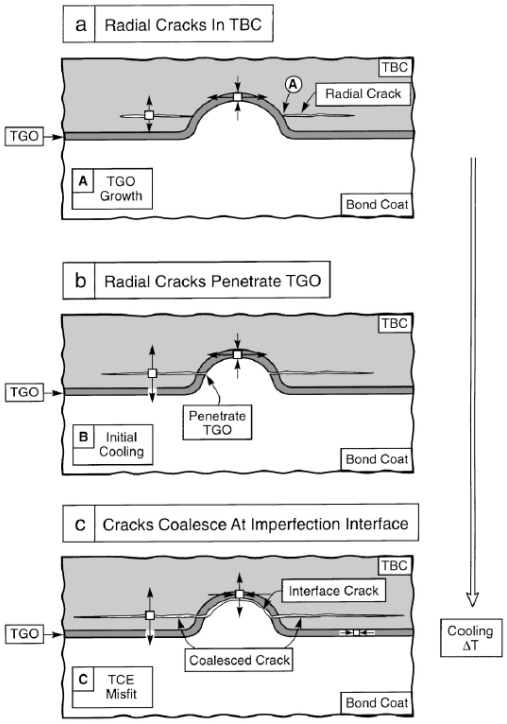

Figure 5 The schematic diagram of cracking pattern in different layers of TBCs as a consequence of residual stress distribution developed around the imperfections (a) Cracks develop within the TC layer (b) Cracks penetrates the TGO layer (c) Cracks coalescence marking the failure of TBCs [93]

The radial crack generated within the TC of Figure 5(a) is caused by tensile hoop stress developed due to TGO growth, where the analytical expression for growth stress within the TC is given. The analytical expressions for stress intensity factor at the crack tip for both inner K_{inner}^{TC} and outer crack edges K_{outer}^{TC} are given by

$$\frac{K_{outer}^{TC}}{\sigma_{TC}^{*hoop}\sqrt{R}} = \sqrt{\frac{\pi}{2}\left(\frac{a_R}{R}-1\right)}\left(\frac{R}{a_R}\right)^{2.4}$$
$$\frac{K_{inner}^{TC}}{\sigma_{TC}^{*hoop}\sqrt{R}} = \sqrt{\frac{\pi}{2}\left(\frac{a_R}{R}-1\right)}\left(\frac{R}{a_R}\right)^{0.55} \quad (1)$$

Here, *R* is redefined as an inner radius of curvature of BC imperfections and a_R is the outer radius of the equatorial ring crack. Considering the crack generated as a consequence of thermal gradient within TBCs, Hutchinson et al [128] proposed analytical expressions for different cracking scenarios, Figure 3. Based on stress analysis, the energy release rates were given for isolated cracks due to CTE mismatch between TC and substrate. In addition to existing cracks that trigger the delamination of TBCs with thermal gradients, another driving force which causes the formation of cracks is the sintering effect. Hutchinson el at[128] developed the energy release rate for the case of no elastic mismatch where the through-thickness energy release rate was evaluated.

The situation described above considers the thermal gradient activated in a high-heat flux environment where equations in [128] do not apply to a system that is thermally cycled within a furnace or when tested in a burner rig. Such a condition, when the TBC experiences a thermal gradient during temperature change within a thermal cycle, was described in [144] where the energy release rate (ERR) for the edge delamination for different positions could be evaluated given the thermal gradient during the cooling period of the thermal cycle. The total energy release rate comprises the energy release rate

generated by CTE mismatch between layers, TGO growth accompanied by metal-oxide phase transformation, a thermal gradient between the TC surface and substrate, as well as thermal shock due to rapid-heating/cooling during thermal cyclic loading. In the presence of a thermal gradient, the ERR of thermal shock could be evaluated quantitatively through the approach by Fleck el al[145]. Similar expressions were used to evaluate the energy release rate and mode mixture generated due to thermal shock. However, the effect of thermal shock is applied throughout the thickness of the TC layer. This effect is captured by different approaches to obtaining the values of stress intensity coefficients compared to that calculated in the thermal gradient-triggered ERR.

These theoretical analyses play an essential role in the development of failure theories and quantitative evaluations of crack driving forces using semi-empirical analytical solutions based on APS or EB-PVD TBCs.

APS-TBCs

YANAR et al [27] briefly summarized and compared typical failure mechanisms between APS and EB-PVD TBCs. It was generally found that both TBCs were susceptible to delamination close to the interface between TC/TGO and TGO/BC layers due to TGO growth as a result of progressive oxidation of the BC layer. For APS-TBCs, the strong mechanical interlocking provided by specifically designed interfacial roughness would impede the crack propagation along the interface. However, the durability of APS-TBCs is weaker than that of EB-PVD TBCs, especially for failure of APS-TBCs occurring in the form of spallation at the TC/TGO interface. This is due to the inter-splat defects generated during the TC fabrication process, which are potential locations for horizontal crack initiation. The FE model conducted by Nayebpashaee et al [89] was also used for failure analysis. The representative volume elements (RVEs) simulating the actual microstructure based on observations from cross-sections of

failed specimens allow the FE software ABAQUS to yield convincing results. According to the resulting computed stresses, three possible failure mechanisms are expected and are listed below.

I. A vertical crack might initiate at a peak of the TC/TGO interface and propagate normal to the interface from the surface of the TC. This crack might be generated when the in-plane tensile stresses are identified at an early stage of thermal cyclic experiments when the TGO is thin.

II. The horizontal cracks propagating along the interface between TGO/BC nucleate once the out-of-plane tensile stress at peak of roughness exceeds a critical value. This crack might be arrested when it reaches the compressive stress zone at the valley of the TC.

III. The compressive stress zone becomes in tension as TGO thickens where neighboring cracks coalescence leading to spallation of the TC.

Sfar et al[94] developed a FE model by integrating a pre-defined wavy defect within a peak of the TC close to the interface as a position for potential crack initiation. The modified crack closure integral method (MCCI) was proposed to evaluate the energy release rate (ERR) and crack propagation was assumed once the ERR for either mode I or mode II was greater than the critical ERR. However, the method was limited by the fact that only the crack in a certain configuration or under certain conditions was able to propagate. Tanaka et al [73] investigated the damage behaviour within a TGO layer under isothermal heating exposure for APS systems. Cr^{3t} luminescence spectroscopy was applied to evaluate the evolution of the in-plane stress as TGO thickness and it was found that decreasing TGO stress with initial increasing time was correlated to the TGO thickness, and also to the local undulation of the TGO layer. The change of TGO stress measured by Cr^{3t} luminescence spectroscopy is a good approach for investigation of local micro-damage evolution and is a promising non-destructive method for TBC examinations.

Another study related to the formation of TGO layer recorded by Chen et al [146] focused on the effect of the different types of pre-oxide TGO layers produced by different preheat treatments on the durability of TBCs. The generation of spinel which briefly discussed in section 1 [69]–[77], was prohibited by applying vacuum heat treatment (VHT) or low-pressure oxidation treatment (LPOT) prior to fabrication of the TC layer onto the BC layer. Thus, these techniques are expected to effectively minimize cracking within the TGO layer by limiting the formation of large amounts of detrimental spinel and in turn improve the durability of APS-TBCs. The FE analysis conducted by Rösler et al[90] focused on the position-dependent stress state and found that the maximum residual stresses generated either at valleys or peaks of imperfections were correlated to CTE mismatch developed upon cooling, and the swelling effect developed during high temperature holding time during thermal cycles. The swelling stress itself was balanced between swelling rate due to phase transformation from metallic BC to oxide TGO layer and creep strain that releases the stress during elevated temperatures. In other words, the durability of TBCs was improved by increasing the magnitude of the creep rate for TGO layers by reducing the grain size of the TGO layer thus lowering TGO stress developed during high temperature holding time.

In addition to the abovementioned numerical FE method, Białas et al[88] applied the cohesive zone method at the BC/TGO interface to simulate the critical conditions for interfacial crack initiation and propagation. The FEA demonstrated that pre-existing interfacial defects facilitated micro-crack propagation parallel to the interface, where the progressive oxidation of the BC led to a tensile zone identified within the TGO layer. The final spallation was assumed when the crack penetration through the TGO layer occurred and neighbouring cracks coalesced at the valley of the TC while the TGO thickened.

Rösler el al[138] conducted FE analysis that revealed the failure of APS-TBCs might be correlated to the shift of maximum tensile stress from the peak of the BC to the valley of the TC. The maximum tensile stress which triggered the failure of TBCs was also evaluated by the critical TGO thickness where the induced growth stress during high temperature holding time facilitated the increase of the out-of-plane tensile stress at the valley of the TC. According to the FE analysis, the maximum tensile stress was further reduced by creep of the BC and TGO layer during the cooling process, which permitted a TBC specimen with thicker TGO layer and longer life span.

A more detailed qualitative analysis on the failure mechanism of APS-TBCs involving the effect of creep of TC and BC, the growth of TGO as well as CTE mismatch was conducted by Freborg[136]. The numerical FE model calculated the thermal residual stress within the TC and BC layers with respect to different positions. The variation of stress states reveals that the failure mechanism of APS-TBCs was possibly dominated by cracking coalescence of : (1) the intial transverse crack at the peak of the BC at small TGO thickness in which the tensile stress was generated due to CTE mismatch between TC and BC layer; (2) the transverse crack found at the valley of the TC generated as a consequence of inverse tensile stress as the TGO thickened at later stages of thermal cycles. The coalescence of cracks penetrated the TGO layers and resulted in final failure of APS-TBCs.

Dong et al [147] investigated the failure mechanism in the presence of thermal gradients for APS-TBCs under thermal cyclic loading. It was found that similar cracking modes were identified between specimens under thermal cycling experiments regardless of the effect of thermal gradient where the majority of cracks within the TC were found to propagate along the non-bonded interface. As the TGO thickens, the crack positions gradually shift to the YSZ/BC interface. It was concluded that the cracking mode of APS-TBCs was not affected by the thermal gradient due to the similar cracking behavior identified with different thermal gradients applied to TBCs. In addition to the proposed analytical

solution evaluating the ERR of thermal gradient, other factors were analyzed for failure mechanisms based on APS systems. Li et at [148] suggested that the cracking path found within the TC could be significantly affected by pre-treatment of the BC layer which different types of oxides (preferred α-alumina, spinel and Cr_2O_3-based oxide) identified at the interface between TC and BC. A failure mechanism for the cracking path of the mixed oxide was developed, Figure 6.

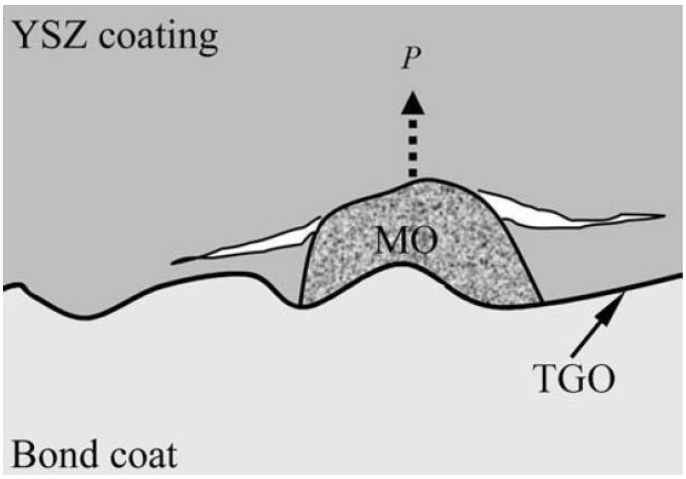

Figure 6 A schematic diagram to show the cracking style of the YSZ near the undulation troughs. MO stands for the mixed oxide [148]

The thickening of TGO layer led to the tension of YSZ surrounding the mixed oxide, which is typically identified at large protrusions at the interface of TC/BC. Such tension would facilitate the crack into the unbonded interface and even into non-molten YSZ porous particles until the associated energy release rate was alleviated and the crack was arrested. It was further suggested that the durability of TBCs would be improved by controlling the pre-treatment condition to allow the formation of a preferred dense, uniform α-alumina layer at the interface between TC and BC layers.

EB-PVD TBCs

As mentioned in the previous section, the work done by YANAR et al [27] briefly summarized the difference in typical failure mechanisms between APS and EB-PVD TBCs. The EB-PVD TBCs demonstrates its better durability due to the strain-tolerance columnar microstructure and better cohesion between TC/BC layers. Yet the failure mechanism of EB-PVD TBCs involved multi-layer cracking. To be different to the failure mechanism of APS-TBCs, the approach to increase the durability of EB-PVD TBCs was to eliminate large rough imperfections and to smooth the surface of the BC, such as with a grit-blasting process applied before the TC fabrication. Yanar et al [51] identified the discrepancies of failure mechanisms of EB-PVD TBCs with different BC layers. It was also mentioned that the reason for multi-layer cracking found in EB-PVD TBCs is due to the interfacial roughness developed due to high temperature instability of the BC. The effect of BC surface geometry on the failure mechanism was further analyzed by Vaidyanathan et al [52], as well as the effect of the grit-blasting process before TC fabrication. Two damage mechanisms are considered to be responsible for the final failure of EB-PVD TBCs. These are given as

I. The localized debonding between TGO and BC caused by the out-of-plane residual stress generated at the peak of BC and concentrated at BC grain boundaries.

II. Cavities formed at the TGO/BC interface generated as a consequence of cyclic plasticity of the BC during thermal cyclic loading conditions.

Using damage mechanism and using fracture mechanics analysis, Vaidyanathan et al [52] showed that the flaw size produced by damage mechanism I reached the critical size for massive spallation of the TC/TGO layer. This critically sized flaw was attributed as the main failure mechanism of EB-PVD TBCs with grit-blasted BC at late stage of thermal cyclic experiments. Choi et al [129] developed failure

models based on edge-delamination and buckling-delamination of the EB-PVD TBCs. The difference in cracking routes between simplified single layer films and multilayer TBCs was described. The energy functions were given to quantitatively evaluate the buckling/edge-delamination with various cracking scenarios. As mentioned in the previous paragraph, the rumpling and ratchetting behavior accompanying the microstructure evolution at the interface is considered to be the critical factor in determining the durability of EB-PVD TBCs. Zhou et al[142] performed the investigation based on Pt-Al BC under thermal cyclic loading conditions to give a better understanding of the variation of interfacial roughness, as well as progressive oxidation of the BC. By comparing the oxide growth rate, phase transformation rate, rumpling rate and stress relaxation within the TGO layer between the tri-layer coating system (TC-BC-Substrate) and the bi-layer system (ONLY contains Pt-Al BC and substrate), experimental results showed the discrepancy between the two groups. This further explicitly demonstrated the detrimental effect of TGO growth and rumpling on the durability of EB-PVD TBCs. Another detailed analysis based on the rumpling/ratchetting effect of EB-PVD TBCs was conducted by Mumm et al [149]. The author considered that as the TGO displaces downward into the BC layer, the rumpling behavior occurred periodically and left voids/small defects at the interface between the TC/TGO layers. The stress intensity factor generated by the rumpling effect was approximated and provides a methodology to characterize the life model of EB-PVD TBCs in [96].

Tolpygo et al [150] studied the degradation of interface between TC/TGO and BC/TGO layer and the parameters used to characterize the interfacial roughness quantified under thermal cyclic conditions. Photostimulated luminescence spectroscopy was used to study the degradation within the TGO layer, where the decrease of strain energy was explained by a convoluted TGO scale that corresponds to an increase in the degree of rumpling of the BC surface.

The preceding sections showed that better performance could be achieved by EB-PVD system

compared to APS-TBCs, as there is a higher strain tolerance in the horizontal direction. This is partially due to the columnar microstructure of the TC where feathery morphology and segmentation cracks are vertical between neighbouring columns. However, the durability of EB-PVD decreases when the feathery morphology disappears with necking developed between adjacent columns. This phenomena, so-called sintering of EB-PVD TBCs, occurs especially during long periods of high temperature service conditions.

Zhao et al [143] investigated the microstructure evolution and failure mechanism of EB-PVD TBCs that were affected by sintering during high temperature isothermal treatment. They measured elastic modulus of the TC as a function of measured depth (from the free surface of the TC) and high temperature exposure time, which provided useful experimental data. The cross-sectional images from the SEM indicated that microstructure with smaller columns underwent a higher sintering effect compared to larger column microstructure, thus necking generation led to a decrease in strain tolerance and early delamination within the TC layer.

Li et al [151] focused on the effect of thermal shock on the failure mechanism of EB-PVD TBCs. Their studies revealed that different cracking routes could be expected from thermal shock tests with various holding temperatures. The difference between cracking routes identified with respect to short, intermediate and long-life groups could be explained by the discrepancies in the magnitude of driving forces generated due to CTE mismatch between layers and TGO growth. Figure 7(a)(b).

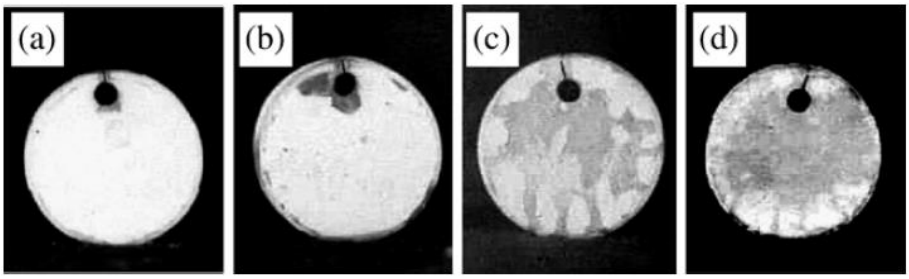

Figure 7 Surface morphologies of the TBCs after thermal shock for (a) 1000 °C/284 cycles, (b) 1050 °C/142 cycles, (c) 1100 °C/41 cycles and (d) 1200 °C/5 cycles, showing different spallation mode at different temperatures: the YSZ coating has spalled in the gray region [151]

Additionally, the phase study revealed that porous and brittle spinel formed during high temperature thermal shock tests facilitated horizontal crack propagation within the TGO along the interface. This degrades the durability of the TBCs and as consequence, the TC fails very rapidly.

For all the abovementioned failure mechanisms, the failure criterion is defined as when the accumulated strain energy (Mode I or Mode II or mix mode) reaches a critical value. For example, a critical value can be the interfacial adhesion of TBCs, which is generally considered to be a material property and independent of thermal history. However, Wu [43] studied the oxide-BC interface by applying a unique cross-sectional indentation technique, and it was found that interfacial adhesion varied dynamically as a function of phase distribution of the BC (β to γ' due to depletion of Aluminum and causes the degradation of interfacial adhesion) and TGO growth rate (*Ni, Ti* migrating to the interface hinders the formation of stable α-alumina and forms less durable titanium oxide), while it had little influence on TGO rumpling and residual stresses.

In addition, with the assistance of failure mechanism analysis, a lifetime prediction model can be proposed based on different cracking scenarios identified at corresponding positions in the TBCs. Similar to the failure mechanism analysis, a variety of methods (e.g. semi-empirical analytical models

or numerical models based on FEA) were applied to conduct lifetime prediction for TBCs. The capability of a lifetime prediction model can be improved through the combination of two methods which allows more factors affecting durability to be integrated into the model. Based on different TBCs, several typical life models are briefed below.

APS-TBCs

An early attempt was made by Miller et al [152] to study the failure of APS-TBCs triggered by oxidation-induced strains with cyclic strains generated in the cooling process. These factors led to crack growth in the ceramic TC layer. Another early lifetime prediction model was reported by Demasi et al [85] through NASA. The lifetime of APS-TBCs (in the form of log time) was plotted as a function of interface temperature between ceramic coating and metallic BC. Vaßen et al [81] proposed a semi-empirical analytical life model based on numerically estimated residual stress distribution. As the crack propagates from its initial size to failure crack size, the lifetime is obtained. The fitting parameter in [81] was calculated using a curve fitting algorithm where only one experimental life data was used. The life model was then improved by Zhang et al [130] where the fitting parameters were fitted to different dwelling temperatures during thermal cyclic loadings. It was established that the discrepancy between estimated and experimental lifetime could be minimized by applying the abovementioned revisions. Evans et al [125] proposed a simplified model to describe the coalescence of cracks within a ligament. In this case, failure was assumed when the TGO reaches critical thickness and since the thickness of the TGO layer can be estimated through a parabolic law, the critical time for spallation can be evaluated. Beck et al [131] developed the analytical expression of lifetime prediction based on crack growth theory under thermal cyclic conditions. Two different cracking models were assumed where the crack generation within the TC can be separated by 1) incubation phase and 2) propagation phase. The lifetime was estimated from the total energy release rate computed by equating the crack growth rate and fitting

parameters. Busso et al [153] developed a numerical lifetime prediction model where the cumulative damage at the peak of the TC layer was triggered by thermal residual stress developed during thermal cyclic conditions. The degradation of intrinsic cleavage strength was correlated to the evolution of localized microstructure damage, which further led to a cleavage-type mechanism failure of APS-TBCs at a macroscopic level. Traeger et al [80] developed a lifetime prediction model based on a numerical method where a pre-defined crack was introduced at the interface of either the peak of the TGO/BC interface or the valley of the TC/TGO layer. The predicted lifetime demonstrated good agreement compared to results from thermal cyclic experiments.

EB-PVD TBCs

Similar to APS-TBCs, lifetime prediction models for EB-PVD TBCs are also related to specific failure mechanism analyses. The factors influencing the lifetime of EB-PVD TBCs, such as substrate materials, chemical doping of the elements, preheat treatment methods, fabrication methods were also investigated in the literature [4], [30], [57], [154]–[158]. The damage model describing either the microscopic localized damage or macroscopic elastic buckling of the TC proposed by Courcier et al [82] was used to conduct lifetime prediction for both isothermal and thermal cycling loading conditions. With the assistance of thermal-mechanical fatigue tests (TMF), the damage mechanism was analyzed based on increasing spallation area for TBCs fabricated on the turbine blade. Strangman et al [97] investigated the possible failure mechanism with its correlated lifetime model based on different types of damage modes. Zhang et al [96] proposed an analytical model to evaluate the lifetime, with the lifetime prediction based on the failure mechanism in EB-PVD TBCs triggered by the rumpling effect. Based on the FE model established from previous work, Busso et al [159] developed a software tool that can be used to predict the remaining life of EB-PVD TBCs. The key process of the system identifies critical

stresses at possible positions for crack nucleation based on well-analyzed failure mechanisms. It is considered as prototype software for further development of a lifetime prediction tool of TBCs.

3. Stress Models for Electron Beam-Physical Vapor Deposition Thermal Barrier Coatings Using Temperature-process-dependent Model Parameters

This chapter addresses objectives 1 and 2 by numerical finite element modelling to estimate the development of residual stresses in EB-PVD TBCs under thermal cycling environment.

B. Zhang, K. Chen, and N. Baddour, "Stress models for electron beam-physical vapor deposition thermal barrier coatings using temperature-process-dependent model parameters," *J. Eur. Ceram. Soc.*, Apr. 2021, doi: 10.1016/j.jeurceramsoc.2021.04.046

[a]*B. Zhang,* [b*]*Kuiying Chen,* [a] *N. Baddour,*

[a] *Department of Mechanical Engineering, University of Ottawa, Canada*

[b] *Structures, Materials and Manufacturing Laboratory, Aerospace Research Center, National Research Council Canada*

Abstract

This article presents a new stress model for EB-PVD TBC to provide insight into TBC failure mechanisms. Cycling-induced and temperature-process dependent model parameters are incorporated into stress analysis of EB-PVD TBC and then used to simulate the variation of mechanical, thermal and inelastic behaviour from metallic bond coat to thermally grown oxide (TGO). This gives a smooth evolution of residual stresses and is more realistic than prior finite element (FE) work. Two types of interfacial roughness approximate profiles are presented and implemented in the FE model. Geometrical parameters are used to model the interface roughness, and residual stresses are then evaluated at specific positions within TBCs. This article's stress analysis establishes a link between stress distribution and the evolution of interfacial roughness during thermal cycles. Consequently, the results are expected to provide insight into the failure modes related to localized interfacial roughness evolution.

Keywords: EB-PVD TBC**,** Stress model, Finite element, Temperature-process dependent model parameters, Failure mechanism analysis.

3.1. Introduction

Thermal Barrier Coating systems (TBCs) have been developed to work as a thermal isolator to protect turbine blade substrates from hot burning gas attacks for decades [10], [12], [13], [101], [160], [161]. Aligning with efforts on new fabrication methods of TBCs, investigations of prolonging the durability of TBCs were also conducted. One of the most significant tasks is to understand the failure mechanisms upon which the lifetime of TBCs can be evaluated numerically [1], [120], [125], [162], [163]. The lifetime prediction methods of TBCs can be categorized as empirical models, physics and/or mechanics-based models where analytical and/or finite element tools are normally used [81], [96], [153], [164]. An early attempt was made by a NASA program [5][6], in which the number of cycles to failure was correlated to critical strain range and critical Thermally Grown Oxide (TGO) thickness. Evans et al. [8] developed a life model where failure is assumed when the multilayer cracks converge within topcoat/TGO/bond coat regions. The life is estimated in terms of the critical TGO thickness. The critical amplitude of roughness measured from the bond coat surface was also a crucial parameter in evaluating lifetime based on specific failure mechanisms in Electron Beam-Physical Vapor Deposition Thermal Barrier Coating (EB-PVD TBC) systems [1]. Courcier et al [82] developed a damage model of EB-PVD TBC that involves a damage parameter describing either the effect of decreasing interfacial strength on coating delamination under isothermal conditions or the effect of overall strain induced by interface rumpling and TGO growth under the thermal cycling process. Busso [153] developed a damage-mechanics-based life prediction model for Air Plasma Sprayed-Thermal Barrier Coating (APS-TBC) systems where two scales of damage, at both microscopic and mesoscopic levels, were investigated. Vaßen et al [81] estimated the life of APS-TBCs by evaluating subcritical crack growth rate by using fitting model parameters**,**

$$\int_{a_0}^{a_f} \frac{da}{a^{m/2}} = \frac{A^* Y^m}{K_{I,c}^m} \int_{t_0}^{t_f} \sigma^m dt \qquad (2)$$

Where a stands for the crack length and $A^{*}Y^{m} / K_{IC}^{m}$ is a fitting parameter. The residual stress σ in equation (2) is used to compute the lifetime t_f through iterating integration of the stress function on the right-hand side and then by equating it to the integration of cracking growth rate on the left-hand side through the fitting parameter. Zhang et al. [164] further improved the life model by using temperature-dependent fitting parameters. As a result, the deviation between the predicted life and measured life data was significantly decreased. Frachon *et al.* [165] proposed a multi-scale and multi-physics approach. Their approach was implemented into the finite element method and used to predict the local stress and strain fields driving the evolution of observed interfacial local damage, which in turn can be adapted to predicting TBC lifetime for long in-service conditions.

In addition to the early proposed semi-empirical life models, stress modelling is also a critical component in lifetime prediction methods [81], [96], [137], [164], [166]–[168]. A small change in stress calculated from a stress model compared with the measured stress within TBCs can significantly affect the lifetime model's performance [81]. Meanwhile, geometrical parameters describing the interface roughness profile are also essential to determine the residual stress distribution [96]. Average values of interface geometry parameters have been applied to stress analysis [67], [87], [135], [136], [164], [129]. However, using temperature-process-dependent model parameters in Finite Element (FE) analysis, the improved maximum residual stresses can be calculated. Consequently, possible positions of crack formation in TBCs could be identified.

This paper aims to enhance the understanding of the failure modes of EB-PVD TBC by developing a stress model that incorporates both geometrical and temperature-process-dependent parameters. Specifically, (a) Two methods to characterize the imperfections close to the TC/TGO and TGO/BC interfaces are developed, and related interface geometrical parameters are defined. (b) Temperature-process dependent model parameters [92] are incorporated into FE models. (c) Failure modes of EB-PVD are then explored based on the stresses calculated at the valley of the TC and the ridge of the BC.

3.2. Compilation of Parameters and Integration in FE Models Using Experimental Data under Thermal Cyclic Condition

In the current section, two types of parameters used for the FE simulations are introduced. Parameters describing mechanical and thermal properties of materials are the elastic modulus and coefficient of thermal expansion for different layers of TBCs. Other parameters used are geometrical parameters illustrating the roughness profile at the interface between each layer. It is noted that these parameters are either temperature-dependent or temperature-process dependent, which implies that the thermal properties and the roughness of the interface change with both temperature and process. It is also noted that by using those process-dependent parameters incorporated into a stress model, a process-dependent stress behaviour, i.e., the cyclic stress in the current study, can be estimated. Compared to previous studies that focus on a defined roughness profile using constant geometrical parameters during geometrical sketching [68], [95], [135], [139], in the present paper, five sets of geometrical parameters characterizing the level of roughness at specific stages of thermal cycles are used in the FE models. It is expected that the resulting stresses would provide a more comprehensive understanding of roughness evolution on the stress states, which in turn helps explore the failure mechanisms of EB-PVD TBCs under the thermal cyclic process.

3.2.1. Simulation of thermal properties for different layers under the cyclic thermal condition

The mechanical and thermal properties of EB-PVD TBCs include the elastic modulus and thermal expansion coefficient (CTE). The elastic modulus of the TC is mainly affected by sintering during a high-temperature exposure period. For EB-PVD TBCs, the columnar structure with large external porosity between each column can be visualized from a Scanning Electron Microscope (SEM) cross-

section image, while small internal porosity and vertical segmentation cracks also exist within each column [139]. Apart from the thermal gradient affecting TC's sintering behaviour, it is assumed in the present study that the sintering of EB-PVD Yttria stabilized Zirconia (YSZ) the consolidation of the internal porosities controls TC. In contrast, the external porosity remains unchanged through high-temperature exposure. For the coordinate system used in the present study, material properties along the in-plane directions represented by subscripts 11 (*x*-direction) and 33 (*z*-direction) are equivalent due to the transversely isotropic assumption of YSZ, while material properties of the out-of-plane direction are represented by subscript 22 (*y*-direction), as illustrated in Figure 8 [32]. For example, the sintering effect on elastic moduli of transversely isotropic E_{11} at 1151°C is shown in Figure 9.

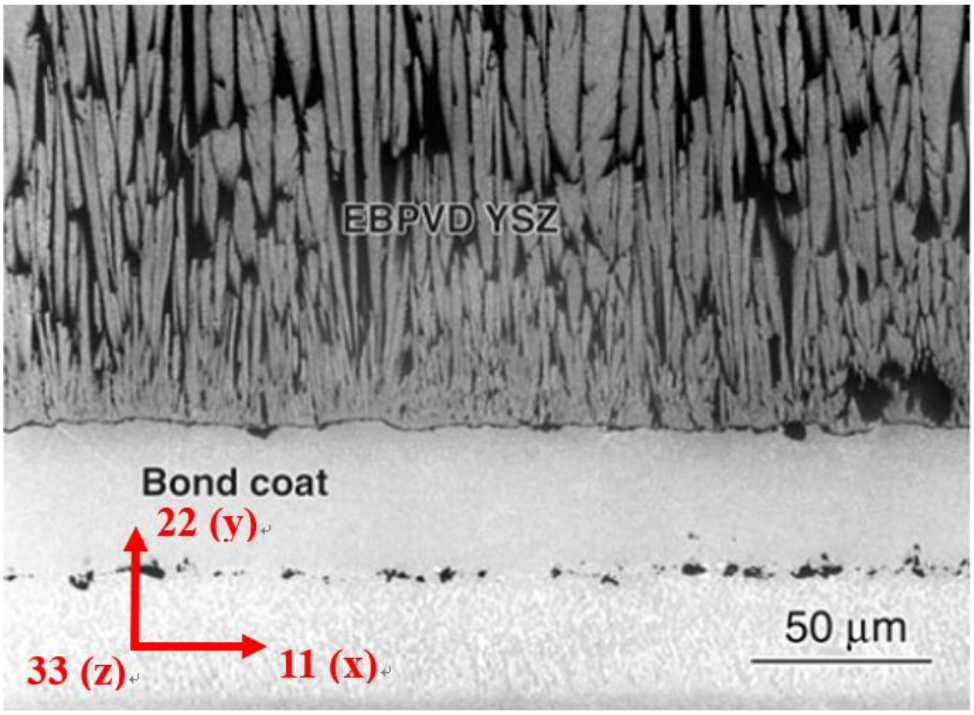

Figure 8 Definition of the transversally isotropic material axis within the bond coat material [32]

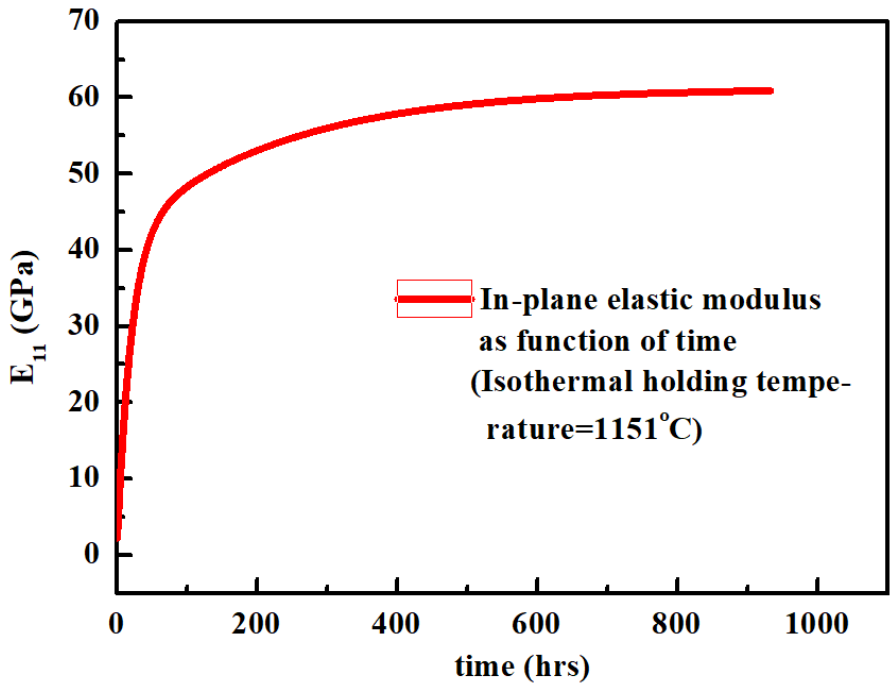

Figure 9 In-plane elastic modulus of TC in EB-PVD coating as a function of time at 1151 °C [139].

The sintering effect on E_{11} can be formulated as [139]

$$E_{11}(t) = \left(\frac{\rho - \rho_0}{1 - \rho_0} \right) \times E_{22}(t) \tag{3}$$

$$\rho = 1 - (p_e + p_i) \tag{4}$$

Where ρ is the total relative density of the material, ρ_o is the value of ρ at an initial time. Additionally, p_i and p_e are relative internal and external porosities of YSZ topcoat, which are related to the relative internal and external densities ρ_i, and ρ_e, respectively. Due to the TC layer's anisotropic property, the out-of-plane elastic modulus E_{22} is calculated from equation (5) [139], and the result is plotted versus the number of thermal cycles, Figure 10.

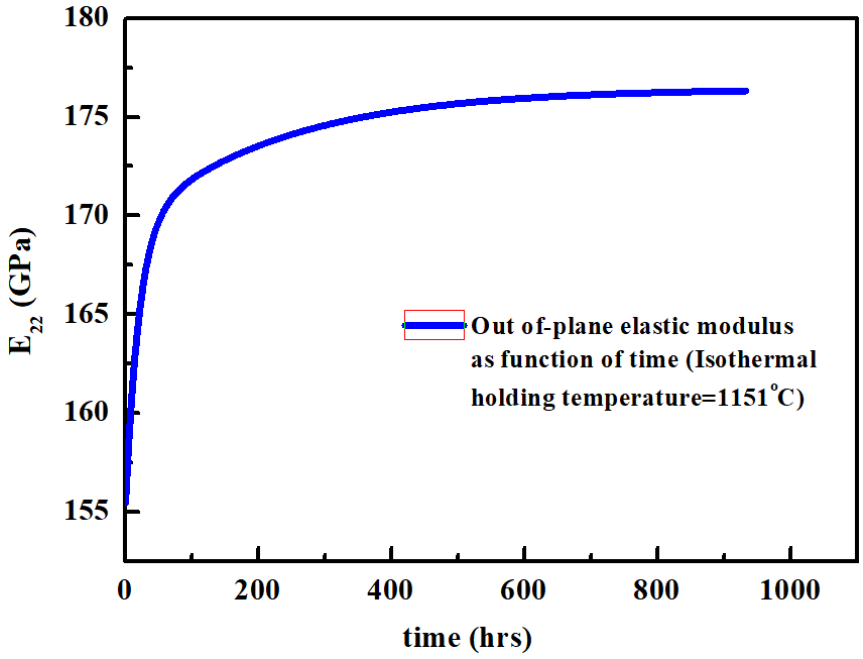

Figure 10 The out-of-plane elastic modulus of TC in EB-PVD coating with respect to time

$$E_{22}(t)=\left[1+\frac{1.5(1-\rho_i)(1-\upsilon_{21})(9+5\upsilon_{21})}{7-5\upsilon_{21}}\right]^{-1}E_{22R} \qquad (5)$$

Here, ν_{21} is the Poisson's ratio in the *x-y* direction, E_{22R} is Young's modulus of fully dense isotropic Zirconia, and *t* is time.

A ratio of the out-of-plane elastic modulus to that of the in-plane is shown in Figure 11.

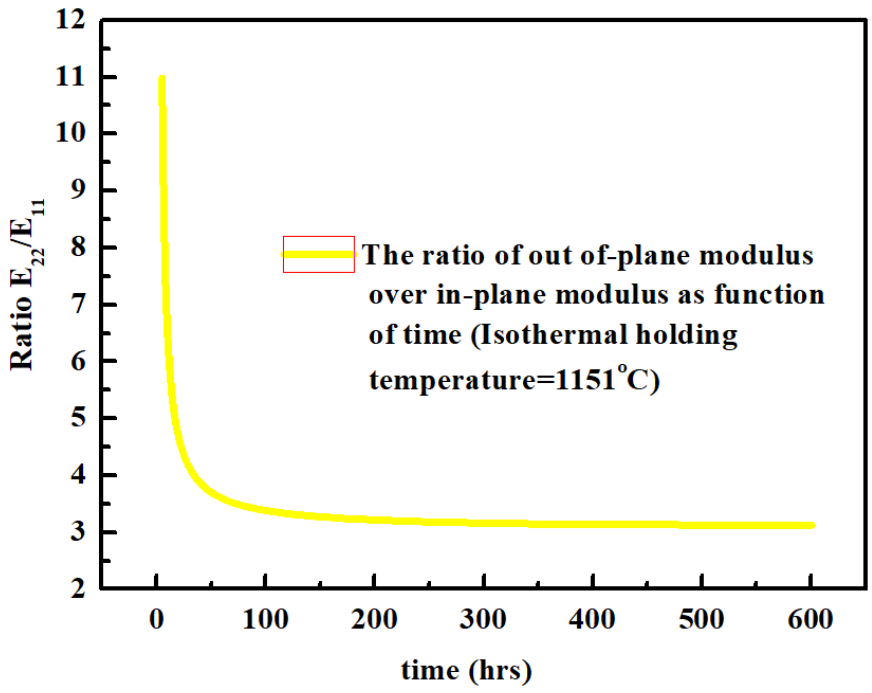

Figure 11 The ratio of the out-of-plane elastic modulus over the in-plane modulus with respect to time

The consolidation and closure of pores within columnar structures resulting from sintering leads to a sharp increase in the in-plane elastic modulus during the initial 50 hours of sintering and then remains a constant ratio of 3.5 for additional 500 hours of sintering. The elastic moduli versus temperature are listed in Table 1 [95], which shows a decreasing pattern as temperature increases after sintering for 100 hours at 1473K.

Table 1 The elastic modulus variation as temperature changes [95]

T(*K*)	293	473	773	973	1173	1373	1473
$E_{11}(GPa)$	67	64	61	59	58	56	56

$E_{22}\left(GPa\right)$	205	196	188	182	178	174	173

It is difficult to measure elastic modulus under the thermal cycling process. Therefore, in this paper, it is assumed that the increasing pattern of elastic modulus upon cooling during thermal cycling follows the same pattern as that of the elastic modulus when heating back. Also, within the dwell period during thermal cycling, the elastic modulus is merely affected by high-temperature sintering. During a thermal cycling period, as the duration of both heating and cooling processes is much shorter than a high temperature dwell period, the effect of sintering on modulus changes can be ignored for this heating/cooling process.

To simulate the changes of elastic modulus versus temperature T during thermal cycling, the moduli in Table 1 are formulated and then fitted approximately by equations (6)-(7) as,

$$E_{22}\left(T\right)=\gamma_2 \exp\left(\frac{\zeta_2}{T+\varpi_2}\right)+E_{20}\left(t\right) \tag{6}$$

$$E_{11}\left(T\right)=\gamma_1 \exp\left(\frac{\zeta_1}{T+\varpi_1}\right)+E_{10}\left(t\right) \tag{7}$$

where γ_i, ζ_i, ϖ_i are fitting parameters (i=1,2). $\gamma_1=41.58387$, $\zeta_1=918.27421\ K$, $\varpi_1=1638.6676\ K$, $\gamma_2=132.27447$, $\zeta_2=814.80164\ K$, $\varpi_2=1574.48149\ K$ are obtained by fitting to the results shown in Table 1. E_{i0}(t) are process-dependent moduli of the TC estimated from isothermal sintering at the end of high-temperature thermal cycles using equation (3) and (5).

The cyclic temperature field pattern used to describe temperature variation within a thermal cycle was chosen as,

$$T = \begin{cases} 112.6 \times t + 20 & (0 \le t < t_1) \\ 1150 & (t_1 \le t < t_2) \\ -112.6 \times t + 6761 & (t_2 \le t < t_3) \end{cases} \quad (8)$$

In an equation (8), t_1, t_2 and t_3 represent durations of heating, dwell and cooling processes. Following equation (7), the cyclic temperature pattern is shown in Figure 12.

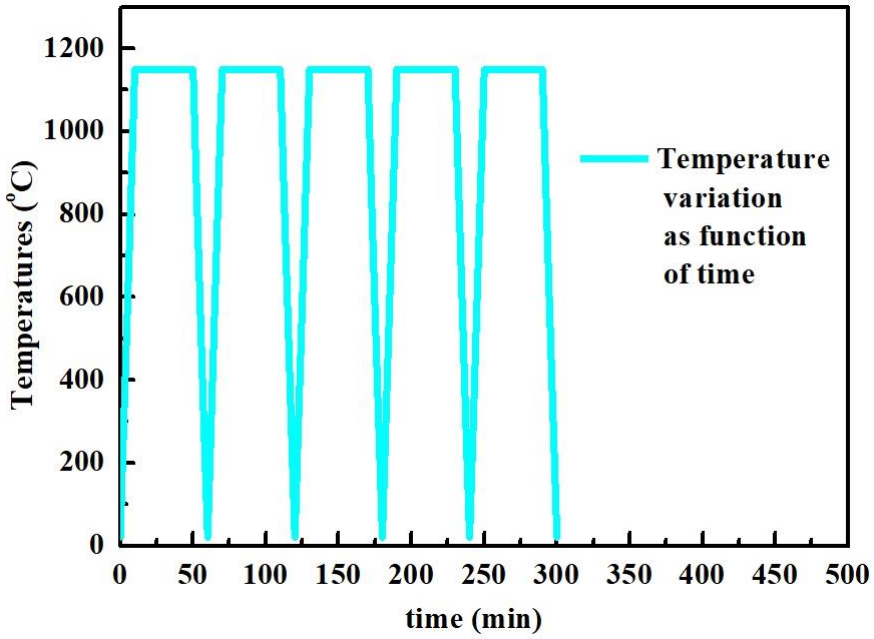

Figure 12 Temperature variation used in simulations under cyclic thermal conditions

The patterns of the in-plane and out-of-plane elastic moduli versus thermal cycles are shown in Figure 13 and Figure 14 for a selected short period, while the entire trend of these two elastic moduli of TC versus thermal processes is depicted in Figure 15.

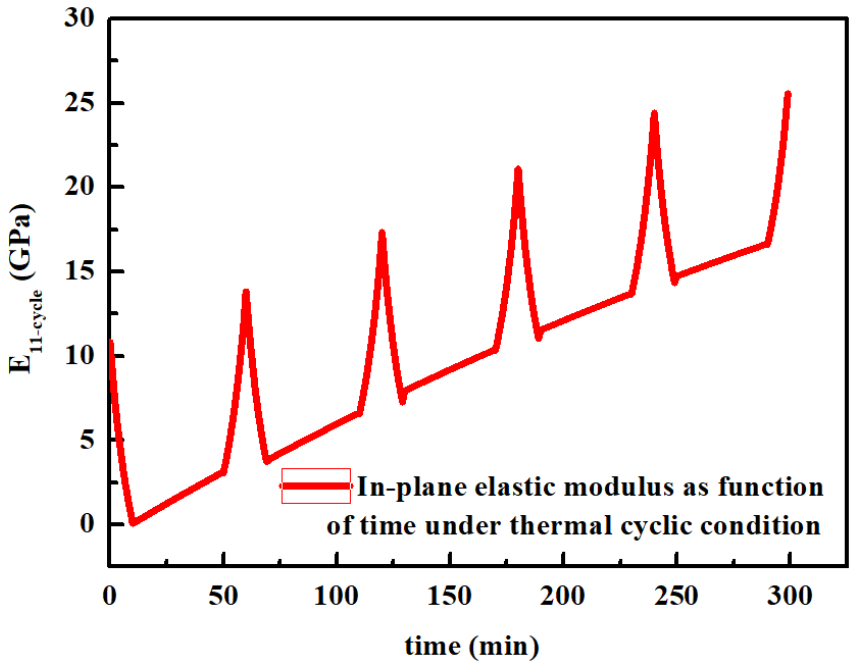

Figure 13 In-plane elastic modulus under cyclic thermal condition

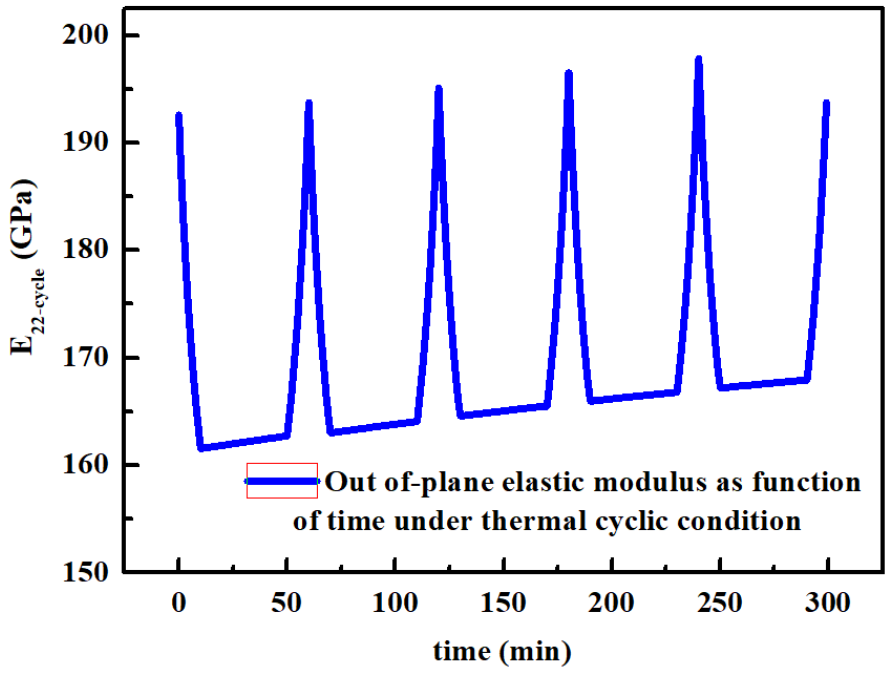

Figure 14 Out-of-plane elastic modulus under cyclic thermal condition

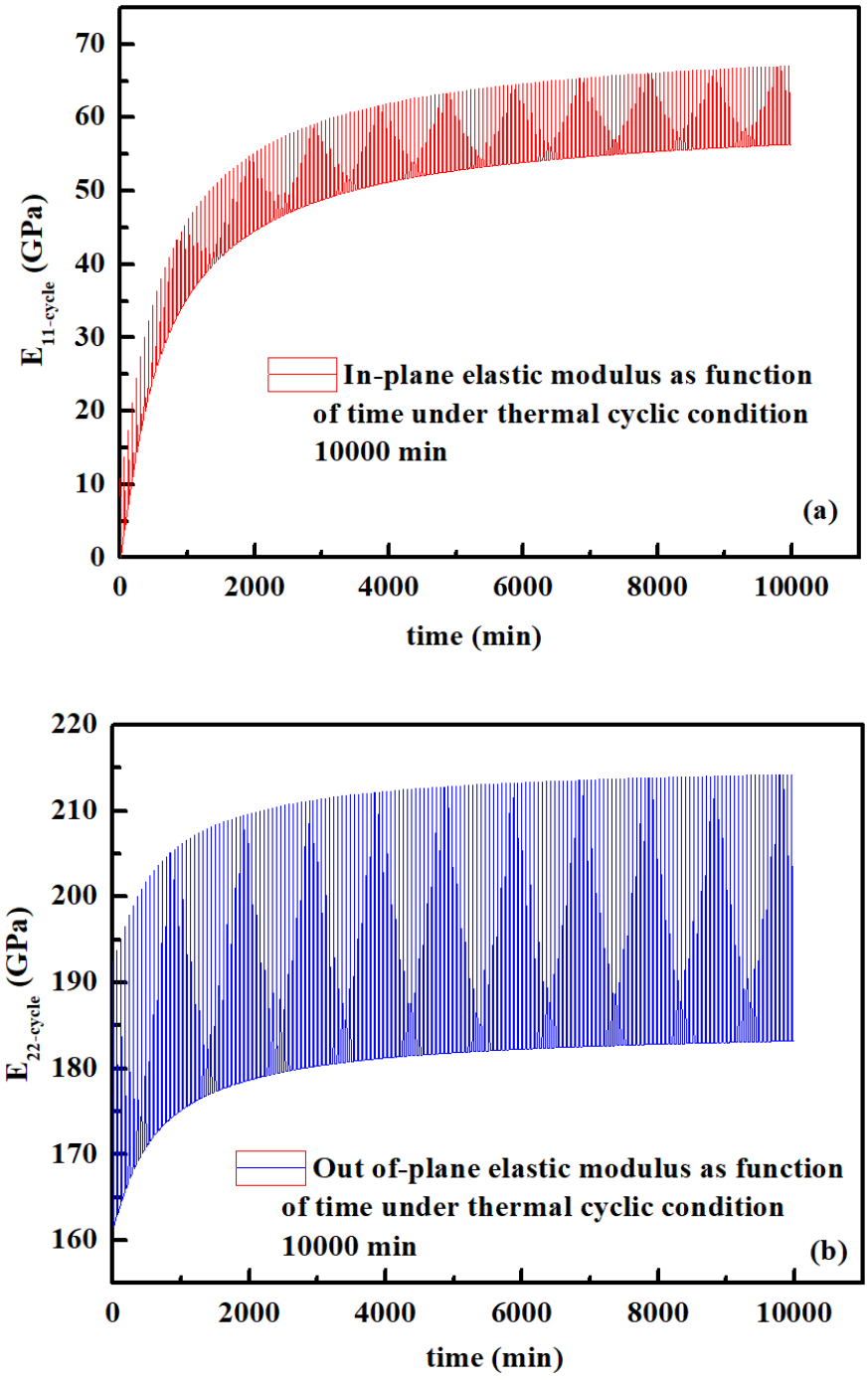

Figure 15 The general trend of elastic moduli as a function of time under cyclic thermal condition (10000 min) (a) in-plane (b) Out-of-plane

The temperature-dependent elastic moduli of BC (E_{BC}) and TGO (E_{TGO}) are described as [95],

$$E_{TGO}(T) = -0.07506 \times T + 448 \tag{9}$$

$$E_{BC}(T) = -0.02329 \times T + 123.9 \tag{10}$$

Also, the temperature-dependent coefficient of thermal expansion α (with the subscript indicating the layer) is described by [95],

$$\alpha_{TBC}(T) = (0.0003636 \times T + 9.615) \times 10^{-6} \tag{11}$$

$$\alpha_{TGO}(T) = (0.001388 \times T + 7.532) \times 10^{-6} \tag{12}$$

$$\alpha_{BC}(T) = (0.005021 \times T + 10.83) \times 10^{-6} \tag{13}$$

Expressions (9)–(13) will be used to calculate thermal and residual stresses in thermal cycling simulations.

3.2.2. Creep, swelling and inelastic behavior of BC/TGO layers during the high-temperature process

The inelastic behaviour for BC/TGO layers are described by creep rate [95] in terms of equivalent von Mises stress σ^V, elastic modulus and temperature *T*. Specifically, the creep rate tensor $\dot{\varepsilon}^{cr}$ for both BC and TGO is expressed as [95],

$$\dot{\varepsilon}_{BC}^{cr}=6.3\times10^{13}\left(\frac{\sigma_{BC}^{V}}{E_{BC}}\right)^{4}\exp\left(-\frac{125}{8.314T}\right) \tag{14}$$

$$\dot{\varepsilon}_{TGO}^{cr}=6.8\times10^{3}\left(\sigma_{TGO}^{V}\right)^{2.3}\exp\left(-\frac{424}{8.314T}\right) \tag{15}$$

Expressions (14) and (15) are used to describe the creep property of (Ni, Pt)Al- BC and α-Al_2O_3 TGO [169], [170]; both of these materials are assumed to be isotropic and homogeneous.

The inelastic behaviour such as the swelling rate of the TGO during progressive oxidation of the BC is described by Busso et al. [153] as,

$$D^{tr}=f_{\beta}^{ini}\dot{f}_{(Ni,Pt)Al}\left(\sqrt{\frac{3}{2}}P\frac{S'}{\tilde{S}}+e_{V}^{T}1\right) \tag{16}$$

Where the inelastic stretching tensor D^{tr} shows the non-recoverable deformation rate induced by oxidation of metallic phase, f_{β}^{ini} represents the initial volume fraction of metallic phase which has not been oxidized and $f_{\beta}^{ini}=0.38$ was chosen according to [95]. P is a coefficient that depends on the shape of the oxide particles. $\tilde{S}$ and S' are the norm and deviatoric components of the aggregate stress tensor. Furthermore, e_{V}^{T} is the mean local dilatational strain induced by the transformation of the initial metallic phase and $\dot{f}_{(Ni,Pt)Al}$ illustrates the evolution of the internal variable $f_{(Ni,Pt)Al}$ that is defined as the normalized fraction of the oxidizing phase which has chemically reacted with O_2, varying in value from 0, before the oxidation begins, to 1 when primary oxidation is complete. If the isothermal load is applied to the TBCs, the parabolic formulae of TGO growth for (Ni, Pt) Al BC is used, and the internal variable $f_{(Ni,Pt)Al}$ is described as,

$$f_{(Ni,Pt)Al}=\frac{A_{TGO}^{Gr}t^{P_{TGO}}}{d_{TGO}^{tot}} \tag{17}$$

Here d_{TGO}^{tot} is the total thickness of the TGO layer in a predefined time, $d_{TGO}^{tot} \approx 4.92\mu m$ according to [92] at 1151°C. A_{TGO}^{Gr} and p_{TGO} are the coefficients of TGO growth rate and growth exponent, respectively. T is the temperature during a dwell period and t is an exposure duration. $\kappa_B \approx 8.314 \ \ KJ/(mol \cdot K)$ is the Boltzmann constant. According to [153], the equation (17) only works for local oxygen concentration, $C_O > C_{Ocr}$ where C_O is oxygen concentration and C_{Ocr} is the critical value of oxygen concentration which defines the onset of oxidation. The equation describing the TGO growth and the evolution of the internal variable under cyclic thermal conditions will be described in the following section. In addition, it is also noticed that the growth strains do not develop isotropically [139]. The ratio of phase transformation strain of normal over parallel to the TGO interface is taken to be 87 and is used in the current modelling [139]. The temperature-dependent yield stresses of both BC and TGO are taken from [68] and [171] and are shown in Figure 16 and Figure 17, respectively.

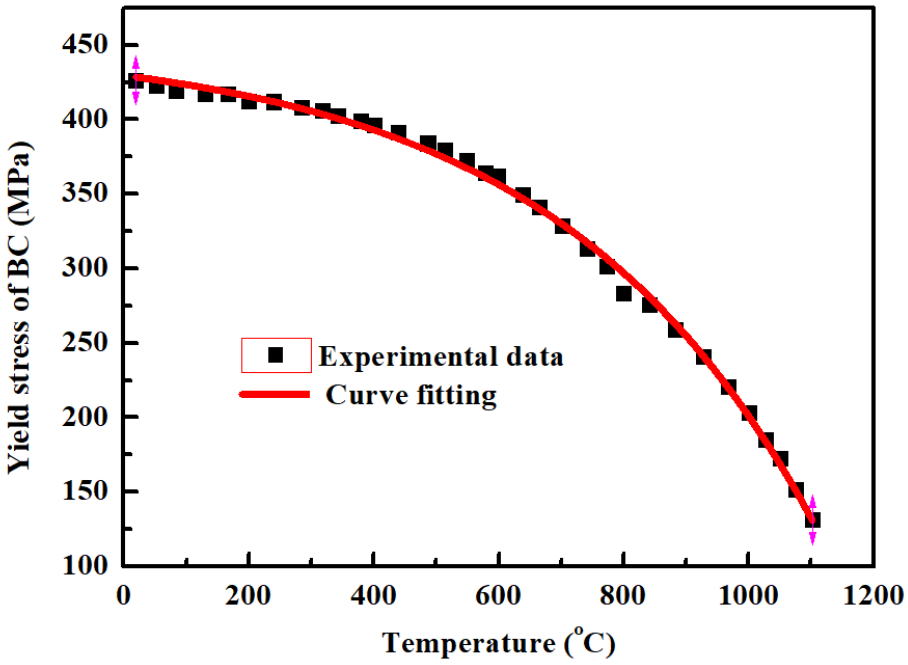

Figure 16 The experimental data of temperature-dependent yield stress of BC [68] together with a fitting curve

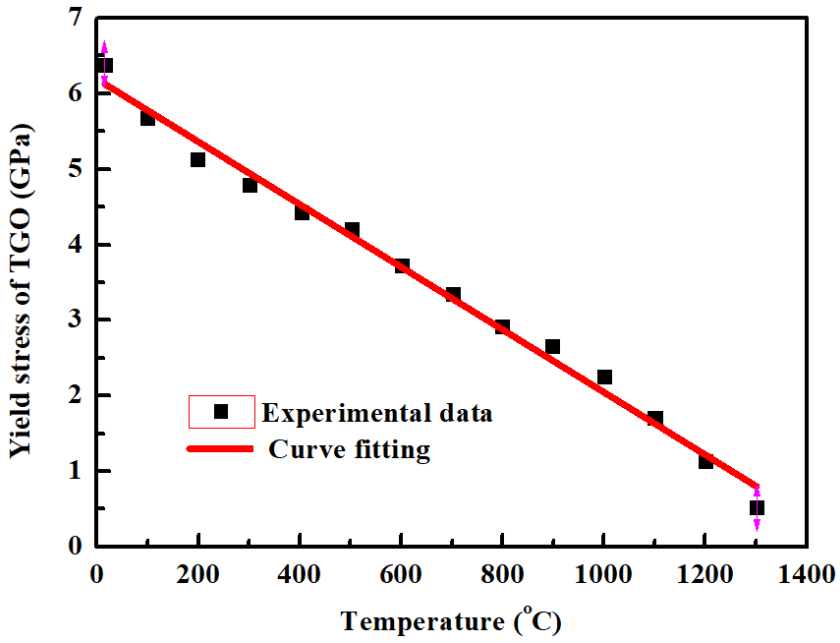

Figure 17 The experimental data of temperature-dependent yield stress of TGO [171]together with a fitting curve

3.2.3. Temperature-process dependent geometrical parameters

According to Wen et al. [92], the geometrical parameters used to characterize the interfacial roughness profile vary versus the number of thermal cycles. Therefore, varying interface roughness profiles could result in stress changes during thermal cycling [67], [95]. The work by Maurel et al. [91] was proposed to model the complex morphology of rough interfaces using Fourier techniques and image analysis. Both 2D and 3D FE models were established using a sinusoidal profile describing the realistic interfacial roughness morphology. The stresses were calculated and illustrated in both crosses- 2D views of cross-section area and 3D views of the bond-coat layer. A key feature of the presently proposed interface model consisting of [91] is the assumption of the similarity between the TC/TGO interface and TGO/BC interface, as the thickness of the TGO layer is much thinner compared to the entire thickness of the

TBC. This approximation avoids a duplicated curvature radius at both TC/TGO and TGO/BC interfaces. The simplification is made aiming to keep the number of parameters small in evaluating residual stresses.

The method to evaluate the roughness profile of EB-PVD TBCs differs significantly from that used for Atmospheric Plasma Sprayed-Thermal Barrier Coating systems (APS-TBCs) [92]. For APS-TBCs, large interface roughness is required to provide mechanical interlocking between the topcoat and the bond coat (TGO) layer [172], [173]. It is assumed that the surface roughness remains unchanged as the thermal cycle proceeds. To simplify the evaluation of thermal stresses between the topcoat and TGO in APS-TBCs, the average roughness is estimated using the amplitude and wavelength for sinusoidal-like interfacial roughness, Figure 18.

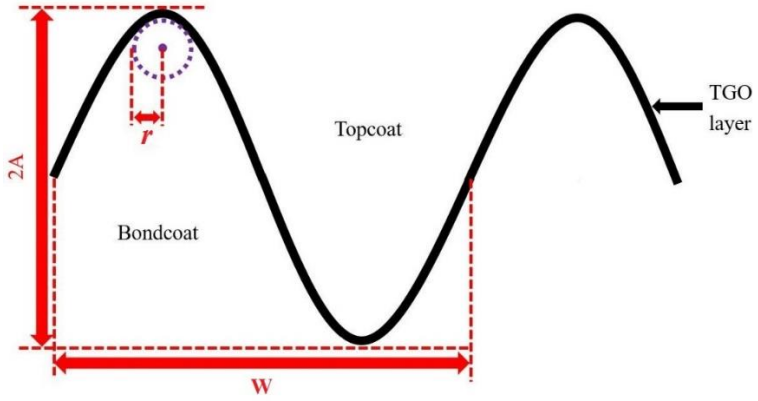

Figure 18 Schematic diagram of interfacial roughness profile simulated according to APS-TBCs [67]

The average roughness measured using a radius of curvature for APS-TBCs is given by

$$r = \frac{W_{APS}{}^{2}}{4\pi^{2}A}, \tag{18}$$

Where A represents the amplitude of localized imperfections, and W_{APS} is a parameter used to define the horizontal length of localized imperfections in APS-TBCs.

It is noted that the radius of curvature r in equation (18) is used to describe the horizontal width for a single localized imperfection at the interface between the topcoat and BC layer within APS-TBCs. These imperfections have dual-effects on the durability of TBCs, i.e., a relatively large interfacial roughness could effectively reduce the stored elastic strain energy during crack propagation. However, these defects also induce stress concentration, especially close to the tip of roughness, enhancing the local energy release rate that facilitates crack initiation [174]–[176].

Some studies characterize the roughness of EB-PVD TBCs by using a similar approach of expression (18) to describe the roughness of APS-TBCs [52], [150]. For EB-PVD TBCs, however, the Pt-modified β-NiAl bond coat is usually treated using grit blasting to flatten the bond coat surface to reduce the interfacial roughness between the bond coat and the topcoat [53], Figure 19.

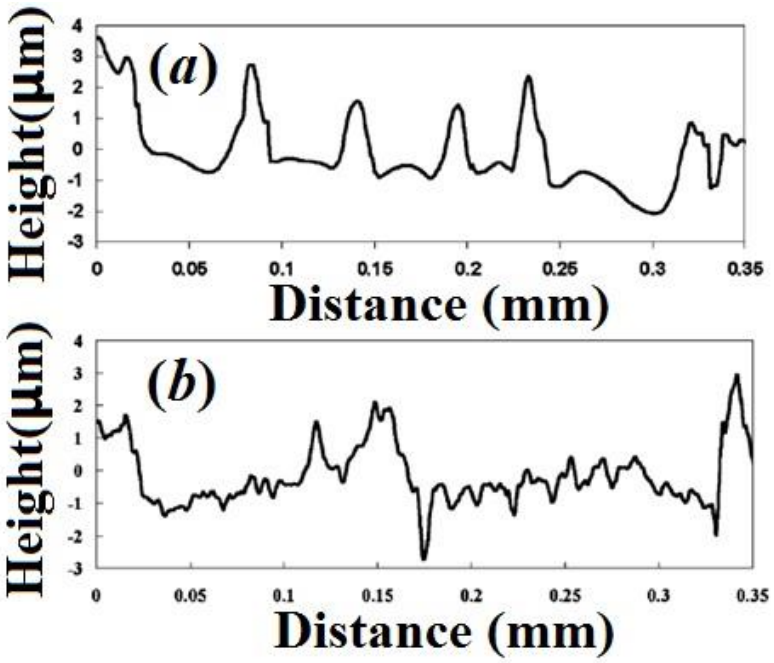

Figure 19 Bond coat surface morphology and profile along the marked line before (a) and after (b) grit blasting [53] in EB-PVD TBCs

Meanwhile, this grit blasting process is also used to compact the bond coat layer and substrate [96]. For EB-PVD TBCs, cracks can be found within the topcoat close to the topcoat/TGO interface layer [149], Figure 20, and cracks can also be initiated at ridge of the bond coat at an early stage of the cyclic thermal experiment for those specimens [52].

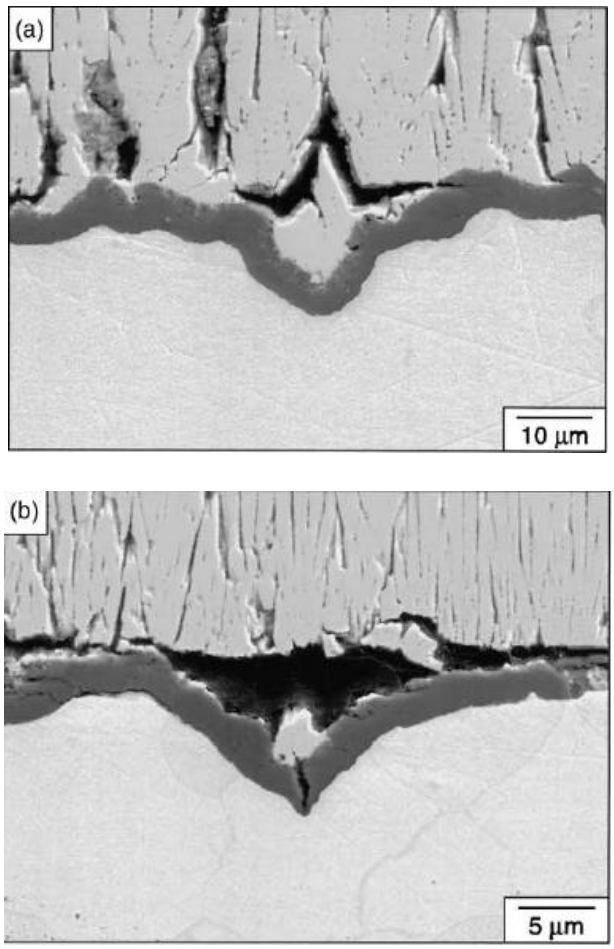

Figure 20 Higher magnification images showing ratcheting imperfections with (a) elliptical and (b) triangular topologies [149]

For EB-PVD TBCs, several methods have been proposed to characterize the interfacial roughness versus both temperature and number of cycles, such as the RMS (root mean square) and tortuosity (L/L_0) [92]. The L and L_0 used for tortuosity are generally defined as the length of the surface

roughness curve and the measured linear distance from the beginning to the end at a specific number of cycles, respectively [92]. Both parameters vary as a function of temperature and thermal cycles. Besides, the evolution of the TGO/bond coat interfacial contours for the bond-coated-only and YSZ-coated sides were measured [142].

The temperature-process dependent parameters used to characterize the interfacial roughness profiles are (a) amplitude of interfacial roughness, (b) width of interfacial roughness. Combining these two parameters with the third parameter of (c) TGO thickness, the geometry of interfacial roughness for the TGO/BC interface can be fully described. These three parameters are discussed in detail in the following.

(a) Amplitude of interfacial roughness

It is noted that the tortuosity (L/L_0) varies as the thermal cycle proceeds and shows temperature-dependent characteristics. The average amplitude of roughness, A, can be expressed as a root mean square roughness parameter (RMS) [150] measured in [92] as,

$$A = \sqrt{2}RMS \tag{19}$$

The resulting average amplitude is plotted in Figure 21.

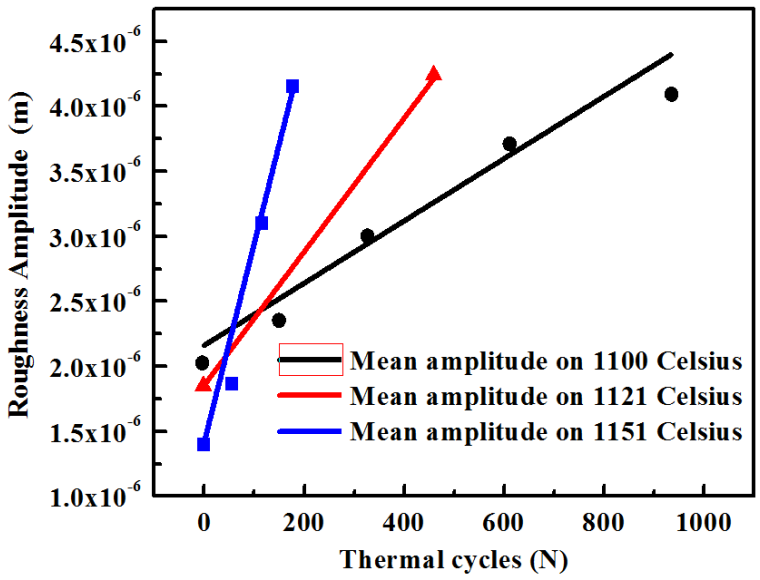

Figure 21 Mean amplitude of roughness with respect to the number of cycles at different temperatures [92]

(b) Width of interfacial roughness

A specific method to characterize the horizontal width of interfacial roughness is necessary to evaluate the stress distribution in EB-PVD TBCs. The random distribution of actual roughness is reflected by an irregular height over each individual protuberate, which can be treated as a uniform distributed rumpling profile, according to Figure 20, either in the form of an isosceles triangle or an ellipse, Figure 22.

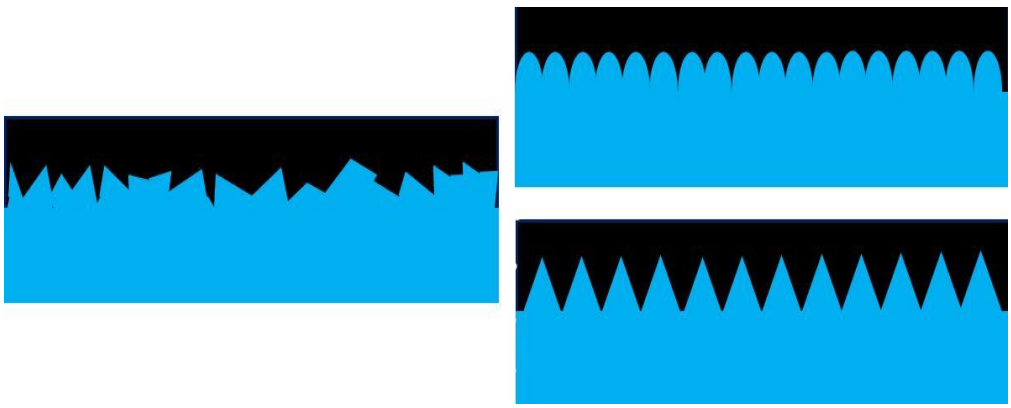

Figure 22 Two ways of equivalent simulated roughness profile according to SEM images

Therefore, the triangle's hypotenuse in each uniform roughness profile is equal to $L/L_0 \times W/2$, where $W/2$ is the half-length of the bottom side, Figure 23.

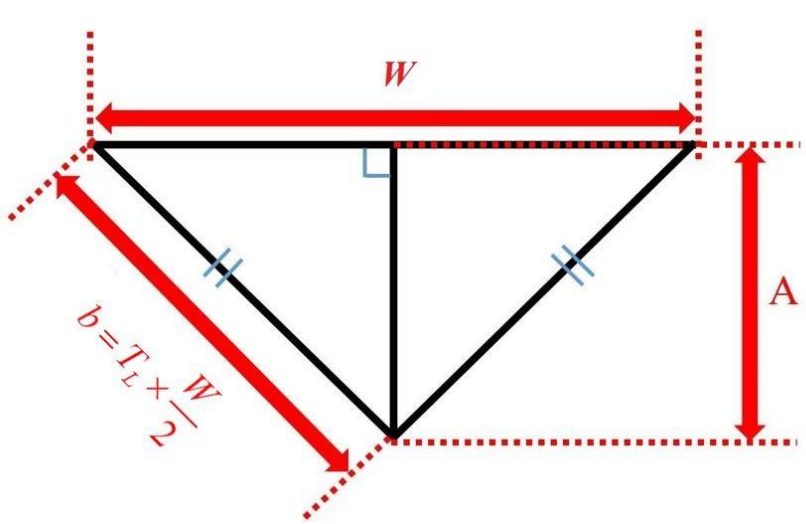

Figure 23 Schematic diagram of interfacial roughness profile approximated in the form of a triangle

It is assumed that an individual interfacial roughness curve and a flat base-side form an isosceles triangle, Figure 23. The base length, W, can represent the horizontal width at an interfacial roughness. The total lengths of two hypotenuses, representing the length of each uniform roughness profile, are described via the product of tortuosity and width, $T_L \times W$, which increases as temperature rises. An average amplitude of roughness represents the height of an isosceles triangle A. Therefore, the length of the hypotenuse b as well as the length of the base-side W can be determined by combining the amplitude (height) and the tortuosity (the ratio of the length of two hypotenuses over the base-side) as,

$$b = T_L \times \frac{W}{2} \tag{20}$$

$$W = \frac{2 \times A}{\sqrt{T_L^2 - 1}} \tag{21}$$

The result of the triangular width of roughness is redefined as W can be obtained by combining tortuosity and amplitude as a function of the number of cycles and temperatures, Figure 24.

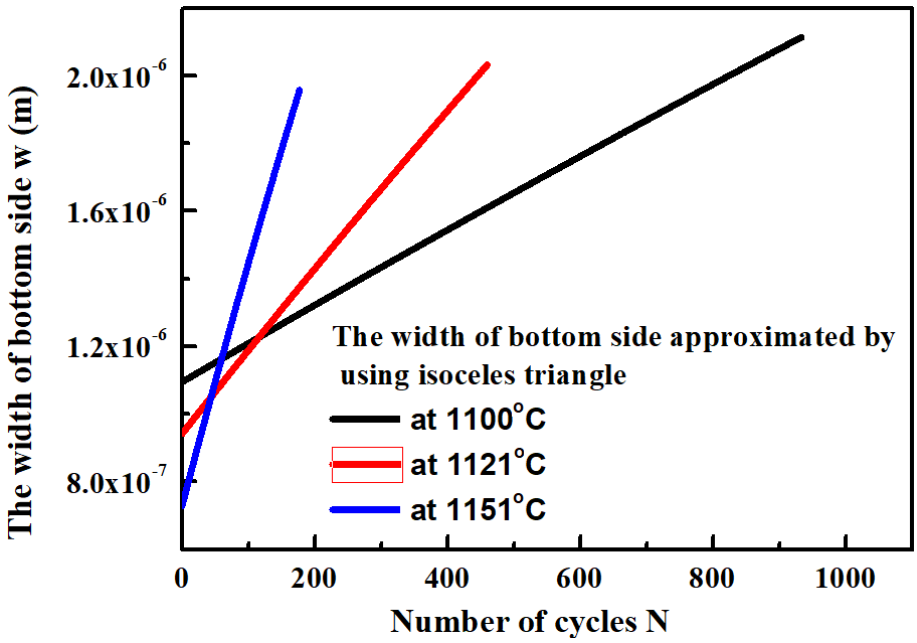

Figure 24 The width of the bottom-side approximated by an isosceles triangle as a function of the number of cycles and temperatures

Similarly, the width of roughness approximated in the form of an ellipse can be represented by the length of the long axis W', Figure 25.

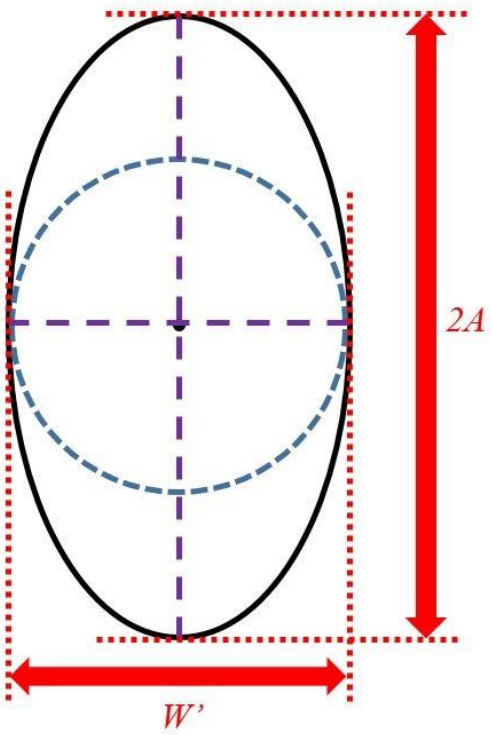

Figure 25 Schematic diagram of interfacial roughness profile approximated in the form of an ellipse

This can be determined by combining the factor of amplitude (long axis) and the tortuosity (the ratio of the length of half perimeter of ellipse over two-fold of short axis), in the equation (22) as,

$$W' = \frac{4 \times A}{\left(2T_L + 2 - \pi\right)} \tag{22}$$

Similar results of the elliptical width of roughness can be obtained by combining the tortuosity and amplitude as a function of the number of cycles and temperatures (Figure 26).

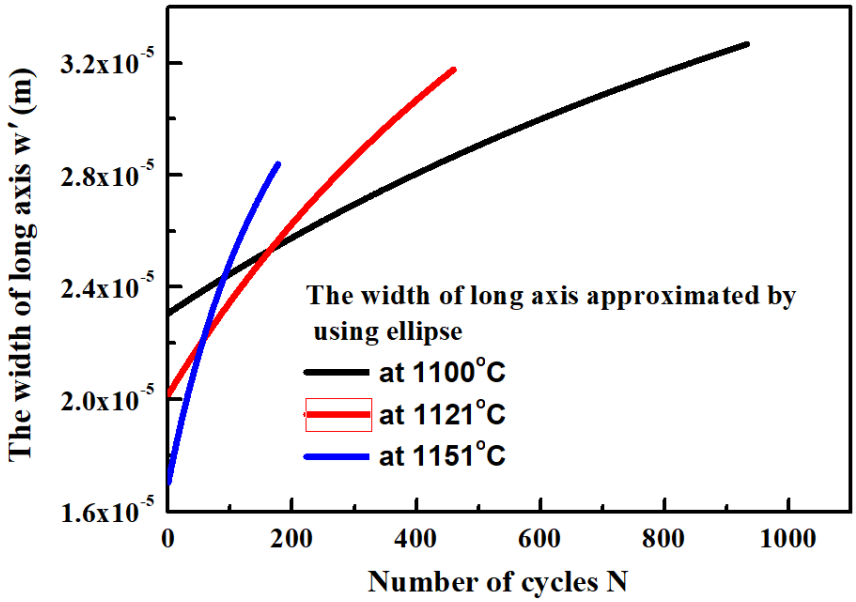

Figure 26 The long axis's width approximated by ellipse as a function of the number of cycles and temperatures

(*c*) TGO thickness

The TGO scale, as a result of progressive oxidation of the BC, exerts a significant effect on the stress distribution within TBCs. Under the isothermal conditions, it is assumed that TGO growth follows a parabolic law given by the equation (23),

$$d_{TGO} = A_{TGO}^{Gr} t^{P_{TGO}} \tag{23}$$

In the present paper, the thermal load is applied under cyclic conditions, and by considering the time-dependent cyclic temperature behaviour, the model parameters in the equation (23) are obtained through fitting to experimental data [92], [139], resulting in the temperature-dependent TGO growth coefficient A_{TGO}^{Gr} expressed in the form of an exponential equation,

$$A_{TGO}^{Gr} = A_{TGO} e^{Q_{TGO}T} + A_{TGO}^{0} \tag{24}$$

With $A_{TGO} = 6.0947 \times 10^{-18} \mu m / min^{P_{TGO}}$, $Q_{TGO} = 0.02577\ 1/K$, $A_{TGO}^{0} = 0.01224 \mu m / min^{P_{TGO}}$, $P_{TGO} = 0.5$. Substituting equation (24) into the equation (23), the TGO growth rate is given by differentiating equation (24) with respect to time,

$$\frac{d}{dt}\left(d_{TGO}\right) = P_{TGO} \times \left(A_{TGO} e^{Q_{TGO} T} + A_{TGO}^{0}\right) t^{P_{TGO}-1} \tag{25}$$

The average TGO thicknesses under cyclic thermal loading are rewritten in the incremental formulation and plotted in Figure 27.

$$d_{TGO}\left(t + \Delta t\right) \approx d_{TGO}\left(t\right) + \frac{d}{dt}\left(d_{TGO}\right) \times \Delta t \tag{26}$$

Meanwhile, the temperature-process-dependent TGO thickness and growth rate are described in Figure 27 (b) and (c) for two cycles, respectively.

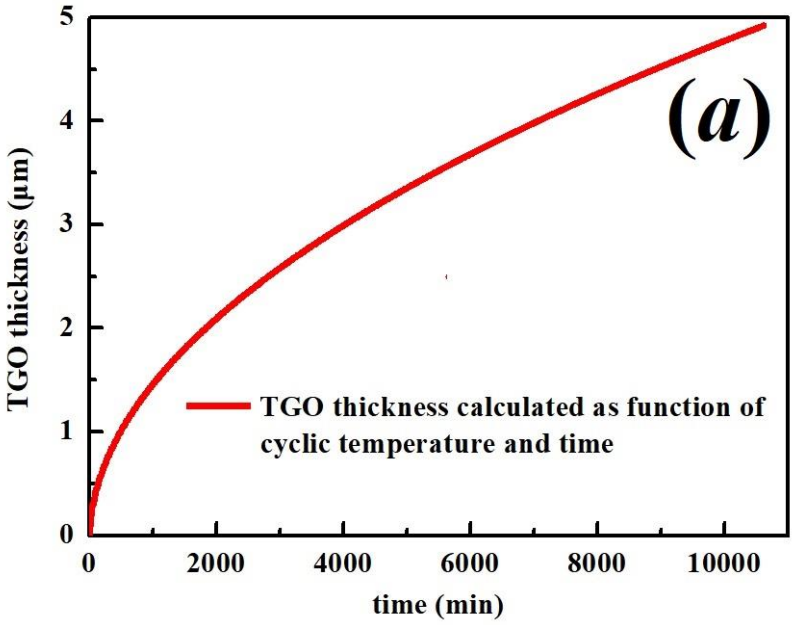
(a)
TGO thickness (μm)
time (min)
TGO thickness calculated as function of cyclic temperature and time
0
1
2
3
4
5
0
2000
4000
6000
8000
10000

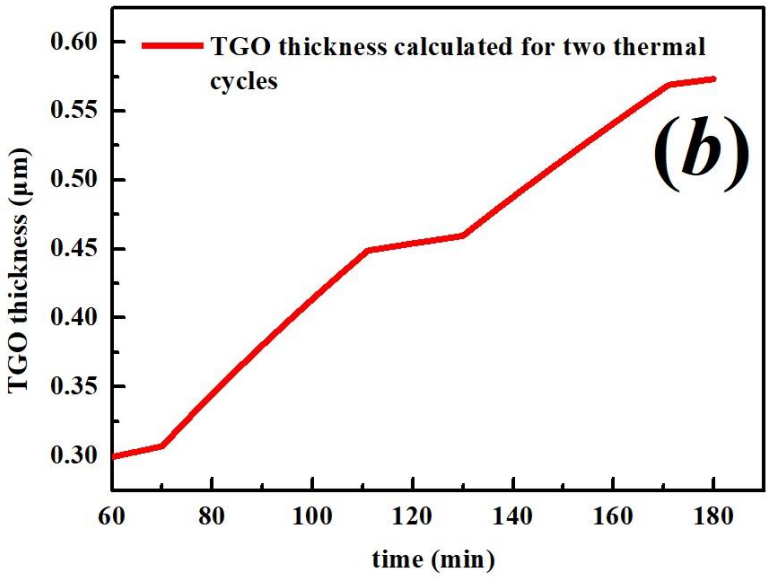
(b)
TGO thickness (μm)
time (min)
TGO thickness calculated for two thermal cycles
0.30
0.35
0.40
0.45
0.50
0.55
0.60
60
80
100
120
140
160
180

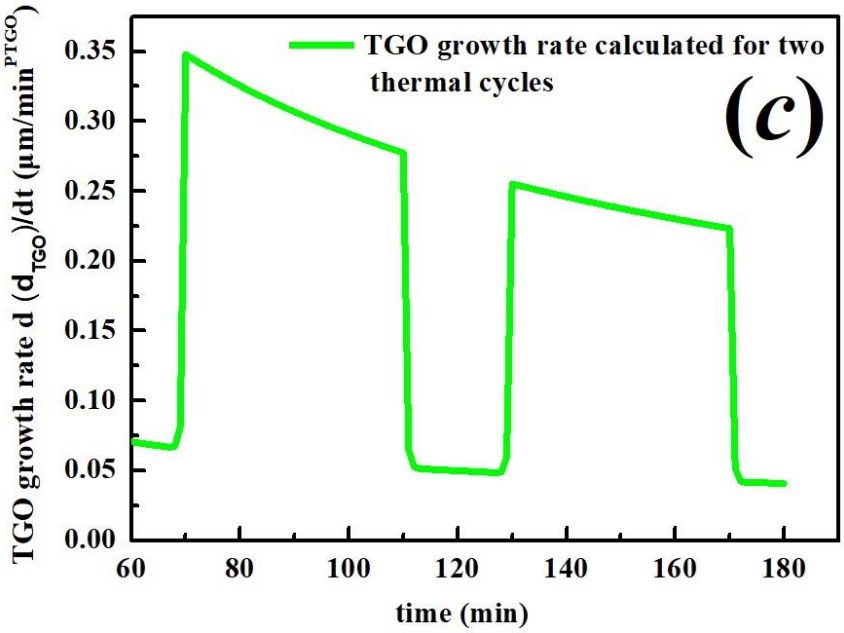

Figure 27 The average TGO thickness for (a) the entire thermal cycles, (b) for two cycles and (c) TGO growth rate for two cycles with respect to the number of cycles at different temperatures

3.3. Finite Element Model

3.3.1. TBCs morphology

The FE model is used to study the effect of interface roughness profiles on thermal residual stresses. The temperature-process dependent model parameters were incorporated into the FE model. The interface geometrical parameters to describe the TBC system are obtained from five specific stages of cyclic thermal tests. These geometrical parameters are then applied to constructing five FE models with triangular roughness approximation. These five sets of FE models are used to study BC roughness's effect on the stresses developed within the TBC system. Besides, to examine the effect of the shape of

the roughness profile on stress distribution, another FE model characterized by an elliptical approximation is generated. The calculated stresses are compared with those using triangular roughness approximation.

After a close inspection of the representative TGO–ceramic interface, its interface morphology can be idealized as a periodic array of saw-tooth type segments, as illustrated in Figure 22. An example is given for a specimen under 177 cycles at the maximum temperature of 1151°C; the corresponding periodic unit cells of the FE model are shown in Figure 28, where Figure 29 shows more details of its interfacial morphology.

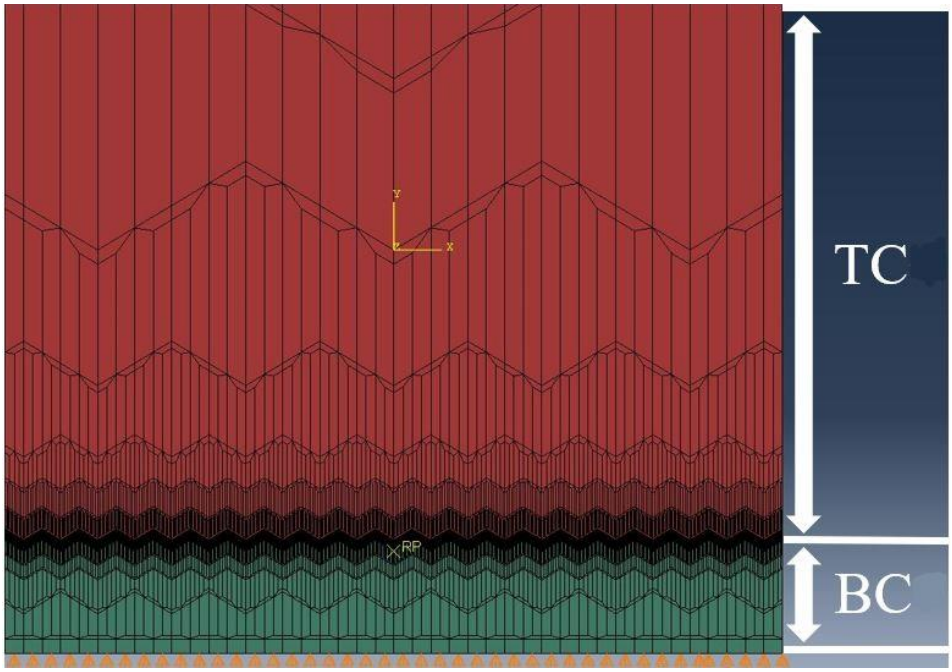

Figure 28 Typical FE mesh used in the TBC model for a bond coat surface roughness ratio.

$$A/W \approx 0.5992$$

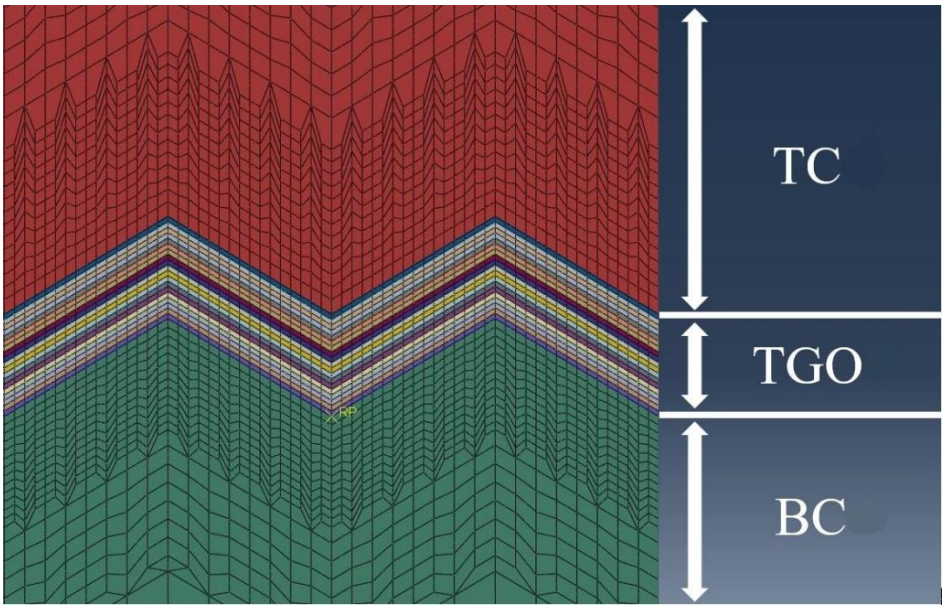

Figure 29 Details about interfacial morphology simulated at 177 cycles from cyclic thermal experiment, the roughness profile is characterized in the form of a triangle

The relevant interfacial length scales can be extracted from the test samples of EB-PVD TBCs given in Figure 21, Figure 24 and Figure 26. Here, the amplitude A of the interface in Figure 23 is approximately 4.12 μm, and the length W of the bottom side is approximately 13.76 μm. Thus, interface morphologies with a ratio of $A/W \approx 0.3$ will be used. The FE meshes consist of 39572 quadratic generalized plane strain elements with full integration.

3.3.2. Transversely isotropic YSZ materials for TC

For simplification, the current 2D FE model is established. The thickness of TBCs in the z-direction is not constrained in stress analysis since the elastic strain is only generated within the defined 2D cross-sectional plane, Figure 8. The transversely isotropic elastic properties of materials are applied to the

plane strain cross-section defined for the TC layer since it is anisotropic between the in-plane and out-of-plane directions. Thus, the resulting fourth-order elastic compliance tensor, *S*, becomes

$$S=\begin{bmatrix} 1/E_{11} & -\upsilon_{21}/E_{22} & -\upsilon_{13}/E_{11} & 0 & 0 & 0 \\ -\upsilon_{12}/E_{11} & 1/E_{22} & -\upsilon_{12}/E_{11} & 0 & 0 & 0 \\ -\upsilon_{13}/E_{11} & -\upsilon_{21}/E_{22} & 1/E_{11} & 0 & 0 & 0 \\ 0 & 0 & 0 & 1/G_2 & 0 & 0 \\ 0 & 0 & 0 & 0 & 1/G_1 & 0 \\ 0 & 0 & 0 & 0 & 0 & 1/G_2 \end{bmatrix} \quad (27)$$

According to the designation of axes in the coordinate system, υ_{21} and υ_{12} are defined as Poisson's ratio in the *x*-*y* direction, υ_{13} is the in-plane Poisson's ratio in the *x*-*z* direction. ν_{23} is the Poisson's ratio in the *y*-*z* direction equivalent to υ_{21} based on the application of orthotropic elasticity within the TC layer. The shear moduli with the same subscripts are also defined and G_{12} G_{23} represent the shear modulus in the *x*-*y* and *y*-*z* direction, respectively, G_{13} defined as the in-plane shear modulus in the *x*-*z* direction. The definition of orthotropic elasticity, i.e., the relative elastic modulus, shear modulus as well as Poisson's ratio in different directions of TC are summarized in Table 2 [139], where *x, y, z* in the FE calculations are indicated by the subscripts 11, 22, and 33, respectively.

Table 2 The definition of orthotropic elasticity by specifying the engineering constants

Parameters	Definition	Conversion to transversely isotropic elastic properties
E_{11}	In-plane elastic modulus in the x-direction	E_{11} estimated by equation(3) and equation(7).

E_{22}	Out-of-plane elastic modulus in the y-direction	E_{22} estimated by equation (5) And equation (6)
E_{33}	In-plane elastic modulus in the z-direction	$E_{33} = E_{11}$
v_{12}	Poisson's ratio in the x-y direction	$\nu_{21} = 0.2$, $\nu_{21} = 0.2$
v_{13}	In-plane Poisson's ratio	$\nu_{13} = 0.12$
v_{23}	Poisson's ratio in the y-z direction	$\nu_{21} = \nu_{23} = 0.2$
G_{12}	Shear modulus in the x-y direction	$G_{12} = G_2 = E_{22}/E_{11} \times G_1$
G_{13}	In-plane Shear modulus	$G_{13} = G_1 = E_{11}/2(1+\nu_{13})$
G_{23}	Shear modulus in the y-z direction	$G_{23} = G_2 = E_{22}/E_{11} \times G_1$

The TBC's temperature distribution is assumed to be spatially homogeneous and to vary cyclically in a pattern illustrated in Figure 12. The peak cycle temperature of 1151^{o}C was identified as a typical TBC metal/ceramic interface temperature. The residual stress will be calculated upon temperature dropping down to 20^{o}C. Because of high-temperature creep, the TBC is treated as stress-free or with small compressive residual stress during the high-temperature dwell period at 1151^{o}C. The TBC surface is assumed to be traction-free, and the symmetric and periodic boundaries on FE models are assumed on the bottom plane of BC $y = 0$, indicating no vertical downward movement occurs through the y-direction due to the support by the BC/substrate.

3.3.2. Phase transformation and oxidation model

There are two effects to consider when study phase transformations of BC oxidation to form oxide (TGO). This progress involves a gradual change of mechanical and creep properties from BC (metal) to TGO (oxide) and initiation of a swelling effect when the TGO starts to form. First, in all FE models, it is assumed that progressive oxidation is dominated by internal oxidation, in which a new oxide layer forms below the existing TGO layer. Second, apart from a specific case where an oxide layer was already incorporated into the TC/BC interface (three layers), all models start with two layers between the topcoat and bond coat.

At the failure life during thermal cycles, it is assumed that the TGO grows and reaches its maximum thickness d_{max} at a specific test temperature. This d_{max} is the result of converting BC into TGO through BC oxidation. In FE modelling, however, this d_{max} was selected as a known input value from the TBC life test. The FE modelling simulates progress on how BC converts into TGO via oxidation and gradually reaches d_{max}. During such progress through thermal cycles, residual stress and its distribution were evaluated and used to assess possible failure behaviour of TBCs. This phase transformation process can be conveniently divided into three stages. In Stage I, the phase transformation of BC to

TGO does not occur. In this stage, the entire d_{max} region is still treated as BC. In Stage II, a transformation of BC to TGO takes place; the d_{max} region is mixed with both BC and TGO. Finally, Stage III indicates the transformation of BC to TGO is complete; this d_{max} region is purely oxide TGO. During stages I - III, the region undergoes a phase transformation from metallic BC to oxide TGO. The mechanical properties given by isotropic elastic modulus for materials in the transitional sublayer are estimated by,

$$E_{tr} = E_{TGO} \times f_{(Ni,Pt)Al} + E_{BC} \times (1 - f_{(Ni,Pt)Al}) \tag{28}$$

Equation (28) describes the elastic modulus of this transition region that undergoes phase transformation. Similarly, the temperature-dependent coefficient of thermal expansion and inelastic creep strain rate for this transition region can be estimated from,

$$\alpha_{tr} = \alpha_{TGO} \times f_{(Ni,Pt)Al} + \alpha_{BC} \times (1 - f_{(Ni,Pt)Al}) \tag{29}$$

$$\dot{\varepsilon}_{tr}^{cr} = \dot{\varepsilon}_{TGO}^{cr} \times f_{(Ni,Pt)Al} + \dot{\varepsilon}_{BC}^{cr} \times (1 - f_{(Ni,Pt)Al}) \tag{30}$$

To implement TGO swelling on the stress distribution during the phase transformation process, it is necessary to obtain the time to initiate the BC conversion to TGO from top to bottom of the transition layer. However, it is evident that the TGO growth rate decreases as the oxidation occurs following the parabolic formulae, Figure 27. This follows since the formation of dense α-Al_2O_3 as a newly formed TGO layer can largely prevent the BC surface from further oxidation. Accordingly, to include the effect of gradually decreased oxidizing rate from the surface to the bottom of the transition layer, several sublayers are further partitioned with an identical thickness within the transition layer, Figure 29. The identical thickness of each sublayer facilitates the meshing process, i.e., a layer of thin transition is uniformly filled by a layer of quadratic generalized plane strain elements. It also provides a convenient way to calculate the related oxidation parameters that are used to describe the progressive oxidation of each sublayer. It takes longer for oxidation to complete at a sublayer close to the bottom of the transition layer compared to that near the surface. Thus, for transition layer in size d_{max}, we can obtain the time-

spent for oxidation completion by iterating the equation (26) and sum the incremental time until TGO reaches the critical thickness,

$$n \times d_{TGO}^{sub} \approx \sum_{N=1}^{N_n} \left[\frac{d}{dt}\left(d_{TGO}\right) \times \Delta t \right] \qquad for \quad n = 1, 2, 3...$$
$$t_n^F = \sum_{N=1}^{N_n} \Delta t \tag{31}$$

where t_n^F is the time for oxidation completion for the transition, *n* indicates the number of the sublayer counting from top to bottom, d_{TGO}^{sub} is the thickness of the sublayer, which is predefined according to the total number of sublayers within the TGO section. N_n is the final iterative number for calculated TGO thickness reaching the entire thickness of *n* sublayers $\left(n \times d_{TGO}^{sub}\right)$. The thickness of each sublayer is given by

$$d_{TGO}^{sub} = \frac{d_{TGO}}{n} \tag{32}$$

For convenience, $d_{max} = d_{TGO}$. To use equation (31) and implement TGO swelling in the transition region in each sub-layer, the TGO growth rate $\frac{d}{dt}\left(d_{TGO}\right)$ equation (25) needs to be specified by each of the sublayers using the equation (31) as

$$\frac{d}{dt}\left(d_{TGO}\right)_i = P_{TGO} \times \left(A_{TGO} e^{Q_{TGO} T} + A_{TGO}^0\right) t^{P_{TGO}-1}$$
$$\frac{d}{dt}\left(d_{TGO}\right)_i = \begin{cases} 0 & if \quad t > t_i^F \qquad\qquad for \quad i = 1 \\ 0 & if \quad t < t_{i-1}^F \quad or \quad t > t_i^F \quad for \quad i > 1 \end{cases} \tag{33}$$

where $\frac{d}{dt}\left(d_{TGO}\right)_i$ is the TGO growth rate for sublayer *i* (*i*=1 to *n*) within the TGO section. It is used to control the growth rate of TGO thickening. It is evident that $\frac{d}{dt}\left(d_{TGO}\right)_i$ decrease versus *n*, according to the equation (33), it takes a longer time for "deeper" sublayers to complete the oxidation process ($\left(t_n - t_{n-1}\right)$ increases versus *n*). Accordingly, the evolution of the internal variable $f_{(Ni,Pt)Al}$ for each sublayer can be rewritten as

$$f_{(Ni,Pt)Al-i} = \begin{cases} \dfrac{\sum_{t=0}^{t_1^F}\left[\dfrac{d}{dt}\left(d_{TGO}\right)_i \times \Delta t\right]}{d_{TGO}^{sub}} & for \quad n=1 \\ \dfrac{\sum_{t=t_{i-1}^F}^{t_i^F}\left[\dfrac{d}{dt}\left(d_{TGO}\right)_i \times \Delta t\right]}{d_{TGO}^{sub}} & for \quad n>1 \end{cases} \tag{34}$$

$$f_{(Ni,Pt)Al-i} = \begin{cases} 0 & if \quad t \le t_i^F \\ 1 & if \quad t \ge t_i^F \end{cases}$$

where $f_{(Ni,Pt)Al-i}$ is the evolution of the internal variable for each sublayer. An example is given for the calculation of $f_{(Ni,Pt)Al-i}$, assuming t_{17}^F and t_{18}^F represent the time for sublayer 17 and 18 to be fully oxidized, respectively, Figure 30.

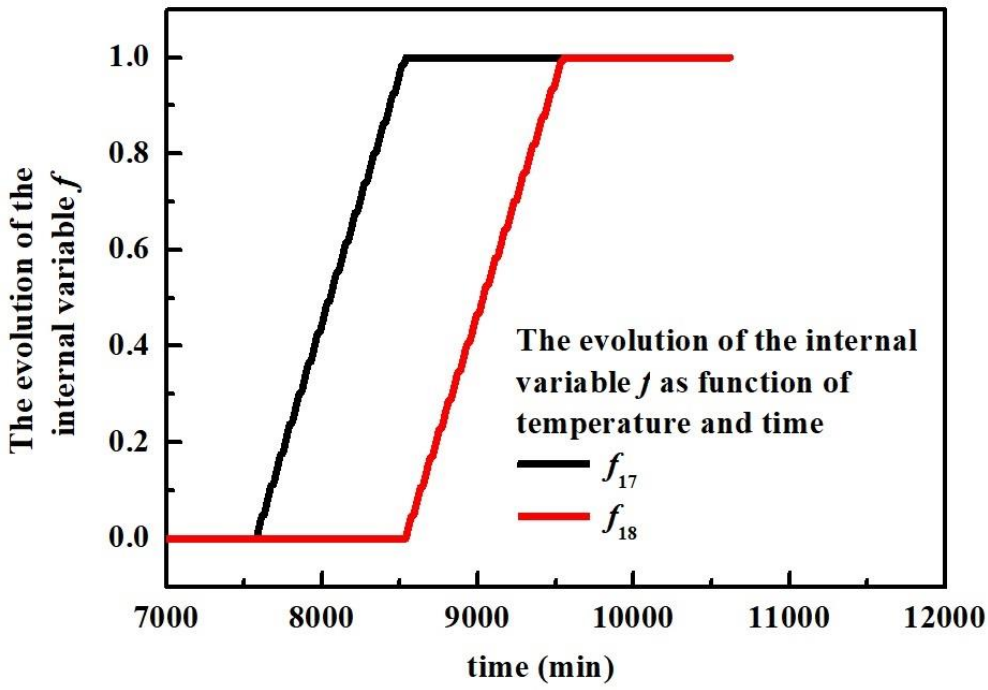

Figure 30 The internal variable f for sublayers 17 and 18 as a function of temperature and time

When the time t is shorter than t_{17}^{F}, the oxidation of sublayer 18 has not yet started, according to the equation (34), the calculated $f_{(Ni,Pt)Al-18}$ is less than zero, and then we reset it to be zero. On the other hand, as t approaches t_{18}^{F}, $f_{(Ni,Pt)Al-18}$ is close to unity. As t surpasses t_{18}^{F}, the oxidation of sublayer 18 has completed. When the calculated $f_{(Ni,Pt)Al-18}$ is larger than unity, it is reset as unity. Accordingly, the mechanical, thermal properties and creep behaviour of the sublayers can be obtained by substituting equations (34) into equations (28)-(30). The FE model of EB-PVD TBCs can now be established based on the previously described constitutive material models. These models are implemented numerically in user-defined subroutines in commercial FE code ABAQUS [177].

3.4. Results and discussion

The stress analysis was conducted at positions where cracks have a high possibility to form according to SEM images. Moreover, the residual stresses estimated under several roughness profiles characterized at selected stages of the life cycle helps explain the failure mechanism. Those positions of interest are also possible locations where the maximum residual stress could be achieved.

3.4.1. The comparison of stress states obtained from the model with different assumptions under the same roughness profile

The out-of-plane stresses calculated for the valley of the TC are illustrated for cases of (i) pure elastic model, (ii) sintering elastic model, (iii) sintering elastic + creep and swelling model as well as (iv) sintering elastic + creep and swelling + plastic model. All stresses are calculated at the location of 1.1μm away from the TC valley within 1000 minutes of thermal cycles, as indicated by the red point in Figure 31.

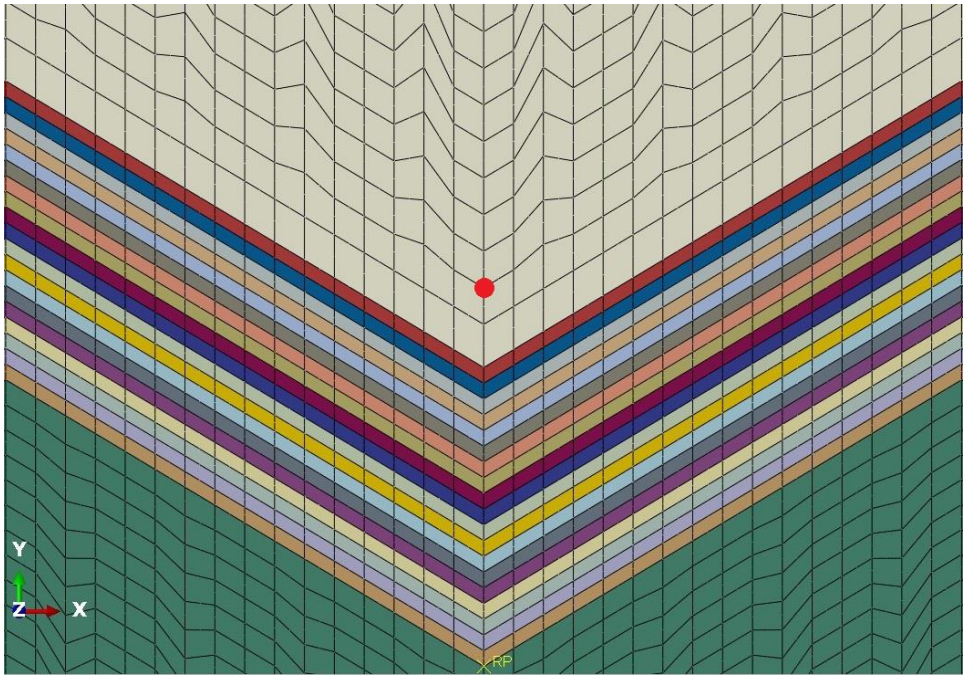

Figure 31 The position at the valley of TC where stresses are calculated from models with different assumptions

For the case of a pure-elastic behaviour, stresses obtained under the no stress assumption during the high temperature dwell period differ from those with existing initial stress, shown in Figure 32 (a) and (b). It is noticed that different stress levels are obtained at initial thermal cycles, which corresponds to the assumption of different initial temperatures. Figure 32(a) illustrates the valley stress at the initiation of thermal cycling at room temperature (20^{o}C). The stress level experiences a fast growth within the first ten minutes, which is explained by the CTE mismatch between layers as TBCs experience temperature increase, equation (8). The valley stress decreases dramatically during the following high-temperature holding period, which is also observed at the valley of TC assuming thermal loads initiated at relatively high temperature at first thermal cycle (T=1150^{o}C during 0-10 min in an equation (8)), Figure 32(b). However, starting at a high temperature, there is no stress at the valley of the TC layer. It is evident that different assumptions of initial temperatures applied to TBCs make a

significant difference in the initial stress state, which further affects the stress level during the whole thermal cycle.

Nevertheless, this stress discrepancy is compensated by the inelastic behaviour of TBCs, i.e., the creep model introduced by equations (14)-(15) and yielding models illustrated in Figure 16 and Figure 17 provide a sufficient stress relaxation within TBCs. The temperature-dependent creep behaviour results in a dramatic drop of stress when the cycle process approaches the high-temperature holding period, Figure 34 and Figure 35. Therefore, it is expected that the initial thermal load with either of high temperature or low-temperature condition has a minimum effect on the stress distribution in later life cycles.

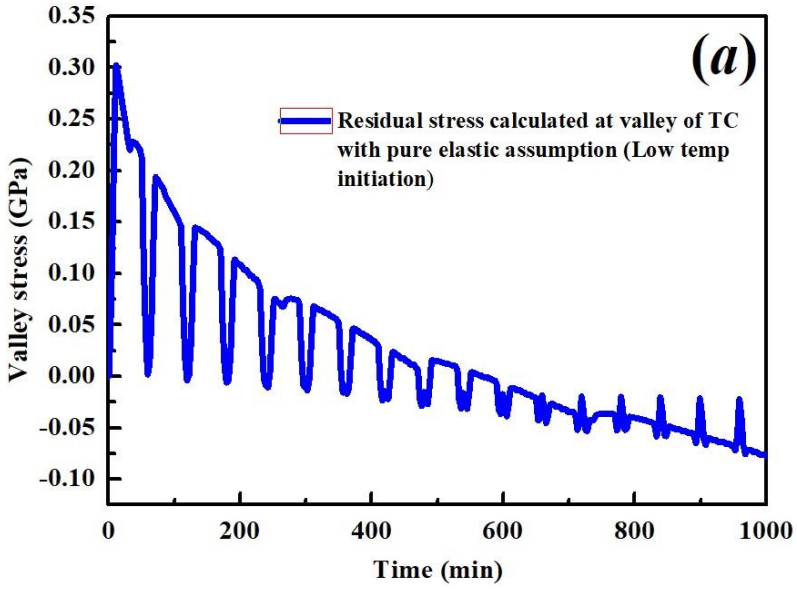

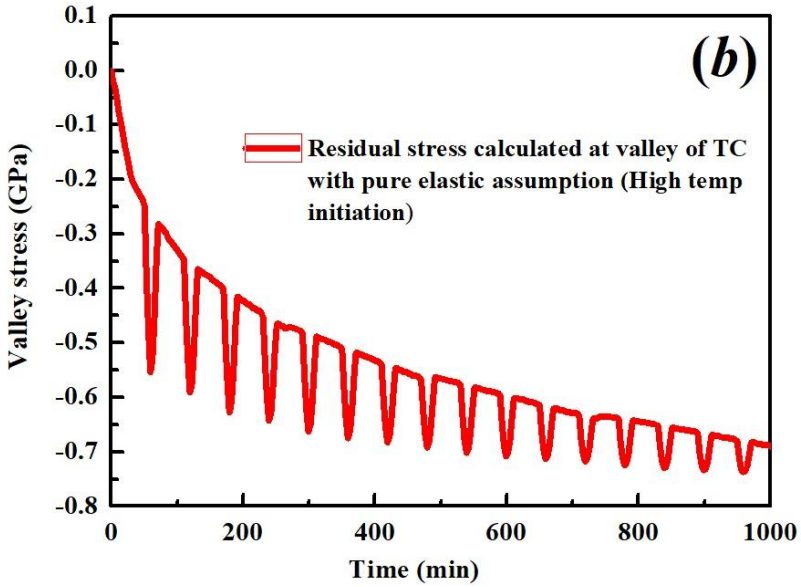

Figure 32 The calculated stress at the valley of TC with the assumption of a stress-free at the beginning of thermal cycles (a) at low temperature(b) at high temperature, the stress decreases during the cooling process

It should be noted that there is a stress inversion during the cooling process when the sintering model of equations (3) - (7)) is incorporated into FE calculations, Figure 33. However, the stress still decreases versus thermal cycles.

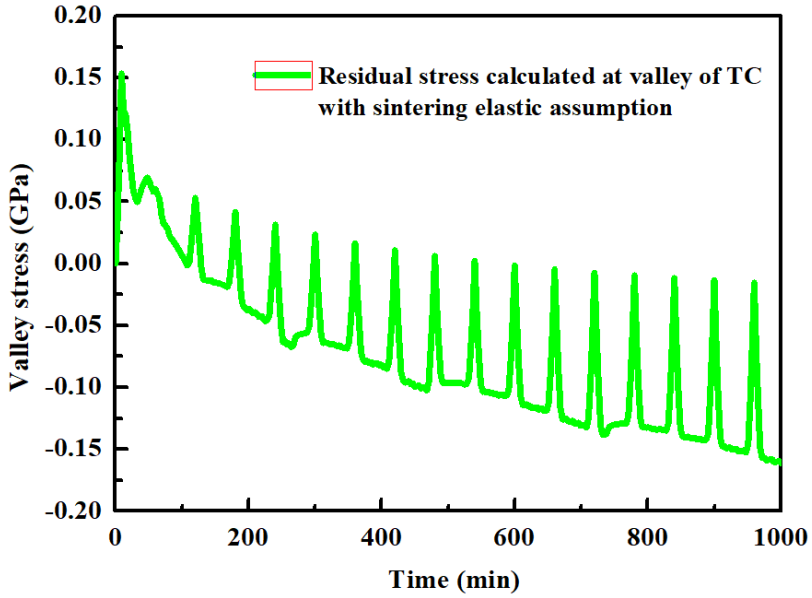

Figure 33 The calculated stress at the valley of TC with sintering elastic model, notice that the stress increase during the cooling process

The trend of calculated stresses at the TC's valley increases as the creep for both BC and TGO and the swelling model of TGO are incorporated into FE calculations, Figure 34.

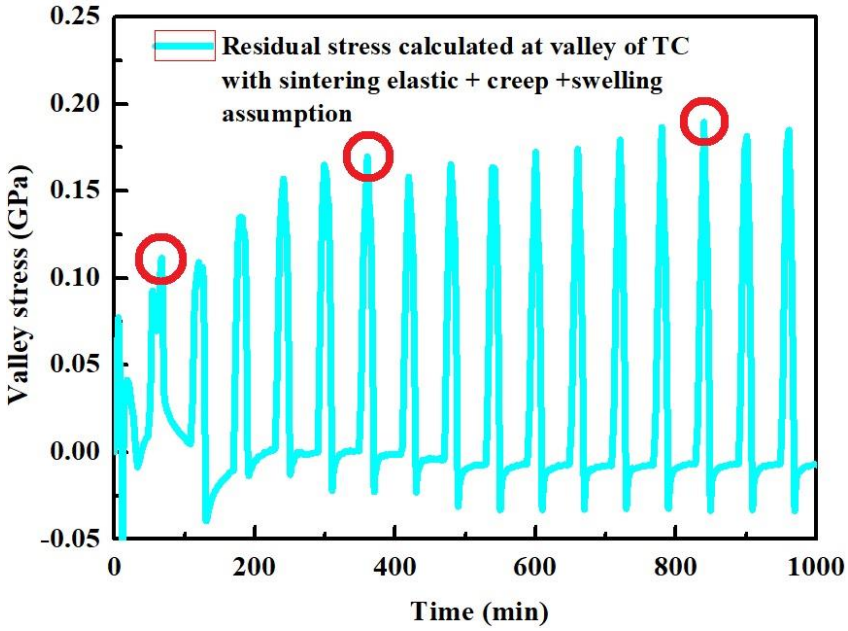

Figure 34 The calculated stress at the valley of TC with the assumption of sintering elastic +Creep & swelling

It was thought that the creep normally reduces stresses [87], [90], whereas the stress in Figure 34 may indicate that swelling increases stress. It is observed that there are several higher stress states highlighted in red circles in Figure 34. Those stresses might occur during the cooling process, where progressive oxidation of a sublayer and initiation of oxidation for the sublayer below completes. The swelling rate for a sublayer at the beginning of oxidation generates relatively large stress. Still, it decreases quickly as the swelling rate (dominated by the rate of evolution of the internal variable $\dot{f}_{(Ni,Pt)Al}$ equation (16)) gradually decreases as the thermal cycle proceeds. $\dot{f}_{(Ni,Pt)Al}$, as indicated in the preceding section, is used to describe the rate of oxidation. $f_{(Ni,Pt)Al}$ reaches the maximum of unity when the value $\dot{f}_{(Ni,Pt)Al}$ becomes the minimum, which means the completion of oxidation for a single sublayer. The calculated stress at the same valley location of TC is illustrated in Figure 35.

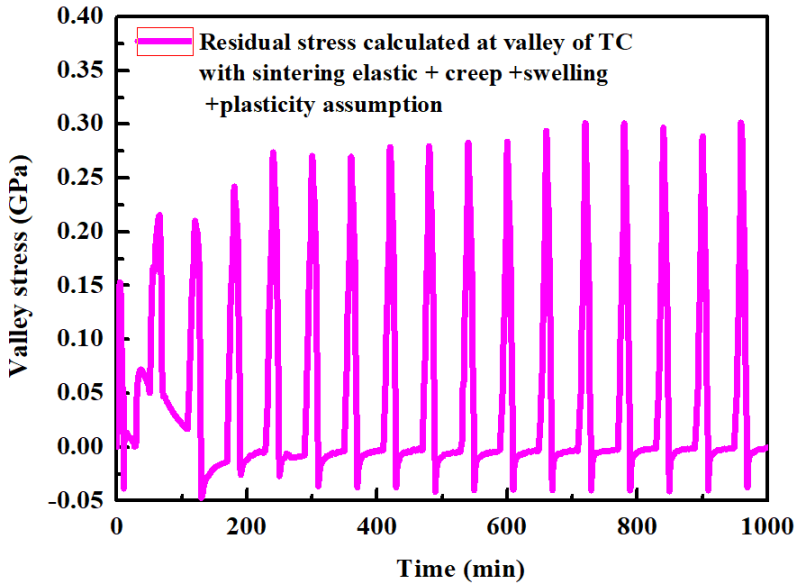

Figure 35 The calculated stress at the valley of TC with an assumption of sintering elastic +Creep & Swelling + Plastic

In addition to a small increase in the stress, there is no apparent difference between the results compared to that shown in Figure 34.

It is noted that no plastic behaviour is included in the stress analysis from the TC, especially for the case related to the residual stress resulting from a cooling period under thermal cycles in the *y*-direction. This is because, for EB-PVD TBCs, the columnar microstructure of the TC provides high stiffness in the out-of-plane direction, which further prevents excessive out-of-plane strain generation [139], [150]. However, it is noticed that a significant effect is expected on BC plasticity when the creep model is incorporated into the FE calculation. Figure 36 (a) and Figure 36 (b) show the calculated maximum cooling stresses at the peak position of BC lying at 1.1 μm away from the interface with and without including plasticity of the TGO/BC during complete life cycles. The calculated stresses, including plasticity, are smoother compared to those without plasticity.

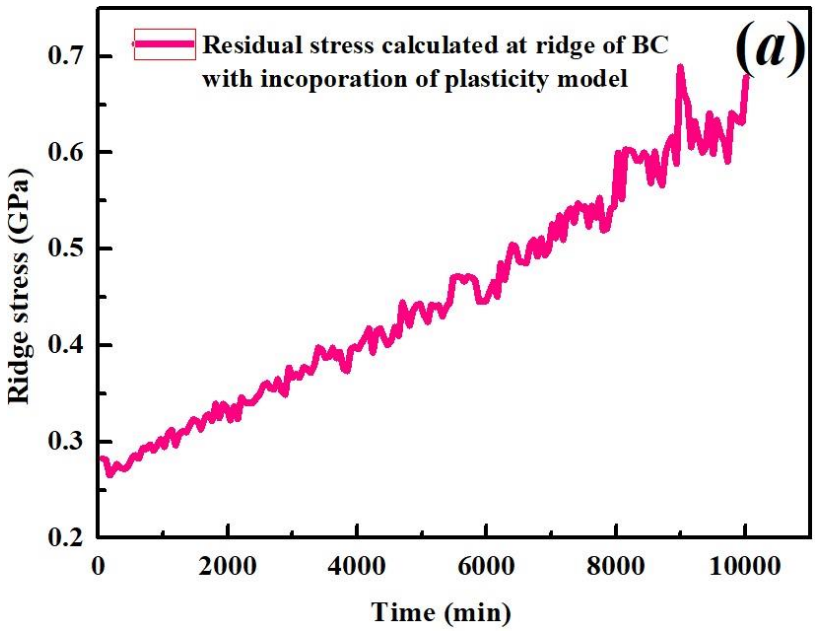

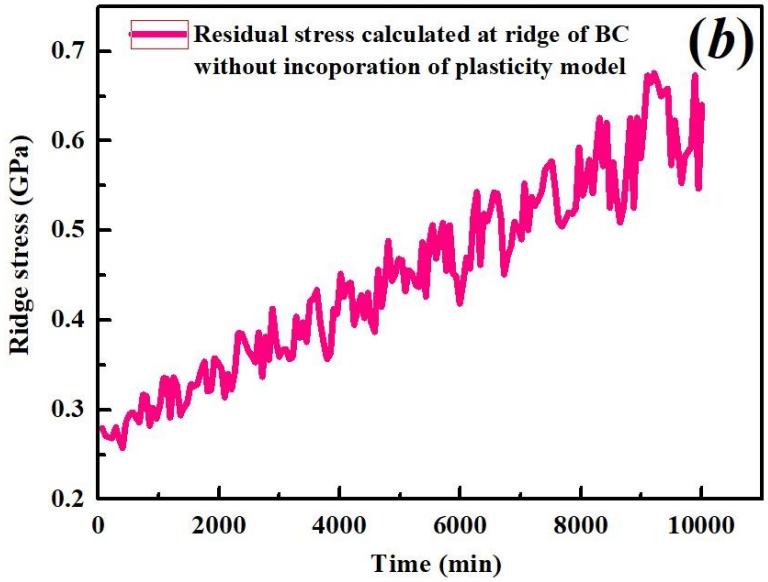

Figure 36 The maximum cooling stress calculated at the peak of BC (a) with plasticity incorporated (b) without plasticity incorporated into FE calculation

3.4.2. Failure mechanism analysis based on the calculated stresses under different roughness approximation

The interface roughness is characterized in an ellipse, and the triangular profile is shown in Figure 37 and Figure 29.

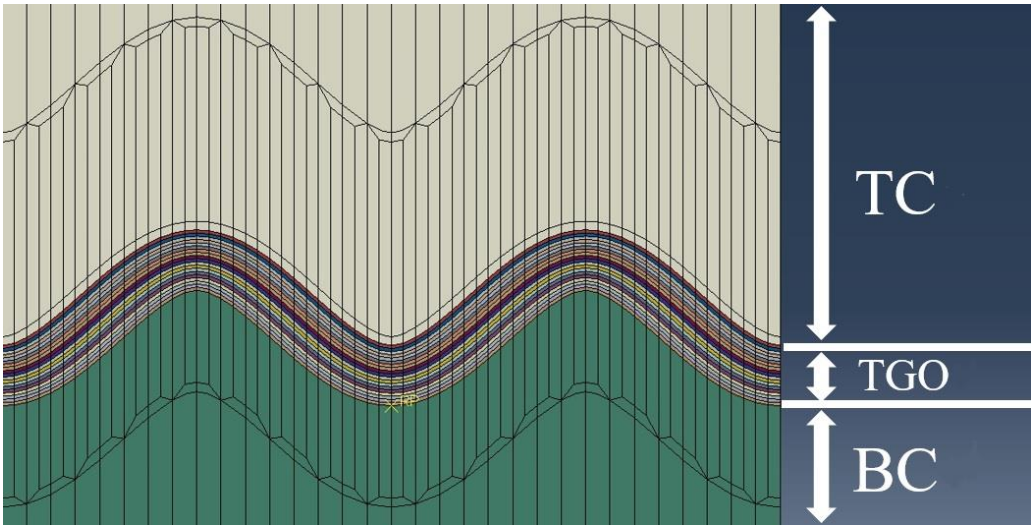

Figure 37 Details about interfacial morphology simulated at 177 cycles from cyclic thermal experiment, the roughness profile is characterized in an ellipse

The calculated residual stresses under these roughness profiles are used to investigate possible correlations between the position of crack initiation and interface roughness, Figure 38.

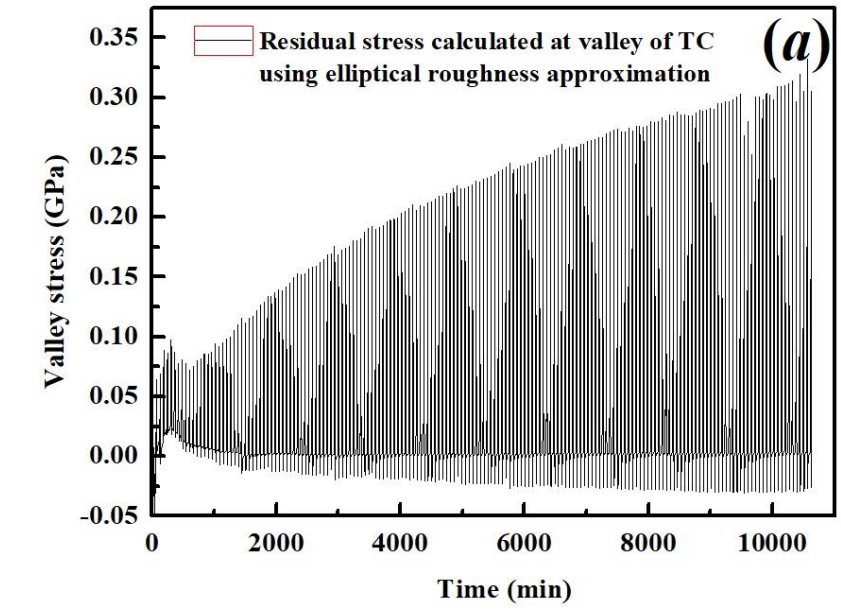
Residual stress calculated at valley of TC
using elliptical roughness approximation
(a)
Valley stress (GPa)
0.35
0.30
0.25
0.20
0.15
0.10
0.05
0.00
-0.05
0
2000
4000
6000
8000
10000
Time (min)

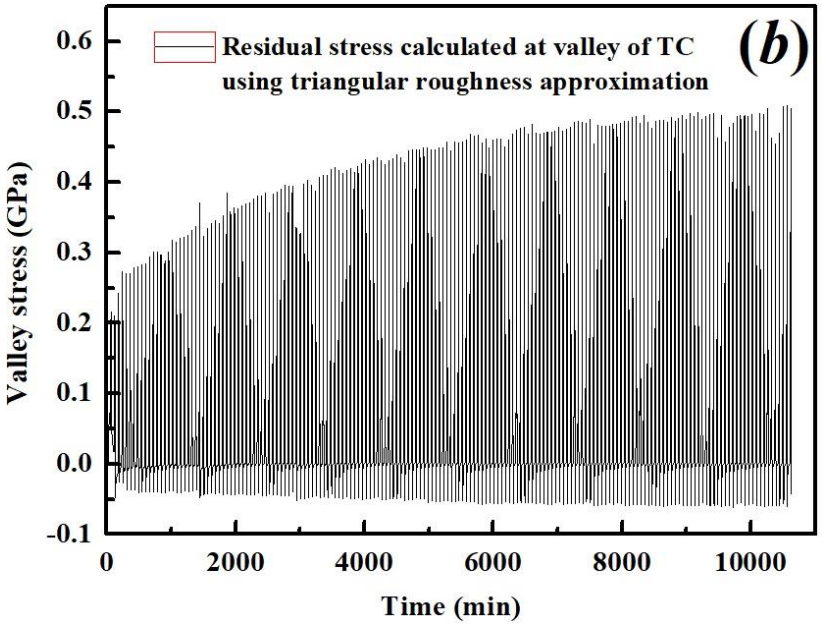
Residual stress calculated at valley of TC
using triangular roughness approximation
(b)
Valley stress (GPa)
0.6
0.5
0.4
0.3
0.2
0.1
0.0
-0.1
0
2000
4000
6000
8000
10000
Time (min)

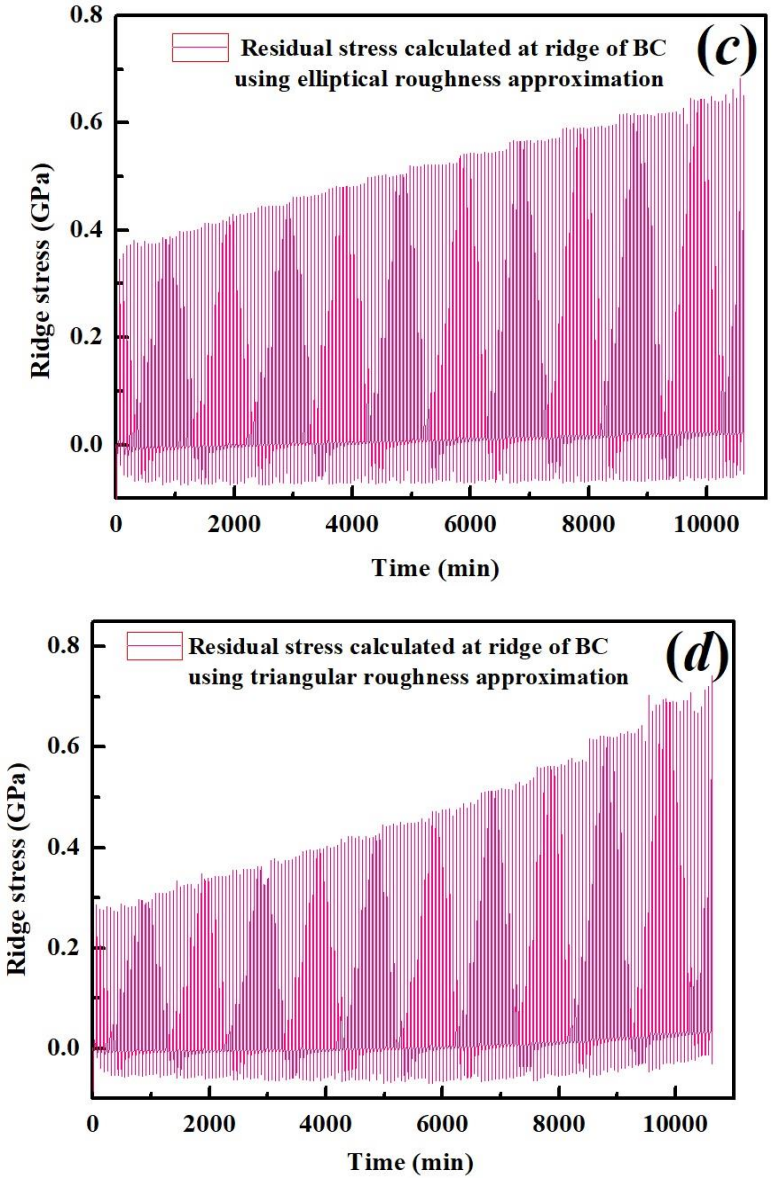

Figure 38 The out-of-plane residual stresses calculated at the valley of TC using (a) elliptical roughness approximation (b) triangular roughness approximation and at the peak of BC using (c) elliptical roughness approximation (d) triangular roughness approximation

Specifically, it was observed:

a) At the valley of TC, relative low stresses are obtained where the roughness is characterized in the form of the ellipse at early stages of thermal cycles, Figure 38(a). In other words, this demonstrates that a higher possibility of early crack initiation occurs at the valley of the TC with a relatively sharp triangular roughness because of high-stress concentration at the shape corner, Figure 38 (b).

b) On the contrary, the possibility for early crack initiation at the peak of BC is higher in the relatively flat elliptical roughness, Figure 38 (c) due to higher out-of-plane stresses compared to the one characterized using triangular roughness profile, Figure 38 (d). The total out-of-plane strain at the valley within the topcoat upon cooling versus time, Figure 39.

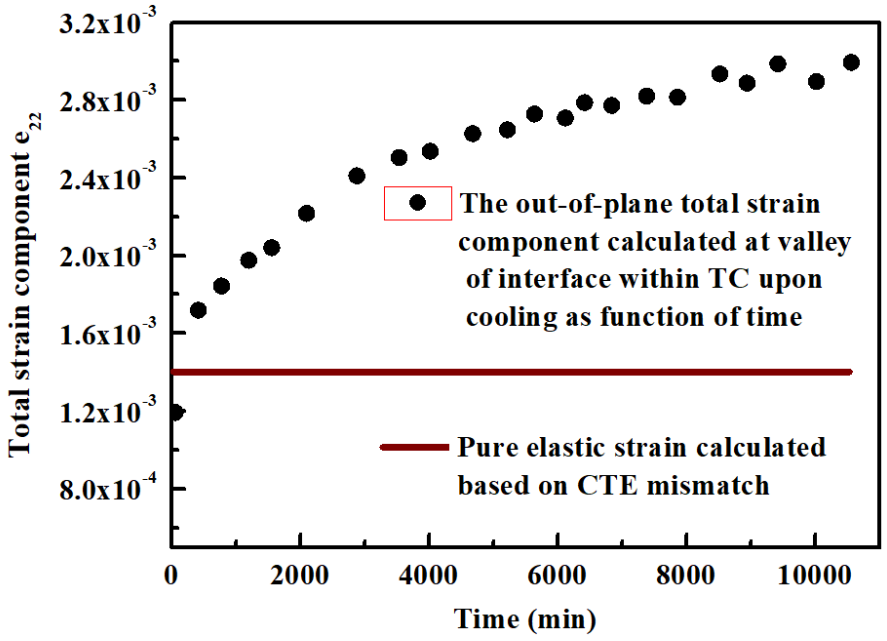

Figure 39 The out-of-plane total strain calculated at the valley of TC where residual stresses are estimated, together with residual thermal strain calculated from [96]

The above figure illustrates the calculated out-of-plane total strain at the valley of topcoat where the interfacial roughness is characterized by amplitude and width using No.5 data of Table 3. It is

evident that upon cooling, the strain shows a similar trend compared to the residual stress estimated from the identical positions of the black curve in Figure 40. The maximum out-of-plane elastic strain due to CTE mismatch is also calculated and plotted together in the above Figure 39. Using the analytical expression of CTE mismatch strain is expressed as [101],

$$\varepsilon_{TGO\_TC}^{thermal} = \eta\left[\left(\alpha_{TGO}-\alpha_{BC}\right)\left(\xi\frac{d_{TGO}A}{y_{TC}W}\right)+\left(\alpha_{TGO}-\alpha_{TC}\right)\right]\exp\left(\delta\frac{A}{W}\right)\times\Delta T \quad (35)$$

Where η, ξ and δ are fitting parameters and can be found in [101]. It should be noticed that in the current FEA model, the TC is only affected by the sintering effect. The discrepancy between the FE calculated total strain and the maximum CTE strain could be explained by the effect of oxidation of BC accompanying TGO swelling that effectively increases the out-of-plane strain calculated at the valley of the TC layer.

Also, five sets of out-of-plane residual stresses are also calculated at the valley of the TC through life cycles, Figure 40, where triangular roughness profiles characterized from selected life cycle stages are used in the FE models.

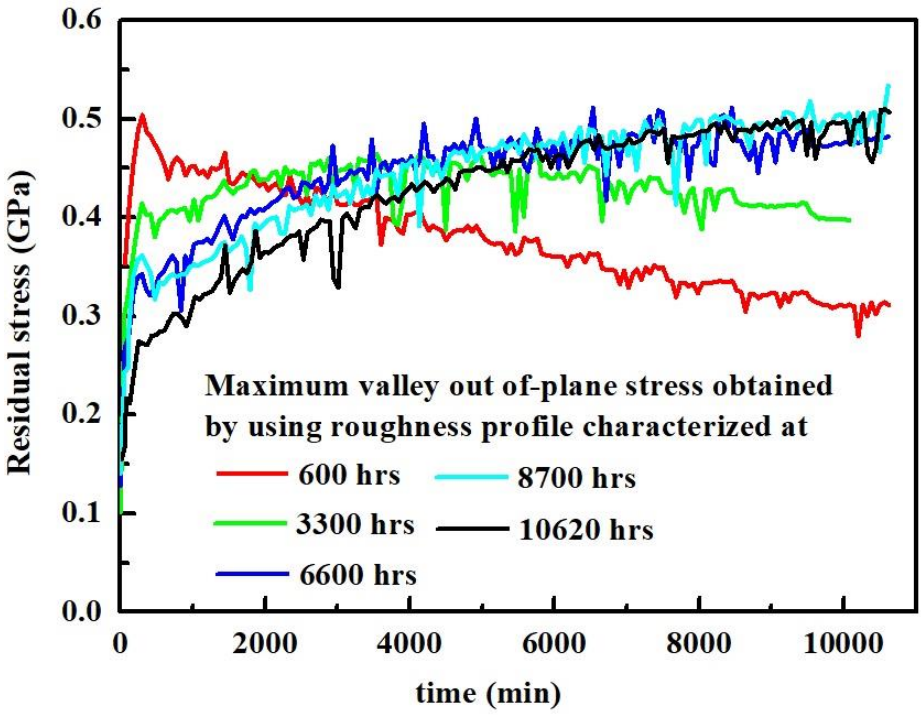

Figure 40 Out-of-plane residual stresses calculated at the valley of TC with different roughness profiles characterized at various stages in life cycles

The roughness parameters characterized from five stages of life cycles are summarized in Table 3.

Table 3 The roughness parameters used in FE models characterized from five stages of life cycles.

No	Cyclic number[a] in Cycles (Hours)	Amplitude in μm	Width in μm
1	10 (600)	1.571	6.893

2	55 (3300)	2.259	9.078
3	110 (6600)	3.100	11.370
4	145 (8700)	3.635	12.666
5	177 (10620)	4.124	13.764

Cyclic number[a] indicates the number of cycles when roughness parameters are characterized from cyclic thermal experiments.

As mentioned in the preceding sections, the parameters characterizing the evolution of the roughness profile under thermal cycles vary versus time. The ratio of amplitude over width is illustrated in Figure 41.

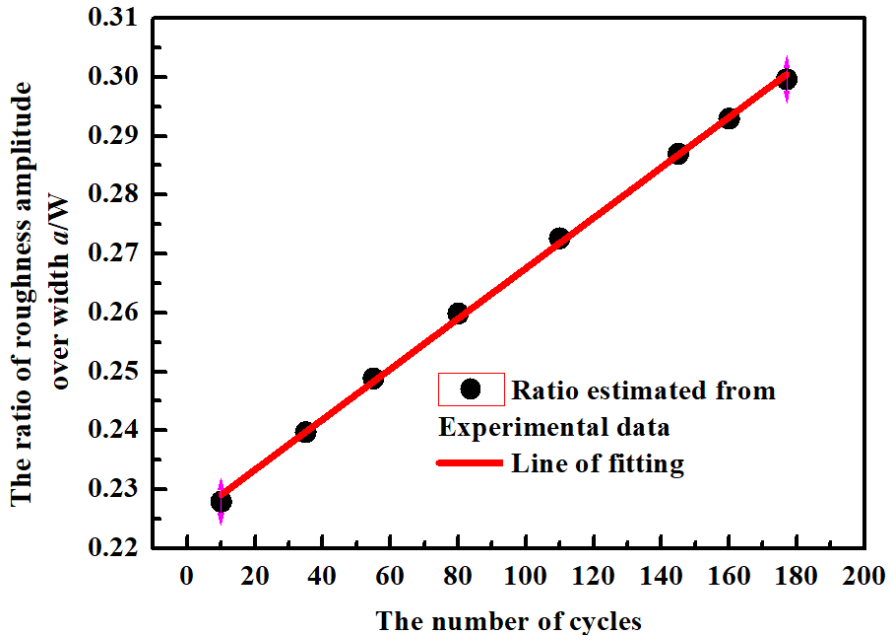

Figure 41 The ratio of amplitude over width as a function of cycles for triangular-formed interfacial roughness

For those interfacial roughness profiles characterized by triangles, the growth of roughness and the sharpness at the triangle's tip increase as the thermal cycle proceeds. The reason behind the roughness evolution may be explained using the calculated stresses under selected roughness profiles, Figure 40. The red curve, compared to others, represents stresses using the roughness profile at the earliest stage of thermal cycles (ten cycles). Stress rises dramatically within a short duration, followed by a gradual decrease in stress. The green curve illustrates the magnitude of stress calculated using the roughness at an intermediate stage of the life cycle. It stays constant for a relatively long period after a significant increase at the beginning of the thermal cycle. The black curve indicates the stress calculated under roughness at the end of the life cycle. The stress is at the lowest stress initially and then remains increasing uniformly throughout the entire lifetime.

Some conclusions can be drawn from the calculated stresses using the selected roughness profile characterized from various stages of thermal cycles. According to Figure 40, it appears that the stress resulting from relatively small size and a blunt tip of roughness increases dramatically within a short period in life compared to the one with a large size and sharp tip of roughness. Based on the temperature-process dependent geometrical parameters characterized from experimentally measured interfacial roughness profiles, it is reasonable to infer that to accommodate relatively large stress generated rapidly at early stages of life cycles within the TC, a geometrical roughness evolution at TGO/BC interface occurs. This could be developed due to plastic deformation caused by either strain rate-dependent massive flow stress triggered by significant creep behaviour of BC, equation (14), or the strain rate-independent plastic behaviour as the calculated equivalent Von Mises stresses reaching the yield strength of BC, Figure 16. The progressive evolution of BC roughness works on inhibition of residual stress at the TC's valley within TBCs since the large roughness results in lower stress levels, Figure 40. However, it also results in a stress concentration effect, which specifically has large effects on stress levels close to the tip of interfacial roughness. This explains the gradual raising of residual stresses at a valley of the TC when using roughness profiles characterized from late stages of thermal cycles.

Comparing the resulting stress from either elliptical roughness or triangular roughness, possible failure mechanism related to the evolution of interfacial roughness can be analyzed. According to [52], [96], two possible failure mechanisms were identified for EB-PVD TBCs. These two failure mechanisms of EB-PVD TBCs differ partially based on the coating interface's roughness, that is a) the cracks nucleate from the voids formed at the TC/TGO interface; b) separation initiates at the ridge of the BC/TGO interface [52]. For cracks initiated within the TC, it is suggested that voids generated within the TC close to the interface are embryonic forms of horizontal cracks, which are introduced by the rumpling effect of the BC, followed by downward displacement of the TGO [82]. As the thermal cycle proceeds, larger voids generated from previous imperfections expand parallel to the interface due to further downward displacements of the TGO layer. Once two neighbouring voids coalescence, the failure-induced crack penetrates the interface between the TC/TGO layer, followed by spallation of the TC where failure is assumed, shown in SEM figures of Figure 42.

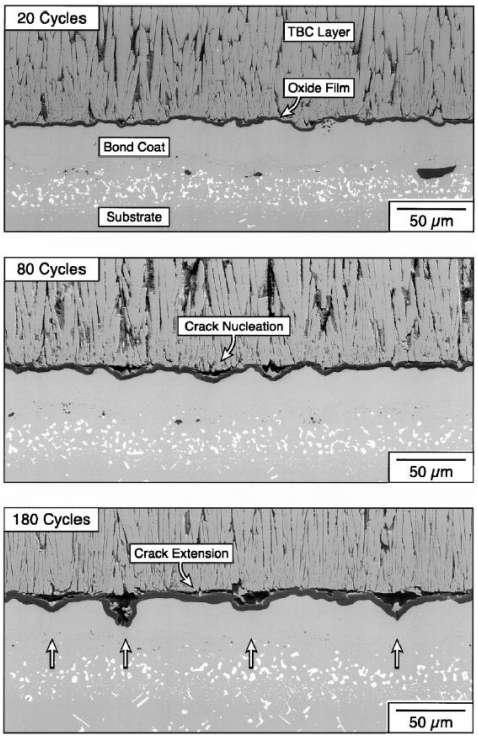

Figure 42 The growth of the TGO as the system cycles and the growth of imperfections by ratcheting [125]

For the multi-layer cracks observed in EB-PVD TBCs, it is suggested that the first stage was nucleation of cracks within the BC. As the TGO thickens, large in-plane stress generated upon cooling leads to the out-of-plane tensile stress within the TGO [52]. Consequently, these neighbouring cracks penetrate the TGO scale and converge within the TC close to the interface. Figure 43 shows the cross-sectional area SEM where the TC has already spalled from the TBC system.

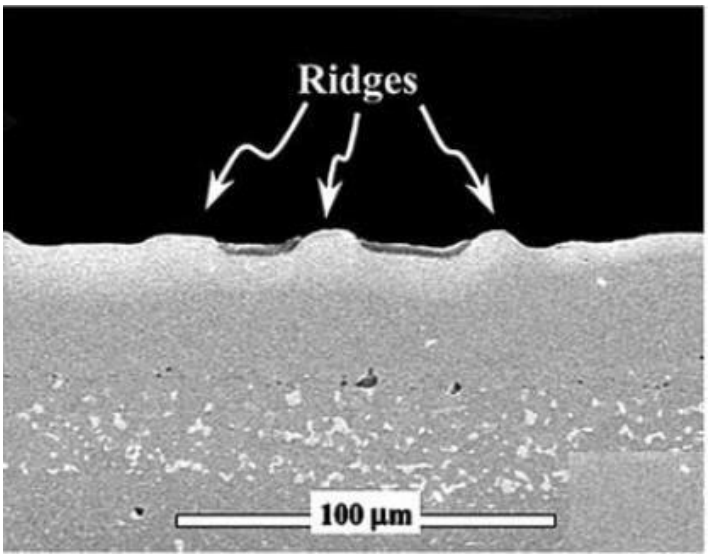

Figure 43 The separation occurred entirely along with the TGO/bond coat interface [52]

The bared BC surface and the remaining TGO ligament between two ridges of the BC indicate the trace of the cracks as analyzed above.

According to [52], the failure mode regarding the crack identified at the BC peak was observed at an early stage among the batch of TBC specimens. This corresponds to the lower stress level identified at the valley of the TC at an early stage of the thermal cycle, with both forms of roughness approximation, Figure 38 (a) and (b), as compared to higher stress levels estimated at the peak of roughness, Figure 38 (c) and (d). On the other hand, those rumpling failures were identified on specimens that failed at intermediate lifetimes, together with cracks observed at the BC peak. The results for stress analysis in the current FE analysis are in accordance with the failure mechanisms described above. Therefore, the FE model's calculated stresses can be used to describe the failure mechanism of EB-PVD TBCs and the effect of the evolution of localized roughness as a function of thermal cycles.

It can be summarized that at the beginning of life cycles, the relatively small and blunt-tip triangular roughness profile would be fast transformed into a form of elliptical roughness in a very short period.

This follows since the residual stress is rapidly relaxed due to significant creep behaviour triggered by massive flow stress within the BC close to the interface during the high-temperature dwell period. The transformed, relatively rounded valley of the TC generates a relatively small level of out-of-plane stress observed at the valley of the TC, which is not large enough for crack initiation, Figure 38 (a). However, with the significant large out-of-plane stress developed at the BC peak, it becomes a possible site for horizontal crack initiation, Figure 38 (c). As the thermal cycle proceeds as described above, the evolution of the interfacial profile gradually makes the roughness larger, resulting in a sharper tip undergoing plastic deformation. This brings stress relaxation during high-temperature dwell duration and changes the geometrical profile at the interface between layers. The elliptical approximated roughness evolves to triangular-formed roughness, which slows the generation of out-of-plane residual stress at the TC's valley, Figure 40.

Nevertheless, during the intermediate to end of a life cycle, the out-of-plane residual stresses developed close to the tip of the valley of the TC increase as a consequence of stress concentration. The stress is large enough to initiate the crack, Figure 38 (b) and coalescence with the crack at the peak of BC due to comparable levels of out-of-plane stress, Figure 38 (d). The schematic diagram of the final resulting multi-layer failure cracks is illustrated in Figure 44.

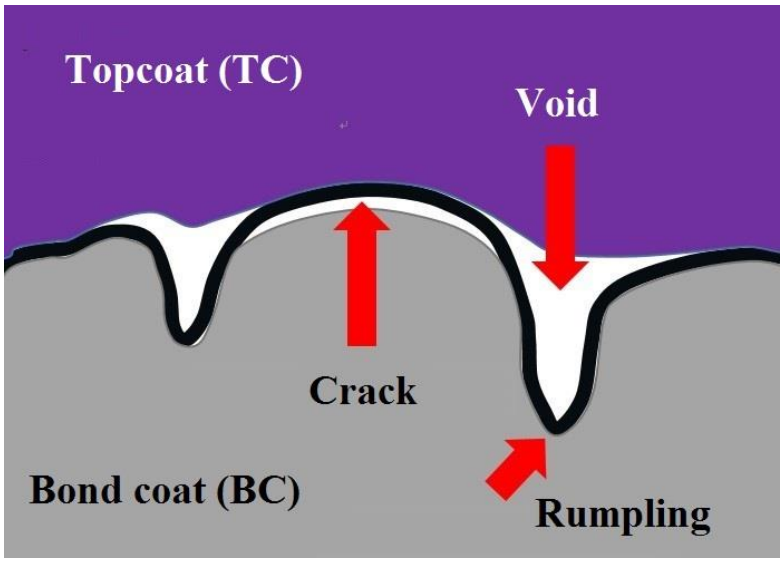

Figure 44 The possible failure mechanism of EB-PVD TBCs at late life cycle stages: Multi-layers cracks are identified

In addition, Hille et al. [178] conducted sufficient work based on numerical calculations and experimental results. The crack behaviour observed directly from samples under thermal cycling FCT has a good agreement with the numerical model, which predicts the crack growth close to the TGO under interface irregularities. The damaged area that the paper referred to focus on the interface between TGO and BC, where propagation of cracks paralleling to the interface is quantitatively evaluated through the crack length as a function of thermal cycles. The research in the present paper focused on both TC/TGO and TGO/BC interface. The cracking behaviour is proposed under quantitative evaluation on the out-of-plane stress state through FEA with the integration of a series of interfacial morphology captured by various stages of thermal cycles. Compared to Hille et al [50], the results might be similar to some extent, but the methodology we used is different.

3.5. Conclusions

This paper aims to improve the accuracy of estimated stress through FE analysis by incorporating temperature-process-dependent parameters into the FE model. The effect of interface roughness on stress distribution was investigated by using two types of specific roughness profiles. Specifically, based on the SEM cross-sectional images of EB-PVD TBCs, roughness profiles in terms of the amplitude and width of imperfections were developed to describe continuous saw-like or elliptical interfacial roughness profiles. Using the evolutional-based material properties combined with the phase transformation model, the FE study in this paper provides insight into the effects of gradual mechanical, thermal and inelastic behaviour of the metallic bond coat and oxide TGO to more-realistic smooth variations of residual stresses.

The cyclic residual stresses at specific positions in the TBCs were calculated using temperature-process dependent model parameters in FE models. Two main conclusions can be drawn from the results of the FE analysis:

A) The residual stresses were calculated for specific cases 1) elastic topcoat, 2) sintering of topcoat, 3) elastic topcoat (sintering) plus creep of bond coat and oxide TGO 4) Sintering topcoat with both creep and yielding of bond coat and oxide TGO for the given roughness profile. Comparing cases 1) and 2), it is noted that incorporating the sintering model into the topcoat reverses the cooling stress as it increases when temperature drops during thermal cycles. Comparing cases 2) and 3), it is concluded that swelling of TGO plays an essential role in facilitating the out-of-plane residual stresses developed within the topcoat. On the other hand, stress relaxation is implemented by including the strain-rate-dependent creep model exerted on the BC and TGO layers. Comparison between case 3) and 4) suggests the importance of the strain-rate independent yielding model of the BC/TGO layer on stress distribution. The results show that it has a more profound effect on the BC's stress distribution by significantly smoothing the BC residual stress rather than within the TC layer.

B) The effect of different interface roughness profiles on residual stresses was also evaluated. It was observed that different stress levels are obtained from the resulting stress by using different interfacial roughness geometries in the FE calculation. The residual stress obtained from the elliptical roughness profile has lower stress levels in the TC and higher stress levels in the BC than the one obtained from the triangular roughness profile at the early stage of thermal cycles. Combined with the resulting stress calculated using a series of roughness profiles from different stages of thermal cycles, it is strongly indicated that the evolution of interfacial roughness is generated through plastic deformation of the BC to accommodate the relatively large residual stress. Correspondingly, the general trend of the developing stress is strongly affected by the shape of the evolving interfacial roughness, specifically at the tip of either the ridge of the BC or the valley of the TC where horizontal cracks might form at maximum out-of-plane residual stress.

4. The Effect of Interfacial Roughness on Residual Stresses in Electron Beam-Physical Vapor Deposition of Thermal Barrier Coatings

This chapter addresses objectives 1 and 2 by conducting failure mechanism analysis via parametric study based on the numerical FE model developed in chapter 3 for EB-PVD TBCs under thermal cycling environment.

B. Zhang, K. Chen, and N. Baddour, "The Effect of Interfacial Roughness on Residual Stresses in Electron Beam-Physical Vapor Deposition of Thermal Barrier Coatings," *Coatings*, vol. 11, no. 3, Art. no. 3, Mar. 2021, doi: 10.3390/coatings11030341

[a]*B. Zhang,* [b*]*Kuiying Chen,* [a] *N. Baddour,*

[a] *Department of Mechanical Engineering, University of Ottawa, Canada*

[b] *Structures, Materials and Manufacturing Laboratory, Aerospace Research Center, National Research Council Canada*

Abstract

Residual stresses play an essential role in determining the failure mechanisms and life of Electron Beam-Physical Vapour Deposition Thermal Barrier Coating system (EB-PVD TBCs). In this paper, a new transitional roughness model was proposed and applied to describing the interfacial roughness profile during thermal cycles. Finite element models were implemented to calculate residual stresses at specific positions close to interface of TBCs using temperature process-dependent model parameters. Combining stresses evaluated at valleys of topcoat (TC) and excessive sharp tip roughness profiles, positions where the maximum out-of-plane residual stresses occur were identified and used to explain possible cracking routes of EB-PVD TBCs as interfacial roughness evolves during thermal cycling.

Keywords: Stress model, FE model, temperature-process dependent parameters, evolution of interfacial roughness, parametric study, transitional roughness approximated model

4.1. Introduction

The residual stresses that develop close to the interface between layers play a significant role in determining the life span of an Electron Beam-Physical Vapor Deposition (EB-PVD) Thermal Barrier Coating (TBC) system. Many attempts have been made using analytical or numerical methods to estimate the stresses which are generated as a consequence of thermal expansion mismatch between layers and the growth of the thermally grown oxide (TGO) [64], [82], [95], [125], [133], [139], [143]. With additional factors taken into consideration and integrated into the stress model, calculated stresses and their distributions are expected to reflect the measured results, based on either isothermal or thermal cycling exposures. To date, process-dependent material properties have been shown to be significant in affecting the magnitude of stress levels, i.e., the variation of elastic modulus and coefficient of thermal expansion versus temperature, the change of strain rate dependent creep or strain rate-independent yielding behaviour. Even a variation of phase components during progressive oxidation of the bond coat (BC) accompanying the swelling rate throughout the whole thickness of the TGO layer also greatly affects the stress levels during thermal cycles. A few analyses also focused on the pattern variation of interfacial roughness profiles, where typical roughness parameters were measured from the observed microstructures and used to characterize the roughness profiles versus temperature and exposure duration. The characterized roughness parameters from thermal cyclic experiments are used as input data in the current study [93]. The cross-sectional images of TBCs were provided at different stages of lifetime to illustrate the roughness variation under thermal cyclic experiments [124]. The effect of additional factors on the TBC durability, such us the TC (topcoat) fabrication method, the high temperature, the cycle frequency and thermal gradient, were demonstrated with interaction of the interfacial roughness [67]. Different failure mechanisms of EB-PVD TBCs were developed based on the roughness level measured in the thermal cyclic experiments with respective energy release rate (ERR) calculated [52]. The effect of grit-blasting process on durability of EB-PVD TBCs are described [149]. However, less effort was made on how a change in interfacial roughness affects the development of residual stresses [67], [93], [124], both of which could be critical in determining the possible positions

where cracks nucleate at the maximum out-of-plane residual stresses estimated from the stress model. This, in turn, has a profound effect on determining the failure mechanisms of EB-PVD TBCs [52], [149].

In this paper, the relationship between different roughness models and stress behaviour at critical positions where maximum stress levels could be obtained is analyzed. Finite Element (FE) models are established by using commercial finite element code ABAQUS. The method to characterize the roughness level of imperfections close to the interfaces is developed based on existing experimental data [92]. The material parameters of different layers are defined and integrated into the FE analysis. Parametric studies are conducted to examine the effect of geometrical parameters on the stress levels at specific positions within different layers including TC, TGO and bondcoat (BC). A transitional model is proposed to illustrate the impact of global distance between imperfections on stress levels within imperfections. Possible failure modes of EB-PVD are further explained using both the variation of global interfacial roughness and the stress at a valley of the TC and ridge of the BC.

4.2. Compilation of parameters and integration into FE models using experimental data under thermal cycles

The methodology used in the present chapter is similar to chapter 3.2 expect that the position of estimated stress is evaluated. The section that is overlapped with chapter 3.2 won't be demonstrate here.

(d) Positions for residual stress evaluations

Compared to prior work described in chapter 3.2 that focused on specific positions close to the interface where only the maximum residual stress was identified [87], the current work calculates residual stresses as a function of position. Therefore, by examining different locations in the FE analysis, it is

possible to find the maximum stress level at which the crack nucleates. Meanwhile, the relationship between the resulting stress and position is established, which, in turn, provides valuable information for establishing analytical stress models. The relative distance between the TC /TGO interface to the positions (y) are shown in Figure 45, at which the stresses will be evaluated specifically.

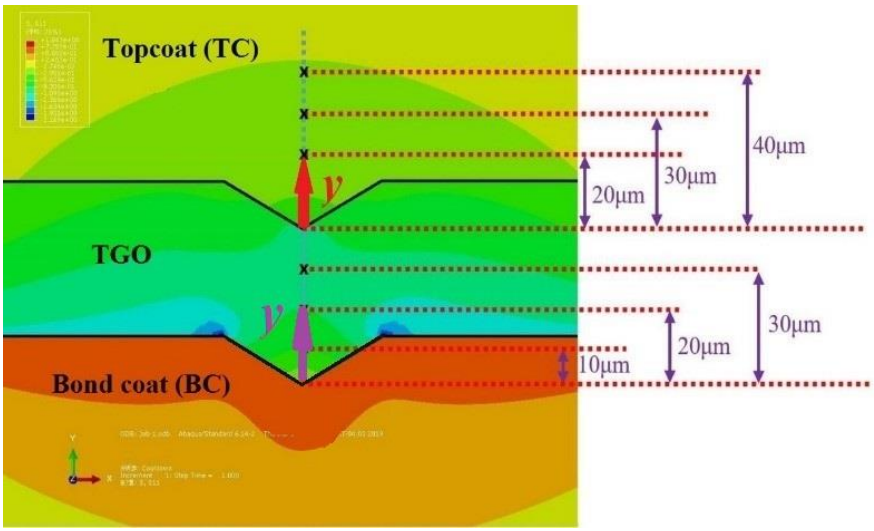

(a)

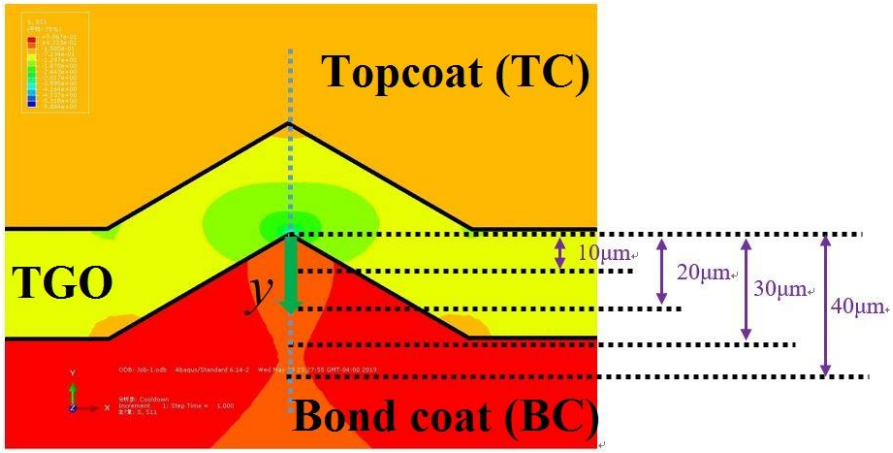

(b)

Figure 45 The schematic diagram of positions where stresses are calculated, (a) the stresses within the TC and TGO layer, (b) the stresses within the BC layer

4.3. FE model

The methodology used in the present chapter is identical to chapter 3.3, which won't be demonstrate here.

4.4. Results and discussion

4.4.1. Parametric study of the effect of local geometrical parameters on stress distribution of TBC

The magnitude of residual stress at a valley of the TBC/TGO interface is governed by not only temperature-dependent material properties such as sintering of the TC and inelastic behaviour of the TGO and BC, but also by the interface roughness between each layer [18], [67], [117] characterized using temperature-process dependent localized geometrical parameters. To analyze the effect of those parameters on residual stresses, a parametric study is conducted where an isosceles triangle is used to approximate the interfacial roughness profile. Three parameters are incorporated into the FE model: (i) A is amplitude and indicates the height of a triangle, (ii) W is the width and indicates the length of the bottom side of triangle applied to defining the shape of triangular imperfection, and (iii) the position y is used to describe the locations (y_{TC}, y_{TGO}, y_{BC}) where the stresses are evaluated, Figure 46.

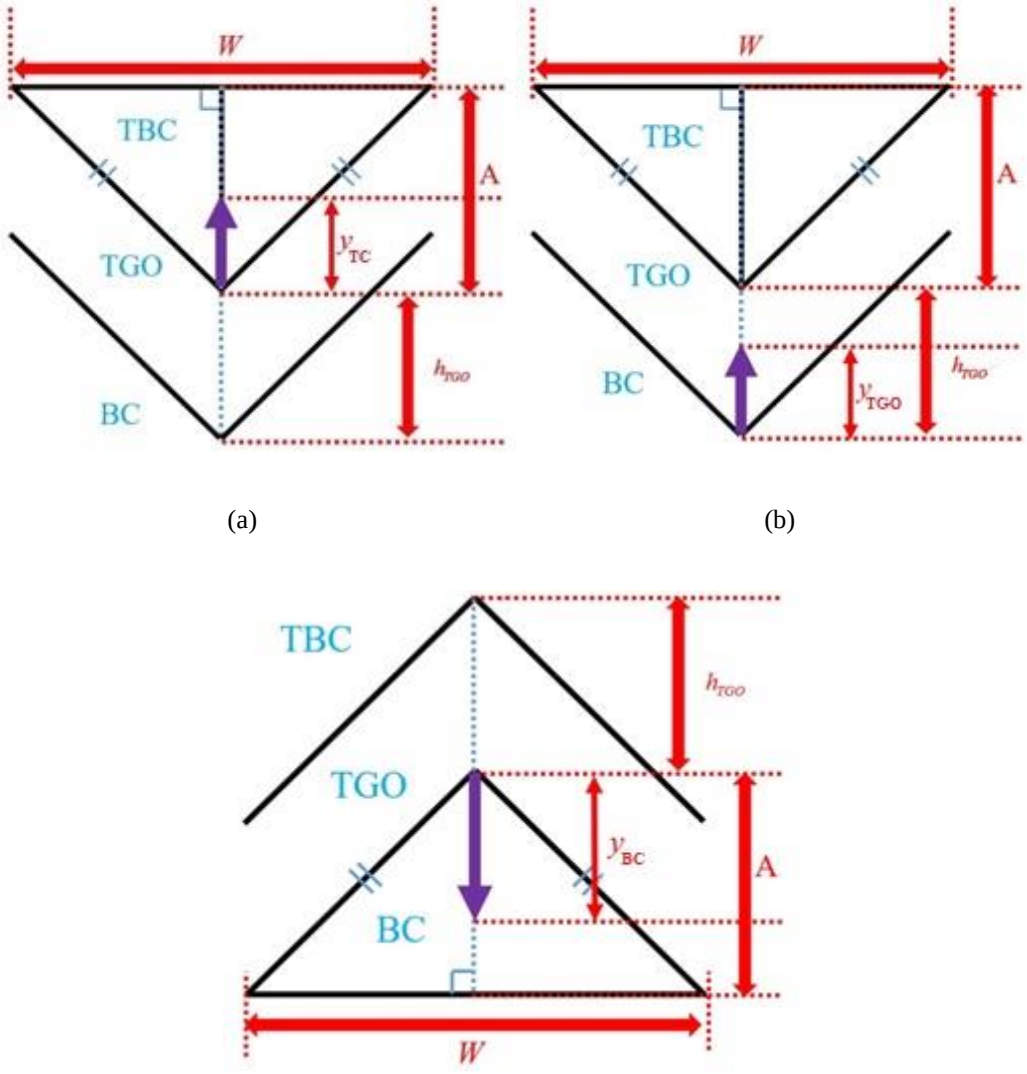

Figure 46: Schematic diagram of individual interfacial roughness profile used for a parametric study where amplitude, width, TGO thickness as well as positions are illustrated for different layers.

To characterize the effect of each parameter on stress, a parametric study using the controlled variants is applied to the FE analysis. At position y, residual stresses are calculated while allowing variations of amplitude A and width W. Also, for a given amplitude *A* and width *W*, stresses are calculated at various positions y. A reference set of parameters used to characterize the roughness

profile are selected from experimental results at the failure cycle of 177 hours of TBC exposed at 1151°C. The geometrical parameters used in the FEA model are presented in Table 4.

Table 4 Reference set of roughness parameters used in the FE model at N=177 hours at 1151°C [92].

Properties	Value	Unit
Amplitude A	4.12	μm
Width W	13.76	μm
Total TGO thickness d_{TGO}	4.92	μm
Relative position y_{TC} or y_{BC}	1.27 (TC) or 0.43 (BC)	μm

(a) The effect of roughness amplitude on stress at the valley of TC and ridge of BC

The effect of roughness amplitude on residual stress is analyzed for both the TC and BC layer. In addition to the amplitude A for the reference group, $0.5A$ and $1.5A$ of the amplitudes are also used for FE calculations. The resulting stresses, together with those from the reference group, are used to assess a correlation of out-of-plane residual stresses versus amplitude. The models depicting the geometric roughness are presented in Figure 47.

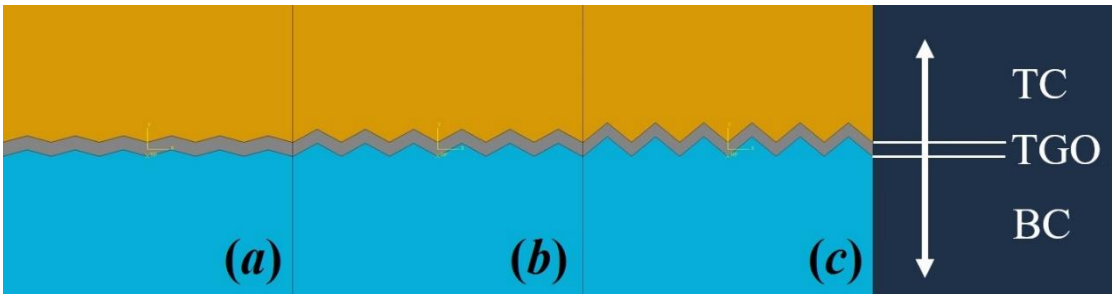

Figure 47 Amplitude variation of (a) $0.5A$, (b) A and (c) $1.5A$ listed from left to right where the rest of the parameters are kept constant

The stresses from the valley of the TC are calculated and plotted in Figure 48 as a function of time.

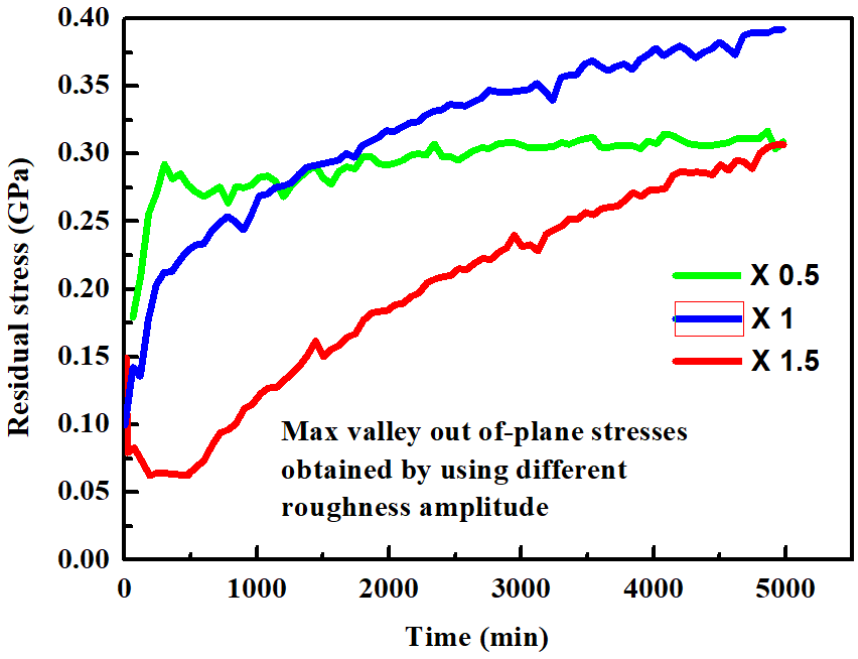

Figure 48 Out-of-plane residual stresses at the valley of TC with different roughness amplitude as thermal cycle proceeds

It was suggested in [95] that increasing the amplitude of imperfection roughness would increase the stress close to the interface, since the stress concentration is boosted by increasing sharpness at the tip of roughness. However, the red curve in Figure 48 shows an opposite effect on stresses in a large roughness amplitude. Because the positions with respect to the interface are identical for these three cases in the FE model, the deeper the amplitude used in interfacial roughness mapping, the narrower the tip at the valley of the TC. It seems that there is an inhibitive effect on the stress estimated at the tip of the TC as the sharpness of the geometrical roughness reaches a critical value. This is reflected by a lower stress obtained from the valley of the TC when $1.5A$ amplitude is used in the FE model. For the stress obtained from the peak of the BC, different amplitudes exerts a profound effect on stress level according to the FE results, as can be seen in Figure 49.

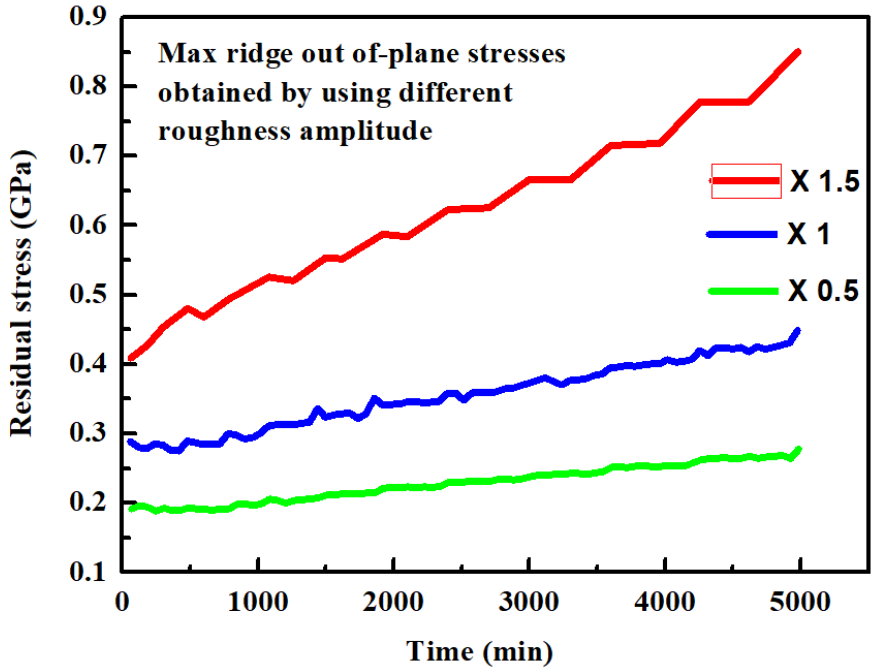

Figure 49 Out-of-plane residual stresses at peak of BC with different roughness amplitudes as thermal cycle proceeds

It is observed that most of the roughness develops during the rumpling of the BC as a consequence of creep during high-temperature exposure. The creep proceeds to accommodate large mismatch stress during a fast heating period. The amplitude of the roughness of the BC surface is directly affected by the rumpling kinetics, resulting in further increase of stress and delamination crack nucleation at the TGO/BC interface. However, for the stresses distributed within the TC, according to the failure analysis in [4][17], it is at the middle stage of thermal cycling that delamination cracks are generated by coalescence of voids located at the valley of the TC. This may indicate that as the thermal cycle proceeds, the increase of roughness amplitude facilitates the development of out-of-plane residual stress at the valley of the TC, while the out-of-plane stress developed at early stage of thermal cycles with initial roughness amplitude is not large enough to initiate crack nucleation. This avoids early crack generation within the TC layer.

(b) Effect of roughness width on stress at the valley of TC and ridge of BC

Similar to the analysis in the preceding section, the effect of roughness width W on residual stress is analyzed for both TC and BC layers. In addition to the width W from the reference group, two other cases of $0.5W$ and $1.5W$ width were studied. The models depicting the geometric roughness are presented in Figure 50.

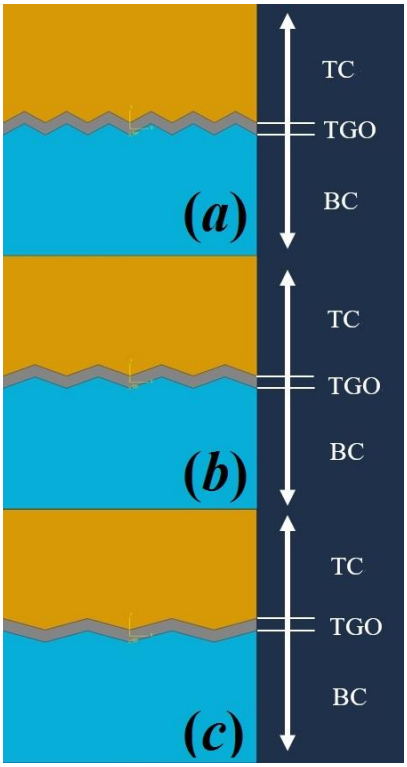

Figure 50 Width variation of (a) $0.5W$ (b) W and (c) $1.5W$ listed from top to bottom where the remaining parameters are kept constant

The stresses at the valley of the TC versus exposure duration are plotted in Figure 51.

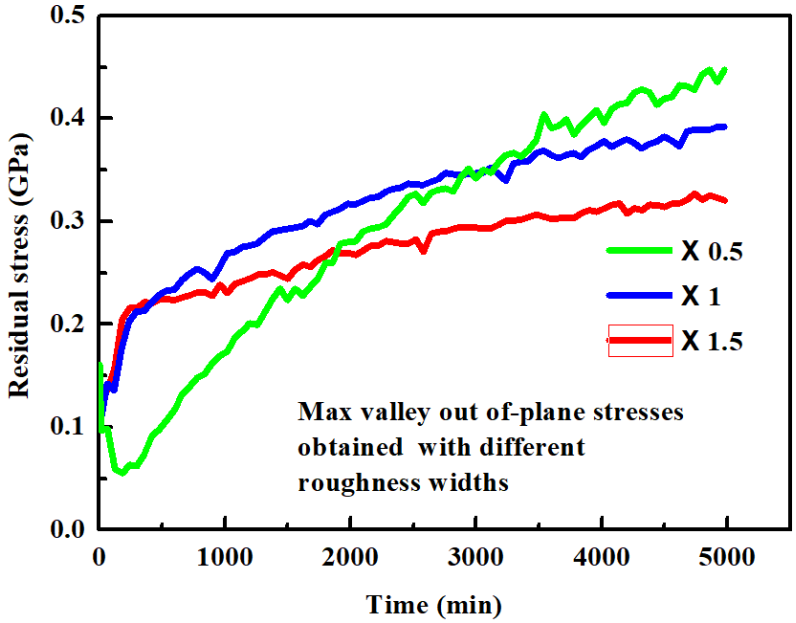

Figure 51 Out-of-plane residual stresses at the valley of the TC with different roughness width versus thermal cycle

Based on Figure 51, it appears that the narrowing width W has a similar effect as increasing the amplitude A on stress distributions. That is, higher stresses are expected for rougher interfacial roughness, characterized either by a higher amplitude (the blue curve in Figure 48) or by a narrower width at the middle stage of thermal cycles (the green curve in Figure 51). However, it should be noted that with an invariant width of the overall TBC FE model, the amount of roughness varies as a function of the individual width of imperfections, Figure 50. It is obvious that more imperfections will be incorporated into FE calculations as the width of individual imperfections is assumed to be narrower. Although there is a rapid growth in residual stress calculated from narrower roughness profiles (the green curve in Figure 51), a lower stress state is obtained initially. This phenomenon can be explained in two aspects. On the one hand, the narrower roughness profiles boost the stress concentration at the valley of the TC, which in turn raises the stress on individual imperfections; this can be seen for the calculated stresses at the peak of the BC, Figure 52. On the other hand, the intensive interaction between

relatively close neighbouring imperfections impedes the development of out-of-plane tensile stresses within the TC.

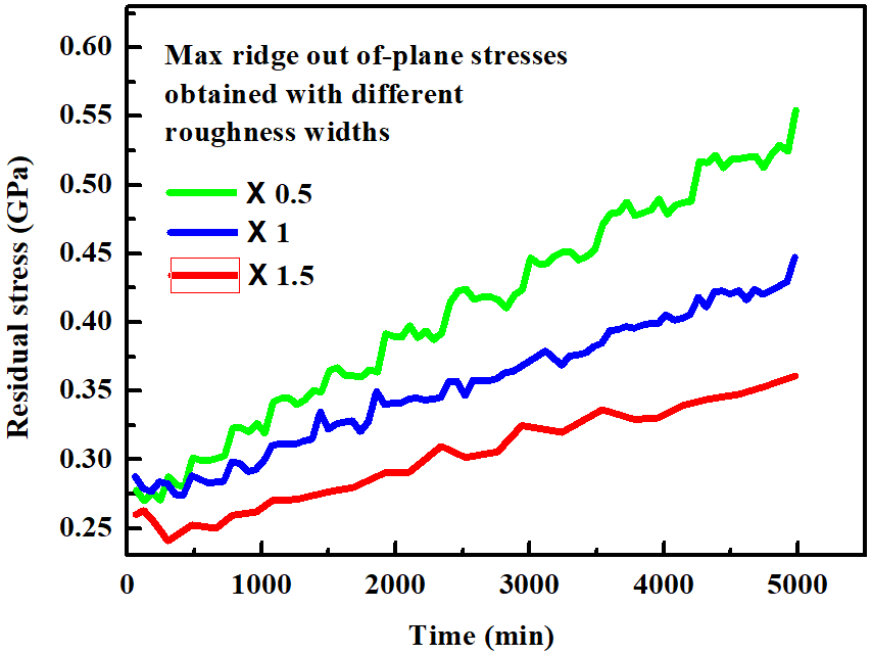

Figure 52 Out-of-plane residual stress at the peak of BC with different roughness width as thermal cycle proceeds

(c) Correlation between positions and stresses at the valley of TC and ridge of BC

The residual stresses were calculated under different amplitudes and widths. Meanwhile, the calculated stresses are different at selected positions at the bottom of the TC and ridge of the BC. Five relative positions with different "*y*" in Figure 45 are selected at the valley of the TC and ridge of the BC close to the interface, where a total of ten residual stresses are calculated, respectively. The geometry of interfacial roughness is characterized using roughness parameters measured at 177 cycles based on amplitude and width experimental data, Table 4. The maximum out-of-plane cooling stresses calculated at different positions away from the valley of the TC are plotted versus time in Figure 53.

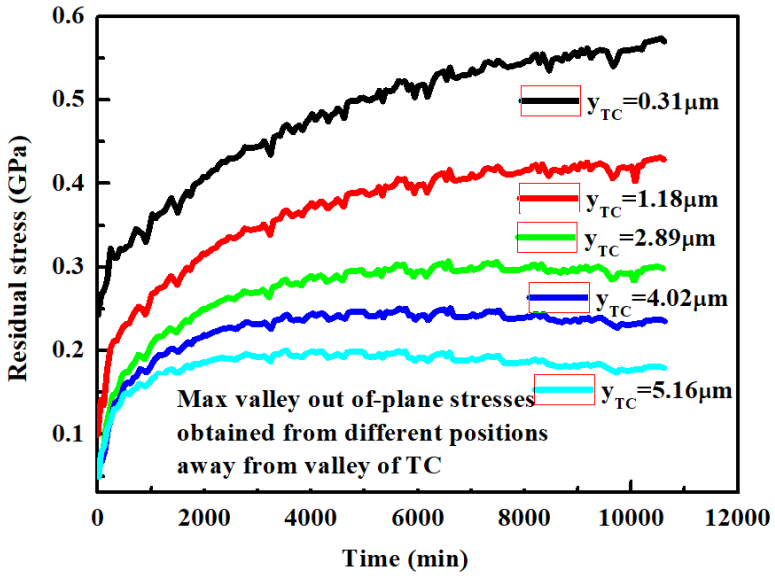

Figure 53 Out-of-plane tensile stresses calculated at the valley of the TC as a function of time at various positions

It is expected that a higher level of stresses close to the interface is due to larger strains from either coefficient of thermal expansion mismatch (CTE mismatch) between different layers or volumetric expansion due to oxidation of the BC layer. It can also be seen that stresses away from the interface increase uniformly compared to those close to the interface. Concerning the complexity of multi-layers in TBC, there exists a relatively large fluctuation of residual stresses close to the interface within the TC. Moreover, it should be mentioned that residual stresses are calculated for the roughness profile with an amplitude equal to 4.12 μm. The cyan curve of stresses illustrated in Figure 53 is at the position of 5.16 μm away from the valley of the BC, a position that is located outside of the valley of TC. The general trend of all curves, including the cyan curve, suggests that the out-of-plane residual stress decreases when moving away from the valley of the TC.

It can be expected that the possible region of cracks where the maximum out-of-plane stress occurs is close to the interface within the valley of the TC. However, it was observed that the positions where the maximum stress occurs are shifted away from the bottom of the TC valley, as previously mentioned.

This is possible for some interfacial roughness observed from the experimental cross-sectional area; for example, the interfacial roughness with a very sharp tip where the ratio of amplitude over width exceeds a critical value.

The higher maximum out-of-plane cooling stress is also obtained close to the interface at the ridge of the BC, as seen in Figure 54. Similar to the residual stresses at the valley of the TC, there is a high possibility for crack nucleation at the peak of the BC close to the interface where the highest out-of-plane residual stress occurs.

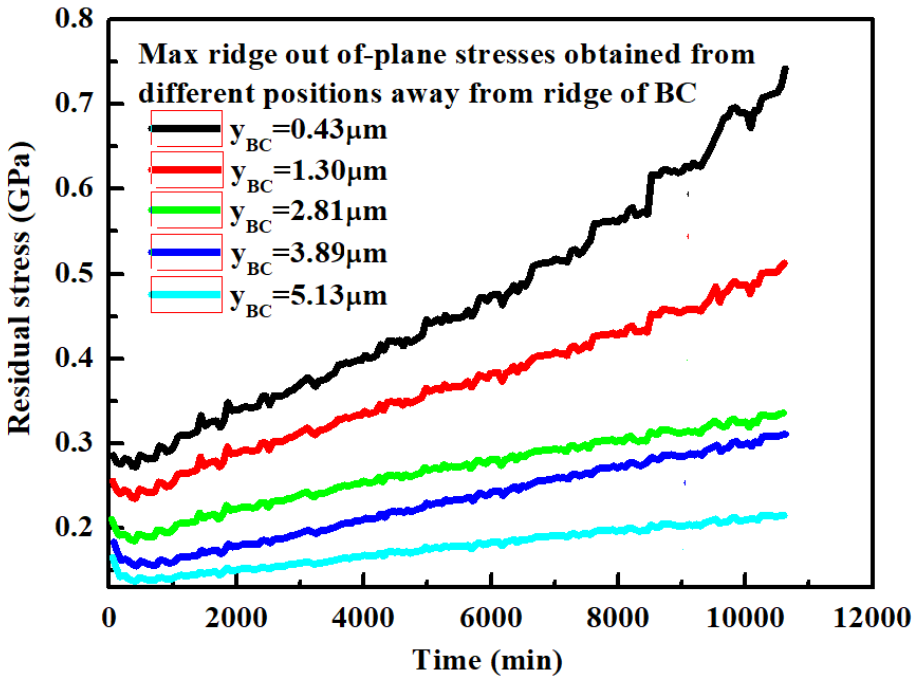

Figure 54 Out-of-plane tensile stresses calculated at the ridge of the BC as a function of time at selected positions

4.4.2. Generalized imperfection model and the impact of distance between imperfections on stress distributions

One of the geometrical parameters used to model the roughness profile, the width of the bottom side of the imperfection, is derived using experimentally measured tortuosity. According to the schematic diagram of triangular approximated roughness in Figure 23, the tortuosity can be expressed as,

$$T_L = \frac{2 \times b}{W} \tag{36}$$

For a single imperfection described in the form of a triangle, the larger the tortuosity, the sharper the angle of the valley. As can be seen in Figure 55, for those two triangular-shaped imperfections, assuming the amplitudes are identical ($A = A'$), the imperfection shown in Figure 55(b) has higher tortuosity than the one in Figure 55(a) ($T_L' > T_L$). According to Equation (21), the one with higher tortuosity has a narrower width, which is shown for a single imperfection model in Figure 55.

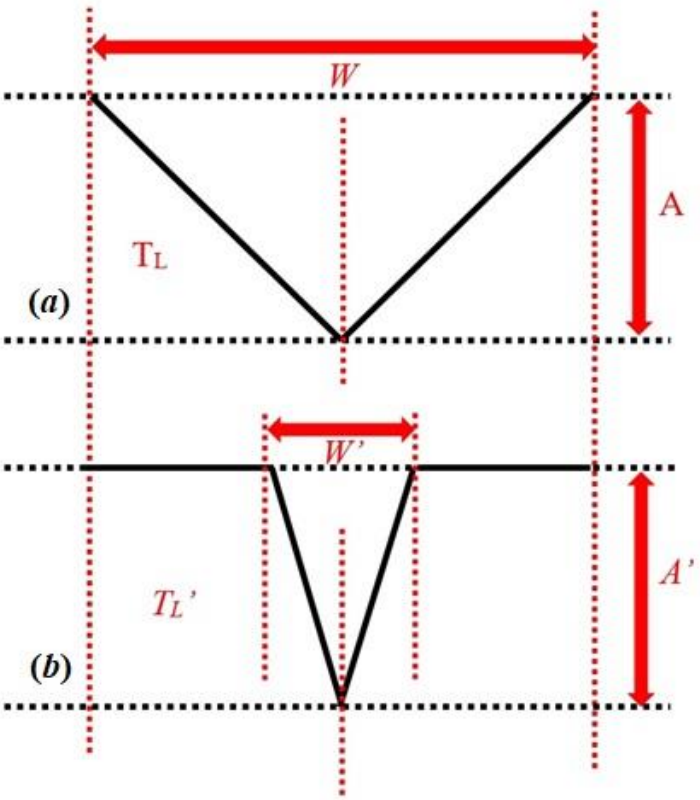

Figure 55 Schematic diagram describing the relationship between tortuosity and width of interfacial roughness imperfection for a single imperfection

However, for multiple imperfections closely located at the interface, it becomes more complicated to estimate the tortuosity for a defined length of the roughness profile. As can be seen in Figure 56, it is still assumed that the amplitudes are identical for triangular approximated imperfection ($A = A'$). This indicates that the tortuosity is higher for the individual "narrower" imperfection in Figure 56(b) than the "wider" one in Figure 56(a). However, this discrepancy can be supplemented by adding additional "wider" imperfections within a defined length. The tortuosity for two sets of connected imperfections, according to Figure 56, might be identical ($T_L' \simeq T_L$).

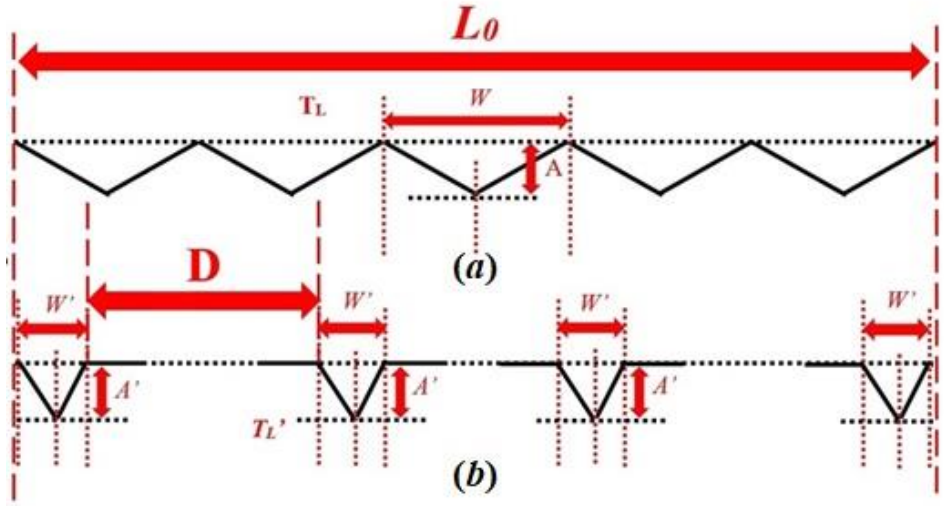

Figure 56 Schematic diagram describing the relationship between tortuosity and width of interfacial roughness imperfection for multiple imperfections

However, it is obvious that the width of an individual imperfection is not the same in the roughness profile of Figure 56(b) as the one in Figure 56(a). This indicates that Equation (21), which is used to estimate the width of the bottom side for interfacial roughness for connected imperfections, is not able to describe the roughness profile when there is the spacing between two imperfections.

The results from the preceding analysis provide a different way to understand the physical implication of tortuosity such that a transitional roughness model is introduced. This transitional model becomes the intermediate between the most simplified continuous roughness model and the generalized model observed from cross-sectional SEM images, Figure 57.

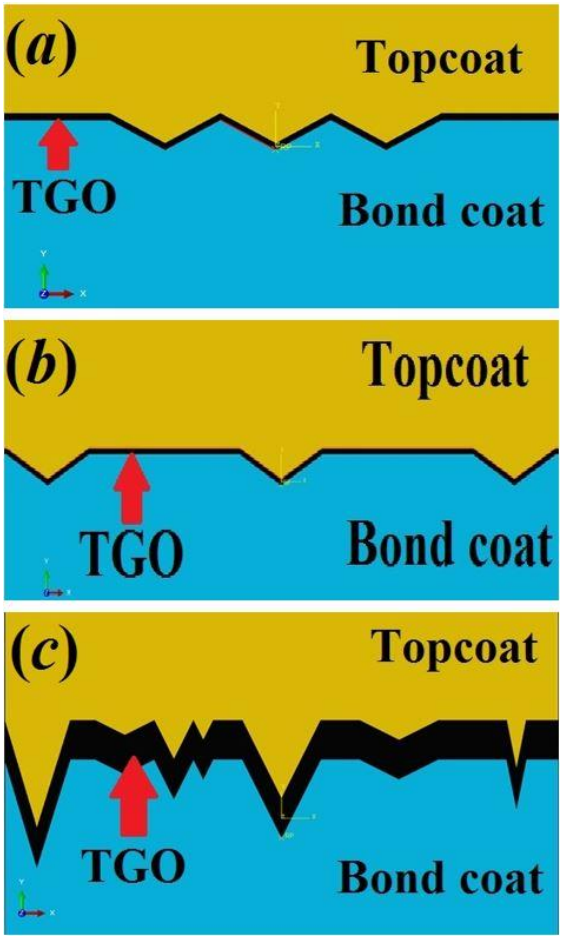

Figure 57 Different models used to describe the interfacial roughness profile (a) Continuous roughness model, (b) Transitional roughness model, (c) Generalized roughness model

According to the profiles of the metal/oxide interface at various stages of thermal cycling in Figure 58, it is appropriate to consider the most simplified continuous roughness model of Figure 57(a) to represent the roughness profile at the initial stage of thermal cycling, where small connected saw-like imperfections dominate. It can also be treated as the intermediate section between two large imperfections at a post-failure stage, where similar roughness profiles can be identified as described above.

The transitional roughness model described in Figure 57(b) is proposed to simulate the roughness at a post-failure stage, Figure 58. The imperfections shown in Figure 57(b) indicate two large imperfections, as highlighted in the circle in Figure 58, where relatively high-stress levels could be localized somewhere at the bottom of the imperfections. The straight line between two imperfections in Figure 57(b) represents the small imperfections in the roughness at a post-failure stage in Figure 58, which will not have a large impact on the stress within the large imperfections. It should be noted that in reality, either the distance between two imperfections or the amplitude of roughness could be varied at different measured positions at interface between layersFigure 57(c). These parameters are taken as their mean values (constant) for the parametric study described below.

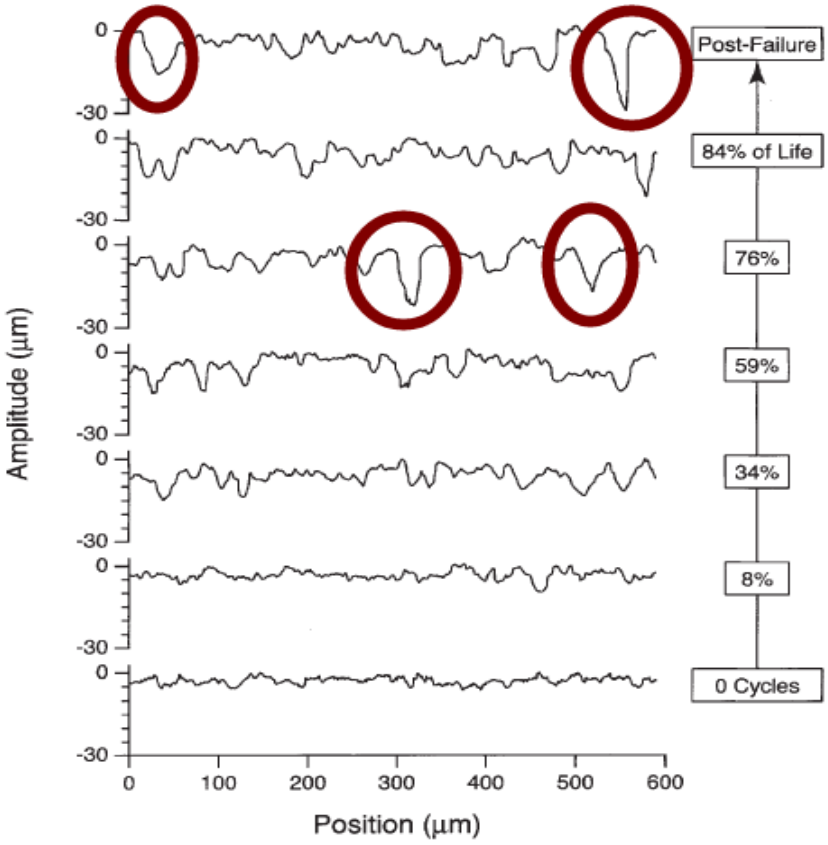

Figure 58 Profiles of the metal/oxide interface extracted from cross-sectional images at various stages of thermal cycling, illustrating the continuous evolution of interface morphology during cyclic exposure [149]

Knowing that distance between imperfections is a global factor compared to the geometrical parameters that are used to characterize the geometry of localized imperfections, it is necessary to conduct another parametric study to evaluate the possible effect of the spacing parameter (D) on the stress level, Figure 56. The spacing parameter (D) is incorporated into the FE models, and other factors, such as the size of the imperfection itself (the amplitude and width), are held constant. The parametric study in the current section only deals with the effect of the global parameters on the stress levels at the valley of TC.

Accordingly, an equation describing the new width of local imperfections is required when spacing is used in the FE model. The spacing incorporated via the tortuosity becomes

$$T_L = \frac{2b'N_r + (N_r - 1)D}{L_0} \tag{37}$$

where b' is the new length of the hypotenuse of the isosceles of triangular-approximated roughness profile after the spacing parameter is included in the FE model. Furthermore, N_r is the number of imperfections at the interface of the current FE model, D is the spacing parameter and L_0 is the total width of the roughness profile described in the FE model, Figure 56. Based on the definition of an isosceles triangle, the new width of the isosceles in triangular-approximated roughness is defined as

$$W_L = 2\sqrt{b'^2 - A^2} \tag{38}$$

where W_L defines the local width of the isosceles in triangular-approximated roughness. Substituting equation (38) into equation (37), the new width of the isosceles in triangular-approximated roughness with a defined number of imperfections *N* can be obtained from

$$W_L = 2\sqrt{\left[\frac{T_L L_0 - (N_r - 1)D}{2N_r}\right]^2 - A^2} \tag{39}$$

Equation (39) only works once equation (37) is satisfied. That is,

$$W_L \times N_r + \left(N_r - 1\right) \times D = L_0 \tag{40}$$

In other words, the spacing parameter has to be determined once the number of imperfections is defined. The spacing could be obtained by substituting equation (39) into equation (40) to yield,

$$D = \frac{{L_0}^2 \left({T_L}^2 - 1\right) - 4{N_r}^2 A^2}{2L_0 \left(N_r - 1\right)\left(T_L - 1\right)} \tag{41}$$

In this study, the amplitude A and tortuosity T_L of roughness are characterized from a reference group, Table 4, as the transitional roughness model simulates the roughness at a post-failure stage. The total width of the roughness profile L_0 was selected as 300 μm since it is wide enough to incorporate roughness with spacing integrated into the model. The global spacing parameter D and local width W_L of imperfections are described as a function of the number of imperfections in the FE model, Figure 59. It is noted that equations (39)-(41) are validated, as there is no spacing between imperfections where the maximum width of local imperfections equals approximately 13.76μm when most imperfections are incorporated into the FE model, Table 4. Importantly, even if the tortuosity and average amplitude are predetermined for a specific number of cycles, it can be seen from Figure 59 that the interfacial roughness profile still needs to be determined from the number of noticeable imperfections N_r within a defined length of interfacial roughness. Figure 60 illustrates different roughness profiles with the same combination of tortuosity and amplitude but different local widths and spacing parameters. Details are given in Table 5.

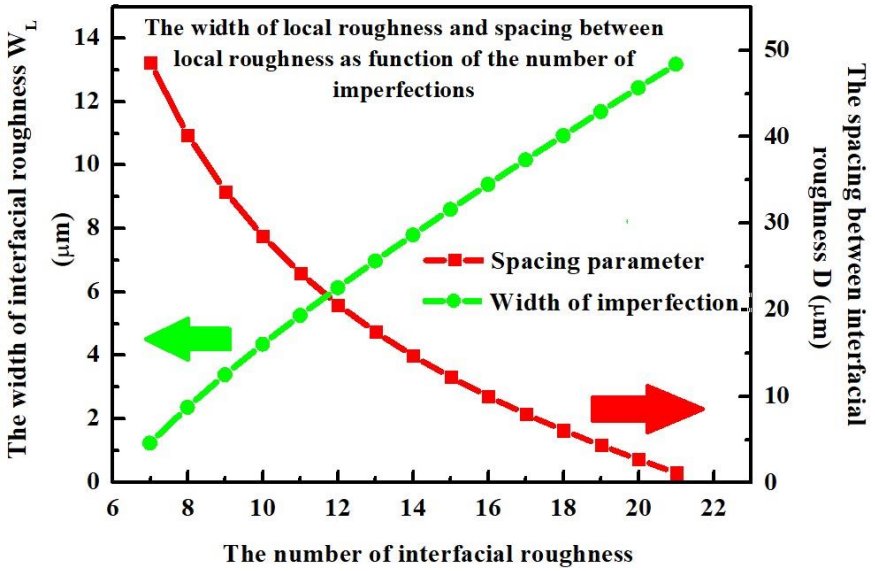

Figure 59 Global spacing parameter D and local width of imperfection W_L as a function of the number of interfacial imperfections

Table 5 Parameters used in FE analysis in terms of the global spacing parameters

No# of FE model	D (μm)	W_L (μm)	No# of imperfections
a	33.68	3.391	9
b	17.44	6.977	13
c	7.95	10.16	17
d	1.164	13.18	21

For all FE cases	
$A\ \ (\mu m)$	4.12
$d_{TGO}\ \ (\mu m)$	4.92

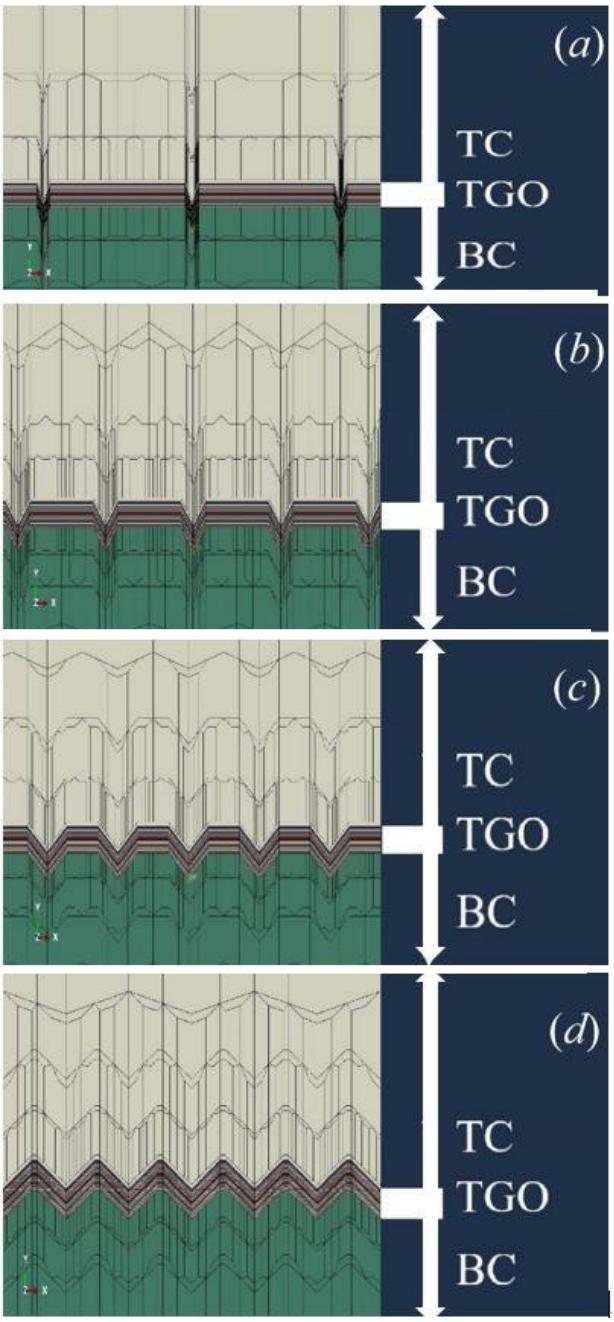

Figure 60 Interfacial roughness profile for different spacing between imperfections

In other words, all four roughness profiles illustrated in Figure 60 are possible interfacial roughness profiles for the post-failure stage when the number of noticeable imperfections N_r is selected based

on Figure 59. The results of the maximum cooling stresses within 5000 minutes calculated from the valley of the TC are plotted in Figure 61.

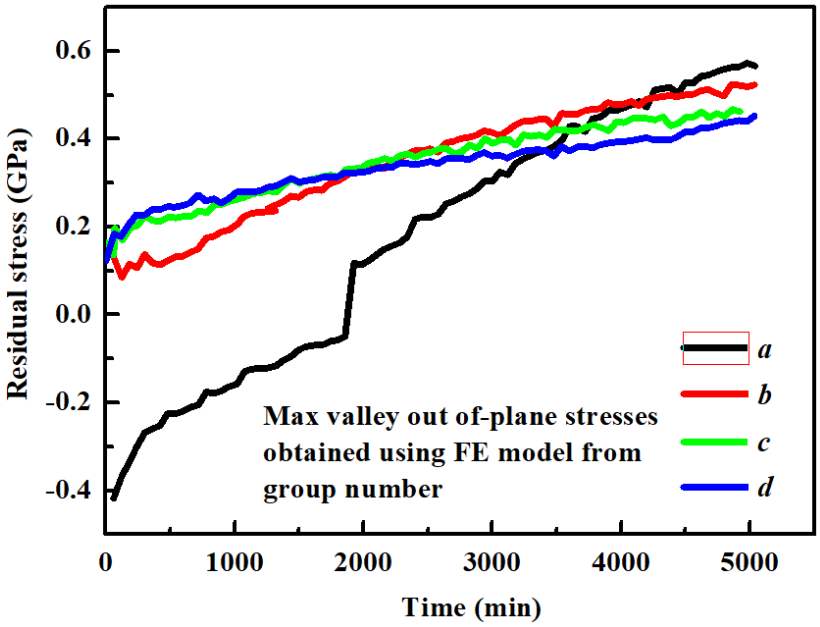

Figure 61 Results of the calculated out-of-plane thermal stresses within the TC with respect to spacing between imperfections

Combining the observation based on the profiles of metal/oxide interface extracted from cross-sectional images at various stages of thermal cycling in Figure 58, it is expected that at the beginning of thermal cycles (thermal cycles < 1500 cycles), the increasing stress is facilitated for roughness profiles with a wider local length and narrower spacing between neighbouring imperfections that can be treated as a plateau between neighbouring imperfections. Nevertheless, the resulting current stress from different transitional roughness models only indicates the variation of stress level at a post-failure stage of lifetime, since the amplitude and tortuosity parameters used in equation (39) and equation (41) are obtained at 177 cycles from cyclic experimental data and fitted into FE models. There exists a potential to describe the geometrical variation for transitional roughness models throughout the life span since the amplitude and tortuosity in equation (39) and equation (41) have been recorded as a function

of thermal cycles [92]. The challenge is to determine the number of noticeable imperfections N as a function of thermal cycles, equation (41) and therefore, it is difficult to define the spacing D as a function of time.

However, it was suggested that the roughness level increases as the thermal cycle proceeds [92], [142], [149]. This indicates that the number of noticeable imperfections N_r should increase as the time approaches the failure time. Incorporating the trend of increasing N_r into equation (39) and equation (41), it can be qualitatively confirmed that the spacing between neighbouring imperfections decreases and the local width increases as a function of time, which demonstrates that the evolution of interfacial roughness might follow the sequence (a) to (d) in Figure 60.

The stresses described in the preceding sections are the maximum out-of-plane residual stresses upon cooling during thermal cycles. For cases of extreme roughness profile in the current study, e.g., the case (a), the ratio of amplitude over local width is greater than unity. It is not surprising that the black curve has the highest rate of increasing stress among all curves in Figure 61 since it has the narrowest width that boosts the stress concentration. It is also not surprising that there exists a stress inversion as the thermal cycle proceeds. It occurs due to a lack of relatively close neighbouring imperfections, as mentioned in section 4.4.1(b). This phenomenon is position-dependent as the current position is located at approximately 1.27 μm away from the bottom of the TC, Table 4. There is a relatively large variation of stresses as a function of time as the position shifts up or down towards or away from the interface.

The introduction of the transitional roughness model gives a proper explanation of the geometrical implication of tortuosity considering global factors. At the same time, it helps the FE model approach the actual cross-section in experimental observation. Theoretically, the experimentally-measured interfacial roughness parameters, characterized by either amplitude, tortuosity and growth of TGO thickness, are statistically mean values within a defined length of interfacial roughness profile during a defined period of the thermal cycle. In reality, the measured value of amplitude, local width for each individual imperfection, as well as spacing between neighbouring imperfections are randomly

distributed, as indicated by Figure 57(c) and Figure 58. To simulate this, a generalized roughness model is established with randomly distributed roughness parameters and integrated into the FE model and shown in Figure 62. For the case of an interface with a randomly distributed roughness profile, the calculated stress becomes more complicated at the valley of the TC, where excessively sharp tip roughness-imperfections are identified.

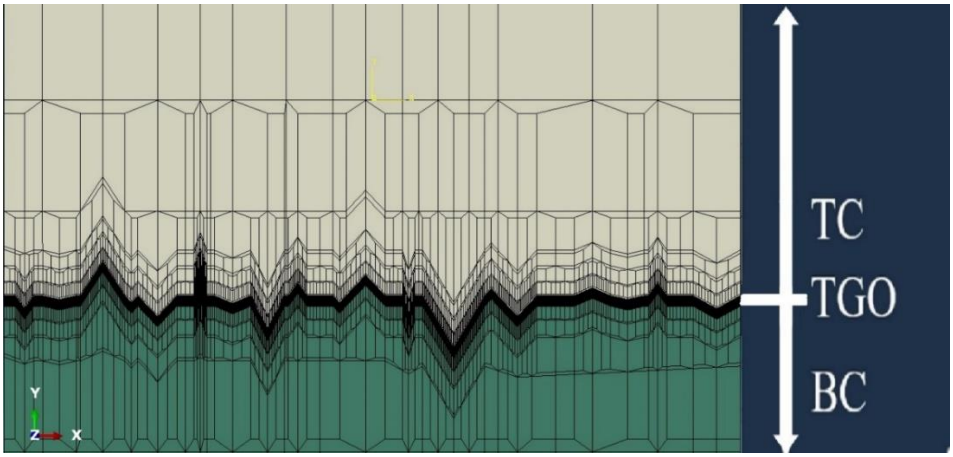

Figure 62 Generalized roughness model using a randomly distributed roughness profile

4.4.3. The effect of stress distribution on positions of cracks within TC and TGO layers

As described in the preceding section, the width of the bottom side estimated by equation (21) fails to characterize the roughness profile when there is spacing between two imperfections. To characterize the interfacial roughness profile at a post-failure stage, a transitional roughness model is proposed where the effect of spacing between imperfections is described by adding parameters into the FE model, equation (41). Generally speaking, the concept of width of imperfection is redefined as the local width of imperfections W_L, which is no longer limited to the description of the length of the bottom side of

the triangular-shaped imperfection, Figure 55. On the other hand, the amplitude measured from experimental data takes the average value according to

$$A = \sqrt{2}RMS = \sqrt{\frac{2}{N}\sum_{i=1}^{N} y_i^{\,2}} \tag{42}$$

The parameters measured experimentally are all average values and provide a general trend as a function of the number of cycles and temperature. In “true” roughness profiles described by the schematic diagram in Figure 57(c), the magnitude of amplitude, as well as the width of imperfections, are randomly distributed for individual imperfections. Compared with the true roughness profile from cross-section images extracted from SEM [149], it is possible that the roughness profile model established by using average geometrical parameters from experimental data fails to reflect the “true” roughness profile at the interface where deep, sharp imperfections could possibly exist at the post-failure stage, as indicated by the highlighted circles in Figure 58.

Deep, sharp imperfections simulated using triangular-shaped roughness profiles imply a relatively high ratio of A/W, as illustrated by Figure 55. This will lead to a stress singularity at the valley of the TC close to the interface. In order to examine the effect of sharpness on the stress distribution, imperfections with a high ratio of A/W in the continuous roughness model with 1.5 times amplitude are selected, Figure 47(c). Out-of-plane residual stresses are then calculated at different positions away from the valley within the TC. In order to compare the difference of residual stresses at the valley of the TC estimated from the FE model, the positions where stress is calculated are selected close to the ones in Figure 53, where original amplitudes were used in the FE modelling process.

The resulting out-of-plane residual stresses are shown in Figure 63 and are compared with the stresses obtained by using the regular roughness-amplitude FE model, Figure 53.

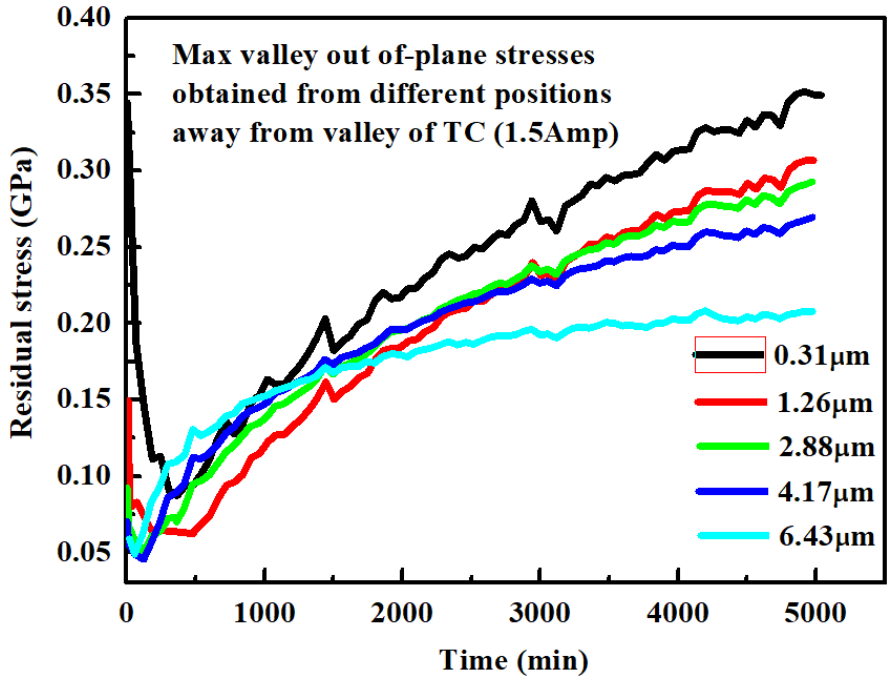

Figure 63 Out-of-plane residual cooling stresses calculated at the valley of TC as a function of time with several selected positions using 1.5A roughness amplitude

It is confirmed again that out-of-plane residual stresses are impeded by the excessive increase in amplitude where a relatively large ratio A/W is expected, especially for stresses close to the interface. This can be seen from the difference in stress magnitude at shallow positions of the bottom of the TC, indicated by the black curve in both Figure 53 and Figure 63. A rapid reduction of stress is identified at initial cycles in varying degrees at different positions. However, all curves remain uniformly increasing throughout the entire calculating time. The cyan curve, similar to the preceding section, indicates the residual stresses outside the valley of the TC. Except for the difference in stress level, there is no discrepancy for stress outside the valley compared to those within the valley, with respect to a general trend of increasing stress. There are no significant differences between the two cyan curves in Figure 63 and Figure 53, yet we obtained stress singularity for a large ratio of A/W in the transitional model in Figure 61. Hence, it is strongly suspected that the lack of difference related to the general trend of

stresses between the two FE results is due to the excessively close neighbouring imperfections simulated from a continuous roughness model that inhibits the variation of residual stresses, as described in section 4.4.1(b).

Stress in the transitional roughness model Figure 60(a) is determined at different positions away from the valley of the TC and shown in Figure 64. It is obvious that there are large discrepancies between the stresses obtained at different positions compared to the stresses obtained through the continuous roughness model. These discrepancies can be explained by the little effect of interaction between neighbouring imperfections on the individual stress level, as there is larger spacing between neighbouring imperfections for the transitional roughness model.

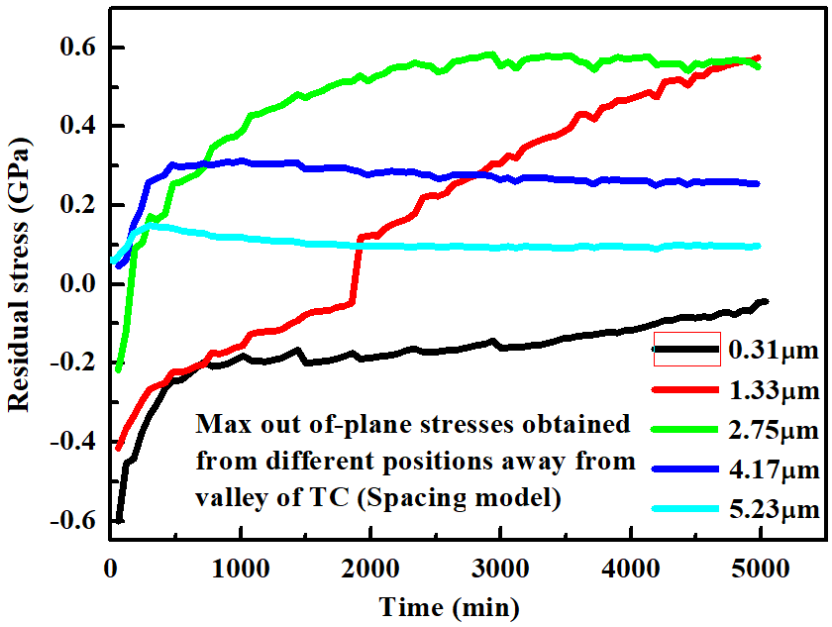

Figure 64 Out-of-plane residual cooling stresses calculated at the valley of the TC as a function of time at several positions using the transitional roughness model

In contrast to Figure 63, the out-of-plane residual stresses close to the valley of the TC (0.31 μm away), indicated by the black curve in Figure 64, are in compression within the entire 5000 minute thermal cycles. This is considered to impede the nucleation and propagation of cracks parallel to the interface. A rapid stress increase is found for stresses just a little above the first position, represented by the red and green curves, respectively, accompanied by a stress inversion, which occurs as a function of position and time. With the positions moving into the shallower portion of the TC, there is an obvious decrease in stress level calculated at 4.17 μm and 5.23 μm away from the bottom of the valley in the TC in later thermal cycles. Similar to the analysis in the preceding section, the cyan curve describes the general trend of residual stresses outside the valley of imperfections. Considering the possible positions where the maximum out-of-plane stress occurs, it is reasonable to expect that a crack might develop somewhere around intermediate positions (positions between 1.33 μm and 2.75 μm away from the bottom of the TC as indicated in Figure 64) as the total roughness amplitude is assumed to be about 4.12 μm.

It is observed that the onset of stress inversion varies as a function of position. It could be expected that the red curve, which has the most rapid growth rate, reaches the critical stress level that triggers the initiation of a horizontal crack. However, it is noted that the time for stress inversion for the red curve occurs relatively late in the thermal cycle. This might indicate that the initiation of a horizontal crack as residual stresses reach critical value could be delayed, which is in agreement with experimental observations [52].

According to the stress analysis above, it can be concluded that the onset of residual stress inversion occurs earlier (black-red-green) as the calculated positions move perpendicularly away from the bottom of the TC /TGO interface. This implies that stress at shallower positions might reach the critical level that initiates a horizontal crack at an earlier stage of thermal cycle. However, current FE models are established where residual stresses are calculated without consideration of interfacial roughness evolution as a function of time. We note that the interfacial roughness grows as a function of the thermal cycle, which implies the shortening of spacing between neighbouring imperfections and the widening of local width for individual imperfections. This, in turn, implies that the positions where the possible

maximum residual stress occurs could also move close to the bottom of the valley within the TC, as indicated by positions where the maximum stress is identified in Figure 63. Combining the schematic diagram in Figure 65 and failure mechanism summarized in [32], and assuming that the shape of the roughness of an individual imperfection becomes sharper as the thermal cycle proceeds, the stress conditions at the valley of the TC may change.

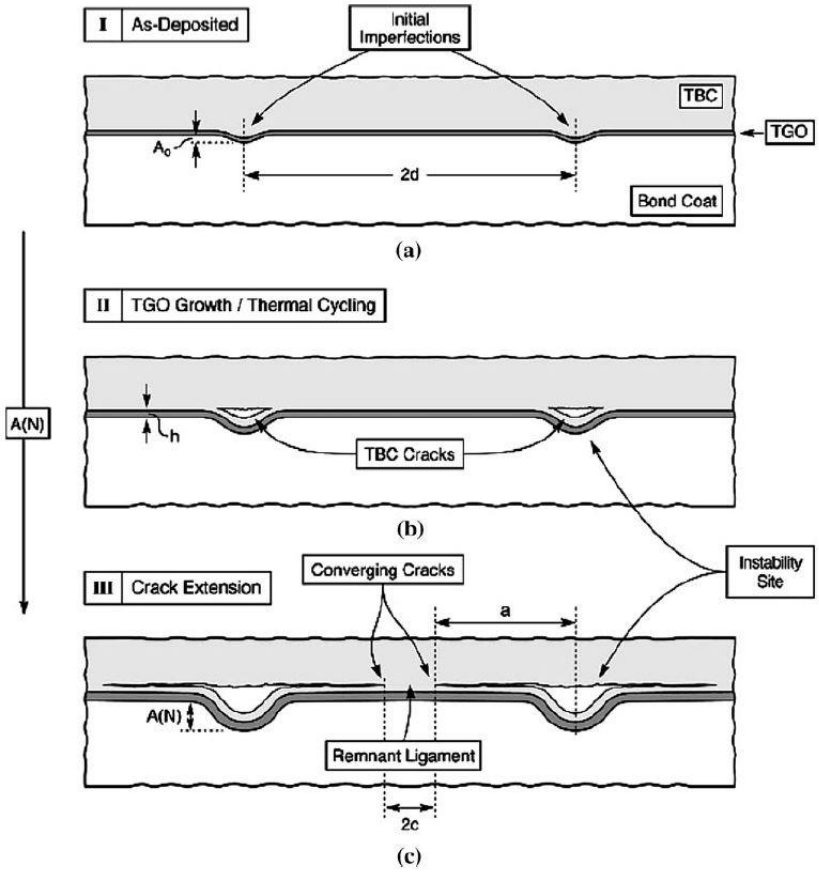

Figure 65 Failure of an EBPVD TBC system driven by a cyclic instability in the thermally grown oxide layer[32]

In order to describe the relationship between positions of maximum stress and possible crack initiation, several stages need to be examined for the entire lifetime with respect to the roughness profile. For Stage “0”, the interfacial roughness at the beginning of the thermal cycle is described in Figure 58

“0 cycles”, where relatively small and uniformly distributed roughness imperfections are identified close to the interface between the TC and the BC, and where the thickness of any pre-existing TGO layer is neglected. The interfacial roughness can be profiled using the continuous roughness model and average roughness parameters from the initial stage of the thermal cyclic experimental results. The maximum residual stress at stage “0” at the initial thermal cycle can be found close to the valley of the TC, although the magnitude of the residual stress is too small to initiate horizontal crack nucleation.

For stage I, as indicated in Figure 65(a), the growth of a few small imperfections could be expected and described as the transitional roughness model with relatively large spacing and short local widths, Figure 60(a). Since there is little interaction between neighbouring imperfections, the rapid growth of valley stress could be expected. It is noted that as the increase in amplitude raises the sharpness of the imperfections, it also facilitates the growth of out-of-plane residual stress to a certain degree. There might be an initiation of horizontal cracks somewhere at intermediate positions where stress inversion takes place within a short period of time (Figure 64, positions between the red and green curve). This rapidly increasing stress is balanced by the creep effect of the BC, especially for the area close to the interface where massive stress relaxation takes place during the high temperature holding time. The creep effect is also reflected by the increase of roughness level, where more imperfections are formed due to inelastic deformation as the thermal cycle proceeds. The resulting shortening of spacing parameter and widening of local width, as well as the growth of roughness amplitude (represented by stage II in Figure 65(b) and 34% to 76% of life cycles in Figure 58), facilitates interaction between neighbouring imperfections and thus inhibits the growth of residual stresses.

Stage II in Figure 65(b) can be described in Figure 60(b) and Figure 60(c) for FE mapping. According to the results from the preceding analysis, the positions of the maximum residual stress start to move back to the valley of the TC. Since the horizontal crack propagates already at a relatively shallow position during stage I, the positions of maximum residual stress might shift the possible cracking positions down, or alternatively, might cause the downward extension of the crack accompanied by an expansion of the crack size perpendicular to the interface within the valley of the TC, as indicated in Figure 65(c).

As the thermal cycle approaches the post-failure indicated by stage III in Figure 65(c), the appropriate FE model is described by either Figure 60(d) or the continuous roughness model where geometrical roughness parameters are taken from experimental data of the post-failure stage thermal cycle. According to the stress analysis in the preceding section, the maximum residual stresses are identified at the bottom of the valley within the TC in Figure 53, where the crack is expected to propagate along with the interface.

The generalized roughness model is introduced with a relatively large roughness level at the interface to attempt to profile the randomly distributed peaks and valleys formed at post-failure stages during cyclic thermal simulation, Figure 58. For stress calculated at a shallow valley with low roughness amplitude, the general trend for out-of-plane residual stresses is the same as the one obtained in the continuous roughness model, i.e., the residual stress is tensile and decreases as the positions move perpendicularly away from the bottom of the TC. However, for stress at a deep valley with high roughness amplitude, the maximum out-of-plane residual stress has unrealistic values and is concentrated at the tip of the bottom of the valley of the TC, as indicated in Figure 66.

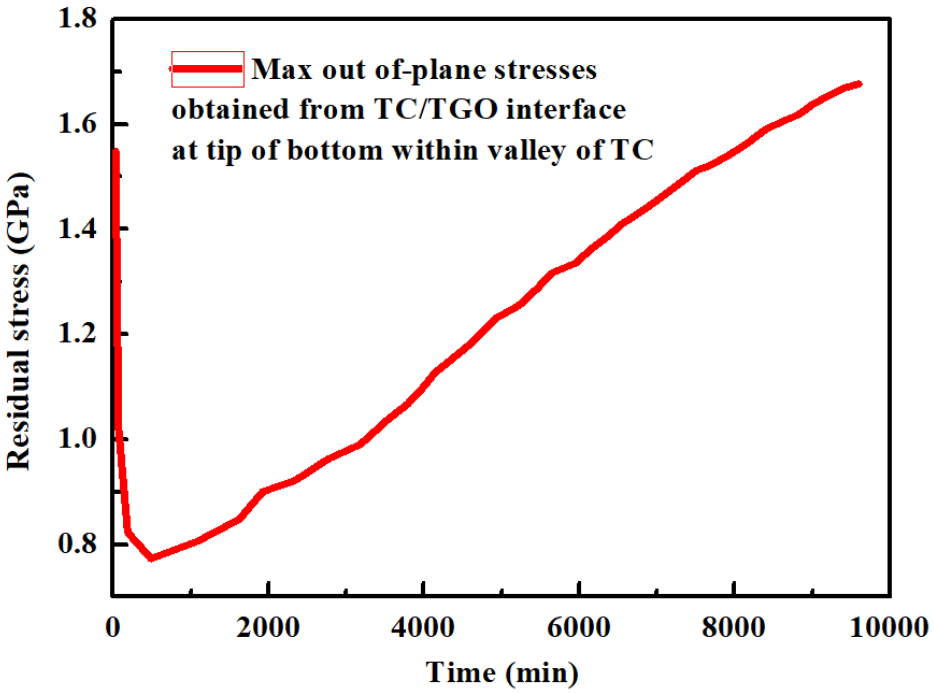

Figure 66 Valley stress at the tip of the bottom at the valley of the TC obtained

from the generalized roughness approximated model

As the results are obtained from the perfect non-cracking FE model, it is reasonable to consider that the magnitude of the stress is large enough to facilitate the crack propagation along the interface between the TC /TGO layer.

It can also be seen that the general trend for residual stresses in Figure 66 is similar to the red curve in Figure 48, where the residual stresses are from closely-located imperfections using the continuous roughness model. There also exists a stress singularity within the TGO layer, in particular at imperfections with relatively large roughness. For imperfections with small roughness levels, the variation of residual stress within the TGO layer is illustrated in Figure 67. It shows the stresses at two randomly selected cycles through FE results.

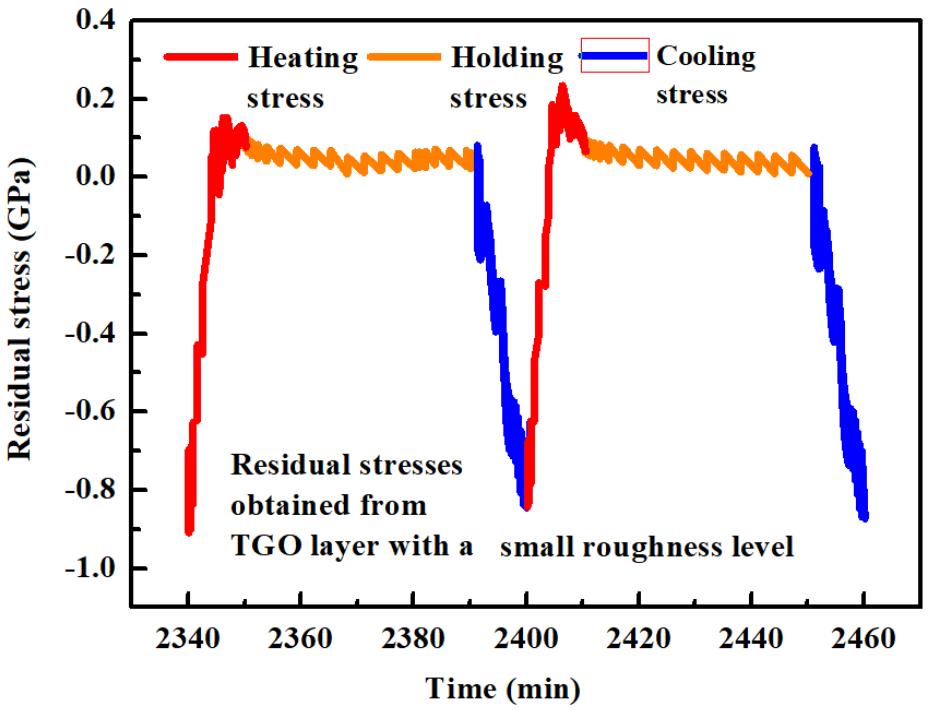

Figure 67 The out-of-plane cyclic residual stress within the TGO layer using a model with small roughness imperfections under cyclic thermal conditions

It is concluded that the magnitude of compressive residual stress increases to the maximum level upon cooling and decreases within about 10 minutes during the reheating period. The overgrowth tensile stress upon the heating process is rapidly relaxed due to the creep effect at high temperatures, resulting in a stress-free state during the holding period. The magnitude of out-of-plane compressive residual stresses within the TGO layer decreases as the thermal cycle proceeds [52], [53], [92], [142]. However, there exists a tensile state for TGO residual stress calculated close to the TC /TGO interface with a relatively large roughness profile, as can be seen in Figure 68.

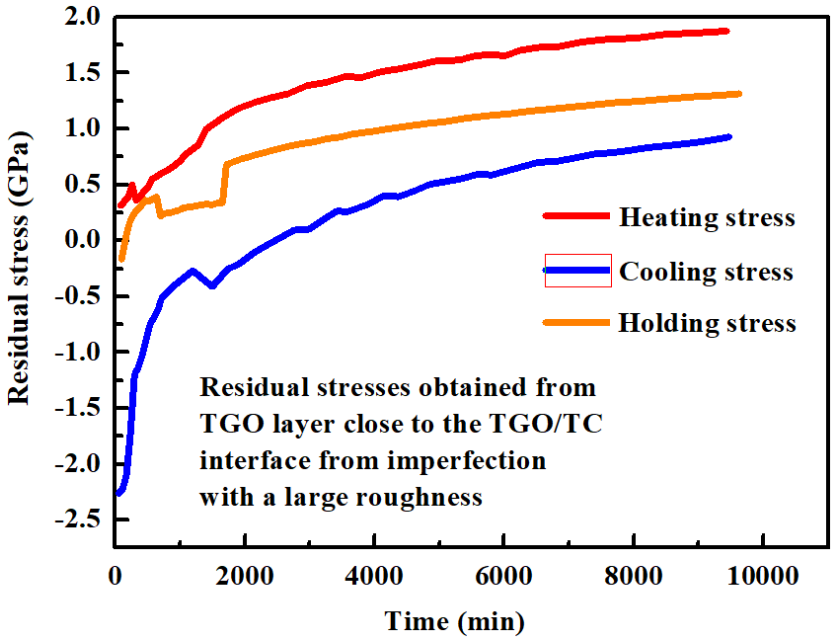

Figure 68 The maximum residual stress calculated within the TGO close to the TC /TGO interface

It should be noted that the "holding stress" is different from the stress obtained in Figure 67, and increases as a function of thermal cycles. This stable increase of holding stress is a consequence of the geometrical discontinuity at the tip of roughness, where the excessive geometrical sharpness results in significant pressure onto the TGO material concentrated in that area. This leads to the failure of stress relaxation. Since stress relaxation is limited during high temperatures, there exists a tensile stress state at the end of the heating process during thermal cycles. This holding stress remains tensile, and its magnitude increases as the thermal cycle proceeds, which leads to a relatively large magnitude of out-of-plane tensile stress at the interface close to the TC /TGO layer. Therefore, it is plausible to expect that the penetration of the horizontal crack occurs at a valley of the TGO layer close to the TC /TGO interface by the convergence of separated cracks within the TC and BC.

Compared to TGO residual stress close to the TC /TGO interface, the stress near the TGO/BC interface is close to the regular stress state of the TGO layer, Figure 69. The cooling stress shows an initial increase of tensile stress and a rapid decrease until reaching the large magnitude of compressive

stress. The initial increase of stress indicates the stress from untransformed metallic BC, and then a rapid decrease suggests the material is undergoing phase transformation. The remaining portion of compressively decreasing out-of-plane stress indicates a typical stress behaviour of fully transformed TGO layer at later thermal cycles, the blue curve in Figure 69 shows the general trend of cooling stress of a TGO layer that undergoes phase transformation from metallic Platinum modified aluminum layer (Pt-Al) to predominated alpha-alumina layer [53], [64]. Although it has a similar sharp roughness with a high ratio of A/W, it is found that the significant creep behaviour of BC reflected by the large creep prefactor shown in Equation (14) would rapidly relax the stress close to the interface of BC/TGO layer, which explains that the stress singularity calculated within the TGO close to the TC/TGO interface (Figure 68) would be hardly observed within TGO close to the BC/TGO interface (Figure 69).

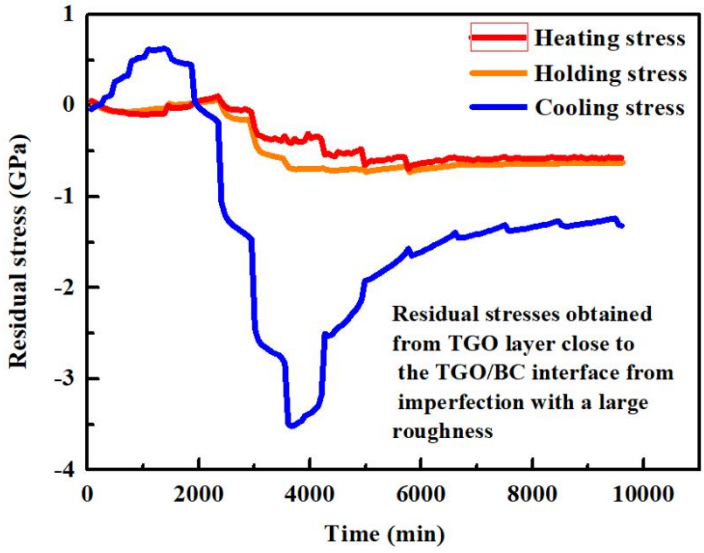

Figure 69 The maximum residual stress calculated within the TGO close to the TGO/BC interface

4.5. Conclusions

In this paper, FE models that use temperature-process dependent model parameters were developed, and the out-of-plane residual stresses are calculated for EB-PVD TBCs at maximum cooling point under thermal cyclic conditions. The interfacial roughness was characterized based on cross-sectional images from SEM, where the roughness amplitude and width of the bottom side of imperfections are defined to describe the continuous saw-like interfacial roughness profile. The FE models were implemented by using transversely isotropic elastic properties, and a parametric study was conducted to determine the effect of different roughness levels on stress distributions on different layers. Based on a different way to comprehend the physical implication of tortuosity, a transitional roughness model was developed to characterize the spacing between imperfections with a redefinition of the local width of triangular-approximated roughness. The transitional roughness model provides a good approximation to simulate roughness between mid-stage to post-failure stages. These developments permit the cracking position to be described as a function of time with the evolution of interfacial roughness and shifting of identified positions of maximum stress. The stress singularities can also be identified at extremely sharp imperfections using either the transitional roughness model or generalized roughness model. Specifically, by calculating stress at different positions within both the TC and TGO layer, the influence of which on possible positions where the crack from different layers coalescence is revealed.

5. Crack Driving Forces of Atmospheric Plasma Sprayed-Thermal Barrier Coatings under Burner Cycling and Isothermal Furnace Cycling Testing Conditions

This chapter addresses objectives 1 and 2 by estimating the energy release rates through analytical solutions for APS-TBCs under different thermal cycling environments.

The content of this chapter will be submitted for publication.

[a]*B. Zhang,* [b*]*Kuiying Chen,* [a] *N. Baddour,*

[a] *Department of Mechanical Engineering, University of Ottawa, Canada*

[b] *Structures, Materials and Manufacturing Laboratory, Aerospace Research Center, National Research Council Canada*

Abstract

The high temperature operation service condition can be used as a working environment to evaluate the durability of Atmospheric Plasma Sprayed-Thermal Barrier Coating systems (APS-TBCs). To evaluate the durability of TBCs within their life span, two different thermal cycling tests, i.e., isothermal furnace cycling and burner rig cycling tests, are designed to investigate the possible crack driving forces that might lead to the failure of TBCs. Although there are many existing analyses on failure and life prediction, there still is a lack of quantitative evaluation and comparison on the crack driving forces under these two different thermal cycling schemes. In this paper, by using revised analytical models, strain energy release rates (ERRs) are estimated and compared between these two testing approaches using experimental data. A new residual stress model is then developed to study the position where the maximum residual stress occurs due to coefficient of thermal expansion (CTE) mismatch at different thermally grown oxide (TGO) thicknesses. The main crack driving forces are identified for two types of thermal cycling experiments. A possible cracking route is found based on the calculated equivalent ERRs with respect to distance from the interface between the topcoat (TC)/TGO layers. The relationship between crack driving force of isothermal furnace vs. burner cycling tests is also elaborated.

Key words: Crack driving forces, isothermal furnace cycling test, burner cycling test, energy release rate, CTE mismatch, TGO growth, thermal gradient, thermal shock, cracking route.

5.1. Introduction

The durability of Thermal Barrier Coating systems (TBCs) plays an essential role in determining the reliability of hot section components of gas turbine engines, thus directly affecting their applicability under different harsh service conditions [125], [179]–[184]. However, it is a challenge to evaluate the durability of TBCs during regular service life since a high cost is required to track and identify the failure mechanisms of a TBC. To date, experiments at selected high temperatures were designed to investigate possible cracking driving forces that could lead to the propagation of microcracks and spallation of the topcoat (TC) [79], [131], [143], [185]–[189]. Among various tests, the thermal cycling test is able to provide useful information that can measure the durability of TBCs. It is known that thermally grown oxide (TGO) is formed during the high temperature dwell period due to progressive oxidation of the metallic bond coat (BC) layer, facilitating crack propagation along the TC/TGO layers or penetrating the TGO scale at the final stage of the TBC's lifetime. A large residual stress is induced as a consequence of coefficient of thermal expansion (CTE) mismatch between different layers during the cooling period where out-of-plane tensile stress is developed at undulations, nucleating cracks close to the interface. The abovementioned TGO growth as well as CTE mismatch between layers are considered to determine the failure mechanism of TBCs under isothermal furnace cycling test (FCT), where the temperature is uniformly distributed throughout entire TBC specimen [81], [96], [130], [142], [190], [191].

The other typical thermal cycling experiments contain a rapid temperature variation and a coolant (either compressed cooling gas or liquid) applied onto the backside of substrate during high temperature dwell time in an integrated thermal cycle. The former introduces a massive thermal shock during heating and cooling periods [23], [145], [192], [193]. The latter leads to a thermal gradient from high heating applied to the surface of the TC with adequate back-side cooling from the bond coat (BC) – substrate interface [194]–[197]. This thermal cycling experiment, also called a burner cycling test, is used to simulate the process of subsonic engine takeoff and shutdown in real service conditions [6], [185], [198],

[199]. To date, research has been conducted to investigate possible failure mechanisms and factors influencing the durability of TBCs via these two types of thermal cycling experiments [194], [200]–[202]. Efforts were also made to understand the crack driving forces behind each thermal cycling experiment using semi-empirical analytical methods. However, there is a lack of studies which quantitatively evaluate the energy release rates (ERRs) and a comparison between these two types of ERRs using analytical models. The work conducted by Li et al. [185] provides a correlation between life data of Atmospheric Plasma Sprayed-Thermal Barrier Coating system (APS-TBCs) with different pre-oxide thicknesses tested in both burner cycling and isothermal furnace. The author discussed the relationship between critical TGO thickness and crack routes.

The experimental data in [185] facilitates the current research work, in which the crack driving forces for APS-TBCs are identified and quantified in terms of energy release rates (ERRs) calculated through modified analytical models. The experimental data from isothermal furnace cycling tests or burner cycling tests are used to calculate parameters of analytical models, where the concept of equivalent time was developed to evaluate the effect of preheat treatment on the process-dependent model parameters in thermal cycling calculations. A new method is proposed to identify the position of the maximum CTE stress developed during cooling, as a function of different TGO thickness. The ERR is calculated as a function of pre-oxide thickness, and the impact of individual ERR on life cycle is evaluated. The difference between ERRs calculated for different thermal cycling tests are discussed. Possible cracking routes are investigated, making use of the position dependent ERRs for different thermal cycling conditions. Finally, the differences between crack driving forces under the two different thermal cycling tests are discussed.

5.2. Compilation of parameters describing the thermal history, life data and interfacial geometry of APS-TBCs

All APS-TBC specimens undergoing thermal cycling experiments experience 4 hours of pre-treatment at 1000℃, followed by another 4 hours pre-treatment at 1080℃ under Argon atmosphere [185]. Further heat treatment includes 20, 50, 105, 225, 300, 350 hours isothermal heating at 1080℃ for different group sets of APS-TBC specimens. Two different thermal cycling experiments were conducted to obtain the APS-TBCs with various life cycles [185]. The temperature profile for the burner cycling test contains 70 seconds of temperature increase to peak temperature and 50 seconds of holding time at 1150℃ measured at the surface of the TC, followed by 120 seconds for the entire TBC to cool down. Compressed air is applied simultaneously to the backside of the substrate, holding the temperature at 935℃ during the high temperature holding time. Thus, a thermal gradient is present throughout the thickness of the TBCs. Considering that (i) the temperature difference between the TC surface and the TGO/BC is much larger than that between the substrate and BC, and (ii) the thermal conductivity of the metallic substrate and BC is much higher than the ceramic TC, the substrate and BC are approximated as an isothermal body with no thermal gradient between them. The temperature profile for a given depth within the TC can be profiled [144]. Considering the entire TC layer is affected by the sintering effect, the temperature at a given position *y* in Figure 70 can be expressed as [144]

$$T_{TC}\big|_y = \left(1+\frac{y}{H}\right)T_{TC} - \frac{y}{H}T_{BC} \tag{43}$$

where H is the total thickness of the TC layer, T_{TC} and T_{BC} are temperatures at the surface of the TC and backside of the BC. The temperature within the TC is plotted in Figure 71 by choosing $\frac{y}{H} = -0.2, -0.4, -0.6, -0.8$. It is evident that the temperature keeps falling with calculated positions close to the BC surface.

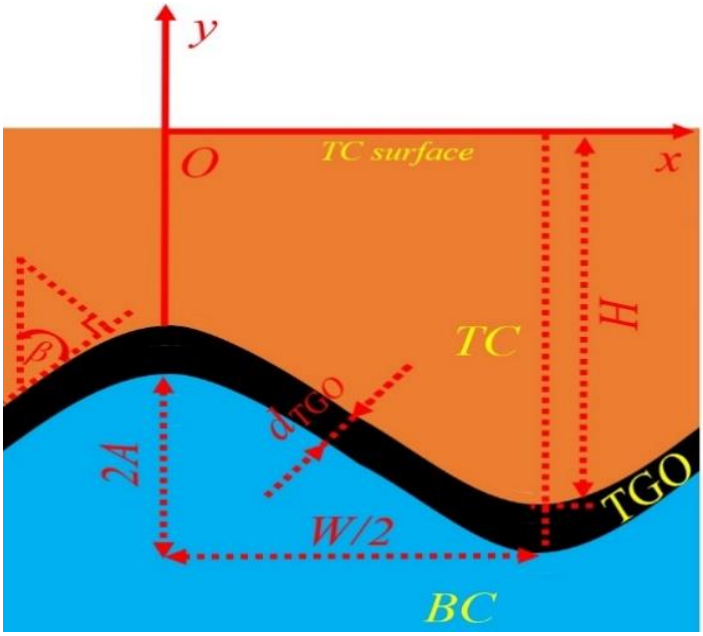

Figure 70 The schematic diagram identifying the parameters used

in the analysis

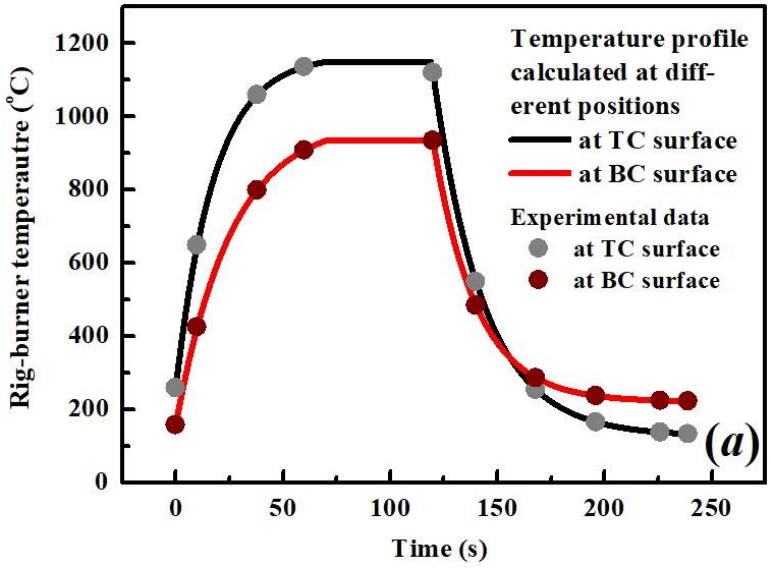

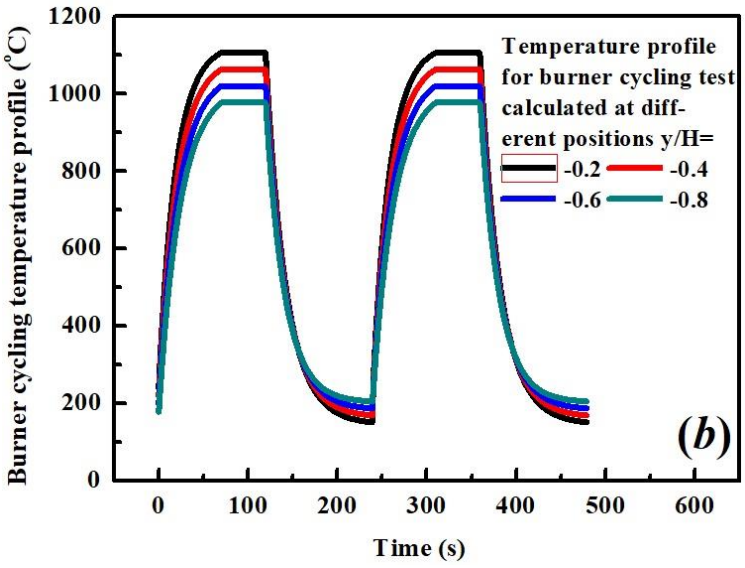

Figure 71 Temperature profile calculated by equation (43) for burner cycling test (*a*) Temperature calculated at TC/BC surface (*b*) Temperature gradient within TC

The temperature profile for the isothermal furnace cycling test contains a rapidly increase of temperature up to 1120℃ (we assume the time taken as 1 minute) [185], held for 26 minutes, followed by 4 minutes of uniform cooling to 80℃ [185]. Accordingly, the temperature profile is plotted in Figure 72.

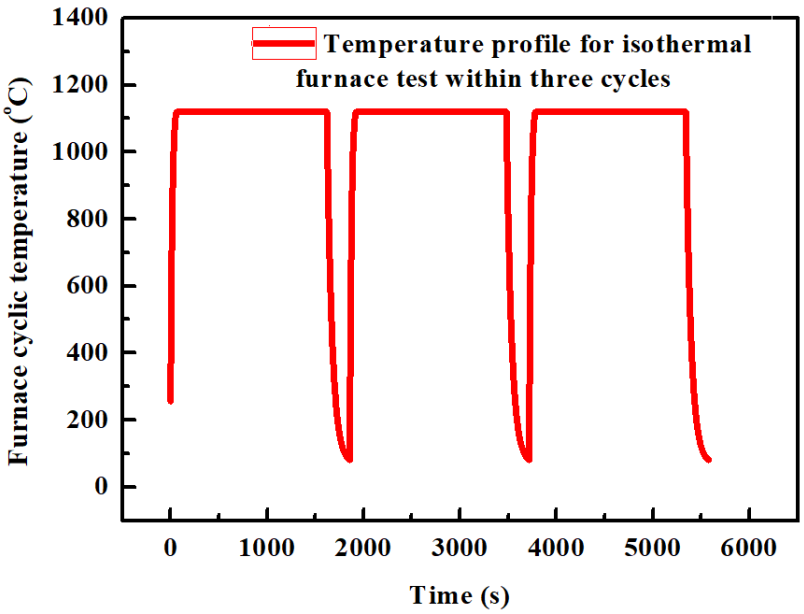

Figure 72 Temperature profile for isothermal furnace cycling test

The life data based on different types of thermal cycling experiments are collected in [185] as a function of thickness of the pre-oxide layer, Figure 73.

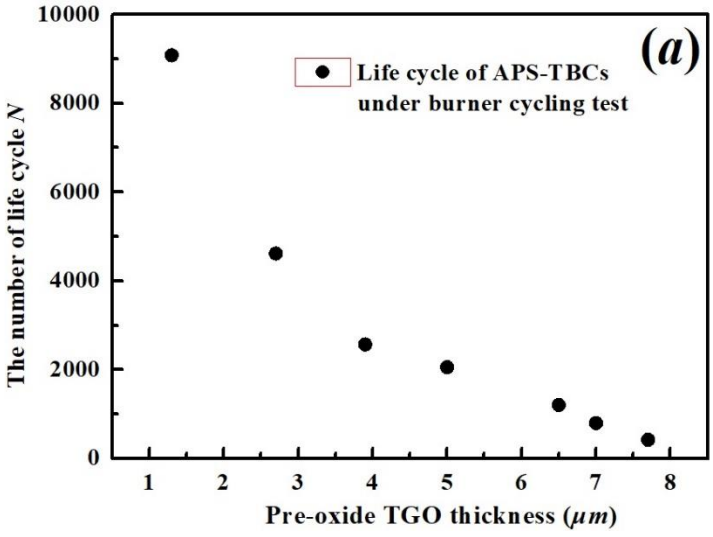

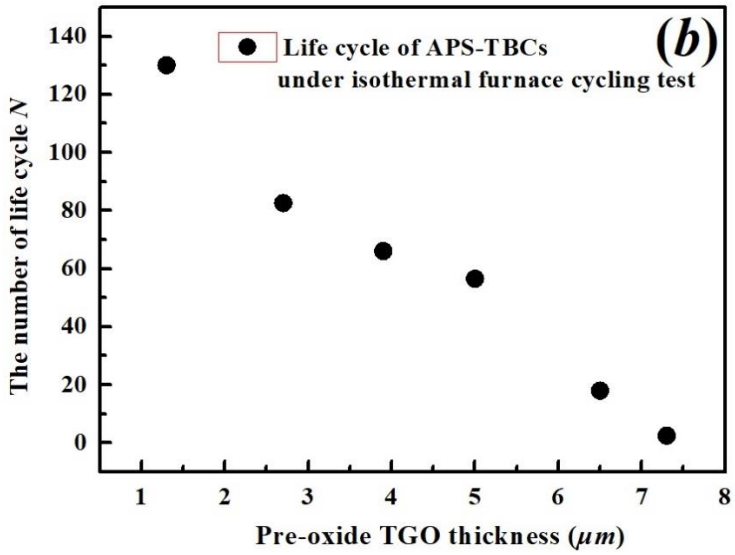

Figure 73 Life cycle of APS-TBCs under (a) burner cycling test (b) isothermal furnace cycling test with respect to different pre-oxide TGO thickness [185]

The scope of the current study focuses on the ERR generated close to the TC/TGO interface within the TC. Therefore, geometrical parameters describing the size of the TC and interfacial morphology based on APS-TBCs are used in the following analytical models. The thickness of the TC, *H*, is 250μm. Using the cosine function to describe the interfacial roughness, the average amplitude *A* and wavelength *W* are chosen as 30μm and 80μm, respectively [131]. Thus, with the 2D coordinate system shown in Figure 70, the roughness curve undulations can be defined as

$$S(x) = A\cos\left(\frac{2\pi}{W}x\right) - (H - 2A) \tag{44}$$

In addition, the angle β between the tangent to the roughness curve and the *y* axis is used to evaluate the effect of roughness level on the CTE ERR, where the angle $\beta(x)$ is given by

$$\beta(x) = \frac{\pi}{2} - \arctan\left(\frac{dS}{dx}\right) \tag{45}$$

All parameters evaluating the material properties during pre-heat treatment and following thermal cycling experiments are described in the supporting documents.

5.3. Analytical models for evaluating energy release rate under different thermal cyclic experiments

It is possible to quantitatively evaluate the ERR through analytical expressions based on either isothermal furnace cycling conditions or burner cycling conditions with a thermal gradient. The effect of thermal gradient and thermal shock on the durability of TBCs is reflected by the generation of extra crack driving forces leading to crack nucleation and propagation within TC. Crack driving forces that exist for both of thermal cycling experiments are also affected, i.e., the ERRs for CTE mismatch and TGO growth are different based on either isothermal cycling conditions or thermal gradient conditions. Using the burner cycling test with thermal gradient, a new analytical expression is proposed to calculate the thermal residual stress generated as a consequence of CTE mismatch between layers upon cooling period. The analytical models used to evaluate the ERR generated due to i) CTE mismatch ii) TGO growth for both isothermal and burner cycling experiments iii) thermal gradient and iv) thermal shock for burner cycling test are described below.

5.3.1. Analytical models for TC ERR generated due to CTE mismatch

(a) Out-of-plane residual stress due to CTE mismatch upon cooling as a function of calculated positions

Neglecting the effect of TGO layer and considering the bi-layer system, it is assumed that the temperature distribution is independent of calculated positions within TBCs for isothermal furnace cycling tests. That is, the temperature close to the TC/BC interface is assumed identical to that at any position within the TC, $T_{TC} = T_{BC} = T$. The in-plane residual strain developed at the interface between the TC/BC due to CTE mismatch upon cooling is described by

$$\begin{aligned} \Delta\varepsilon_{Interface}^{CTE} &= \Delta\alpha\Delta T \\ &= \left[\alpha_{BC}(T) - \alpha_{TC}(T)\right] \times \Delta T \\ &= \left[\alpha_{BC}(T_{BC}) - \alpha_{TC}(T_{BC})\right] \times \left(T_{BC}^{hold} - T_{BC}\right) \end{aligned} \tag{46}$$

where $\Delta\varepsilon_{Interface}^{CTE}$ is the CTE strain, $\alpha_{BC}(T_{BC})$ and $\alpha_{TC}(T_{BC})$ are temperature dependent coefficients of thermal expansion for BC and TC, respectively. ΔT is the temperature difference between the BC peak temperature at high temperature holding time T_{BC}^{hold} and the BC temperature at a given time upon cooling T_{BC}. Equation (46) also applies to calculate the CTE strain close to the TC/BC interface within the TC when a thermal gradient exists, since $\lim_{y \to \text{-H}} T_{TC}(y) \approx T_{BC}$.

However, it is a challenge to estimate the CTE strain generated at an arbitrary position (y=y_0) within the TC since the temperature at a distance y_0 away from the interface $T_{TC}\big|_{y=y_0}$ is different from that calculated at the interface (approximated by T_{BC}). Therefore, a new equation is developed by revising

the analytical expression in [130] to calculate the out-of-plane residual stress generated at a given position $y=y_0$ within the TC due to CTE mismatch for a tri-layer system with a thermal gradient. The equation is given by

$$Amp_{TC}^{CTE}\left(y\right)=-\chi\Lambda\left\{\left[\alpha_{TGO}\left(T_{BC}\right)\times\left(T_{BC}^{hold}-T_{BC}\right)-\alpha_{TC}\left(T_{TC}\big|_{y=y_0}\right)\times\left(T_{TC}^{hold}\big|_{y=y_0}-T_{TC}\big|_{y=y_0}\right)\right]+\left[\left(\alpha_{BC}\left(T_{BC}\right)-\alpha_{TGO}\left(T_{BC}\right)\right)\times\left(T_{BC}^{hold}-T_{BC}\right)\times\left(\frac{A}{W}\right)\left(\frac{A}{g\left(y\right)}\right)\right]\right\} \tag{47}$$

where χ is a fitting parameter. $\Delta T_{TC}\big|_{y=y_0}$ is the TC temperature difference at a given position $y=y_0$ between the peak temperature at high temperature holding time $T_{TC}^{hold}\big|_{y=y_0}$ and the temperature at given time upon cooling $T_{TC}\big|_{y=y_0}$. $\alpha_{TC}\left(T_{TC}\big|_{y=y_0}\right)$ is the coefficient of thermal expansion at given time and position upon cooling. $\alpha_{TGO}\left(T_{BC}\right)$ and $\alpha_{BC}\left(T_{BC}\right)$ are coefficients of thermal expansion for TGO and BC. The combination of geometrical parameters $\left(\frac{A}{W}\right)\left(\frac{A}{g\left(y\right)}\right)$ suggests the effect of interfacial roughness on the amplitude of stress level. $\Lambda=4\kappa_{TC}\mu_{TC}\Big/\left(\kappa_{TC}+\frac{4}{3}\mu_{TC}\right)$, where κ_{TC} is the bulk modulus and μ_{TC} is the shear modulus of the TC given by

$$\kappa_{TC}=\frac{E_{TC}\left(T_{TC}\big|_y,t\right)}{3\left(1-2\nu_{TC}\right)} \tag{48}$$

$$\mu_{TC}=\frac{E_{TC}\left(T_{TC}\big|_y,t\right)}{2\left(1+\nu_{TC}\right)} \tag{49}$$

Furthermore, $g(y)$ is a position-dependent weighting factor responsible for evaluating the effect of i) stress generated due to the interaction between layers (CTE mismatch), or ii) ERR generated from neighboring layers (TGO growth)

$$g(y)=\frac{1}{\exp(-\xi\times y-\gamma)} \tag{50}$$

where $\xi=0.05$ and $\gamma=\xi\times\left(H-\frac{1}{3}A\right)$.

The CTE stress is considered too large to be accommodated by pure elastic strain. Except for cracking of the TC, the rest of the elastic energy is released by inelastic deformation of the TC, which is introduced by yielding behavior that dominates at low temperature. Considering the Von Mises yield criterion, the following equations for stress can be used once the calculated Von Mises stress is larger than the yielding strength given by

$$\sigma_{ij}=\eta_{ij}\sigma_Y+\frac{1}{3}\delta_{ij}\sigma_{kk} \tag{51}$$

Here, σ_{ij} is the Cauchy stress tensor, $\eta_{ij}=\frac{s_{ij}}{\sigma_V}$ where s_{ij} is deviatoric stress tensor, σ_V is Von Mises stress, δ_{ij} delta Kronecker, and $\frac{1}{3}\delta_{ij}\sigma_{kk}$ is hydrostatic pressure. Given the out-of-plane residual stress $\sigma_{22}=Amp_{TC}^{CTE}(y)$, the in-plane strain ε_{33} can be calculated according to general Hook's law as

$$\varepsilon_{33}=\frac{1}{E}\left[\sigma_{33}-\upsilon(\sigma_{11}+\sigma_{22})\right] \tag{52}$$

A general plane strain condition is applied to the current analytical mode and yields $\varepsilon_{33}=0$. σ_{33} can be described by re-arranging equation (52) as

$$\sigma_{33}=\upsilon(\sigma_{11}+\sigma_{22}) \tag{53}$$

Assuming the $\sigma_{11} = \sigma_{33}$ yields

$$\sigma_{11} = \frac{\upsilon \sigma_{22}}{(1-\upsilon)} \tag{54}$$

The equivalent Von Mises stress used to predict yielding of materials under multiaxial loading conditions is defined as [203]

$$\sigma_V = \sqrt{\frac{(\sigma_{11}-\sigma_{22})^2 + (\sigma_{22}-\sigma_{33})^2 + (\sigma_{33}-\sigma_{11})^2 + 6(\tau_{12}^2 + \tau_{23}^2 + \tau_{13}^2)}{2}} \tag{55}$$

There are no shear components for general strain conditions, thus $\tau_{12} = \tau_{23} = \tau_{13} = 0$ in equation (55). Substituting equations (52)-(55) into equation (51), the corrected residual stress is developed as

$$Amp_{TC\_22}^{CTE} = \begin{cases} Amp_{TC}^{CTE}(y) & \sigma_V < \sigma_Y \\ \dfrac{Amp_{TC}^{CTE}(y) - \frac{1}{3}\delta_{ij}\sigma_{kk}}{\sigma_V}\sigma_Y + \frac{1}{3}\delta_{ij}\sigma_{kk} & \sigma_V \geq \sigma_Y \end{cases} \tag{56}$$

(b) Identification of variation of position of maximum CTE stress as a function of TGO thickness based on interfacial roughness model

Typically, the failure mechanism of APS-TBCs reveals that delamination cracks are initiated at the BC where out-of-plane tensile stress develops when the TGO is negligible. The out-of-plane residual stress state at a valley of the TC changes from compression to tension, which leads to horizontal crack nucleation. The delamination crack penetrates the thin TGO layer and results in spallation of the TC. Nevertheless, some FE studies have demonstrated the possibility of TC spallation due to the maximum tensile zone developed within the TC layer, i.e., the tensile zone was found at a peak of the TC at early

stages of thermal cycles [94], [136] and flanks of interfacial roughness [88], [94] as the TGO thickens. These FE studies introduced the pre-existing cracks in their modeling process and the stress inversion was also observed at the valley of the TC as TGO thickens. In addition, the shifting of crack routes was observed when TGO thickness reaches a critical value for both isothermal furnace cycling test and burner cycling test with thermal gradient [185]. That is, crack nucleation was initially identified from defects of the interface between the lamellar structure (far away from the interface between TC/TGO) and propagated horizontally as TGO is thin. Meanwhile, the crack was found to propagate close to the interface when the TGO thickens. The crack identified close to the interface between TC/TGO layer is located at a valley of TC and triggers the spallation of TC, which indicates that the maximum out-of-plane stress should at the same position. Based on the discussion above, a model describing the variation of location of out-of-plane maximum tensile zone as a function of TGO thickness can be proposed, Figure 74.

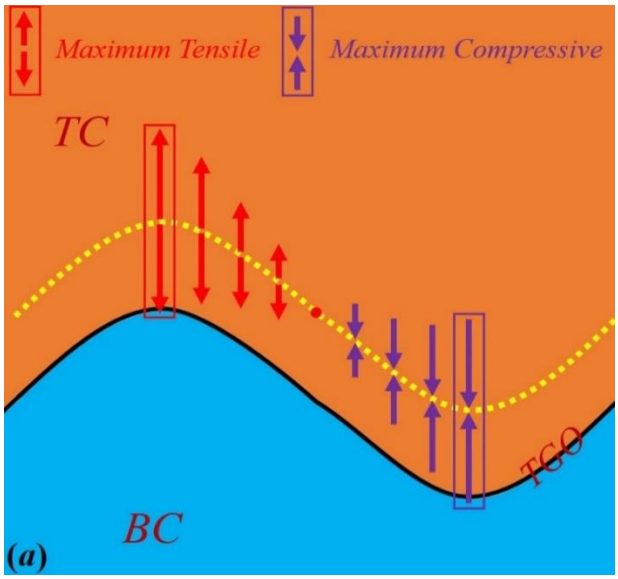

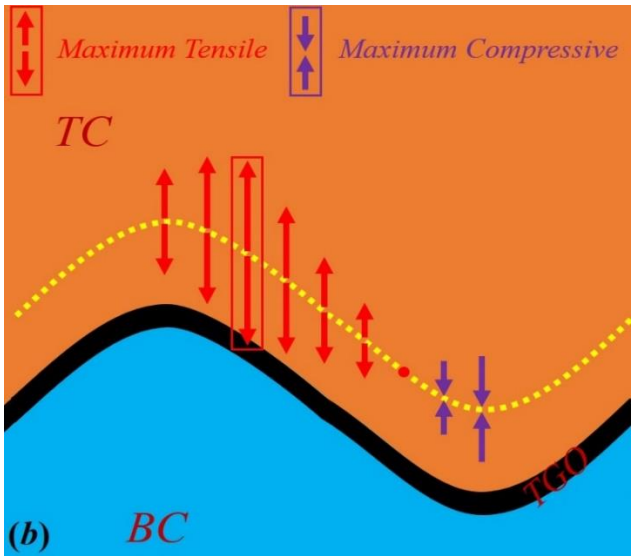
Maximum Tensile
Maximum Compressive
TC
TGO
(b)
BC

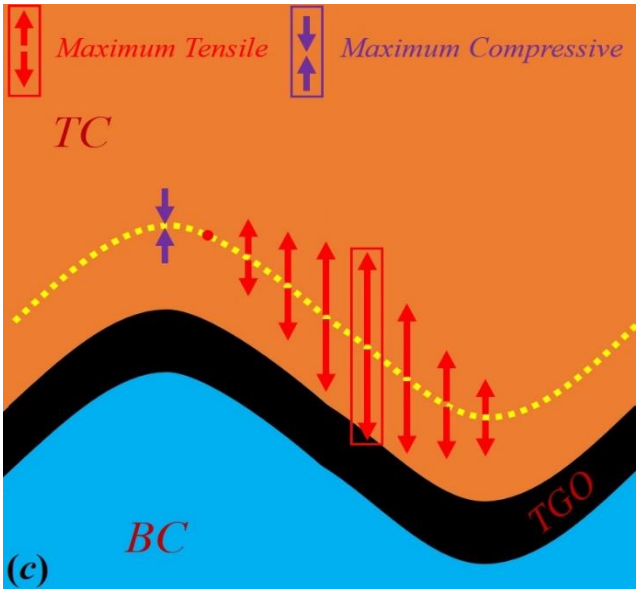
Maximum Tensile
Maximum Compressive
TC
TGO
BC
(c)

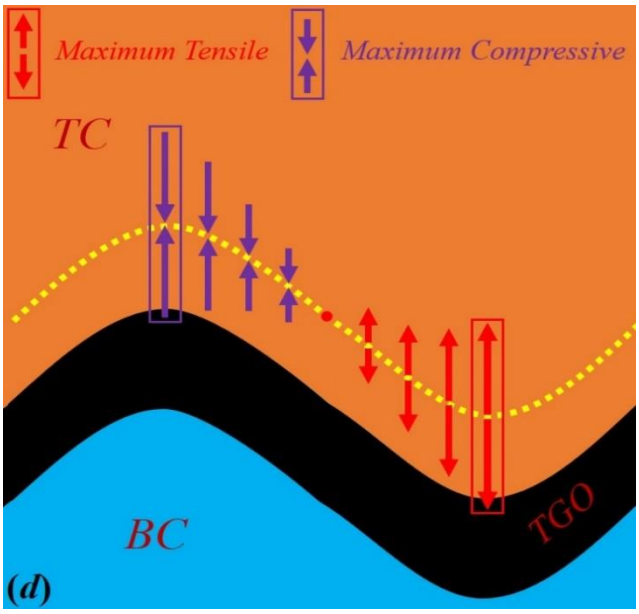

Figure 74 The variation of maximum tensile zone as function of TGO thickness

The location of the out-of-plane maximum tensile stress shifts downward from the peak of the TC to the valley of the TC along the interfacial roughness as the TGO thickens. The *x*-coordinate indicating the position dependency for out-of-plane stress can be derived from

$$l(x)=\cos\left[\frac{2\pi}{W}\left(x+\frac{W}{2}\frac{d_{TGO}}{d_{TGO}^{max}}\right)\right] \tag{57}$$

where d_{TGO}^{max} is the maximum TGO thickness where the position of maximum stress shifts to the valley of the TC. According to [185], the failure was assumed once TGO thickness reaches 8-9μm. Therefore, it is reasonable to assume that $d_{TGO}^{max}=8.5\mu m$, which corresponds to the TGO thickness when stress inversion at the bottom of the TC complete.

With the proposed equation (57) and equation (56), it is viable to evaluate the out-of-plane CTE stress at a given (x, y) coordinate for the current 2D APS-TBC from

$$\sigma_{TC}^{CTE}\left(y,x\right)=Amp_{TC\_22}^{CTE}\times l\left(x\right) \tag{58}$$

(c) The energy release rate of TC cracking due to CTE mismatch considering the interfacial roughness profile

The stress intensity factors for both mode I and mode II were given in [204] describing the crack driving forces where crack orientation was at an angle to the tensile out-of-plane stress. As illustrated in Figure 74, given the interface and angle between out-of-plane residual stress and direction of crack propagation is β(x), the crack length *b* and out-of-plane stress $\sigma_{TC}^{CTE}\left(y,x\right)$, the stress intensity factors are described through [204],

$$\begin{aligned} K_{I_{slope}} &= \sigma_{TC}^{CTE}\left(y,x\right)\sqrt{\pi b}\sin^2\beta\left(x\right) \\ K_{II_{slope}} &= \sigma_{TC}^{CTE}\left(y,x\right)\sqrt{\pi b}\sin\beta\left(x\right)\cos\beta\left(x\right) \end{aligned} \tag{59}$$

The mix mode ERR is given by

$$\begin{aligned} G_{slope} &= \frac{K_I^2}{\bar{E}_{TC}\left(T_{TC}\big|_y,t\right)}+\frac{K_{II}^2}{\bar{E}_{TC}\left(T_{TC}\big|_y,t\right)}=\frac{\left(\sigma_{CTE}^{TC}\left(y,x\right)\sqrt{\pi b}\right)^2}{\bar{E}_{TC}\left(T_{TC}\big|_y,t\right)}\times\sin^2\beta\left(x\right) \\ &= G_{flat}\times\sin^2\beta\left(x\right) \end{aligned} \tag{60}$$

The $\sin^2\beta\left(x\right)$ is considered to quantitatively evaluate the effect of interfacial roughness on the crack driving forces which inhibits the crack propagating along the undulations. The ERR for crack triggered by CTE stress on flat interface G_{flat} is described [131] and modified into equation (60), yielding

$$G_{TC\_slope}^{CTE}=\frac{\left(1-\upsilon_{TC}^{2}\right)\sigma_{TC}^{CTE}\left(y,x\right)^{2}}{2E_{TC}\left(T_{TC}\big|_{y},t\right)}\times H\times\sin^{2}\beta\left(x\right) \tag{61}$$

Assuming that the crack is initiated at position x_{MAX} where maximum ERR $G_{TC\_slope}^{CTE}$ is generated, it is critical to calculate the coordinate x_{MAX} by setting the first derivative of equation (61) equal to 0. Considering all x-dependent parameters in equation (61) and integrating the value of *A*, *W* and h_{TGO}^{max}, yields

$$\frac{d}{dx}f\left(x\right)=\frac{d}{dx}\left[A\left(x\right)\times B\left(x\right)\right]=0 \tag{62}$$

where

$$\begin{aligned}A\left(x\right)&=\cos^{2}\left[\frac{\pi}{40}\left(x+40\times\frac{d_{TGO}}{8.5}\right)\right]\\B\left(x\right)&=\sin^{2}\beta\left(x\right)=\sin^{2}\left[\frac{\pi}{2}-\arctan\left[-\frac{3\pi}{8}\sin\left(\frac{\pi}{40}x\right)\right]\right]\end{aligned} \tag{63}$$

Solving equation (62) gives

$$x_{MAX}=-\frac{80}{17}d_{TGO}+40k\qquad k\in Z \tag{64}$$

where *k* is an integer. For the present coordinate system, x_{MAX} is always negative. *k* equals 0 with x_{MAX} varying from -6.11μm to -40μm as the TGO thickens from 1.3μm to 8.5μm. Thus, the ERR for the crack driving force generated by CTE mismatch within the TC can be estimated by integrating equation (64) into equation (61).

Equation (61) can be used to calculate the crack driving force at a given position for either isothermal furnace cycling conditions or burner cycling conditions. For the isothermal case, equation

(47) is simplified given $T_{BC}^{hold} = T_{TC}^{hold}\big|_{y=y_0}$, $T_{BC} = T_{TC}\big|_{y=y_0}$ where $\alpha_{TGO}\left(T_{BC}\right)$, $\alpha_{TC}\left(T_{TC}\big|_{y=y_0}\right)$, $\alpha_{BC}\left(T_{BC}\right)$ and Λ are independent of calculated depth *y*. The discrepancies between calculated ERR for isothermal and burner cycling tests with thermal gradient will be discussed in section 5.4.

5.3.2. Analytical models for TGO ERR generated due to TGO growth

As described in appendix A.1.1 and A.1.2, all specimens experience isothermal preheating treatment at elevated temperature with various durations to produce pre-oxide TGO scales of different thickness. These specimens are then designed to undergo either isothermal furnace cycling testing or burner cycling testing. The stress generated due to TGO growth is described by equation (66) where $\varepsilon_{TGO}\left(t\right)$ is obtained by integrating equation (65) with respect to time to give

$$\dot{\varepsilon}_{TGO}\left(t\right) = f_2^{ini}\,\dot{f}\left(t\right)\left(P\frac{S'}{\tilde{S}} + e_V^T\mathbf{1}\right) \tag{65}$$

$$\sigma_{TGO}\left(T_{BC},t\right) = \frac{E_{TGO}\left(T_{BC}\right)\times\varepsilon_{TGO}\left(t\right)}{1-\nu_{TGO}} \tag{66}$$

where f_2^{ini} is the initial volume fraction of metallic phase β-NiAl, which has not been oxidized, and $f_2^{ini}\approx 0.526$ [135]. $\tilde{S}$ and S' are the norm and deviatoric components of the aggregate stress tensor, respectively. *P* is a coefficient depending on the shape of the oxide particles. e_V^T is the true mean volumetric strain from phase transformation. $E_{TGO}\left(T_{BC}\right)$ and ν_{TGO} are temperature-dependent elastic modulus and Poisson's ratio of the TGO layer. The details of obtaining $f\left(t\right)$ and e_V^T are described in the supplementary document. Similar to the form of analytical expression for the crack

driving force due to CTE mismatch, the ERR for crack triggered by TGO growth stress is described as [131]

$$G_{TGO}^{GR} = \frac{\left(1-\nu_{TGO}^{2}\right)}{2E_{TGO}\left(T_{BC}\right)} \times \sigma_{TGO}^{2}\left(T_{BC},t\right) \times d_{TGO} \times Y^{2} \tag{67}$$

As mentioned in the appendix A.1.2, there exists a large discrepancy between TGO growth behavior under the two types of thermal cycling tests for the current study. The growth of TGO layer under burner cycling testing is limited due to moderate temperatures at the BC surface and inadequate elevated exposure time. For the isothermal cycling test, the growth of the TGO layer is more evident for the group of specimens which has a thinner pre-oxide TGO layer. The difference in resulting TGO ERR from the two thermal cycling tests will be discussed in section 5.4.

5.3.3. Analytical models for TC ERR generated due to thermal gradient

The introduction of back side cooling during the high temperature holding time and rapid heating/cooling lead to a massive thermal gradient under the burner cycling test, Figure 71(a). This temperature difference within the TC between the surface and position close to the TC/TGO interface is a critical crack driving force where the crack might form in a different way. That is, the isolated crack forms and propagates parallel to the interface. In the other case, the crack is connected to the free edges of the TC [128], Figure 75.

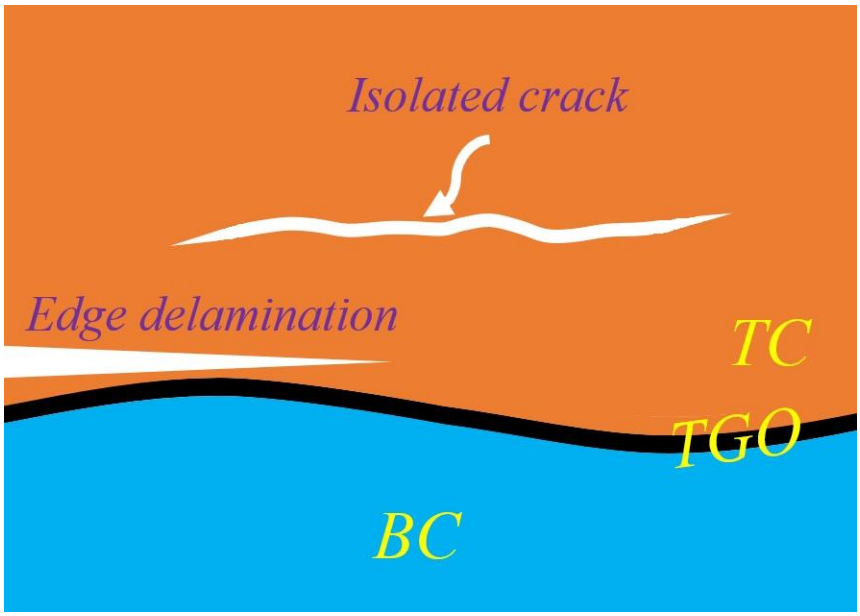

Figure 75 Schematic of the three potential modes of delamination of a TBC in the presence of a thermal gradient [128]

The methods used to calculate the ERR depends on the thermal gradient developed either during high temperature holding time or rapid cooling. Two different analytical methods are demonstrated in the following sections.

(a) The ERR generated due to thermal gradient developed at high temperature holding time

The analytical solutions to calculate the crack driving force due to the high heat flux developed for isothermal high temperatures can be found in [128]. As shown in Figure 75, two possible crack routes are given and corresponding ERR are proposed.

For an isolated interface crack developed within the TC parallel to the interface, a thermal gradient is assumed between the upper and lower faces, considering the crack as insulated where this temperature

difference facilitates crack propagation, Figure 75. A moment $M_{0TC\_insul}^{TH\_GR}$ and force $F_{0TC\_insul}^{TH\_GR}$ are imposed on the detached section to fit the gap, and are described by [128]

$$\begin{aligned} F_{0TC\_insul}^{TH\_GR} &= \frac{1}{2}\bar{E}_{TC}\left(T_{TC}\big|_y, t\right)\alpha_{TC}\left(T_{TC}\big|_y\right)\Delta T_{TC/interface} H \\ M_{0TC\_insul}^{TH\_GR} &= -\frac{1}{12}\bar{E}_{TC}\left(T_{TC}\big|_y, t\right)\alpha_{TC}\left(T_{TC}\big|_y\right)\Delta T_{TC/interface} H^2 \end{aligned} \tag{68}$$

Here, $\Delta T_{TC/interface}$ is approximated as the difference between the temperature measured at a position within the TC, $T_{TC}\big|_y$ and temperature measured at the interface T_{BC}. By restoring the edge of the spalled TC to the remaining section of TBCs and assuring the continuity of moment, force, displacement and rotation, the analytical solution of final moment $M_{TC\_insul}^{TH\_GR}$ and force $F_{TC\_insul}^{TH\_GR}$ can be obtained by [128]

$$\begin{aligned} F_{TC\_insul}^{TH\_GR} &= \frac{(b/H)(a_{22}+12b/H)F_{0TC\_insul}^{TH\_GR} - 12(b/H)a_{12}M_{0TC\_insul}^{TH\_GR}/H}{\aleph} \\ \frac{M_{TC\_insul}^{TH\_GR}}{H} &= \frac{12(b/H)(a_{11}+b/H)M_{0TC\_insul}^{TH\_GR}/H - (b/H)a_{12}F_{0TC\_insul}^{TH\_GR}}{\aleph} \end{aligned} \tag{69}$$

Here, $\aleph = (a_{11}+b/H)(a_{22}+12b/H) - a_{12}^2$. The value of compliance coefficient a_{ij} depends on the ratio of TC crack length over TC thickness $\frac{b}{H}$ and first Dundurs' elastic mismatch parameters, equation tabulated in [205].

Accordingly, the stress intensity factors for mode I and mode II are given by

$$\begin{aligned} K_I^{ISOTHEM} &= c_{21}F_{TC\_insul}^{TH\_GR}/\sqrt{H} + 2\sqrt{3}c_{22}M_{TC\_insul}^{TH\_GR}/H^{3/2} \\ K_{II}^{ISOTHEM} &= c_{11}F_{TC\_insul}^{TH\_GR}/\sqrt{H} + 2\sqrt{3}c_{12}M_{TC\_insul}^{TH\_GR}/H^{3/2} \end{aligned} \tag{70}$$

Similar to the compliance coefficient a_{ij}, stress intensity coefficients c_{ij} also depend on the ratio of TC crack length over TC thickness $\frac{b}{H}$ and first Dundurs' elastic mismatch parameters tabulated in [205].

The corresponding ERR and mode mixture for isolated interface crack developed under isothermal heat flux environment are described by [128]

$$G_{TC}^{ISOTHEM\_insulated} = \frac{1}{2}\left(\frac{1}{\bar{E}_{TC}\left(T_{TC}\big|_y, t\right)} + \frac{1}{\bar{E}_{BC}\left(T_{BC}\right)}\right)\left[\left(K_I^{ISOTHEM}\right)^2 + \left(K_{II}^{ISOTHEM}\right)^2\right]$$
$$\psi = \tan^{-1}\left(\frac{K_{II}^{ISOTHEM}}{K_I^{ISOTHEM}}\right) \quad (71)$$

For the crack connecting to the free edge of the TC, there are two factors that need to be considered including i) the effect of thermal gradient that induces the bending moment into TBCs and ii) the heating the TBCs above the stress-free temperature T_{dep} induces the CTE misfit between TC and BC during high temperature holding time, which further results in residual compression within the TC. The corresponding analytical expressions are given to describe the stress as a consequence CTE mismatch $\bar{\sigma}_{TC\_edge}^{TH\_GR}$ and thermal gradient $\Delta\sigma_{TC\_edge}^{TH\_GR}$, developed within TC [128] as

$$\Delta\sigma_{TC\_edge}^{TH\_GR} = \bar{E}_{TC}\left(T_{TC}\big|_y, t\right)\alpha_{TC}\left(T_{TC}\big|_y\right)\left(T_{TC}\big|_y - T_{TC}\big|_{surf}\right) \quad (72)$$

$$\bar{\sigma}_{TC\_edge}^{TH\_GR} = 2\bar{E}_{TC}\left(T_{TC}\big|_y, t\right)\left\{\alpha_{BC}\left(T_{BC}\right)\left(T_{BC} - T_{dep}\right) - \alpha_{TC}\left(T_{TC}\big|_y\right)\left(\frac{T_{TC}\big|_y + T_{TC}\big|_{surf}}{2} - T_{dep}\right)\right\} \quad (73)$$

Here, $T_{TC}\big|_{surf}$ is the TC surface temperature. The corresponding steady-state ERR for edge delamination crack developed under isothermal heat flux environment is described by

$$G_{TC}^{ISOTHEM\_edge} = \frac{\left(\bar{\sigma}_{TC\_edge}^{TH\_GR}\right)^2 H}{2\bar{E}_{TC}\left(T_{TC}\big|_y, t\right)} + \frac{\left(\Delta\sigma_{TC\_edge}^{TH\_GR}\right)^2 H}{24\bar{E}_{TC}\left(T_{TC}\big|_y, t\right)} \tag{74}$$

(b) The ERR generated due to thermal gradient developed upon cooling

Analytical solutions have been proposed to calculate the crack driving force due to thermal gradient generated from rapid temperature change upon cooling [144]. Similar to the method described in the isothermal case in section 5.3.1(a), an in-plane stress $\sigma_{TC\_Cool}^{TH\_GR}(y)$ is assumed at a given depth within the uncracked coating where the corresponding unit force $P_{TC\_Cool}^{TH\_GR}$ (force/length) and unit moment $M_{TC\_Cool}^{TH\_GR}$ (moment/length) are given in [144]. Depending on the position where the crack was identified, the mixed mode ERR $G_{TC\_interf}^{TEMPVARY}$ and mode mixture $\phi_{TC\_interf}^{TEMPVARY}$ are determined, when the crack is close to the interface, ($d \approx H$ Figure 75) as

$$G_{TC\_interf}^{TEMPVARY} = \frac{H}{6\bar{E}_{TC}\left(T_{TC}\big|_y, t\right)}\left[3\left(\bar{\sigma}_{TC\_Cool}^{TH\_GR}\right)^2 + \left(\sigma_{0TC\_Cool}^{TH\_GR}\right)^2\right] \tag{75}$$

$$\phi_{TC\_interf}^{TEMPVARY} = \tan^{-1}\left(\frac{\sqrt{3}\bar{\sigma}_{TC\_Cool}^{TH\_GR}\tan\omega - \sigma_{0TC\_Cool}^{TH\_GR}}{\sqrt{3}\bar{\sigma}_{TC\_Cool}^{TH\_GR} + \sigma_{0TC\_Cool}^{TH\_GR}\tan\omega}\right) \tag{76}$$

where

$$\begin{aligned}\bar{\sigma}_{TC\_Cool}^{TH\_GR} &= E_{TC}\left(T_{TC}\big|_y, t\right)\alpha_{TC}\left(T_{TC}\big|_y\right)\Delta T\big|_{surf/interf}\left(0.5-\Phi\right)\Big/\left(1-\upsilon_{TC}\right)\\ \sigma_{0TC\_Cool}^{TH\_GR} &= E_{TC}\left(T_{TC}\big|_y, t\right)\alpha_{TC}\left(T_{TC}\big|_y\right)\Delta T\big|_{surf/interf}\Big/2\left(1-\upsilon_{TC}\right)\end{aligned} \tag{77}$$

The dimensionless ratio of mismatch strains Φ is described by

$$\Phi = \frac{\left[\alpha_{BC}\left(T_{BC}\right)-\alpha_{TC}\left(T_{TC}\big|_y\right)\right]\Delta T\big|_{interf}}{\alpha_{TC}\left(T_{TC}\big|_y\right)\Delta T\big|_{surf/interf}} \tag{78}$$

The temperature quantity $\Delta T\big|_{surf/interf}$ is given by $\Delta T\big|_{surf/interf} = \Delta T\big|_{surf} - \Delta T\big|_{interf}$, which indicates the instantaneous difference between the temperature drop at the surface $\Delta T\big|_{surf}$ and at the TC/BC interface $\Delta T\big|_{interf}$, provided the temperature at BC and TGO layer are identical. For plane strain conditions, ω=52.1° [144].

For a crack located above the interface ($d < H$ in Figure 75), The mode I $K_{I\_TC\_above}^{TEMPVARY}$ stress intensity factor and ERR $G_{I\_TC\_above}^{TEMPVARY}$ are described by

$$K_{I\_TC\_above}^{TEMPVARY} = \frac{P_{TC\_Cool}^{TH\_GR}\sqrt{d}}{\sqrt{2\cos\omega}} \tag{79}$$

$$G_{I\_TC\_above}^{TEMPVARY} = \frac{\left(K_{I\_TC\_above}^{TEMPVARY}\right)^2}{\bar{E}_{TC}\left(T_{TC}\big|_y, t\right)} \tag{80}$$

The crack driving force $G_{TC}^{TEMPVARY}$ is determined using different equations for a crack nucleated at the interface $G_{TC\_interf}^{TEMPVARY}$, or above interface $G_{I\_TC\_above}^{TEMPVARY}$.

5.3.4. Analytical models for TC ERR generated due to Thermal shock

Due to the rapid heating/cooling process under the burner cycling test, the effect of thermal shock on the nucleation of a delamination crack should be considered and included into the total ERR. The cracking driving force for thermal shock with existence of thermal gradient was evaluated by Fleck et al [145]. Neglecting the effect of the first and second Dundurs' elastic mismatch parameters for simplicity, the stress intensity factors for mode I and mode II are obtained from (81) [145],

$$\begin{aligned} K_{I\_TC}^{TH\_SH} &= 0.434\frac{P_{TC}^{TH\_SH}}{\sqrt{\hat{A}H}} + 0.558\frac{M_{TC}^{TH\_SH}}{\sqrt{\hat{I}H^3}} \\ K_{II\_TC}^{TH\_SH} &= 0.558\frac{P_{TC}^{TH\_SH}}{\sqrt{\hat{A}H}} - 0.434\frac{M_{TC}^{TH\_SH}}{\sqrt{\hat{I}H^3}} \end{aligned} \tag{81}$$

where dimensionless unit $\hat{A}$ and $\hat{I}$ are used to characterize the equivalent area and moment of inertia of TC materials. For isotropic APS TC with homogeneous temperature distribution, $\hat{A}=1$ and $\hat{I}=\frac{1}{12}$ are assumed for rectangular 2D TBCs. Nevertheless, the effect of thermal gradient is considered in the current model where the equivalent area $\hat{A}$ and equivalent moment of inertia $\hat{I}$ are used and described in the supporting documents. The mode I and mode II stress intensity factors are used to calculate the mixed mode ERR and mode mixture for thermal shock developed under burner cycling test, described by

$$G_{TC}^{TH\_SH} = \frac{1-\upsilon_{TC}^2}{E_{TC}\left(T_{TC}\big|_y, t\right)}\left[\left(K_{I\_TC}^{TH\_SH}\right)^2 + \left(K_{II\_TC}^{TH\_SH}\right)^2\right] \tag{82}$$

$$\psi = \tan^{-1}\left(\frac{K_{II\_TC}^{TH\_SH}}{K_{I\_TC}^{TH\_SH}}\right) \tag{83}$$

5.4. Results and discussion

The abovementioned energy release rates suggest that the crack might nucleate at a different stage within thermal cycle, i.e., the crack driving force generated due to CTE mismatch plays a role only upon cooling. Although the growth of the TGO layer occurs mostly during the high temperature holding time, the TGO ERR was generated during the preheat treatment, where the pre-oxide TGO layer formed. The effect of thermal gradient and thermal shock on the durability of APS-TBCs might only be estimated under burner cycling test. In order to evaluate the effect of specific ERR (i.e. generated within a specific duration in the thermal cycling test) on the lifetime, a normalization process is introduced where the equivalent ERR is evaluated through

$$\tilde{G}_i^k = \frac{\sum_{N=1}^{N_f} \sum_{t_j=1}^{t_j^f} G_i^k\left(t_j\right)}{t_f} \tag{84}$$

where i indicates the layer where the crack driving force is calculated, k indicates the type of ERR that is responsible for the corresponding crack nucleation and propagation, j is the stage of thermal cycle (heating/holding/cooling), and t_j^f is the total time for specific stage j within a thermal cycle. For example, if the holding and cooling period for a burner cycling test is 50s and 120s, then $t_{hold}^f = 50$ and $t_{cool}^f = 120$, respectively. $G_i^k\left(t_j\right)$ stands for the ERR generated within layer i at each second of t_j. N and N_f are the number of thermal cycles and life cycle, respectively. The numerator of equation (84) is the sum of specific ERR generated for the entire lifetime, where the denominator

$t_f = N_f \times \left(t_{heat}^f + t_{hold}^f + t_{cool}^f \right)$ is lifetime as a function of pre-oxide TGO thickness. Equation (84) is capable of evaluating the equivalent ERR with respect to pre-oxide TGO thickness.

Another criterion used in the current study estimates the average ERR as a function of number of thermal cycles, as indicated by

$$\bar{G}_i^k \left(N \right) = \frac{\sum_{t_j=1}^{t_j^f} G_i^k \left(t_j \right)}{t_j^f} \tag{85}$$

The numerator in equation (85) is the sum of specific ERR generated within one cycle. Equation (85) enables the evaluation of the average ERR generated within a specific duration as a function of thermal cycle. The following discussion will address the different type of ERRs.

5.4.1. Calculated TC equivalent energy release rate generated due to CTE mismatch

As described in the preceding section, the ERR due to CTE mismatch only develops upon cooling during thermal cycles. Therefore, the equivalent ERR due to CTE mismatch can be written as

$$\tilde{G}_{TC}^{CTE} = \frac{\sum_{N=1}^{N_f} \sum_{t_{cool}=1}^{t_{cool}^f} G_{TC\_slope}^{CTE} \left(t_{cool} \right)}{t_f} \tag{86}$$

The equivalent ERR are calculated at 1μm away from interface within the TC and shown in Figure 76 for the isothermal furnace cycling test and burner cycling test.

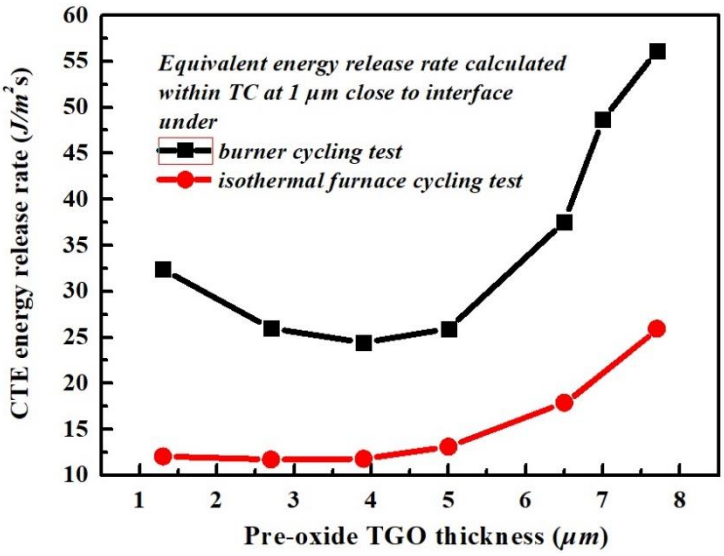

Figure 76 The equivalent CTE ERR as function of pre-oxide TGO thickness for isothermal furnace cycling test and burner cycling test

Each thermal cycle in the burner cycling test contains 120s cooling time, which yields 120 of calculated $G_{TC\_slope}^{CTE\_burner}\left(t_{cool}\right)$. The calculated $\tilde{G}_{TC}^{CTE\_burner}$ evaluates the effect of the sum of CTE ERR generated upon cooling for all thermal cycles on the scale of lifetime. With the calculated ERR based on a flat interface G_{flat} multiplying the angle parameter sin2β in equation (60), there is inevitably a decrease in CTE when the effect of geometry of roughness surface is included (wings of imperfection). On the other hand, if the value of the mix mode fracture toughness of TC is assumed to be independent of position within the TC, the decreasing of CTE ERRs estimated as pre-oxide TGO thickness varies from 1.3μm to 3.9μm shown in Figure 76 indicates that there might be less CTE ERRs generated as the maximum out-of-plane tensile stress is identified at wings of imperfections. The cracking process might be inhibited or slowed at wings of imperfections due to the engineering-designed interfacial roughness characteristics, which is frequently mentioned as the effect of "mechanical interlocking" between layers [46], [172], [206]–[209]. However, interfacial roughness with excessive amplitude would induce extra

tensile stress at the peak of the TC according to the FE analysis [67]. This in turn facilitates crack initiation at early stages of life cycle. Therefore, the balance between the effect of cracking inhibition and the effect of stress concentration (both due to TC roughness) is critical for controlling cracking behavior and hence the durability of APS-TBCs.

Each thermal cycle in the isothermal furnace cycling test contains 480s cooling time, which yields 480 of calculated $G_{TC\_slope}^{CTE\_isoth}\left(t_{cool}\right)$. Two conclusions can be made by comparing the calculated equivalent ERR from burner cycling test $\tilde{G}_{TC}^{CTE\_burner}$ to the isothermal furnace cycling test $\tilde{G}_{TC}^{CTE\_isoth}$.

A. Compared to the CTE ERR $\tilde{G}_{TC}^{CTE\_burner}$ generated under burner cycling test with thermal gradient, there is less of a decrease for CTE ERR $\tilde{G}_{TC}^{CTE\_isoth}$ generated under isothermal furnace cycling test for group sets of TBCs with pre-oxide TGO thickness smaller than 5μm. This can be explained by the difference of experimental conditions that affect variation of the model parameters as a function of number of cycles, e.g., the sintering process-dependent elastic modulus $E_{TC}\left(T_{TC}\big|_{y},t\right)$, as well as the TGO thickness-dependent position of maximum CTE stress (x_{MAX}). For burner cycling conditions with existing thermal gradient and relatively short high temperature hold time, there is limited sintering and TGO growth within the cycling experiments. This makes the position (x_{MAX}) and magnitude of maximum CTE stress independent of the number of thermal cycles, equation (58). In addition, the average CTE ERR $\bar{G}_{TC}^{CTE\_burner}\left(N\right)$, calculated using equation (61) and equation (85), is dominated by positions where the maximum CTE ERR is identified, x_{MAX}. This in turn, is determined by pre-oxide TGO thickness d_{TGO}, equation (64). However, the calculated $\bar{G}_{TC}^{CTE\_burner}\left(N\right)$ is not affected much by the number of thermal cycles, Figure 77. Consequently, the equivalent CTE ERR for the burner cycling test also demonstrates the pre-oxide thickness-dependent behavior, where the calculated energy fluxes fluctuate as function of positions to obtain the maximum ERRs, as can be seen in the black curve in Figure 76.

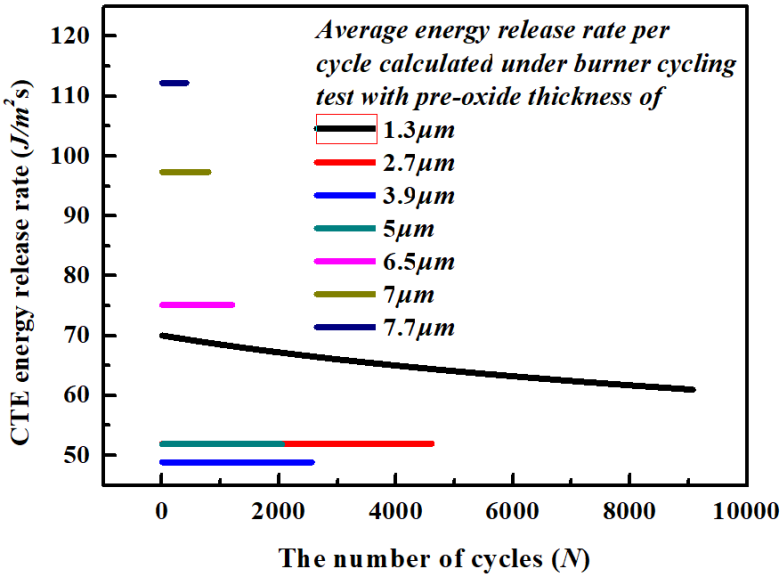

Figure 77 the calculated average CTE ERR as function of number of cycles with respect to different pre-oxide thickness for burner cycling test

However, for the isothermal furnace cycling test, the relatively higher temperature and longer holding time makes sintering behavior more effective within the TC and facilitates growth of the TGO layer under high temperature holding time, specifically for the group of TBCs with shorter preheat treatment (TBCs with pre-oxide thickness smaller than 5μm). This makes the position and magnitude of maximum CTE stress vary as a function of thermal cycle for each group of TBCs with its own pre-oxide thickness. In other words, the TBCs under isothermal furnace cycling tests with pre-oxide thickness smaller than 5μm all experience the shifting of position of maximum CTE stress from somewhere at the ridge of the TC to somewhere close to valley of TC. This is reflected by the cyclic-dependent average CTE ERR $\bar{G}_{TC}^{CTE\_isoth}(N)$, illustrated in Figure 78. The increase of CTE ERR at a later stage of life cycle makes the equivalent CTE ERR less affected by the geometrical factors that decrease the CTE ERR with intermediate TGO thickness for the group of TBCs with pre-oxide thickness smaller than 5μm, see the red curve in Figure 76.

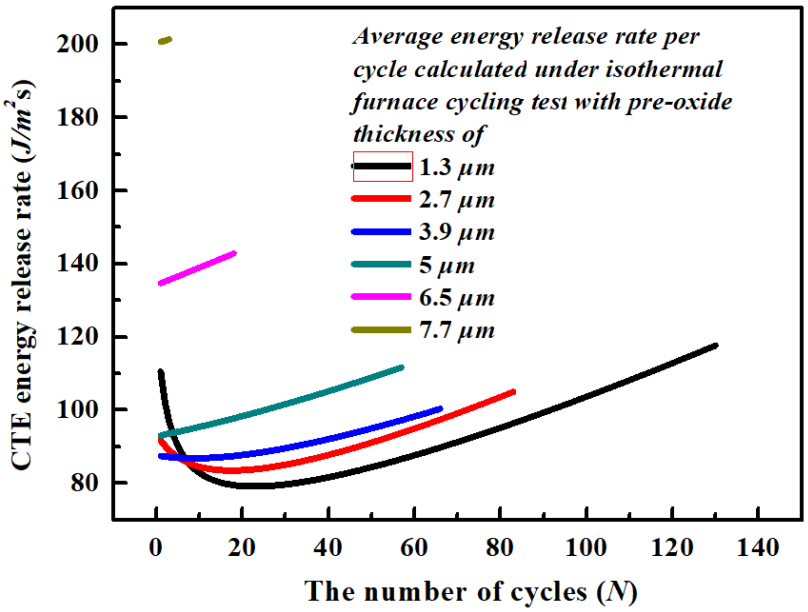

Figure 78 the calculated average CTE ERR as function of number of cycles with respect to different pre-oxide thickness for isothermal furnace cycling test

B. For the calculated equivalent CTE ERR, Figure 76, a similar significant increase in both curves can be observed with respect to pre-oxide thickness in the range of 5-7.7μm. This shows that as long as the TGO reaches the critical thickness (regardless of TGO growth from either pre-heat treatment or under isothermal cycling test), there is a similarity for the cracking mode between the two different cycling experiments. This agrees with the conclusion in [185] that the cracking routes shift from positions far away from the interface (where cracks nucleate at lamellae interface and propagate horizontally), to positions close to the interface between TC/TGO layer followed by rapid crack propagation.

5.4.2. Calculated TGO equivalent energy release rate generated due to TGO growth

The equivalent ERR due to TGO growth is described by

$$\tilde{G}_{TGO}^{GR} = \frac{\sum_{N=1}^{N_f}\left[\sum_{t_{heat}=1}^{t_{heat}^f} G_{TGO}^{GR}\left(t_{heat}\right) + \sum_{t_{hold}=1}^{t_{hold}^f} G_{TGO}^{GR}\left(t_{hold}\right) + \sum_{t_{cool}=1}^{t_{cool}^f} G_{TGO}^{GR}\left(t_{cool}\right)\right]}{t_f} \tag{87}$$

The equivalent ERR are calculated within the TGO layer and shown in Figure 79 as a function of pre-oxide thickness for isothermal furnace cycling test and burner cycling test.

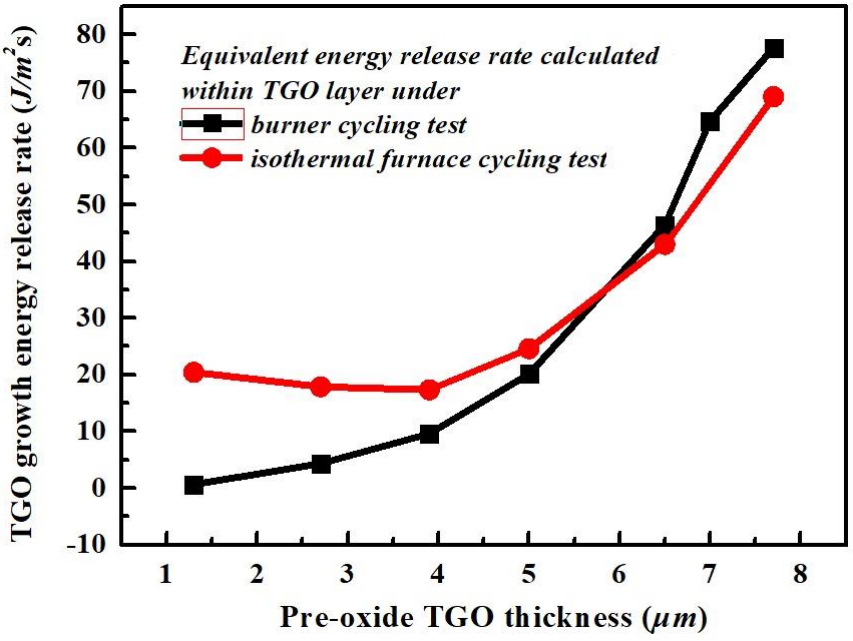

Figure 79 The equivalent TGO ERR as function of pre-oxide TGO thickness for isothermal furnace cycling test and burner cycling test

In addition to the fact that both of curves increase as the pre-oxide layer thickens, there are three conclusions obtained by comparing the calculated equivalent TGO ERR from the burner cycling test $\tilde{G}_{TGO}^{GR\_burner}$ to the isothermal furnace cycling test $\tilde{G}_{TGO}^{GR\_isoth}$.

A. For both burner cycling test and isothermal furnace test, the TGO ERR are already generated during preheat treatment time, where the pre-oxide TGO layer formed before the thermal cycling test started. This is especially for the group set of TBCs which has 350 hours preheat treatment with 7.7μm pre-oxide thickness. It is expected that there exists a large TGO ERR which facilitates the propagation of delamination cracks at the interface between the TC/TGO. It also further explains the relatively short life cycle for such groups of TBCs. Upon heating and cooling under thermal cycling conditions, there is a limited TGO growth. Nevertheless, the variation of temperature-dependent TGO elastic modulus might still lead to the fluctuation of TGO ERR within a thermal cycle. As mentioned in the Appendix A.1.2, for the burner cycling test with thermal gradient, due to the low temperature at the BC surface and the relative short high temperature holding time, there is limited TGO growth measured for the groups at the end of cycling experiments [185] (except for the TBCs with pre-oxide thickness of 1.3μm). However, the accumulated TGO stress generated due to progressive oxidation of BC during preheat treatment is introduced for TBCs under further burner cycling tests. Nevertheless, the elastic modulus of TGO and TGO thickness is independent of number of cycles. Therefore, similar to the average CTE ERR calculated under the burner cycling test, the average TGO ERR $\bar{G}_{TGO}^{GR\_burner}(N)$ calculated using equation (67) and equation (85) is dominated by pre-oxide TGO thickness, and is not affected much by the number of thermal cycles, Figure 80. Hence, the equivalent TGO ERR $\tilde{G}_{TGO}^{GR\_burner}$ for burner cycling test basically describes the TGO ERR under isothermal preheat treatment.

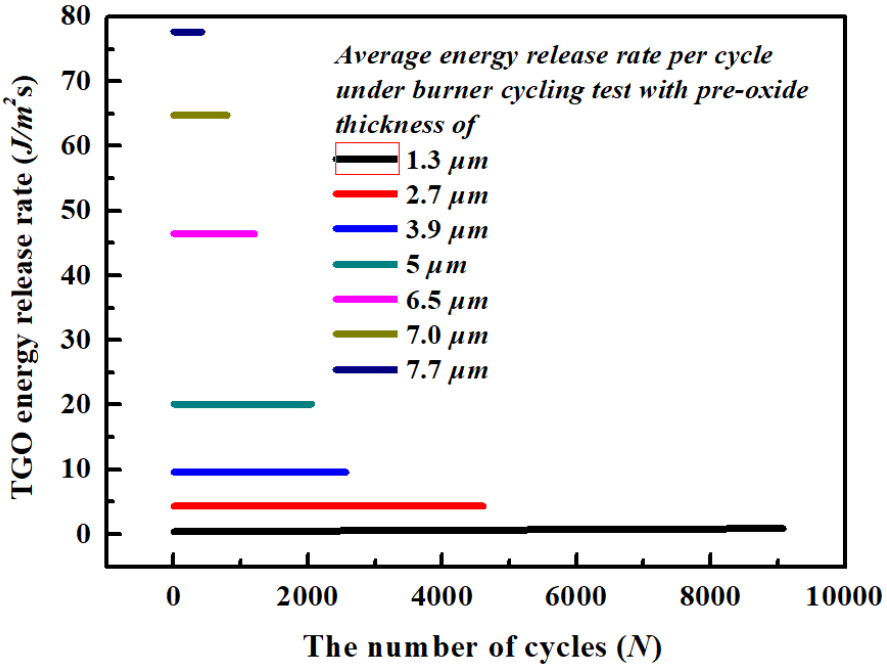

Figure 80 the calculated average TGO ERR as a function of number of cycles with respect to different pre-oxide thickness for burner cycling test

B. It becomes difficult to understand the general trend for calculated equivalent TGO ERR $\tilde{G}_{TGO}^{GR\_isoth}$ under isothermal furnace cycling test as its initial decrease and then later increase are similar to equivalent CTE ERR $\tilde{G}_{TC}^{CTE\_burner}$ under burner cycling test. As $\tilde{G}_{TC}^{CTE\_burner}$ is significantly affected by geometrical parameters, the initial decrease and the later increase of the red curve in Figure 79 is affected by TGO growth under isothermal furnace cycling test, based on different groups with various of pre-oxide thickness. According to the calculated TGO thickness under isothermal furnace cycling conditions (supporting documents), Figure 110 the relatively thin pre-oxide layer (1.3μm) is not capable of playing a role as the "protective layer" for BC further oxidation under high temperature holding time under isothermal furnace cycling test. With a longer life span (130 cycles), the relatively thicker TGO layer (6.21μm) is formed at the end of the lifetime which leads to a continuous increase of average TGO ERR $\bar{G}_{TGO}^{GR\_isoth}(N)$ as a function of number

of cycles, black curve in Figure 81. This provides a higher equivalent TGO ERR $\tilde{G}_{TGO}^{GR\_isoth}$ at a smaller pre-oxide thickness.

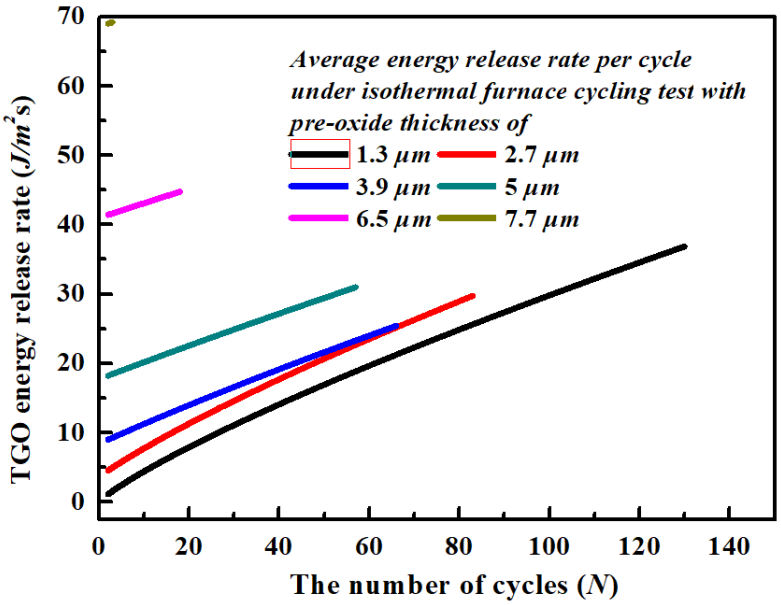

Figure 81 the calculated average TGO ERR as function of number of cycles with respect to different pre-oxide thickness for isothermal furnace cycling test

With further increase of pre-oxide thickness, the thicker pre-oxide layer starts to play a role in inhibiting the progressive oxidation of BC, which lower the TGO growth rate for the further BC oxidation during high temperature holding time. With the shorter life span corresponding thicker pre-oxide layer, the later oxidation further limits the growth of TGO layer under isothermal furnace cycling conditions (final TGO thicknesses are 5.78μm and 5.49μm for TBCs with pre-oxide thickness of h_{TGO}^{i} =2.7μm and 3.9μm, respectively). This results in lower average TGO ERR $\bar{G}_{TGO}^{GR\_isoth}(N)$ as a function of number of cycles, as can be seen from red and blue curves in Figure 81, as well as lower equivalent TGO ERR $\tilde{G}_{TGO}^{GR\_isoth}$ for h_{TGO}^{i} =2.7μm and 3.9μm (Figure 79).

For the group set of TBCs where pre-oxides are thicker than 5μm, although there is little TGO growth under thermal cycling conditions, the average TGO ERR is still higher compared to the group sets with pre-oxide layer thinner than 5μm. This can be explained by the higher initial pre-oxide thickness which provides enough TGO ERR and lasts throughout entire thermal cycling life cycle, as can be seen by the dark cyan, magenta and dark yellow curves in Figure 81. This gives higher equivalent TGO ERR $\tilde{G}_{TGO}^{GR\_isoth}$ for h_{TGO}^{i}=5.0μm, 6.6μm and 7.7μm in Figure 79.

C. There exists an intersection between two equivalent TGO ERR curves as a function of pre-oxide thickness, Figure 79. For same pre-oxide thickness, the effect of temperature profile of the two different thermal conditions on the calculated equivalent TGO ERR $\tilde{G}_{TGO}^{GR}$ is reflected by: i) the difference in further growth of TGO layers determined by high temperature holding time (26min for isothermal and 50s for burner) and temperature at the BC surface (1120^{o}C for isothermal and 935^{o}C for burner) ii) the difference in elastic modulus of the TGO layer. The i) leads to higher equivalent TGO ERR under isothermal furnace cycling test whereas ii) leads to the higher equivalent TGO ERR under burner cycling test. It is evident that the intersection of the two curves in Figure 79 is located at the position corresponding to pre-oxide thickness around 5.5-6μm. The calculated equivalent TGO ERR for isothermal furnace cycling tests are higher than for burner cycling test, as pre-oxide thickness is thinner than 5.5μm. This indicates that the effect of the rapid growth of TGO under isothermal furnace cycling conditions (i) suppresses the effect of the lower elastic modulus under higher temperature (ii). This leads to $\tilde{G}_{TGO}^{GR\_isoth} > \tilde{G}_{TGO}^{GR\_burner}$ as pre-oxide thickness is smaller than 5.5μm. On the other hand, the TGO growth under isothermal furnace cycling conditions is limited since pre-oxide thickness is thicker than 5.5μm. Here, the effect of higher elastic modulus under thermal gradient condition (ii) suppresses the effect of growth of TGO layer (i), which leads to $\tilde{G}_{TGO}^{GR\_isoth} < \tilde{G}_{TGO}^{GR\_burner}$ as pre-oxide thickness is higher than 5.5μm.

5.4.3. Calculated TC equivalent energy release rate generated due to thermal gradient for burner cycling test

A thermal gradient is introduced by applying compressed air to the back-side of the BC during high temperature holding time for APS-TBCs under burner cycling test. The temperature difference at various of depths within the TC is also present upon cooling due to the rapid temperature drop on the surface of the TC. The crack driving forces due to the thermal gradient are calculated using equations described in section 5.3.3 where equivalent ERR is calculated by equation (88) and demonstrated in Figure 82 for insulated cracks $\tilde{G}_{TC}^{ISOTHEM\_insulated}$ and edge delamination $\tilde{G}_{TC}^{ISOTHEM\_edge}$ during high temperature holding time.

$$\tilde{G}_{TC}^{ISOTHEM\_insulated} = \frac{\sum_{N=1}^{N_f} \sum_{t_{hold}=1}^{t_{hold}^f} G_{TC}^{ISOTHEM\_insulated}\left(t_{hold}\right)}{t_f} \tag{88}$$

$$\tilde{G}_{TC}^{ISOTHEM\_edge} = \frac{\sum_{N=1}^{N_f} \sum_{t_{hold}=1}^{t_{hold}^f} G_{TC}^{ISOTHEM\_edge}\left(t_{hold}\right)}{t_f} \tag{89}$$

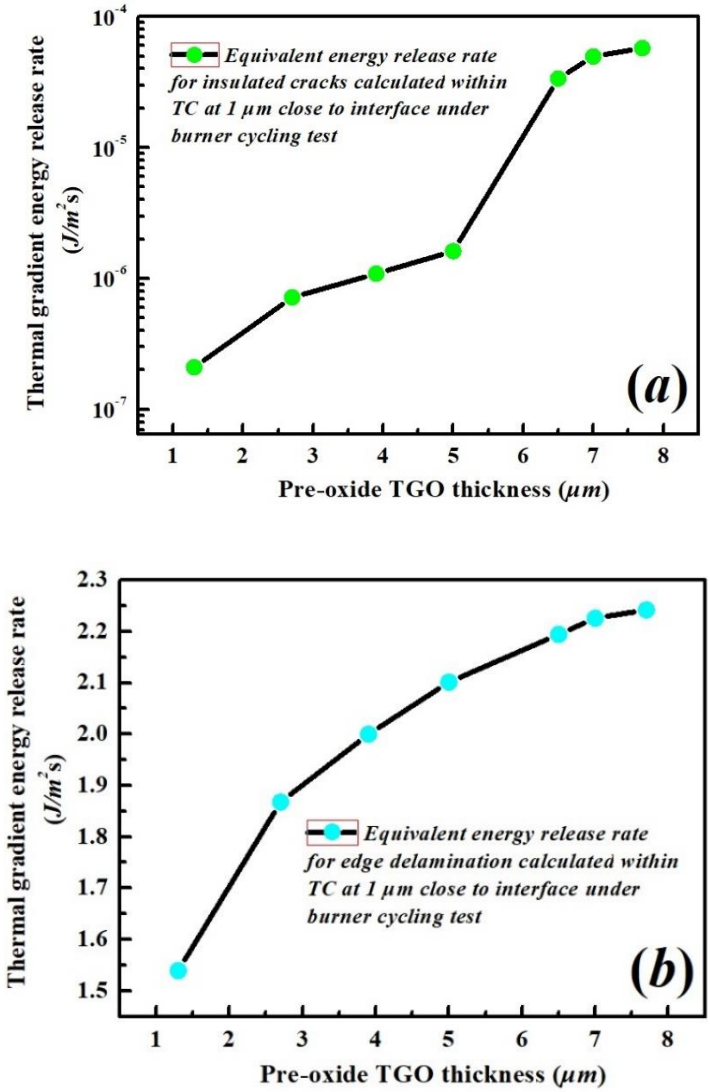

Figure 82 The equivalent thermal gradient ERR as a function of pre-oxide TGO thickness for burner cycling test assuming (a) insulated cracks (b) edge delamination crcaks within TC

It is evident that both calculated thermal gradient ERR increase as the pre-oxide thickness becomes thicker, where the calculated $\tilde{G}_{TC}^{ISOTHEM\_insulated}$ is a few orders of magnitude lower than that of $\tilde{G}_{TC}^{ISOTHEM\_edge}$. This indicates that it is unlikely for $\tilde{G}_{TC}^{ISOTHEM\_insulated}$ alone to provide enough energy to nucleate the delamination cracks within the TC layer. This is consistent with the description by

Hutchinson and Evans [128]. The situation changes when the delamination is connected to a free edge. Here, the equivalent thermal gradient ERR $\tilde{G}_{TC}^{ISOTHEM}$ generated during high temperature holding time is calculated by combining $\tilde{G}_{TC}^{ISOTHEM\_insulated}$ and $\tilde{G}_{TC}^{ISOTHEM\_edge}$ together, where the magnitude of equivalent ERR is approximated by $\tilde{G}_{TC}^{ISOTHEM\_edge}$.

Given the existence of thermal gradient throughout the thickness of TC layer, the time-dependent material parameters, such as TC elastic modulus $E_{TC}\left(T_{TC}\big|_{y},t\right)$ and TGO growth d_{TGO}, are nearly constant as a function of number of cycles when estimated 1 μm away from the bottom of the TC. This shows that the growth of the crack length *b* during isothermal conditions (discussed in Appendix A.1.3) might be the only factor that leads to the variation of the coefficients a_{ij} (equation (144)) and c_{ij} (equation (145)) as a function pre-oxide thickness, which further affects the thermal gradient ERR. Nevertheless, for pre-oxide thickness smaller than 5μm, the variation of crack length is a function of TGO thickness where there is basically no TGO growth under burner cycling test. This indicates that b/H is constant throughout the life span for TBCs with pre-oxide thickness smaller than 5.5μm. For pre-oxide thickness larger than 5.5μm, the length of the isothermal crack grows dramatically as a function of time. However, the a_{ij} and c_{ij} are approximated as constant (b/H) to a relatively large ratio [128]. Therefore, we have shown that all parameters used for estimating thermal gradient ERR in equation (146) and equation (149) are independent of time, which results in $\bar{G}_{TC}^{ISOTHEM\_insulated}$ and $\bar{G}_{TC}^{ISOTHEM\_edge}$ (via equation (85)) being constant throughout the life cycle with respective to their pre-oxide thickness.

The equivalent thermal gradient ERR $\tilde{G}_{TC}^{TEMPVARY}$ developed upon cooling is calculated by equation (90) and illustrated in Figure 83.

$$\tilde{G}_{TC}^{TEMPVARY} = \frac{\sum_{N=1}^{N_f} \sum_{t_{cool}=1}^{t_{cool}^{f}} G_{TC}^{TEMPVARY}\left(t_{cool}\right)}{t_f} \tag{90}$$

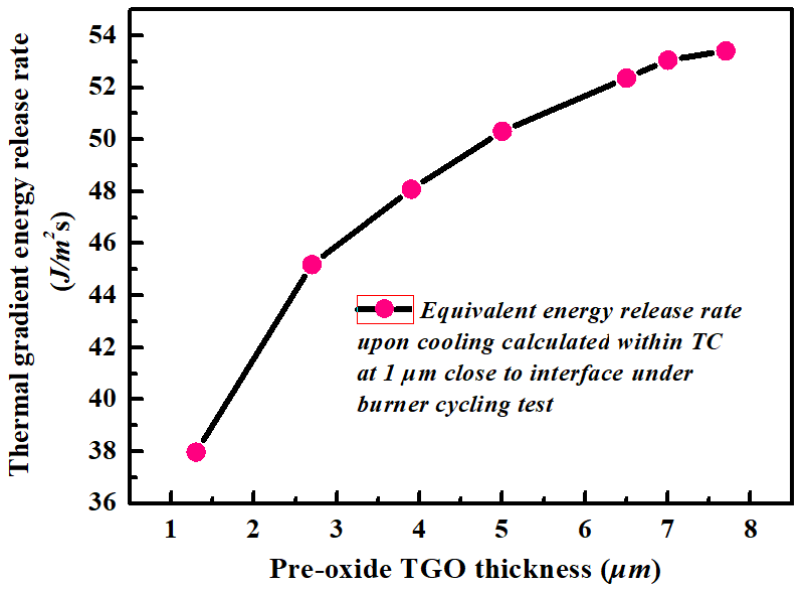

Figure 83 The equivalent thermal gradient ERR developed upon cooling as function of pre-oxide TGO thickness for burner cycling test

The equivalent thermal gradient ERR $\tilde{G}_{TC}^{TEMPVARY}$ increases as a function of pre-oxide thickness. Comparing to the $\tilde{G}_{TC}^{ISOTHEM}$ generated during high temperature holding time, the $\tilde{G}_{TC}^{TEMPVARY}$ generated upon cooling is more likely to be responsible for crack nucleation under thermal gradient conditions due to its large magnitude. In addition, the thermal gradient ERR $G_{TC}^{TEMPVARY}$ upon cooling is illustrated as a function of time with respect to different pre-oxide thickness, Figure 84.

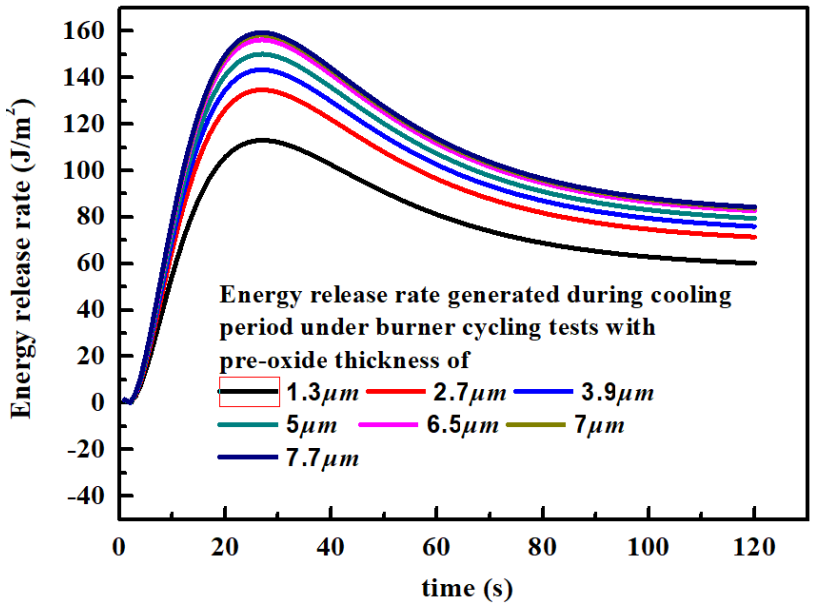

Figure 84 The thermal gradient ERR developed upon cooling as function of time for different pre-oxide TGO thickness

A higher thermal gradient ERR is expected as pre-oxide thickness increases. This might be explained by the higher elastic modulus of the TC $E_{TC}\left(T_{TC}\big|_{y},t\right)$ corresponding to the longer sintering process obtained by preheat treatment. The maximum thermal gradient ERR $G_{TC}^{TEMPVARY}$ is calculated at the middle stage upon cooling, followed by a drop in ERR to the end of the cycle. This is consistent with the results obtained by Evans [144]. The fluctuating curve in Figure 84 is affected by the CTE stress generated due to thermal gradient, where a temperature difference is expected at different depths within the TC (153).

With the calculated results described above, it is practicable to define an equivalent total ERR due to the thermal gradient generated at different stages under burner cycling test, equation (91). The calculated total equivalent ERR is shown in Figure 85.

$$\tilde{G}_{TC}^{THGR} = \frac{\tilde{G}_{TC}^{ISOTHEM} + \tilde{G}_{TC}^{TEMPVARY}}{t_f} = \frac{\sum_{N=1}^{N_f}\sum_{t_{hold}=1}^{t_{hold}^f}\left[G_{TC}^{ISOTHEM\_insulated}\left(t_{hold}\right)+G_{TC}^{ISOTHEM\_edge}\left(t_{hold}\right)\right]+\sum_{N=1}^{N_f}\sum_{t_{cool}=1}^{t_{cool}^f}G_{TC}^{TEMPVARY}\left(t_{cool}\right)}{t_f} \quad (91)$$

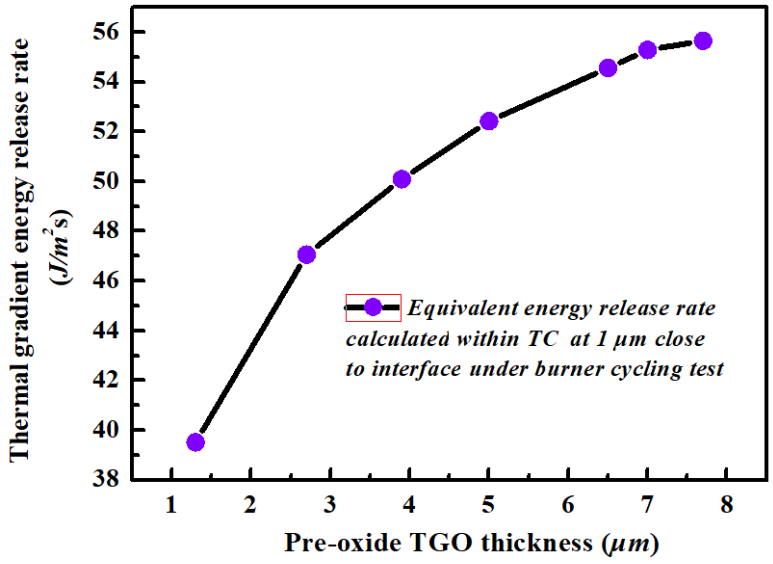

Figure 85 The equivalent total thermal gradient ERR as function of pre-oxide TGO thickness for burner cycling test

5.4.4. Calculated TC equivalent energy release rate generated due to thermal shock for burner cycling test

The effect of thermal shock on the durability of APS-TBCs on the scale of lifetime is evaluated by equivalent thermal shock ERR described by equation (92). The result is illustrated in Figure 86.

$$\tilde{G}_{TC}^{TH\_SH} = \frac{\sum_{N=1}^{N_f}\left[\sum_{t_{heat}=1}^{t_{heat}^f} G_{TC}^{TH\_SH}\left(t_{heat}\right) + \sum_{t_{cool}=1}^{t_{cool}^f} G_{TC}^{TH\_SH}\left(t_{cool}\right)\right]}{t_f} \tag{92}$$

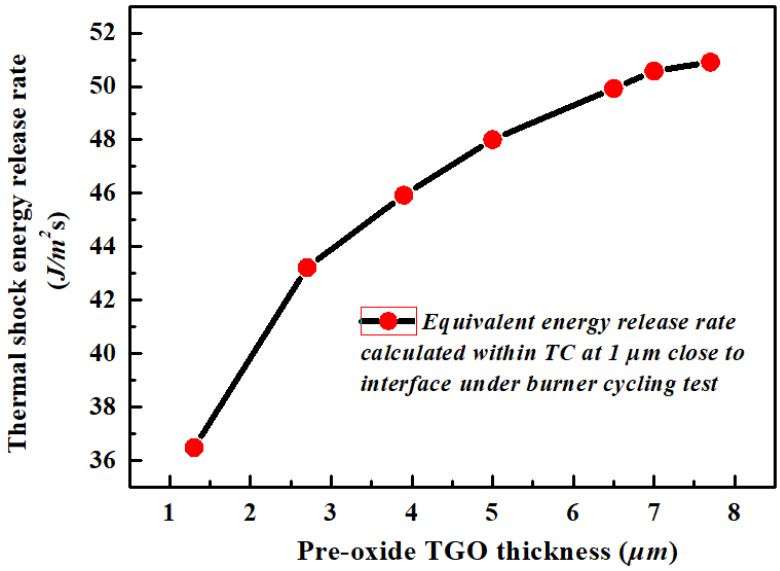

Figure 86 The equivalent thermal shock ERR as function of pre-oxide TGO thickness for burner cycling test

It is evident that the thermal shock ERR increases as a function of pre-oxide thickness. Compared to the effect of thermal gradient (where the ERR might be different as the evaluated depth changes within TC), the effect of thermal shock applies to the entire TBCs. This is reflected by the equivalent area $\hat{A}$ and equivalent moment of inertia $\hat{I}$, which are evaluated throughout the thickness of TC (described in the appendix A.2.3 in supporting documents).

The rapid change of equivalent $\hat{A}$ and $\hat{I}$ at the beginning of thermal cycles and end of high temperature holding time corresponds to the high rate of temperature variation, which in turn leads to the variation of calculated thermal shock $G_{TC}^{TH\_SH}$, Figure 87.

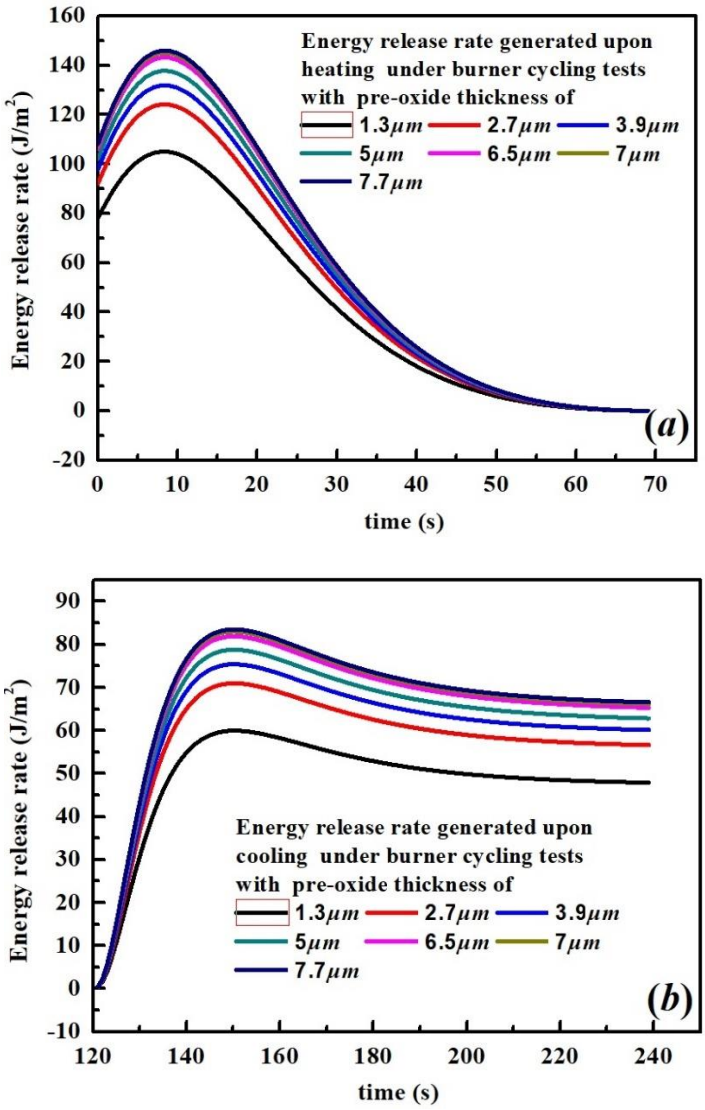

Figure 87 The thermal shock ERR developed upon (a) heating (b) cooling as function of time for different pre-oxide TGO thickness

Like the calculated thermal gradient ERR $G_{TC}^{TEMPVARY}$ upon cooling, instead of showing at the beginning of calculated time, there is a short time interval for ERR $G_{TC}^{TH\_SH}$ to reach its maximum

value whenever heating or cooling starts. The behavior might be explained by the time-delay for the entire TBC to respond to the heating/cooling since the heating source/compressed air is applied to the surface of the TBC. The maximum value is higher for ERR G_{TC}^{TH-SH} developed upon heating but it experiences a rapid drop at a later stage. This is related to the essence of thermal shock. It refers to the process where a component experiences a sudden change in thermal stresses and strains of large magnitude, when the heat flux and component temperature gradient change abruptly [210]. At the later stage of heating/cooling process, the variation of temperature becomes uniform, which makes the thermal shock ERR drop dramatically. The difference between the decrease of thermal shock ERRs for heating and cooling processes can be explained by the variation of elastic modulus, i.e., the drop of elastic modulus upon heating makes the decrease of thermal shock ERR more evident. However, the increase of elastic modulus upon cooling flattens the curves of ERRs at later stages of the cooling process. Considering the calculated ERR described from section 5.4.1 to section 5.4.4, it is evident that most ERR is developed upon cooling, indicating that a higher possibility for crack nucleation occurs upon cooling rather than at other stages of the thermal cycling test.

5.4.5. Calculated equivalent energy release rate as function of calculated depth

The equivalent ERR in section 5.4.1 to section 5.4.4 are calculated 1μm away from the interface between TC/TGO, where the current analytical models allow the estimation of crack driving forces at different depths with respect of pre-oxide thickness. Taking the pre-oxide thickness d_{TGO}^{Pre} as 7.7μm, the equivalent ERRs for different crack driving forces under burner cycling test are shown in Figure 88 as a function of distance away from the interface. The calculated equivalent ERRs, indicated by the spot in Figure 88(a)-(d), are selected at positions close to the interface or surface of the TC, rather than at the middle of the TC layer.

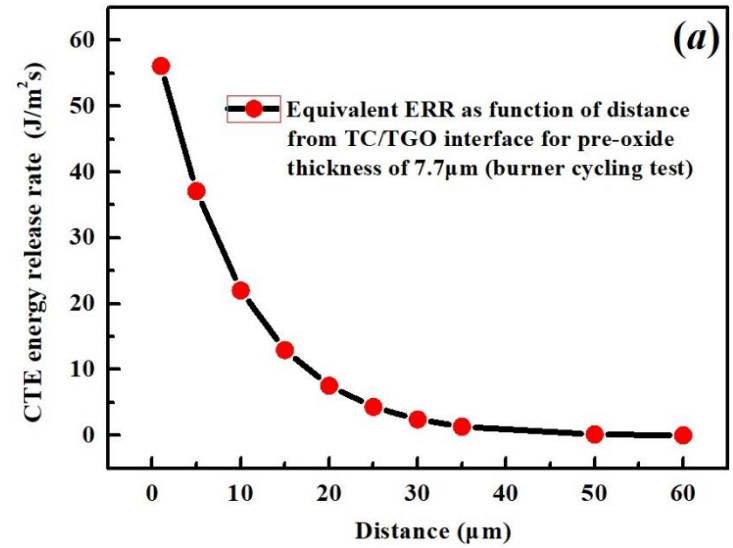
(a)
Equivalent ERR as function of distance from TC/TGO interface for pre-oxide thickness of 7.7µm (burner cycling test)
CTE energy release rate (J/m²s)
Distance (µm)
0
10
20
30
40
50
60

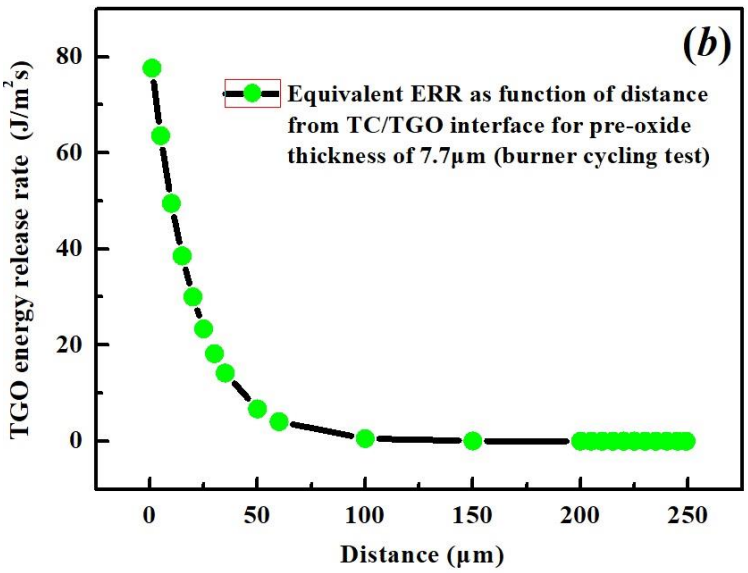
(b)
Equivalent ERR as function of distance from TC/TGO interface for pre-oxide thickness of 7.7µm (burner cycling test)
TGO energy release rate (J/m²s)
Distance (µm)
0
20
40
60
80
0
50
100
150
200
250

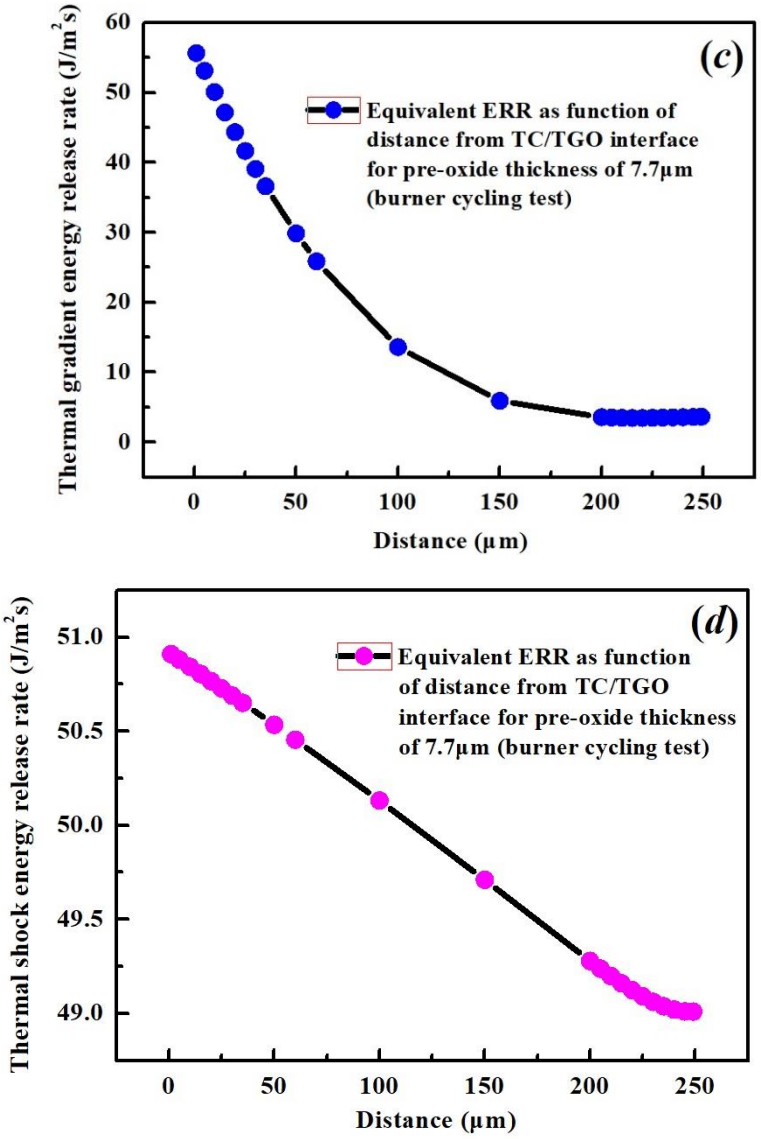

Figure 88 the equivalent ERR as function of calculated distance away from TC/TGO interface under burner cycling test due to (a) CTE misfit (b) TGO growth (c) thermal gradeint (d) thermal shock

It can be seen from Figure 88 that the equivalent ERRs decrease further away from the interface. Nevertheless, there are differences in magnitude among equivalent ERRs. The one most affected by distance is the CTE ERR, Figure 88(a). Regardless of the position of the *x*-coordinate, the calculated out-of-plane CTE stress is approximated to be zero as the distance away from interface reaches 60µm.

This indicates that upon cooling, the region further than 60μm from the interface is in compression, where the CTE ERR is zero. Therefore, the equivalent CTE ERR is calculated only for the distance within 60μm. In comparison, distance does not affect for equivalent ERR generated due to thermal shock, Figure 88(d). This might suggest that the effect of thermal shock is exerted throughout the entire TBC.

Similar to the results from burner cycling test, the results for equivalent ERRs under isothermal furnace cycling tests are shown in Figure 89 as a function of distance.

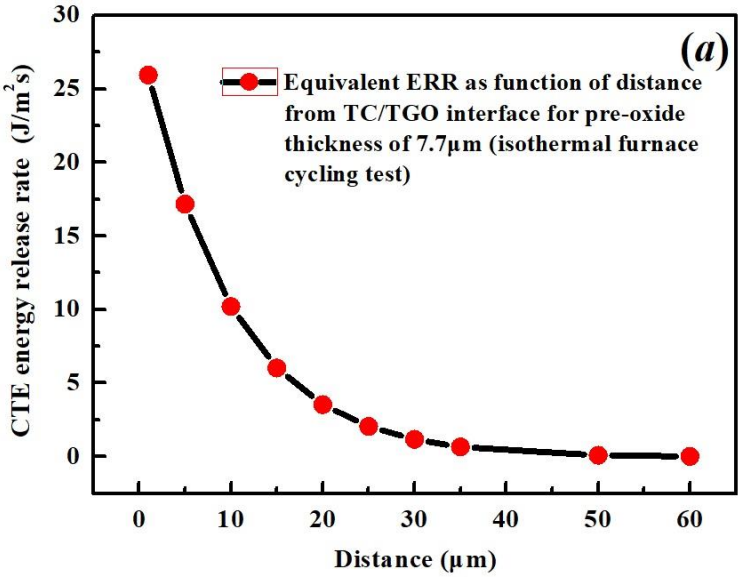

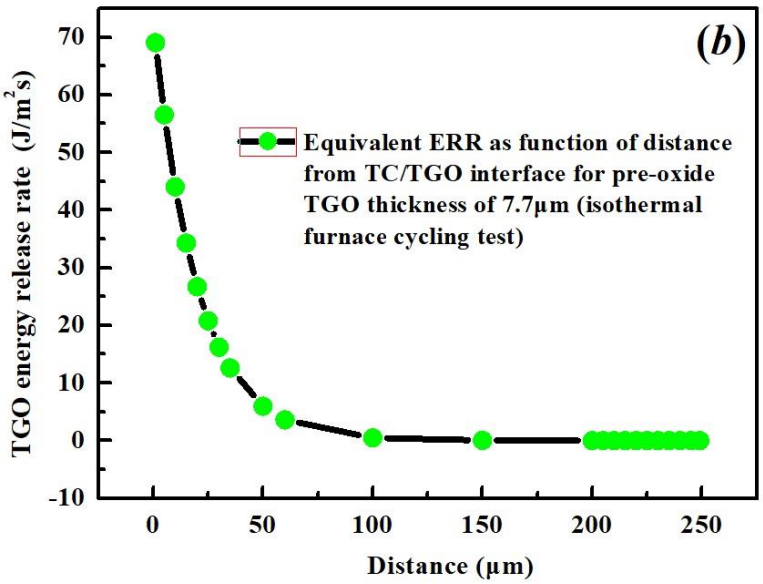

Figure 89 the equivalent ERR as function of calculated distance away from TC/TGO interface under iaothermal furnace cycling test due to (a) CTE misfit (b) TGO growth

Comparing the equivalent CTE and TGO ERR, the magnitudes of ERR obtained from the isothermal test are lower than from the burner test (see section 5.4.1 and section 5.4.2). The difference in equivalent ERRs obtained from two thermal cycling tests also suggests the differences in possible cracking modes, which is different from the conclusion made in [185]. From the burner cycling test results, the thermal gradient and equivalent thermal shock ERR with relative high value close to the surface of TC indicate the possibility for vertical crack propagation perpendicular to the interface and penetrating in the direction of the TC thickness. This results were also suggested in [32], [128].

However, for the isothermal furnace cycling test, all equivalent ERR drop to zero when the position is close to the surface of the TC. This indicates that the maximum ERR is only possible close to the interface, where the nucleation of delamination cracks is found. The cracks propagate along the interface and lead to the spallation of the TC, which marks the failure of APS-TBCs.

5.5. Conclusions

In this paper, crack driving forces for APS-TBCs are quantified via energy release rate (ERR) with respect to the pre-oxide thickness under different thermal cycling conditions (burner cycling test with existence of thermal gradient and isothermal furnace cycling test). The material properties are characterized under two separate thermal treatments, isothermal preheating and further thermal cycling test, where the concept of equivalent time is developed to connect the related parameters between the two different thermal processes. A new method to characterize the shifting of maximum out-of-plane CTE stress is proposed. An analytical approach to describe the effect of interfacial roughness on the ERR is introduced to evaluate the crack driving force due to CTE mismatch between layers. The effect of TGO growth on the crack driving force is considered for both thermal cycling tests. The effects of thermal gradient and thermal shock on the durability of APS-TBCs are estimated based on the burner cycling test. The calculated results of equivalent ERR demonstrate a high pre-oxide thickness dependency, where differences are found for the calculated equivalent ERR due to CTE mismatch and TGO growth in burner cycling and isothermal furnace cycling tests. The effect of "mechanical interlocking" is demonstrated via equivalent CTE ERR as a function of pre-oxide thickness. There exists a time-delay behavior for calculated equivalent ERR generated due to the thermal gradient and thermal shock. The calculated equivalent ERR obtained with respect to distance reveals the possibility of thermal shock playing a critical role for the formation of through-thickness cracks within the TC.

In addition, for the isothermal furnace cycling test, it has been demonstrated that the ERR generated due to TGO growth plays a critical role in determining the durability of APS-TBCs. In real service conditions at elevated temperatures, there exists back-side cooling on TBCs by the application of cooling air or water flowing through the metal substrate where the ERR generated due to TGO growth is limited. The limited TGO growth also makes the position of identified maximum CTE stress independent of thermal cycle. For the burner cycling test that simulates the temperature profile of an engine for short-time take-off/landing (e.g. for subsonic engine service conditions), there exists a large

ERR generated as a consequence of thermal gradient due to temperature differences identified at different positions within the TC. Temperature differences arise from cooling, as well as thermal shock due to the rapid heating/cooling process. These two factors are expected to be the main crack driving forces for short-time thermal cycling service conditions, where the thermal gradient might introduce different crack routes. Real engine service conditions typically feature longer high temperature holding time and a slow heating/cooling process (also back-side cooling), for example the engine serving civil aircraft. Under such conditions, it is expected that the fraction of thermal gradient ERR generated during high temperature holding time increases, while the ERR generated due to thermal shock decreases. Although a relative low temperature will be expected at the BC surface with the existence of a thermal gradient, the relative long holding time makes it possible for slow TGO growth. This might be another crack driving force after long-time service. The corresponding position for maximum CTE stress will shift downwards along the interface gradually as the TGO thickens. Therefore, the cracking mode and failure mechanism for TBCs under real engine service conditions with longer high temperature holding times might be similar to isothermal furnace cycling tests. Still, the magnitude of the crack driving force is expected to be different, since a thermal gradient exists under the thermal cycling conditions for engine serving civil aircraft.

6. The evolution of progressive erosion rates of EB-PVD TBCs under thermal cycling conditions based on a stochastic approach

This chapter addresses objective 3 by evaluating damage generated by erosion of EB-PVD TC through analytical solutions under thermal cycling environments.

The content of this chapter has been submitted for publication.

[a]*B. Zhang*, [b*]*Kuiying Chen*, [a] *N. Baddour*,

[a] *Department of Mechanical Engineering, University of Ottawa, Canada*

[b] *Structures, Materials and Manufacturing Laboratory, Aerospace Research Center, National Research Council Canada*

Abstract

The aim of this paper is to investigate the erosion behavior for electron beam-physical vapor deposition (EB-PVD) thermal barrier coating (TBC) systems under thermal cycling conditions. The erosion rates are estimated based on modified analytical expressions where parameters are fitted to temperature-process dependent experimental data. A stochastic approach is applied as erosion parameters are selected to approximate the erosion occurrence in real engine service conditions. The analytical model is validated by experimental temperature-dependent and sintering-time based erosion rates. A pseudo-ductile erosion manner is identified for the present silica particles EB-PVD topcoat (TC) erosion system above intermediate temperatures (about 220^{o}C) due to the softening of partial molten silica particles, which increase the cutting wear and decrease the experimental deformation wear. The erosion rates are found to decrease as temperature increases but increase as the thermal cycle proceeds. This is explained by propagation of sintering cracks developed at elevated temperatures. The parametric study indicates that both erosion parameters and thermal cycling parameters have a profound effect on the erosion mechanism of EB-PVD TC. Conclusions are made based on two types of erosion mechanisms under different thermal cycling conditions corresponding to two different engine service conditions.

Key words: Erosion, EB-PVD TBCs, temperature-dependent model parameters, stochastic approach, pseudo-ductile erosion manner, sintering crack

6.1. Introduction

Research into the failure mechanisms for electron beam-physical vapor deposition (EB-PVD) thermal barrier coating TBC systems in the hot section of gas turbine engines has been conducted for decades [82], [96], [97], [143], [211]–[214]. Apart from the damage and crack driving forces caused by residual stress generated by bond coat (BC) oxidation and coefficient of thermal expansion mismatch (CTE mismatch) between different layers, the erosion of the coating system is considered a secondary problem described by impact of external particles on the surface of the top coat (TC) during temperature variation or high temperature dwell time [97], [98], [215]–[219]. The superior durability of EB-PVD coatings compared to that of atmospheric plasma sprayed-thermal barrier coating systems (APS-TBCs) is obtained partially due to its feathering-like columnar microstructure [100], [139], [220]–[222]. For erosion resistance specifically, the columnar boundaries have been shown to effectively inhibit cracks propagating parallel to the interface within the TC due to the erosion caused by impact of external particles [216], [217], [217], [223]. However, considering the harsh conditions under which these high temperature protective coatings serve, it is necessary to investigate the mechanism of the erosion process under temperature profiles simulating real service circumstances. Experimental data of erosion rates for EB-PVD TC against different erodent were collected at temperatures ranging from room temperature (RT) up to 910℃ [224], [225]. Several numerical studies were conducted where erosion rates were estimated based on developed computer models [216], [226]–[228]. Nevertheless, there is a lack of studies focusing on evaluating the erosion behavior of EB-PVD TBCs under thermal cycling conditions. Furthermore, related research on the effect of thermal cycling parameters on erosion behavior is rarely found.

In the present study, erosion and erosion rates are estimated as a function of the number of thermal cycles based on a stochastic approach and existing analytical solutions [229]. Model parameters are fitted to experimental data considering the effect of temperature variation and time-dependent sintering behavior. The analytical solutions are modified to incorporate additional factors determining the

resistance of the target material against erosion, where a stochastic approach is introduced with randomly selected erosion parameters to approximate the erosion rates in real service conditions. In addition, a parametric study is conducted to evaluate the effect of erosion parameters, including impact velocity, accumulated impact mass and impact angles and thermal cycling parameters, i.e., the duration of high temperature dwell time on the erosion rates. Two erosion modes are identified at different stages of thermal cycles as a function of the ratio of high temperature dwell time over total cycling time.

6.2. Analytical models for evaluating the erosion rates under different thermal cycling experiments

Experimentally measured erosion rates for TBCs were tabulated in [224] for various impact angles at selected temperatures. For EB-PVD TBCs, the erosion tests were conducted using either spherical alumina particles with a 40 μm diameter at 540^{o}C with an impact velocity of 122 m/s [230], or spherical silica particles with a 60 μm diameter at room temperature (RT) with an impact velocity of 170 m/s and at 910^{o}C with an impact velocity of 300 m/s [225], respectively. It is evident that the measured erosion rates shown in Table 18 from Appendix B.1 demonstrate a temperature-dependent behavior with respect to different test temperatures. That is, the coatings were eroded in a brittle manner under RT and 540^{o}C, as the erosion rate increases with impact angle, where the maximum erosion rate was found at high impact angle (90^{o}). However, the coating was eroded in a pseudo-ductile manner, according to [225], under 910^{o}C whereas the maximum erosion rate was found at a shallow impact angle (30^{o}) with a decrease in erosion rate as the impact angle increased. It should be noticed that a pasty deposit of erodent silica was identified at the surface of the TC for the erosion experiment conducted at glancing angles at elevated temperature [225]. This suggests that during the high temperature erosion process, there exists a softening/partial melting of erodent silica particles while impinging on the heated TC surface. The softened silica erodent is capable of pulling out fracture sections of coatings that otherwise not be removed at a relative shallow angle [216], [224], [225]. This results in pseudo-ductile erosion at

elevated temperatures. In the present study, erosion rates are calculated under thermal cycling conditions, where both brittle and pseudo-ductile erosion are expected during different stages of cycling temperatures.

Neilson et al [229] proposed an analytical model where the total erosion damage is described by a combination of cutting wear and deformation wear. The former is associated with eroding forces parallel to the surface under eroding attack, whereas the latter is associated with the eroding force component normal to the surface. The kinetic energy components of the impacted particles are also considered with respect to directions normal and parallel to the target material surface. Those energies are absorbed in the target material surface and account for either deformation or cutting wear. Neilson et al defined the cutting wear kinetic energy ϕ and deformation wear kinetic energy ε, which are absorbed by the target material surface to release a unit mass of eroded material. The analytical expression of total erosion is given by [229]

$$W_t = \begin{cases} \underset{(A)}{\dfrac{\frac{1}{2}MV^2\cos^2\alpha\sin n\alpha}{\phi}} + \underset{(B)}{\dfrac{\frac{1}{2}M\left(V\sin\alpha - K\right)^2}{\varepsilon}} & \alpha < \alpha_0 \quad (1A) \\ \underset{(C)}{\dfrac{\frac{1}{2}MV^2\cos^2\alpha}{\phi}} + \underset{(B)}{\dfrac{\frac{1}{2}M\left(V\sin\alpha - K\right)^2}{\varepsilon}} & \alpha \geq \alpha_0 \quad (1B) \end{cases} \tag{93}$$

where

$$n = \frac{\pi}{2\alpha_0} \tag{94}$$

Here, *Wt* is the total amount of erosion produced by the accumulated total mass *M* of erodent at the attack angle α with erodent velocity *V*. In equation (93), section B accounts for the deformation wear at large angles and sections A and C accounts for cutting wear at small angles, respectively [229]. The W_t in equation (93) is calculated based on the attack angle α, as it increases from glancing angle to large angle. For small angles of attack, the particles may sweep onto the surface and finally leave again with a residual amount of parallel kinetic energy [229]. As the attack angle α increases, there exists a critical angle called α_0 where the residual parallel component of particle velocity is zero, where equations (1A) and (1B) predict the same erosion ($sin(n\alpha_0)=1$). For hard materials subject to deformation wear, there exists a critical impact velocity *K* below which no erosion takes place.

Applying the experimental measured erosion rate from Table 18 from appendix B.1 to equation (93), the parameters characterizing the erosion behavior including $\alpha_0, n, \varepsilon, \phi$ are calculated and tabulated in Table 19 at a selected temperature, impact velocity as well as the type of erodent. The details are described in appendix B.1. It is noted that with the term "$\sin n\alpha$" (α varies from 0 to α_0) in section A of equation (1A), the calculated erosion from equation (1A) is less than that calculated from equation (1B). In other words, statistically, for a stochastic erosion experiment with random impact angles, the average erosion rate for a target material with large α_0 is less than that with small α_0. According to Table 19, the larger α_0 is calculated at higher temperature, which indicates the total erosion rate is smaller than that calculated at RT. This result is in accordance with those from [231]. Therefore, α_0 is approximated as a quadratic function of temperature by

$$\alpha_0 = 8.31\times10^{-6}T^2 + 0.0082T + 19.47 \qquad (95)$$

Here, *T* is the temperature profile of the thermal cycling condition and is described in section 6.3.1. *n* is evaluated by substituting equation (95) into equation (94).

Unlike the α_0 and *n*, it is evident that the calculated cutting wear kinetic energy ϕ and deformation wear kinetic energy ε depend on more than the variation in temperature, Table 19 from appendix B.1. Hence, for the present study, we consider that the cutting wear kinetic energy ϕ and deformation wear kinetic energy ε are determined by multiple factors. The parameters characterizing the properties of the erodent and target material, and the erosion experimental parameters have a profound effect on the kinetic energies. These parameters are used to re-evaluate the kinetic energies and are described in the following sections.

6.2.1. Parameters affecting deformation wear kinetic energy ε

Sheldon et al [232] studied the plastic deformation of target material under eroding impact. The impact-induced plastic strain is large enough to exceed the ultimate plastic strain and results in rupture at the surface of the target material. Sheldon et al demonstrated that the material removed by the impacting particle flows out around the sides of the cavity by the advancing particle until the displaced material is sufficiently strained to break off [232]. For a spherical particle with a diameter *D* and density ρ_P impacting the target material with velocity *V* normal to the surface, the depth created by impacting erodent that left *q* at the surface of the target material, the removed material amount *W* per gram of impacting particle is proportional to q^3, and is given by [232]

$$W \sim q^3 = \frac{D^3 V^3 \left(\rho_P\right)^{1.5}}{H_V^{1.5}} \tag{96}$$

where H_V is the Vickers hardness of target material.

Considering the erosion generated from a stream of erodent with accumulated mass *M*, the deformation wear W_d can be approximated by the mass lost due to impact-removed material as

$$W_d = \eta \rho_T q^3 \tag{97}$$

where ρ_T is the surface density of the target material, and η is a fitting parameter. Substituting equation (96) into equation (97) and considering the critical impact velocity *K*, the deformation wear W_d can be rewritten as

$$W_d = \eta' \times \rho_T \times \frac{\rho_P \left(\frac{4}{3}\pi R\right)^3 V'^2 V' \sqrt{\rho_P}}{H_V^{1.5}} \tag{98}$$

where $V' = V - K$ and R is the radius of spherical erodent.

To describe the amount of deformation wear with equation (93) and substituting equation (98) in section (B) of equation (93) with $\alpha = 90^o$ and accumulated total mass $M = \rho_P \left(\frac{4}{3}\pi R\right)^3$, the deformation wear kinetic energy ε can be derived as

$$\varepsilon = \eta'' \frac{H_V^{1.5}}{(V-K)\rho_T \sqrt{\rho_P}} \tag{99}$$

where the critical impact velocity *K* is given by [233]

$$K = \frac{\pi^2}{2\sqrt{10}} \frac{\sigma_y^{2.5}}{\sqrt{\rho_P}} \left[\frac{1-\upsilon_P^2}{E_P} + \frac{1-\upsilon_T^2}{E_T} \right]^2 \tag{100}$$

The E_P , υ_P and E_T , υ_T are elastic moduli and Poisson ratios of erodent and target material, respectively. Note that the parameters used to describe the properties of the target material equations (99)-(100) are temperature-process-dependent as the erosion rate is evaluated under thermal cycling conditions. Therefore, it is expected that the deformation wear kinetic energy ε is a function of both temperature and time, as will be demonstrated in section 6.3.

6.2.2. Parameters affecting cutting wear kinetic energy ϕ

As for the approach to evaluate the deformation wear kinetic energy, a similar method is used to evaluate the parameters affecting the cutting wear kinetic energy ϕ. Evans [234] postulated that a lateral fracture initiates within a zone that extends to the elastic-plastic interface at full penetration. The maximum depth of penetration for spherical particles on impact, $Z_{\max}$, is given by [216], [224], [235] and revised as

$$Z_{\max} = \left(\frac{5\pi\rho_P V^2 k}{4H_V} \right)^{\frac{2}{5}} \left(\frac{R^3}{\sqrt{r}} \right)^{\frac{2}{5}} \qquad (101)$$

where *k* is a constant. *r* is defined as the radius of the contact point between erodent and target materials[216].

Considering the erosion generated from a stream of erodent with accumulated mass *M*, the cutting wear W_c can be approximated by the mass lost due to material removed from impact as

$$W_c = \zeta \rho_T Z_{\max}^3 \qquad (102)$$

Here, ζ is a fitting parameter. Substituting equation (101) into equation (102), equation (102) becomes

$$W_c = \xi' \times \frac{\rho_T \times \left(\rho_P \frac{4}{3} \pi R^3 \right) \rho_P^{\frac{1}{5}} V^2 \left(V^2 \right)^{\frac{1}{5}}}{\left(H_V \right)^{\frac{6}{5}}} \times \left(\frac{R}{r} \right)^{\frac{3}{5}} \qquad (103)$$

To describe the amount of cutting wear with equation (93), we substitute equation (103) in section (A) or section (C) of equation (93) with $\alpha = 0^o$ and accumulated total mass $M = \rho_P \left(\frac{4}{3} \pi R \right)^3$. The cutting wear kinetic energy ϕ can then be shown to be given by

$$\phi = \xi'' \times \frac{\left(H_V\right)^{\frac{6}{5}}}{\rho_T \rho_P^{\frac{1}{5}} V^{\frac{2}{5}}} \times \left(\frac{r}{R} \right)^{\frac{3}{5}} \tag{104}$$

In the present study, under the silica erodent with impact velocity V=170m/s and V=300m/s, average diameter 2*R*=60μm, the erosion regime is identified to be Mode I (erosion-lateral cracking/near surface plasticity) by using the erosion maps[216], [217], [224], as indicated by the red point in Figure 90, where the lateral cracks are mostly located at near surface region as a result of small particle erosion [8]. By using the erosion maps, the radius of the contact point between erodent and target materials $r \approx 58.51 \mu m$ for V=300m/s and $r \approx 44.23 \mu m$ for V=170m/s are also obtained, respectively.

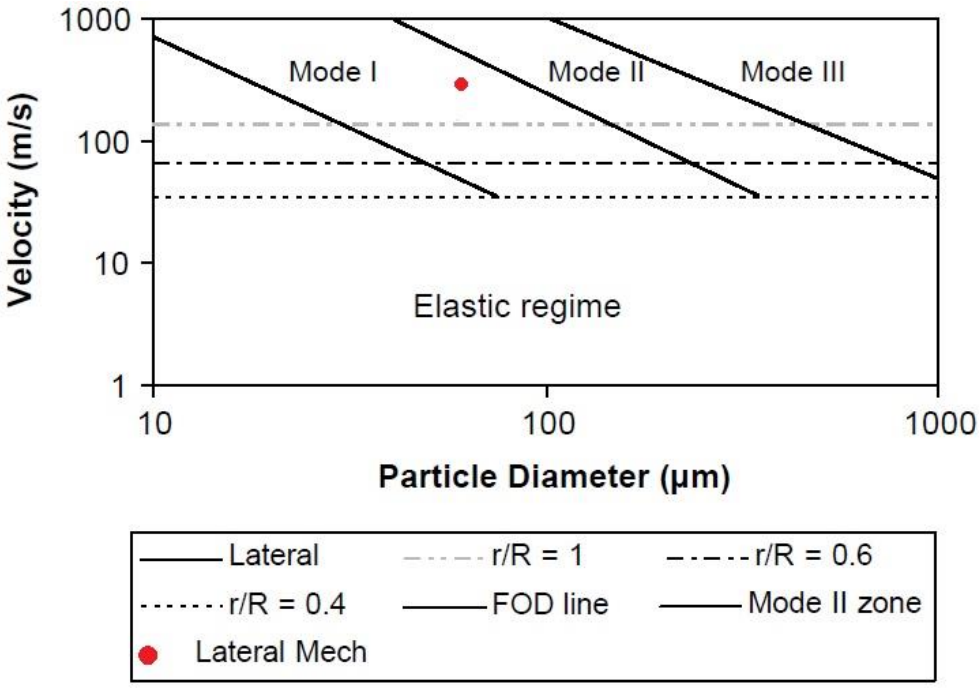

Figure 90 Erosion map for EB PVD TBCs eroded with silica [217] where red spot marks the case for erodent with impact velocity 300m/s and average diameter 60μm

Rewriting equation (99) and equation (104) into equation (105), it should be noted that the term $\left(\frac{H_V^n}{\sqrt{\rho_P}V}\right)^m$ exists for both deformation wear kinetic energy ε and cutting wear kinetic energy ϕ, which indicates that both type of kinetic energies are affected by Vickers hardness, density of target material and velocity of impacting erodent.

$$\varepsilon = \eta'' \times \frac{1}{\rho_T} \frac{H_V^{\frac{3}{2}}}{\sqrt{\rho_P}V'}$$
$$\phi = \xi'' \times \frac{1}{\rho_T} \left(\frac{H_V^3}{\sqrt{\rho_P}V}\right)^{\frac{2}{5}} \times \left(\frac{r}{R}\right)^{\frac{3}{5}} \quad (105)$$

Nevertheless, the discrepancy between the exponent n on the Vickers hardness and overall exponent m suggests a difference in the effect of each parameter on the kinetic energy for cutting wear and deformation wear processes.

6.2.3. Stochastic erosion process for EB-PVD TBCs under thermal cycling conditions

During service operations, the material properties including cutting wear kinetic energy ϕ and deformation wear kinetic energy ε, temperature-dependent n, α_0 differ at each impact event during thermal cycles, which lead to different erosion rates. The erosion rate normally follows a random pattern. Therefore, the erosion rate under thermal cycling conditions is evaluated at a random time (corresponding to a random temperature in the thermal cycle) with random impact angles for the given thermal cycles, where a stochastic approach is applied. It is assumed that there are P randomly selected ($P \in [1, 3600]$) impacts occurring at randomly selected times t_i ($i = 1, 2, 3...P$) within a thermal cycle consisting total 3600s. For each impact at random time t_i, the erosion occurs with a random mass, randomly selected impact angle α_i and constant velocity V, as shown in Figure 91.

$$\underbrace{\begin{bmatrix} i=1 \\ t_i = t_1 = 1s \\ m_i = m_1 \\ \alpha_i = \alpha_1 \end{bmatrix}[\ ]\begin{bmatrix} i=2 \\ t_i = t_2 = 3s \\ m_i = m_2 \\ \alpha_i = \alpha_2 \end{bmatrix}\begin{bmatrix} i=3 \\ t_i = t_3 = 4s \\ m_i = m_3 \\ \alpha_i = \alpha_3 \end{bmatrix}[\ ]\ldots\begin{bmatrix} i=P \\ t_i = t_P = 3599s \\ m_i = m_P \\ \alpha_i = \alpha_P \end{bmatrix}[\ ]}_{3600s\ \ for\ \ a\ \ specific\ \ cycle\ \ number\ \ N}$$

Figure 91 The schematic diagram of stochastic process

where $\left[\ \right]$ indicates no erosion occurs at that time point, $\begin{bmatrix} i \\ t_i \\ m_i \\ \alpha_i \end{bmatrix}$ indicates it is the i^{th} erosion that occurs at time t_i with impact mass m_i and impact angle α_i. It is then assumed that the accumulated impact mass for a thermal cycle is a constant M, where

$$M = \sum_{i=1}^{P} m_i \tag{106}$$

For the total accumulated erosion occurring within a specific number of cycles, the total erosion can be calculated by a sum of cutting wear including the components for $\alpha_i < \alpha_0$ and $\alpha_i \geq \alpha_0$ ($i = 1, 2, 3 \ldots P$), as well as the deformation wear, equation (107).

$$\begin{aligned} W_c &= \begin{cases} \sum_{i=1}^{P_A} \dfrac{\frac{1}{2} m_i V^2 \cos^2 \alpha_i \sin\left[n(T) \alpha_i \right]}{\phi} & for \quad \alpha_i < \alpha_0 \\ \sum_{i=1}^{P_B} \dfrac{\frac{1}{2} m_i V^2 \cos^2 \alpha_i}{\phi} & for \quad \alpha_i \geq \alpha_0 \end{cases} \\ W_d &= \sum_{i=1}^{P} \frac{\frac{1}{2} m_i \left(V \sin \alpha_i - K \right)^2}{\varepsilon} \\ W_t &= W_c + W_d \end{aligned} \tag{107}$$

Here, P_A is the total times of impacts with impact angle $\alpha_i < \alpha_0$ and P_B is the total times of impacts with angle $\alpha_i \geq \alpha_0$ ($P = P_A + P_B$). In addition, the erosion rate W_r (g/Kg) is calculated from

$$W_r = \frac{W_t}{M} \tag{108}$$

The variables that need to be determined stochastically include (a) the total number of impacts P occurring within a specific number of cycles ($P \in [1, 3600]$) (b) the time t_i for erosion occurring at

a specific number of cycles ($i = 1, 2, 3...P$) with (c) the impact mass m_i and (d) impact angle α_i for erosion at each moment in a thermal cycle. The total number of stochastic simulations for erosion rate calculated at a specific number of cycles is assumed to be 10^6. With a large number of "sampling calculations", the final erosion rate is found to follow a normal distribution and is calculated with a mean and standard deviation $\mu \pm 2\sigma$ using a normal distribution, as will be discussed in section 6.4.1.

6.3. Model parameters under thermal cycles

6.3.1. Temperature profile for thermal cycling conditions

In a practical environment for EB-PVD TBCs, the cycling temperature profile is assumed to consist of 10 minutes of increase from room temperature (RT) to 1400°C, 40 minutes high temperature dwell time ($t_{HIGH} = 40$) followed by 10 minutes of temperature drop. The cyclic temperature field pattern used to describe temperature variations within a thermal cycle was chosen as

$$T = \begin{cases} A_{INC} \times \exp\left(-\dfrac{t}{W_{INC}}\right) + T_{INC} & 0 \le t < t_1 \\ 1673.15 & t_1 \le t < t_2 \\ A_{DEC} \times \exp\left(-\dfrac{t - t_2}{W_{DEC}}\right) + T_{DEC} & t_2 \le t < t_3 \end{cases} \quad (109)$$

In equation (109), t_1, t_2 and t_3 represent the time at the end of heating, dwell and cooling processes, respectively. $A_{INC} = -1385.96$, $W_{INC} = 110.11$, $T_{INC} = 1679.11$ and $A_{DEC} = 1405.82$, $W_{DEC} = 150.11$, $T_{DEC} = 267.33$ are fitting parameters for the heating and cooling process. Following

equation (109), the cycling temperature pattern is fitted by temperature profile in [185] and shown in Figure 92 .

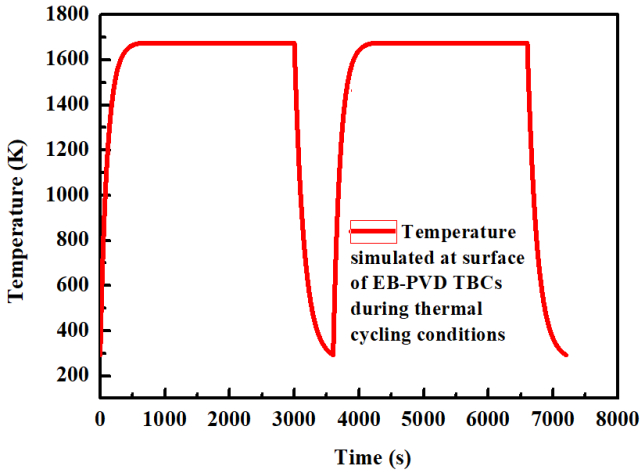

Figure 92 The surface temperature profile of EB-PVD TBCs [185]

The effect of high temperature dwell time on the erosion rate is discussed in section 6.4.2, whereas different erosion rates are calculated based on the variation of the ratio of high temperature dwell time to total thermal cycle time, $Rt = t_{HIGH} / t_{cycle}$.

6.3.2. Material properties of EB-PVD TC under thermal cycling conditions

The goal of the current research is to investigate the erosion rate of EB-PVD TBCs under high temperature thermal cycling conditions. Therefore, the parameters used to evaluate the properties for the target material in equation (105) are considered to be temperature-dependent, whereas the properties of erodent are obtained from the ambient temperature with a relative short contact time during the erosion process. Nevertheless, there exists a variation of material properties of erodent relative to the target material at different temperature ranges, reflected by different erosion behavior observed between the low temperature (brittle erosion) and high temperature (pseudo-ductile erosion). The

correlation of material properties between erodent and target material is described using fitting parameters for cutting and deformation wear kinetic energies and will be demonstrated in section 6.3.3.

The measured data in [224] showed different types of erodent applied to erosion tests at selected temperatures. Silica particles are chosen to be the erodent against EB-PVD TBCs as target material for the current study. The parameters of erodent used in equation (105) are tabulated in Table 6.

Table 6 The parameters of silica erodent at ambient temperatures

Type of erodent	Density (Kg/m^3)	Radius of particle (μm)	Elastic modulus (GPa)	Poisson's ratio
SiO_2	2320	60	65.2[236]	0.17[236]

The mechanical properties of target material in equation (105) include density, Vickers hardness, yield strength and Poisson's ratio used in the analytical expression for critical velocity in equation (23). In addition to the temperature and time-dependent behavior, it is necessary to point out that these mechanical properties vary as a function of orientation for the anisotropic TC of EB-PVD TBCs.

(a) Variation of density of EB-PVD TC under thermal cycling conditions

The variation of total relative density ρ_{rl} as a function of sintering time is given by [139]

$$\rho_{rl} = \rho_i + \rho_e - 1 \tag{110}$$

where ρ_i and ρ_e are relative internal (intra-columnar) and external (inter-columnar) density of YSZ TC. It is assumed that the variation of relative density is only affected by microstructure change, i.e., ρ_{rl} increases due to the sintering effect at elevated temperature as a consequence of pores shrinking during the high temperature dwell period [139]. The density of the TC is given by

$$\rho_T = \rho_{dense} \times \rho_{rl} \tag{111}$$

where $\rho_{dense} = 5650\ kg/m^3$ is the density of full dense YSZ[147]. The variation of total density as a function of cycling time is calculated and illustrated in Figure 93.

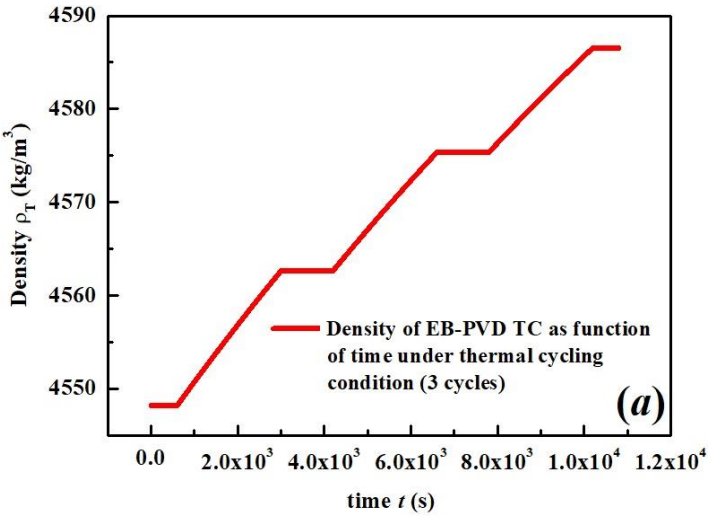

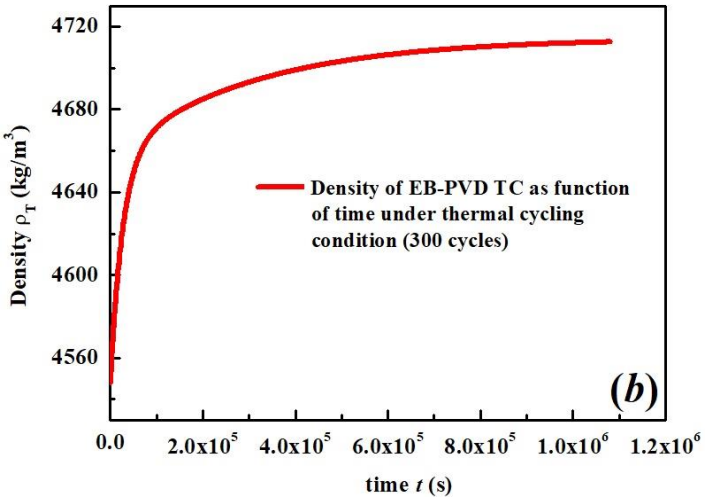

Figure 93 Density of YSZ TC as function of time (a) for first three cycles (b) full 300 cycles

(b) Variation of out-of-plane elastic modulus of EB-PVD TC under thermal cycling conditions

The method used to describe the cycling-dependent out-of-plane elastic modulus of TC was presented in chapter 3.2.1 which won't be demonstrate here.

(c) Variation of anisotropic Vickers hardness of EB-PVD TC under thermal cycling conditions

The Vickers hardness H_V is required in estimating both cutting wear and deformation wear kinetic energies ε, ϕ in equation (105). The Vickers hardness H_V in equation (105) has different values in

the in-plane and out-of-plane directions for the anisotropic TC layer of EB-PVD TBCs. The temperature and time-dependent Vickers hardness H_V is evaluated using analytical models.

Similar to the elastic modulus, the time-dependent Vickers hardness H_V is affected by the sintering of the TC during high temperature exposure time [8], [237]. The inter-columnar cracks disappear from the surface of the TC after TBC exposure at 1400°C [8]. The previous clear columnar structure gap that sintered together during high temperature dwell time leads to an increase in hardness. The H_V was fitted to experimental data in [8] and is given by

$$H_V^{in}(t) = A_{1H}^{sint} \times \exp\left(-\frac{t}{Q_{1H}^{sint}}\right) + A_{2H}^{sint} \times \exp\left(-\frac{t}{Q_{2H}^{sint}}\right) + C_{in\_0} \qquad (112)$$

$$H_V^{out}(t) = B_{1H}^{sint} \times \exp\left(-\frac{t}{W_{1H}^{sint}}\right) + B_{2H}^{sint} \times \exp\left(-\frac{t}{W_{2H}^{sint}}\right) + C_{out\_0} \qquad (113)$$

$H_V^{in}(t)$ and $H_V^{out}(t)$ are time-dependent Vickers hardness, A_{iH}^{sint}, Q_{iH}^{sint} and C_{in_0} are fitting parameters for the in-plane hardness where $B_{iH}^{sint}, W_{iH}^{sint}$ (i = 1, 2) and C_{out_0} are fitting parameters for the out-of-plane hardness, respectively. The values of fitting parameters are tabulated in Table 7. The calculated Vickers hardness as function of high temperature dwell time at 1400°C in illustrated in Figure 94.

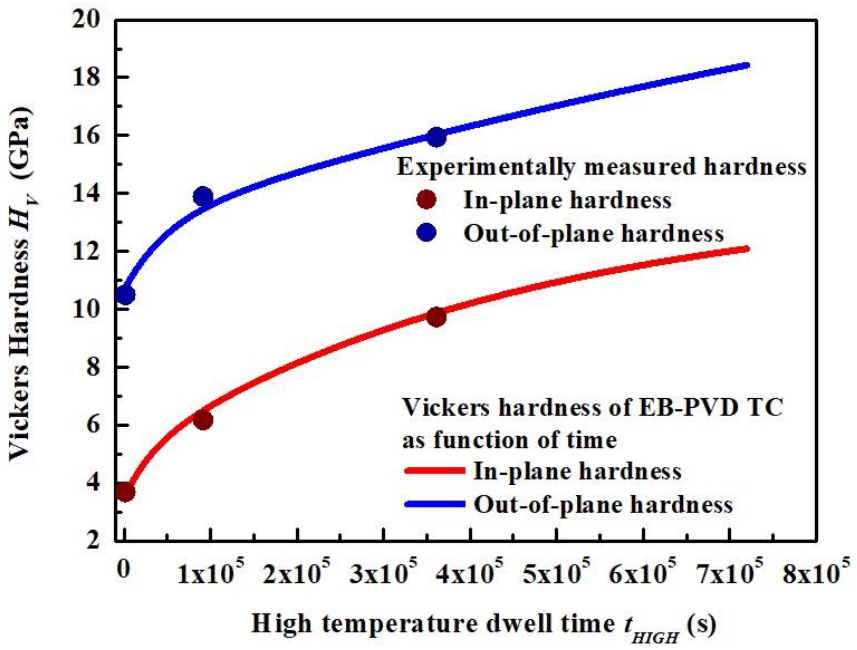

Figure 94 The variation of Vickers hardness during high temperature dwell time at 1400°C due to sintering effect, together with experimental data in [40]

The temperature-dependent cycling Vickers hardness was studied in [238] where the experimentally measured Vickers hardness was obtained through temperature-variant indentation tests for EB-PVD ranging from room temperature up to 800°C. To simulate the changes of Vickers hardness versus temperature T during thermal cycling, experimentally measured moduli in [238] are formulated and then fitted approximately by as

$$H_V^{in}(T) = A_H^T \times \exp\left(-\frac{T-273.15}{Q_H^T}\right) + H_{\text{in\_0}}(t) \tag{114}$$

$$H_V^{out}(T) = B_H^T \times \exp\left(-\frac{T-273.15}{W_H^T}\right) + H_{\text{out\_0}}(t) \tag{115}$$

where $H_V^{in}(T)$ and $H_V^{out}(T)$ are temperature-dependent Vickers hardness, A_H^T, Q_H^T and B_H^T, W_H^T are fitting parameters tabulated in Table 7. $H_{\text{in\_0}}(t)$ and $H_{\text{out\_0}}(t)$ are process-dependent hardness of the TC estimated from isothermal sintering at the end of high-temperature thermal cycles using equation (112) and equation (113), respectively.

Table 7 Fitting parameters used in calculation of Vickers hardness

Fitting parameters	values
A_{iH}^{sint}	-8.99942 (i=1) -1.49089 (i=2)
Q_{iH}^{sint} (K)	126.95095(i=1) 9.01642(i=2)
C_{in_0} (GPa)	13.9525
B_{iH}^{sint}	-14.22029 (i=1) -2.30728 (i=2)
W_{iH}^{sint} (K)	412.31215 (i=1)

	13.62966 (i=2)
C_{out_0} (GPa)	27.1841
A_H^T	0.31257
Q_H^T (K)	332.07745
B_H^T	0.31257
W_H^T (K)	332.07745

The assumptions are made that the hardness follows the same pattern on heating as on cooling, and that the effect of sintering on hardness can be neglected during this heating/cooling process. The temperature-process-dependent Vickers hardness can thus be estimated from equations (112)-(115). The pattern of the out-of-plane elastic moduli versus thermal cycle is shown in Figure 95 for a selected short period. Therefore, the Vickers hardness of the target material under thermal cycling conditions is evaluated by substituting H_V^{in} into the cutting wear kinetic energy ϕ and H_V^{out} into the deformation wear kinetic energy ε, equation (105).

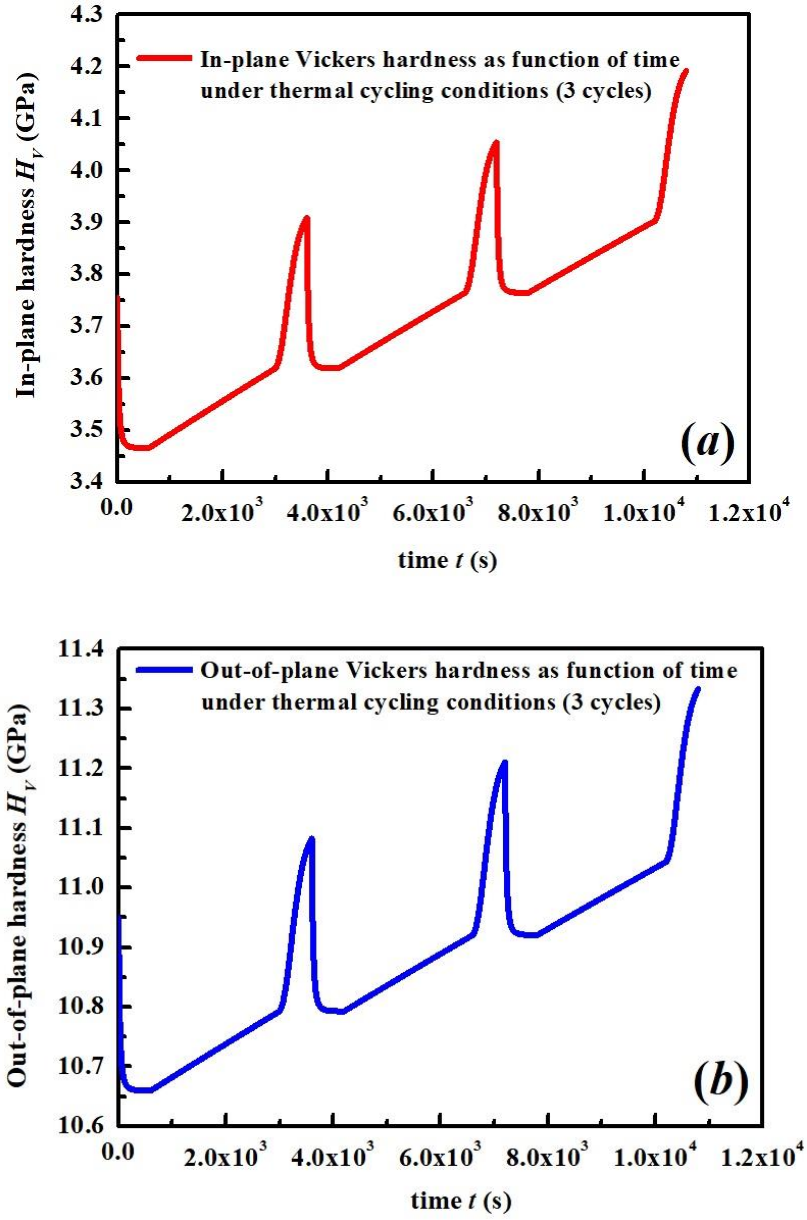

Figure 95 Calculated temperature process-dependent TC hardness for first three cycles (a) in-plane Vickers hardness (b) Out-of-plane Vickers hardness

(d) Variation of yield strength of EB-PVD TC under thermal cycling conditions

The yield strength of the target material plays a significant role in determining the critical velocity for deformation wear in equation (23). The temperature-dependent yield strength of 7YSZ material was used in [239], where the yield strength decreases as temperature raises. The experimentally measured yield strength with a linear fitting is illustrated in Figure 96.

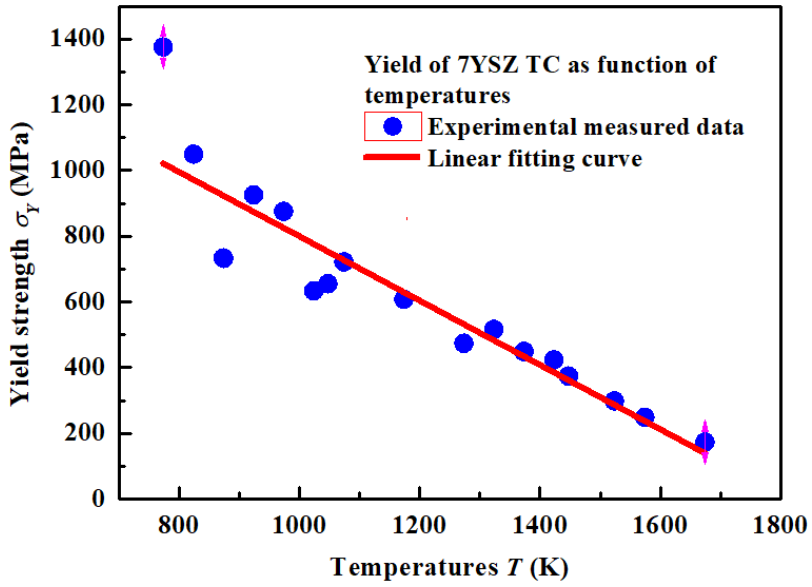

Figure 96 The yield strength of 7-YSZ as a function of temperature [239]

In the present study, the sintering effect during high temperature dwell time leads to a shrinkage of micro pores within the columnar structure, which results in an increase in density and yield strength. Therefore, the temperature-process dependent yield strength of EB-PVD TC is evaluated by equation (116), considering the pore closure as a consequence of the sintering effect at elevated temperatures by

$$\sigma_Y = \frac{\rho_T}{\rho_{dense}} \times \left(k_Y T + \sigma_{Y0} \right) \tag{116}$$

where $k_Y = -1.029 \ 1/K$ and $\sigma_{Y0} = 1865.51 \ Mpa$ are fitting parameters in Figure 96. The density ρ_T is given by equation (111). The calculated cyclic yield strength and yield strength estimated during high temperature dwell time are illustrated in Figure 97 as a function of time,

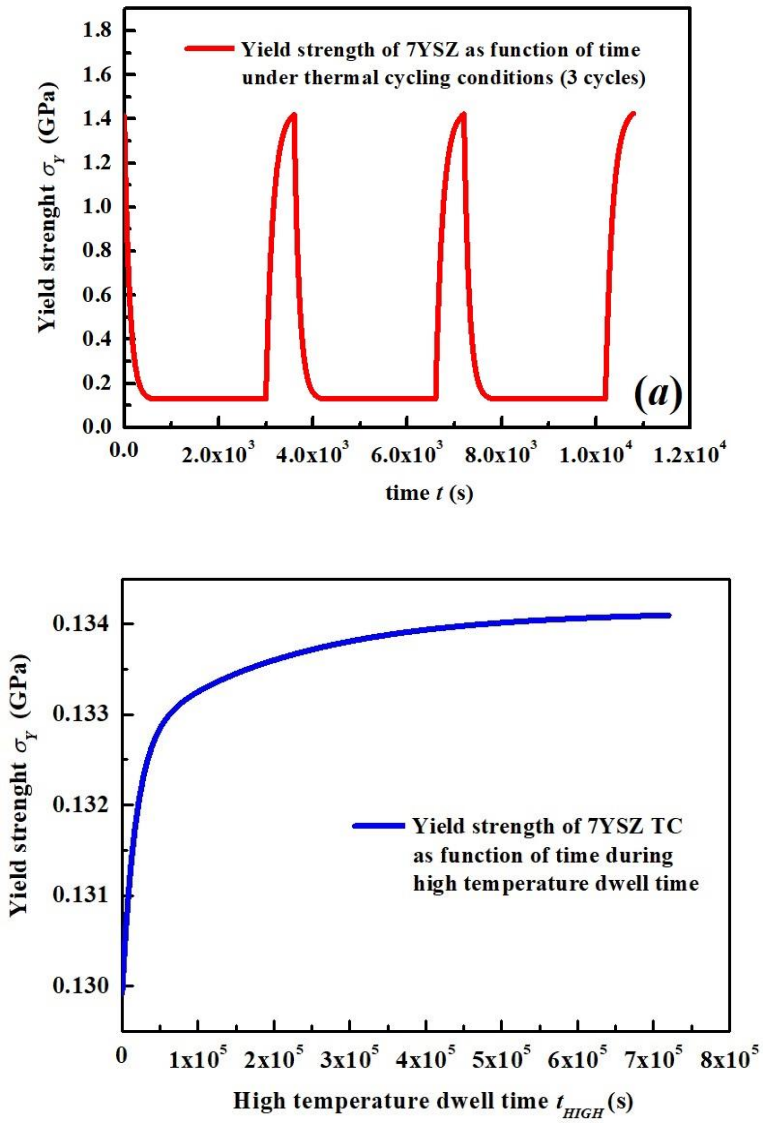

Figure 97 The calculated yield strength of 7 YSZ TC of EB-PVD TBCs as a function of time (a) for three cycles (b) during high temperature dwell time

6.3.3. Characteristics of cutting wear and deformation wear kinetic energy of EB-PVD TC under thermal cycling conditions

With the temperature-process-dependent parameters determined in the preceding sections, it is possible to evaluate the cutting and deformation wear kinetic energies as a function of thermal cycle. The experimental data used is based on erosion rates that were experimentally measured at room temperature (RT), 540℃ and 910℃ [225], [230], and in which the kinetic energies were calculated as described in the supporting document. However, the difference in erosion experimental settings at these temperatures makes it a challenge to evaluate the target material properties against erosion process. That is, the type and size of erodent for erosion experiments conducted at 540℃ are different from that conducted at RT and 910℃, where impact velocities are different at the three temperatures. For the present work, the experimental data measured at RT and 910℃ are selected to eliminate the effect of erodent type and size on target material properties. The kinetic energies for cutting wear ϕ and deformation wear ε are calibrated by calculating energies at RT and 910℃, and fitted by the fitting parameters η'' and ξ'' in equation (105). Meanwhile, the effect of high temperature sintering on the target materials are further evaluated in kinetic energies, where the sintering effect introduces potential inter-columnar cracks and further decreases the erosion resistance of target material.

(a) Fitting temperature-dependent model parameters η'' and ξ''

To minimize the effect of the time-dependent sintering on the cutting wear and deformation wear kinetic energies, the η'' and ξ'' are fitted by model parameters calculated at the first thermal cycles. For the deformation wear kinetic energy ε, the temperature dependent fitting parameter can be obtained by substituting the model parameters calculated at RT and 910℃ for silica erodent into the analytical expression for deformation wear in equation (105). The calculated results are tabulated in Table 8.

Table 8 Calculated fitting parameters η'' , ξ'' based on deformation wear/ cutting wear kinetic energy ε

Temperature (℃)	Impact velocity (m/s)	Deformation wear kinetic energy (m^2/s^2)	Calculated fitting parameters η''	Cutting wear kinetic energy (m^2/s^2)	Calculated fitting parameters ξ''
20	170	7.90×10^5	0.0289	7.90×10^5	1.3452
910	300	1.17×10^6	0.5582	8.33×10^6	1.0508

Based on temperature ranging from RT to 1400℃ during thermal cycling conditions, a linear relationship is assumed between the fitting parameter and temperatures as

$$\eta''(T) = A_\eta \times T(K) + B_\eta \tag{117}$$

where $A_\eta = 0.0005947$ and $B_\eta = -0.1454$. Therefore, the temperature-dependent deformation wear kinetic energy is obtained by substituting equation (117) into equation (105).

Similarly, for the cutting wear kinetic energy ϕ, the temperature dependent fitting parameter can be obtained by substituting the model parameters into equation (105). The calculated results are tabulated in Table 8. Based on temperature ranging from RT to 1400°C during thermal cycling conditions, a linear relationship is assumed between the fitting parameter and temperatures as

$$\xi''(T) = C_\xi \times T(K) + D_\xi \tag{118}$$

where $C_\xi = -0.0003303$ and $D_\xi = 1.442$. Therefore, the temperature-dependent cutting wear kinetic energy is obtained by substituting equation (118) into equation (105).

(b) Evaluation of the sintering effect on cutting wear and deformation wear kinetic energy

Wellman et al [217], [219] revealed that the high temperature sintering effect plays a significant role in determining the erosion rate of EB-PVD TBCs. It was suggested that sintering at the surface of the TC during high temperature dwell time triggers the densification of porous 7YSZ material, which potentially leads to nucleation of sintering cracks. These cracks tend to propagate within feathering-like columns at early stage of TBC lifetime and are stopped by columnar boundaries which act as an inhibitor and potentially decrease the erosion damage by external particles [217], [219]. However, as the high temperature exposure of EB-PVD TBCs proceeds, the vertical gaps and segmentation cracks between the feather columnar structures disappear, whereas the neighboring columns tend to sinter together. This facilitates the nucleation of inter-columnar sintering cracks that propagate parallel to the surface of the TC. The formation of inter-columnar cracks between neighboring columns leads to the increase of erosion rates by impact of external particles for EB-PVD TC[217], [219]. In addition, the excessive

erosion process will lead to a significantly decrease of erosion resistance [218], which facilitates the erosion process of EB-PVD TBCs. Therefore, it is necessary to incorporate the effect of sintering cracks on the kinetic energies in order to evaluate the sintering effect on the time-dependent thermal cycling erosion behavior. This is described mathematically by

$$\begin{aligned} \varepsilon(T,t) &= \varepsilon(T)\times\frac{1}{f(a)} \\ \phi(T,t) &= \phi(T)\times\frac{1}{\mathrm{g}(a)} \end{aligned} \tag{119}$$

where a is the sintering crack length, $\varepsilon(T,t)$ and $\phi(T,t)$ are temperature-process-dependent deformation wear and cutting wear kinetic energy, respectively. The effect of sintering cracks on the decrease of deformation wear kinetic energy and cutting wear kinetic energy is described by $f(a)$ and $\mathrm{g}(a)$, equation (120). The fitting parameters are obtained from experimentally measured erosion rates as a function of sintering time at different elevated temperatures [217] and are tabulated in Table 9. The details of the modelling process are described in appendix B.2 and model calibration is described in appendix B.3.

$$\begin{aligned} f(a) &= A_{crack}\times\exp\left(\frac{a}{\mathrm{Q}_{crack}}\right)+y_{\varepsilon} \\ \mathrm{g}(a) &= B_{crack}\times\exp\left(\frac{a}{\mathrm{W}_{crack}}\right)+y_{\phi} \end{aligned} \tag{120}$$

Table 9 Fitting parameters used in calculation of kinetic energies

Fitting parameters	Values for V=300m/s	Values for V=170m/s

A_{crack}	9.14166×10^{-4}	1.34675×10^{-7}
Q_{crack}	-3.73973	-1.20293
y_{ε}	0.62356	0.70749
B_{crack}	2.76605×10^{-6}	6.64357×10^{-17}
W_{crack}	-1.96022	-0.50085
y_{ϕ}	0.60787	0.69595

Substituting equation (120) into equation (119) gives the temperature-process-dependent cutting wear kinetic energy ϕ and deformation wear kinetic energy ε. The calculated results at impact velocity V=300m/s are demonstrated in Figure 98. Similar calculated results are obtained at impact velocity V=170 m/s but with higher magnitudes of cutting wear and deformation wear kinetic energies since the lower velocity is used in equation (105).

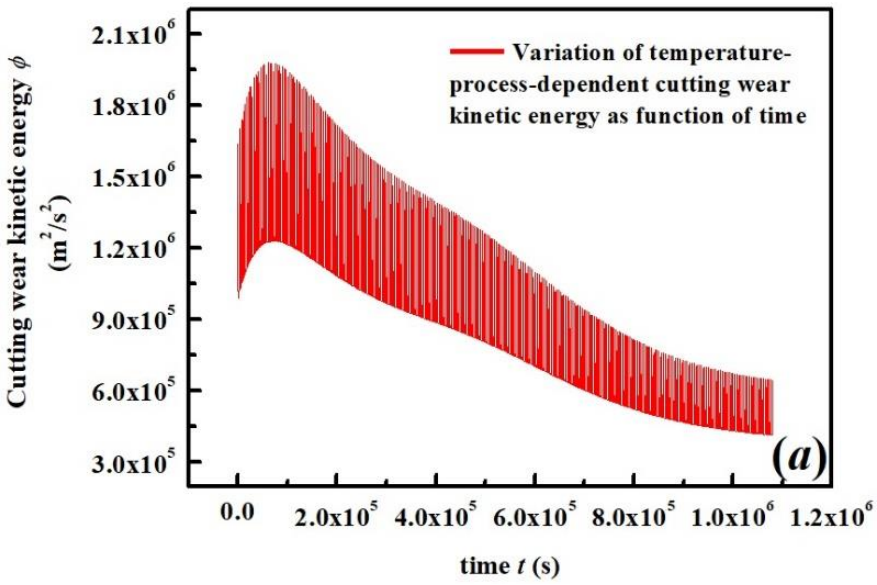
Variation of temperature-process-dependent cutting wear kinetic energy as function of time
Cutting wear kinetic energy ϕ (m^2/s^2)
2.1x10^6
1.8x10^6
1.5x10^6
1.2x10^6
9.0x10^5
6.0x10^5
3.0x10^5
0.0
2.0x10^5
4.0x10^5
6.0x10^5
8.0x10^5
1.0x10^6
1.2x10^6
time t (s)
(a)

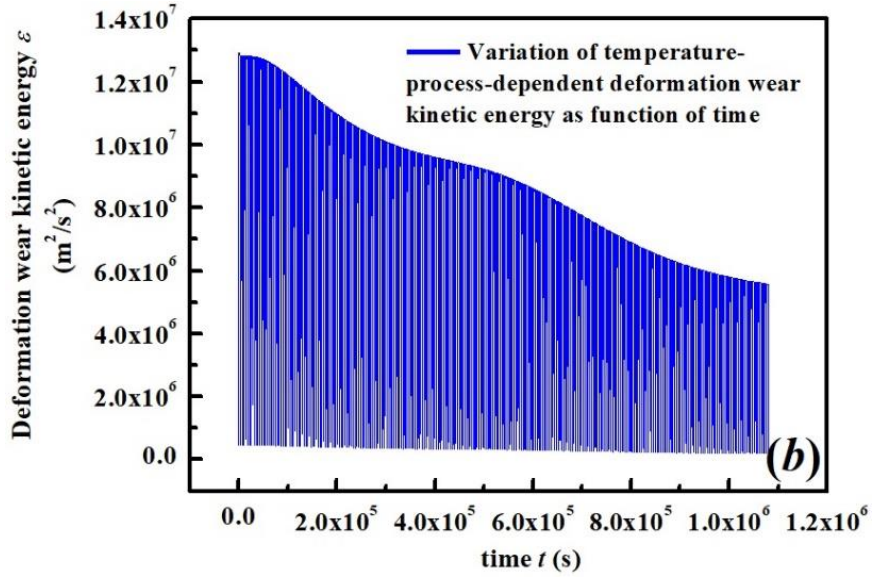
Variation of temperature-process-dependent deformation wear kinetic energy as function of time
Deformation wear kinetic energy ε (m^2/s^2)
1.4x10^7
1.2x10^7
1.0x10^7
8.0x10^6
6.0x10^6
4.0x10^6
2.0x10^6
0.0
2.0x10^5
4.0x10^5
6.0x10^5
8.0x10^5
1.0x10^6
1.2x10^6
time t (s)
(b)

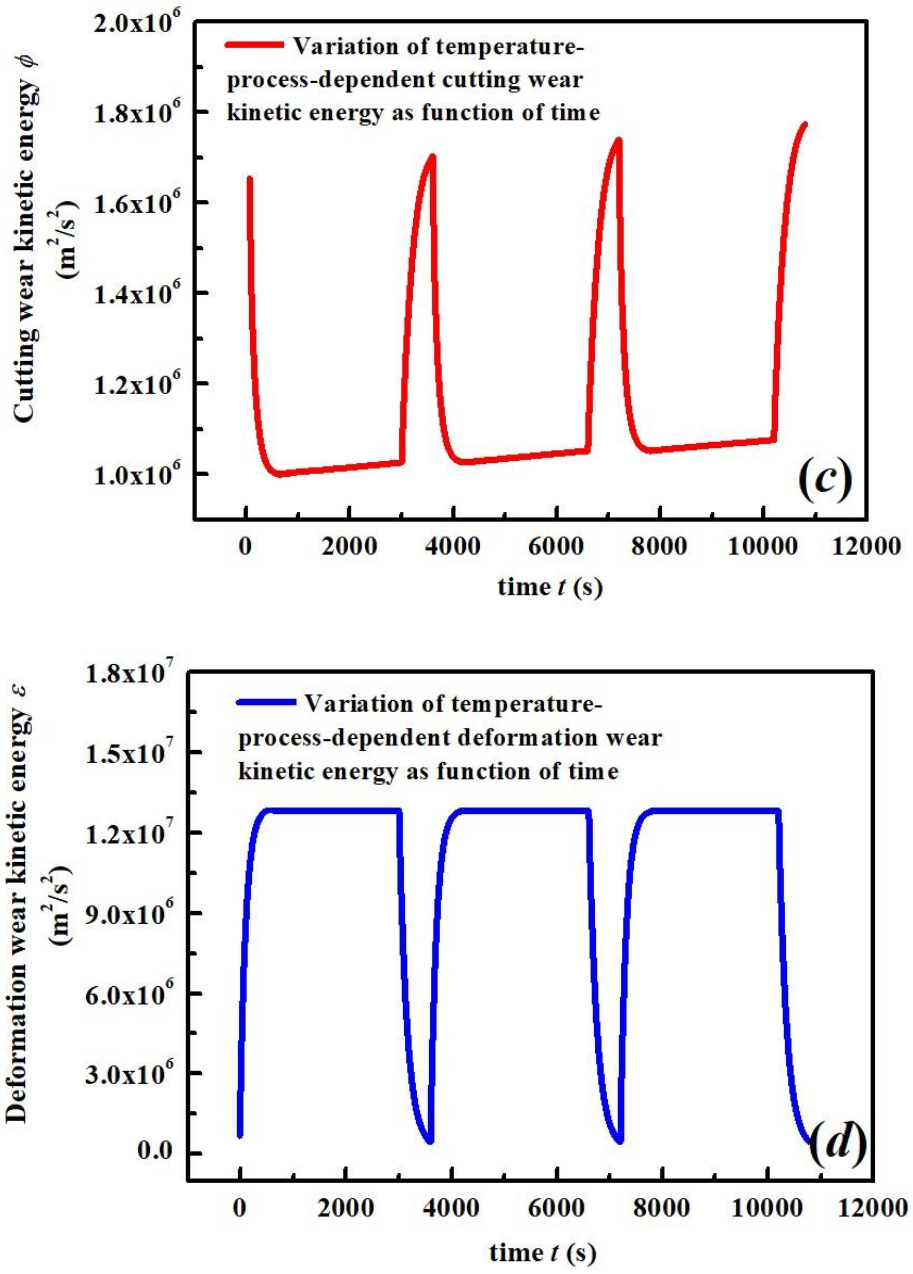

Figure 98 The variation of kinetic energy for V=300m/s as a function of time (a) cutting wear in full cycle (b) deformation wear in full cycle (c) cutting wear with three cycle (d) deformation wear with three cycle

According to Figure 98(a) and (b), both kinetic energies decrease as a function of time, which indicates that more erosion is expected with TBCs under longer sintering time. Meanwhile, the calculated results indicate that deformation wear kinetic energy increases and cutting wear kinetic

energy decreases when temperature increases. Based on the experimental data and past studies, an explanation for the calculated temperature-dependent kinetic energies is given below.

The maximum erosion rates identified at shallow angles at elevated temperatures were described in [216], [224], [225]. A softening/partial melting/pasty of erodent silica particle does more damage at glancing angles according to the erosion data at 910^{o}C tabulated in Table 18. This might suggest an increase in cutting wear, corresponding to a decrease in cutting wear kinetic energy as temperature increases. This softening of erodent could also explain the temperature-dependent deformation wear kinetic energy, which corresponds to a decrease of erosion rate at large impact angles at elevated temperatures. The experimentally measured erosion rates at 90^{o} for EB-PVD TC are tabulated in Table 10 [224].

Table 10 The experimentally measured erosion rates at with impact angle 90^{o} for EB-PVD TC as function of temperatures [224]

Temperature (^{o}C)	Erodent	Impact velocity (m/s)	Erosion rates (g/kg)	Erodent	Impact velocity (m/s)	Erosion rates (g/kg)
RT	40μm alumina particles	/	/	60μm silica particles	170	17.4
540		122	14.7		/	/
705			25.0			

815			25.6			
910		/	/		300	5.4

It is evident that for silica erodent, deformation wear suggested by erosion rate measured at large angles drops dramatically at elevated temperatures, even if a higher impact velocity was applied. Note that the erosion rate of EB-PVD under alumina particles attack increases as temperature increases, which is opposite to that of silica erodent. For the present study, it is considered to treat the erodent and target material as a system, i.e., the cutting/deformation kinetic energy must be evaluated considering the temperature-dependent material properties of both coating system and erodent. For a silica particle - EB-PVD TC erosion system, while a softening/half melting silica particle impacts the surface of EB-PVD TC (silica softens at 500^{o}C [240]) at high temperature at large angles, it is possible that the partial melting silica erodent remains at the surface of target materials, which reduces the actual measured erosion rates. This further leads to a decrease in calculated deformation wear and a corresponding increase in deformation wear kinetic energy as a function of temperature. On the other hand, for alumina particle - EB-PVD TC erosion system, it is possible that erosion rates measured at elevated temperatures reveal the actual deformation wear, considering the alumina particles are more heat-resistant and unlikely to be stuck on the surface of the TC. This explains the increasing erosion rates as temperature increases in Table 10. Nevertheless, it is reasonable to consider that the variation of cutting/deformation wear at elevated temperatures reveals the effect of different thermophysical properties of erodent on erosion rate for the target material, which is revealed by temperature-dependent fitting parameters $\eta''(T)$ and $\xi''(T)$ in evaluating the kinetic energy for the present study.

6.4. Results and discussions

The calculated erosion W_c and erosion rate W_r for thermal cycling conditions are explained in the present section. A parametric study is conducted to study the effect of impact velocity, impact angles and accumulated erodent mass on the erosion rate vs. number of cycles. The effect of ratio Rt of high temperature dwell time over total time of thermal cycle on the erosion rate is also discussed.

6.4.1. Temperature-time dependent erosion rate during thermal cycling based on variation of erosion parameters

Based on the determined temperature-process-dependent model parameters, the current analytical model can predict the erosion and erosion rate of silica particle- EB-PVD TC erosion systems under thermal cycling conditions using a stochastic approach. As described in section 6.2.3, considering the randomly determined a) total number of impacts *P*, (b) time t_i for erosion at a specific number of cycles with (c) impact mass m_i and (d) impact angle α_i for erosion in a thermal cycle as an independent event, the erosion and erosion rates can be estimated by statistical methods based on a massive number of repeated independent experiments. The calculated erosion rate is shown to follow a normal distribution with mean value and standard deviation $\mu \pm 2\sigma$ based on 68-95-99.7 rule. An example is given in Figure 99, where the calculated erosion rates at the 10th cycle are shown with impact velocity 300m/s and 170m/s, respectively.

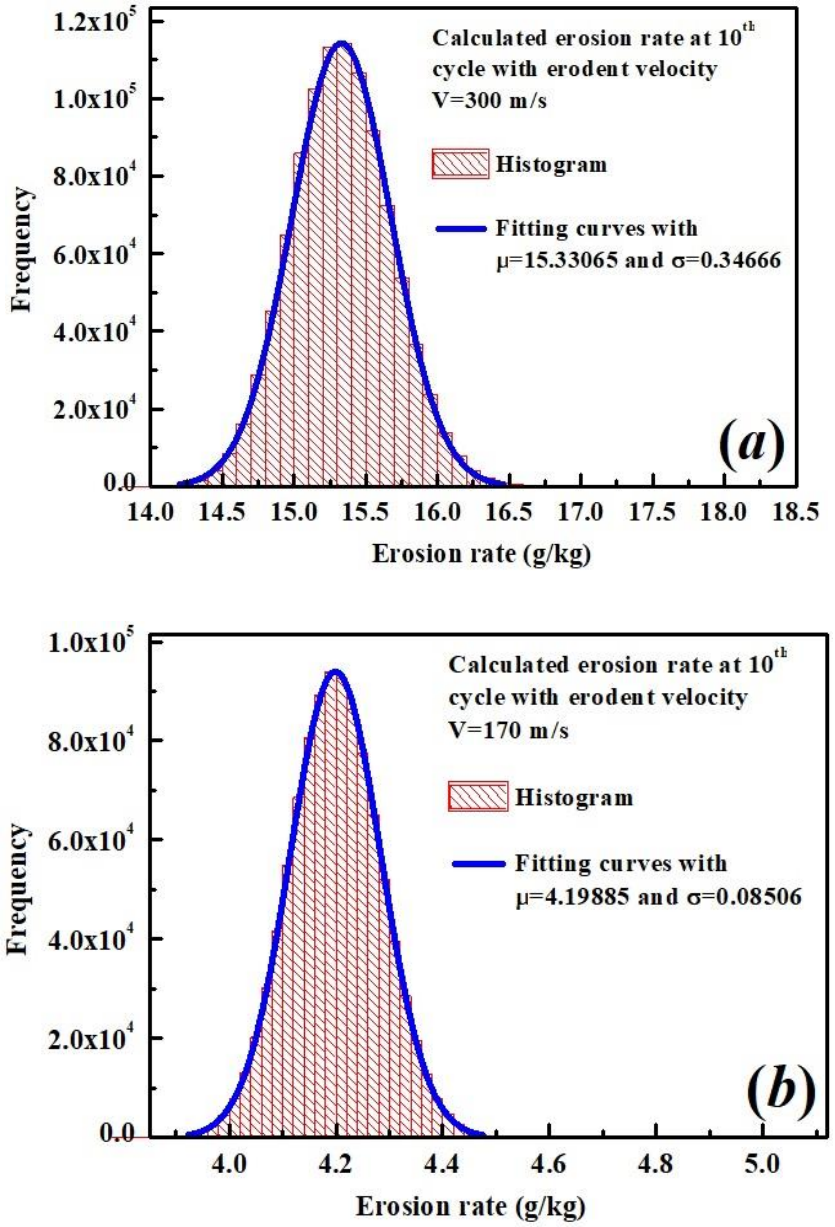

Figure 99 the calculated erosion rate at the 10th cycle with impact velocity (a) V=300m/s (b) V=170m/s

(a) The calculated erosion rate vs. thermal cycles and impact velocity

The effect of impact velocity on erosion rates is evaluated using the parameters in Table 11. The calculated erosion rates are illustrated in Figure 100 as a function of cycles at two different impact velocities.

Table 11 Parameters used to calculate erosion rates for different impact velocities

No# of Cycle	Temperatures (^oC)	Impact angles (^{o})	Impact mass (kg)	Impact velocity (m/s)
Determined cycle number N ranging from [10, 300]	Randomly selected T ranging from [RT, 1400]	Randomly selected α ranging from [5, 90]	Randomly selected m_i ranging from [0, M]	Determined V: 170,300

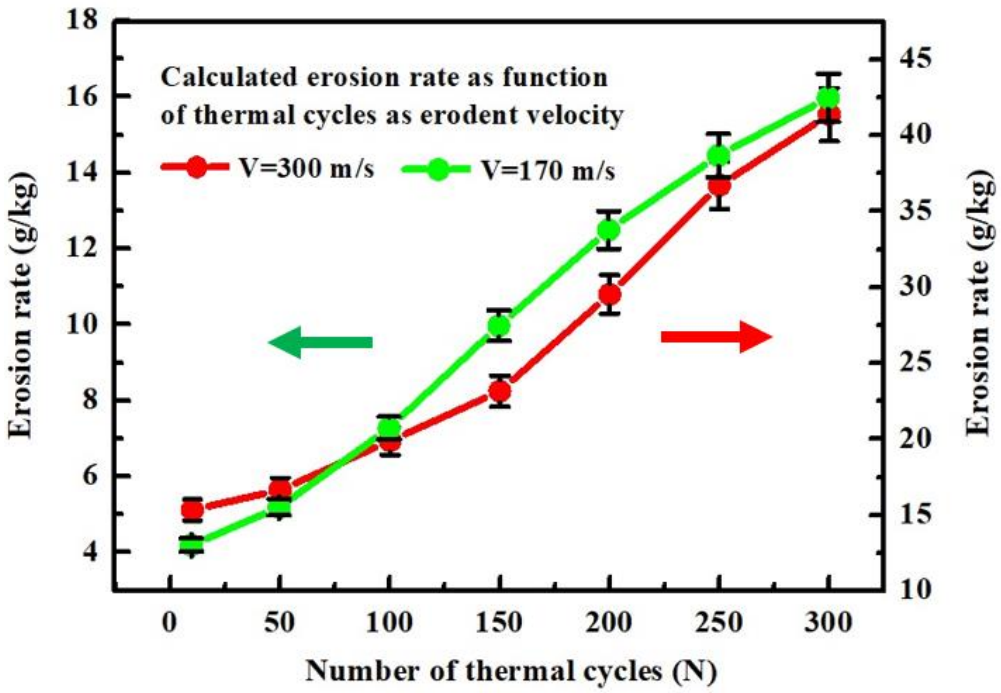

Figure 100 The calculated erosion rate as a function of cycles at impact velocities V=300m/s and V=170m/s

It is evident that both erosion rates increase as a function of cycles, and normally large impact velocity results in heavy erosion. A particle with a larger impact velocity generates a larger kinetic energy (equation (107)) whereas cutting wear/deformation wear kinetic energy decrease as impact velocity increases. In addition, a larger impact velocity might lead to propagation of sintering cracks, which potentially results in the propagation of delamination cracks due to the erosion impact with a thicker coating spalled off the surface of the TC as it undergoes the cutting wear damage from glancing angles.

(b) The calculated erosion rate vs. accumulated erodent mass under thermal cycles

The effect of accumulated mass on erosion is discussed based on parameters tabulated in Table 12. The erosions are calculated as a function of accumulated mass ranging from 1 to 100 grams at various stages of thermal cycles, Figure 101.

Table 12 Parameters used to calculate erosion rates for different impact velocities

No# of Cycle	Temperatures (^oC)	Impact angles (^{o})	Impact mass (g)	Impact velocity (m/s)
Determined cycle number N ranging from [10, 300]	Randomly selected T ranging from [RT, 1400]	Randomly selected α ranging from [5, 90]	Determined accumulated mass M ranging from [10, 1000]	Determined V: 300

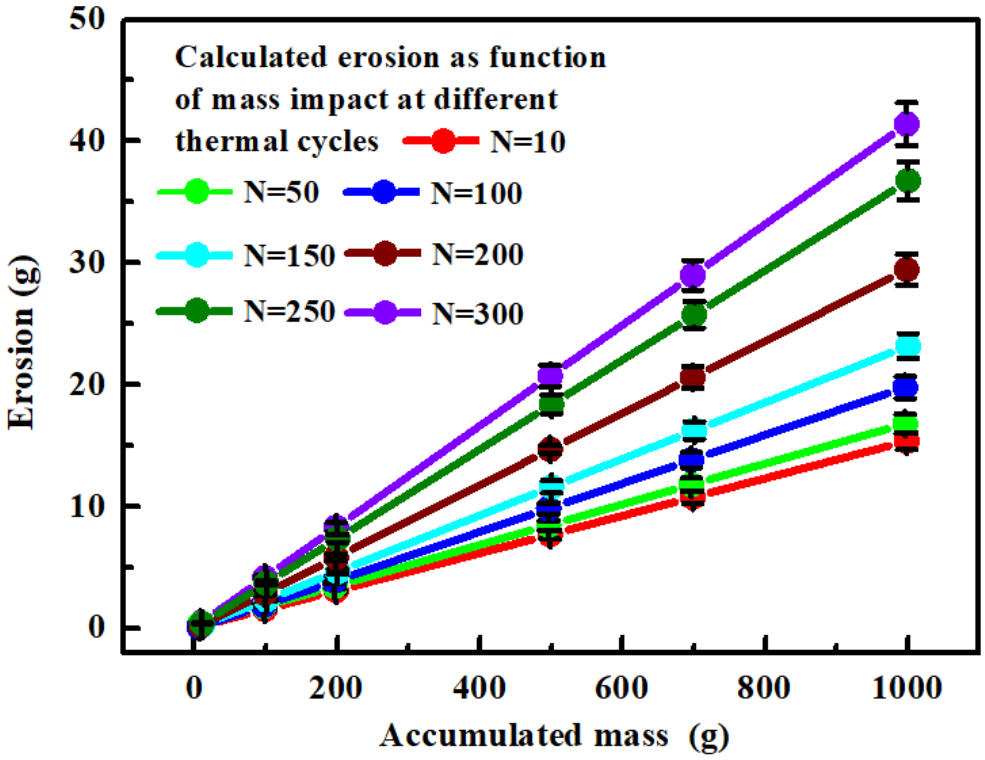

Figure 101 The calculated erosion as a function of accumulated mass at different number of cycles

It is evident that a linear relationship is obtained for erosion as function of accumulated mass, which the erosion rate (slope of curves) is constant for each number of cycles. For erosion calculated at different stages of thermal cycles, it is suggested that the growth of sintering cracks plays a significant role in lowering the magnitude of kinetic energies, Figure 98, which results in higher erosion estimated at later stages of thermal cycles.

(c) The calculated erosion rate vs. impact angles under thermal cycles

The effect of impact angles on erosion is discussed based on parameters used tabulated in Table 13. The erosion rates are calculated as a function of impact angles ranging from 5° to 90° at various stages of thermal cycles, Figure 102.

Table 13 Parameters used to calculate erosion rates for different impact angles

No# of Cycle	Temperatures (^oC)	Impact angles (^{o})	Impact mass (kg)	Impact velocity (m/s)
Determined cycle number N ranging from [10, 300]	Randomly selected T ranging from [RT, 1400]	Determined impact angles α ranging from [5, 90]	Randomly selected m_i ranging from [0, M]	Determined V: 300

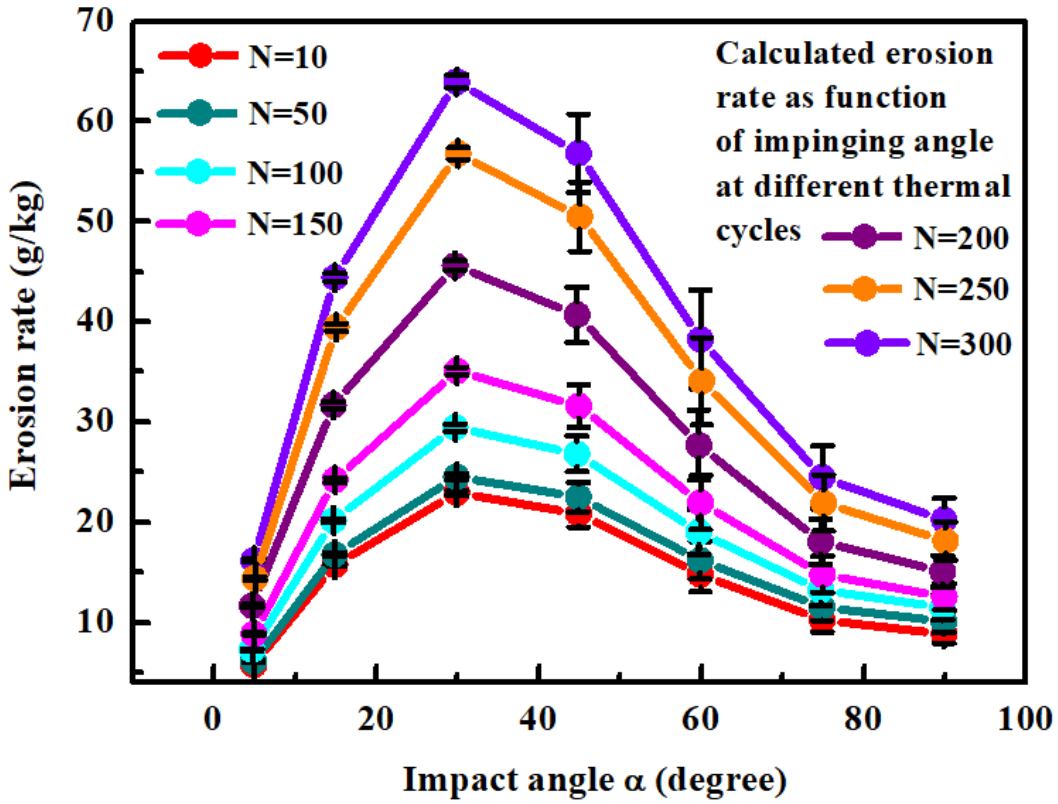

Figure 102 The calculated erosion rate as function of impact angle α for different number of cycles

Because of propagation of sintering cracks on the durability of the TC, the erosion rate calculated at later stages of thermal cycles is higher than that estimated from earlier stages of thermal cycles. This is reflected by the increase of peak erosion rates, estimated at 30° as thermal cycle proceeds. In addition, all the erosion curves estimated as a function of impact angle suggest that erosion for EB-PVD TC under thermal cycling conditions occurs in a pseudo-ductile erosion manner. This is correlated to the erosion behavior under elevated temperatures. In the present work, it is expected that the pseudo-ductile erosion might be estimated for temperatures above 220°C, Figure 130(a) from appendix B.3. Statistically, the probability for erosion occurring during high temperature dwell time equals the ratio of high temperature dwell time over total time of thermal cycle $Rt = \frac{2}{3}$. Therefore, a relatively large probability of erosion occurs at elevated temperatures, making the cyclic erosion pseudo-ductile, where the sintering effect leads to an increase in maximum erosion rate calculated at glancing angles.

6.4.2. Temperature-time dependent erosion rate during thermal cycling experiments based on variation of thermal cycling parameters

Apart from the effect of erosion parameters on erosion (rates), the parameters controlling the thermal cycling conditions might also exert a profound effect on erosion behavior for EB-PVD TC. To date, two different thermal cycling tests were developed for examining the performance of TBCs. The first is an isothermal furnace test, which consists of a slow heating/cooling period with a relatively long high temperature dwell time. This facilitates propagation of sintering cracks at elevated temperatures [96], [97], [241], [242]. The second test is a burner cycling test (burner rig test), which consists of a rapidly heating and cooling periods, with a relatively short high temperature dwell time. This is used to simulate a process of subsonic engine takeoff and shutdown in real service conditions [6], [185], [198], [199]. Irrespective of the effect of rate of temperature change on erosion behavior, it is expected that the ratio of high temperature dwell time over total time of the thermal cycle will have significant effect on erosion behavior of EB-PVD TC. This is evaluated and described in the following sections.

(a) The calculated erosion rate as function of ratio of high temperature dwell time over total cycling time at various stage of thermal cycles

According to the Figure 130 in appendix B.3, the calculated erosion rate decreases as temperature increases due to the overall increase of temperature-dependent kinetic energies. On the other hand, the propagation of sintering cracks during high temperature dwell time facilitates erosion at elevated temperatures, which results in an overall increase of erosion rates at later stages of thermal cycles, Figure 100-Figure 102. It appears that two opposite mechanisms dominate the high temperature erosion

behavior for EB-PVD TC. The results illustrated in Figure 130 only consider the erosion rates estimated during temperature variation at the first cycle, without involving factors such as sintering time-dependent parameters. To investigate the effect of high temperature on the erosion of EB-PVD TC, it is necessary to estimate the erosion rate as function of ratio of high temperature dwell time over total time at different stages of thermal cycles.

The effect of high temperature dwell time on erosion is discussed based on parameters tabulated in Table 14. The erosion rates are calculated as a function of the ratio of high temperature dwell time over total time ranging from 0.2 to 0.67 at various stages of thermal cycles, Figure 103.

Table 14 Parameters used to calculate erosion rates for different high temperature dwell time

No# of Cycle	Temperatures (^oC)	Impact angles (^{o})	Impact mass (kg)	Impact velocity (m/s)	Ratio of $Rt = \frac{t_{HIGH}}{t_{cycle}}$
Determined cycle number N ranging from [10, 300]	Randomly selected T ranging from [RT, 1400]	Randomly selected α ranging from [5, 90]	Randomly selected m_i ranging from [0, M]	Determined V: 300	Determined Rt ranging from [0.2, 0.67]

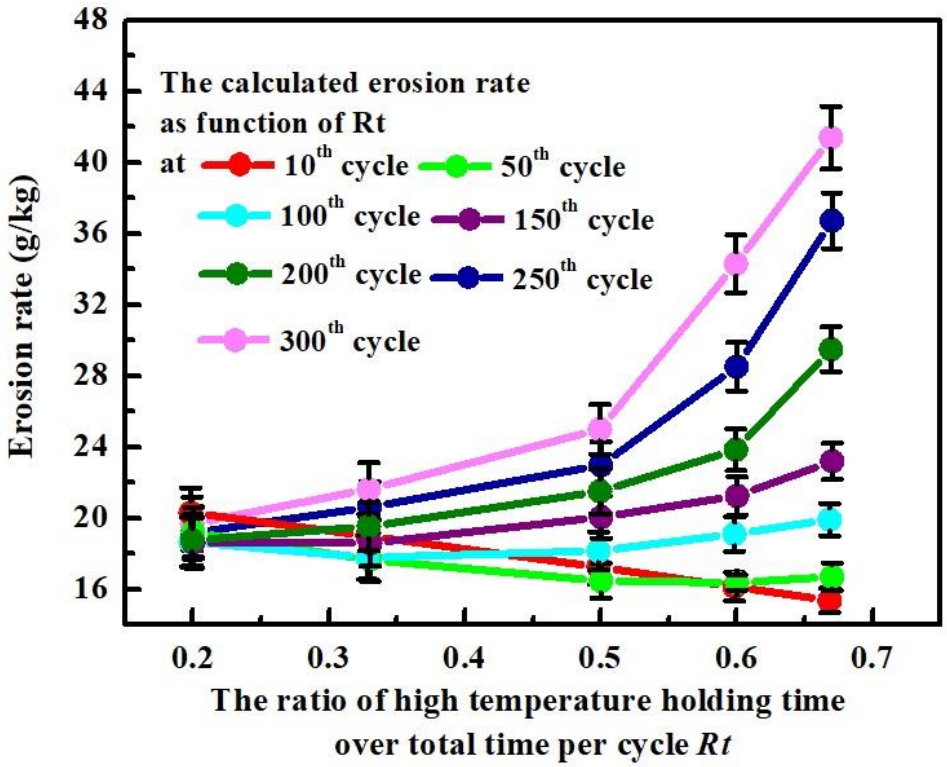

Figure 103 The calculated erosion rate as function of ratio of high temperature dwell time over total time for different number of cycles

Two different erosion modes are identified with respect to different stage of thermal cycles. It is evident that for early stage of thermal cycles, the erosion behavior is dominated by temperatures, i.e., the longer the high temperature dwell time (so the higher the ratio *Rt*), the higher the probability that erosion occurs at elevated temperatures. As the sintering crack is inhibited at early stages of the thermal cycles, the estimated erosion rates follow the results indicated by the red curve in Figure 103, where the overall erosion rates decrease as high temperature dwell time increases. For the later stage of the thermal cycles, the erosion behavior is dominated by the sintering effect of the TC, i.e., sintering of the TC at later stages of thermal cycles results in sintering cracks reorienting at deeper planes away from the surface of the TC, Figure 129 from appendix B.2. This in turn might further lead to a larger amount of fractured TC pulled out under cutting wear at glancing angles, thus leading to an increased erosion rate.

(b) The calculated erosion rate as function of accumulated erodent mass for different ratio of high temperature dwell time over total cycling time

The conclusion made in (a) of section 6.4.2 is further validated by erosion estimated as a function of accumulated mass, with selected ratios of high temperature dwell time over total cycling time at selected stages of thermal cycles, Table 15. The calculated erosions are shown in Figure 104 considering the ratio of high temperature dwell time over total cycling time as 0.2 and 0.67.

Table 15 Parameters used to calculate erosion rates as function of accumulated mass with selected different high temperature dwell time and number of cycles

No# of Cycle	Temperatures (^oC)	Impact angles (^{o})	Impact mass (g)	Impact velocity (m/s)	Ratio of $Rt = \frac{t_{HIGH}}{t_{cycle}}$
Determined cycle number N ranging from [10, 300]	Randomly selected T ranging from [RT, 1400]	Randomly selected α ranging from [5, 90]	Determined accumulated mass M ranging from [10, 1000]	Determined V: 300	Determined Rt ranging from [0.2, 0.67]

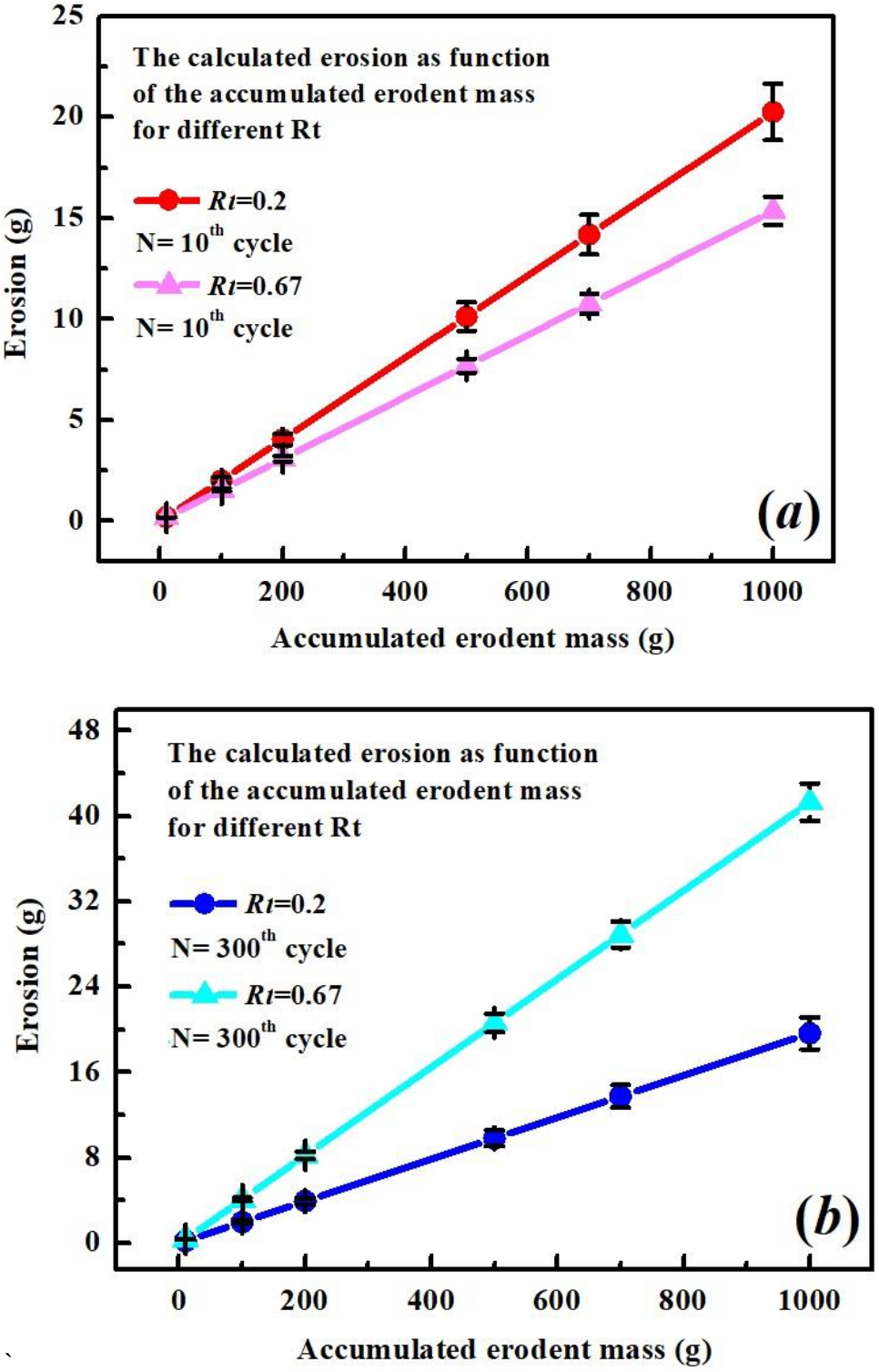

Figure 104 Calculated erosion as function of accumulated mass with various of ratio of high temperature dwell time over total cycling time ratio at different stage of thermal cycles (a) N=10 (b) N=300

According to Figure 104(a), higher erosion is obtained with lower ratio of high temperature dwell time over total cycling time, which indicates temperature-dependent erosion at early stages of the thermal cycles. In Figure 104(b), higher erosion is obtained from a higher ratio *Rt* when the propagation of sintering cracks facilitates further erosion at later stages of the thermal cycles. Note that the discrepancy between the two curves in Figure 104(a) is smaller than that obtained in Figure 104(b). This might suggest that the effect of sintering cracks on the erosion of EB-PVD TC is higher than that dominated by temperature at early stage of thermal cycle.

(c) The calculated erosion rate as function of impact angles for different ratio of high temperature dwell time over total cycling time

The erosion rates are also investigated as a function of impact angles at selected ratio of high temperature dwell time over total cycling time, Table 16. The calculated erosion rates are shown in Figure 105, considering the ratio of high temperature dwell time over total cycling time as to 0.2 and 0.67.

Table 16 Parameters used to calculate erosion rates as function of impact angles with selected different high temperature dwell time and number of cycles

No# of Cycle	Temperatures (^oC)	Impact angles (^{o})	Impact mass (kg)	Impact velocity (m/s)	Ratio of $Rt = \frac{t_{HIGH}}{t_{cycle}}$
Determined cycle number N=10,300	Randomly selected T ranging from [RT, 1400]	Determined impact angles α ranging from [5, 90]	Randomly selected m_i ranging from [0, M]	Determined V: 300	Determined Rt=0.2, 0.67

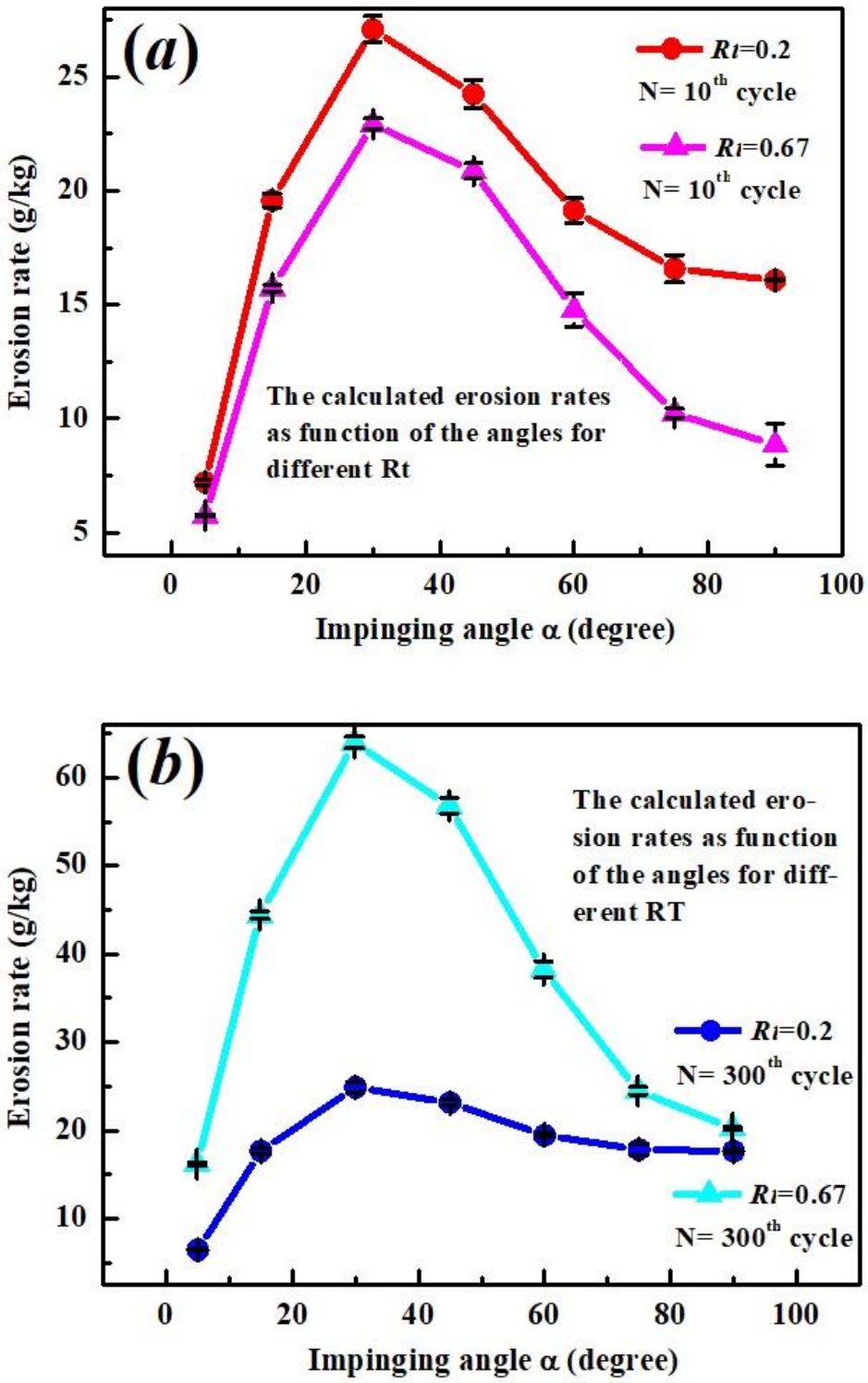

Figure 105 Calculated erosion as function of impact angles with various of ratio of high temperature dwell time over total cycling time ratio at different stage of thermal cycles (a) N=10 (b) N=300

Similar to the conclusion made from Figure 104, the temperature-dependent erosion behavior and sintering effect dominate at early stages and at late stages of thermal cycles, respectively. Pseudo-ductile erosion is found for the erosion curves, where the maximum erosion rates are identified at nearly 30^{o} at either earlier or later time of the thermal cycles.

6.5. Conclusions

A stochastic approach was used to evaluate the erosion behavior of EB-PVD TC under thermal cycling conditions. With experimentally measured erosion rates under different temperatures, the temperature-process dependent model parameters used in analytical expressions were determined. Specifically, the cutting wear and deformation wear kinetic energy were re-evaluated considering material properties of the erodent and target material and by fitting experimentally measured erosion data. For silica particle-EB-PVD TC erosion system, pseudo-ductile erosion was identified for temperatures approximately above 220^{o}C. This is correlated to the increased cutting wear at glancing angles and decrease of deformation wear at high angles due to the softening and partial molten silica particles at elevated temperatures. The erosion and erosion rate obtained by the stochastic approach was found to follow a normal distribution and the calculated results were presented with a mean value and standard deviation $\mu \pm 2\sigma$, based on 68-95-99.7 rule. A parametric study was conducted to reveal the relationship between erosion and the impact velocity, accumulated erosion mass as well as impact angles. Additionally, it was identified that the erosion behavior of EB-PVD TC is dominated by either temperature variations at early stages of thermal cycles or by the sintering effect at later stages of thermal cycles.

The results for the present study should also be considered by combining damage and failure mechanism analysis for EB-PVD TBCs under thermal cycling conditions. For abovementioned two different thermal cycling experiments, the failure mechanism of EB-PVD TBCs under a burner cycling test usually accompany with a sufficient thermal gradient exists throughout the thickness of TC layer with thermal shock developed with a duration of temperature variation. Apart from these "internal factor" of damage mechanism caused by the change of temperature field, extra attention should be focused on erosion damage at early stages of thermal cycles, according to estimated erosion (rates) for small ratio of *Rt*. The temperature-dependent erosion behavior is expected to be maximum at low temperature in a brittle manner. The isothermal furnace test with a long period of high temperature dwell time is used to simulate the engine serving for civil aircraft. Apart from the "internal factors" of failure mechanism of EB-PVD TBCs that involve the coefficient of thermal expansion mismatch as well as TGO growth, there exists a significant sintering effect at the surface of the TC which leads to extensive propagation of sintering cracks at deep planes within the TC layer. This potentially makes erosion occurring at later stages of the thermal cycles produce a large amount of damage at the surface of TC, according to estimated erosion (rates) for large ratio of *Rt*. This facilitates the spallation of the TC and leads to catastrophic failure.

7. Summary and Conclusions

The conclusion of the Ph.D. research work is addressed based on objectives developed at the initial stage of the study. The research objectives were completed and summarized in published journal papers that are described below.

7.1. Development of stress models based on either numerical or analytical method——Research objective 1

Model parameters describing the variation of material properties under different thermal conditions can be used to describe the residual stress generated as a function of time. In this thesis, numerical methods were applied to investigate the stress distribution within TC, TGO and BC layers in EB-PVD TBCs as a consequence of different driving forces, i.e., the residual stress developed upon cooling due to CTE mismatch between layers and TGO stress generated during high temperature holding time due to dilatational strain generated by progressive oxidation of BC where phase transformation occurs from metallic phase to oxidizing phase. The development of residual stress close to the interface is significantly affected by the evolution of either localized/global interfacial roughness where the shifting of positions of maximum stress identified furtherly have a strong influence on cracking behavior/failure mode of EB-PVD TBCs. This was fully described in Chapter 3 and Chapter 4. For APS-TBCs, the stress study was conducted by analytical methods, where the residual stresses were estimated by analytical expressions. The residual stresses were generated considering driving forces including CTE

mismatch between layers, TGO growth, thermal gradient throughout the TC layer and thermal shock due to the rapid duration upon heating and cooling process. Using the resulting stresses, the ERRs were calculated to investigate the effect of different crack driving forces on the durability of APS-TBCs generated under different thermal cycling experiments. This was fully described in Chapter 5.

7.2. Failure mechanism analysis based on qualitative and quantitative evaluation——Research objective 2

The failure mechanism analysis was conducted for both APS and EB-PVD TBCs given that the stress analysis was conducted and described in Chapters 3-5. It is noted that research on failure mechanism analysis had been done for both type of TBCs, yet there was a lack of studies regarding which failure theories are connected to evolution of variables or specific service environments. In this thesis, the failure mechanism was evaluated quantitatively based on APS-TBCs under different thermal environments. The equivalent energy release rates (ERRs) were estimated at specific pre-oxide TGO thickness, and a comparison was made for calculated energy flux obtained under burner cycling tests and isothermal furnace tests. Specifically, the presence of thermal gradient leads to the generation of corresponding ERR where the rapid heating/cooling rate of burner cycling test introduced thermal shock which was considered to be another crack driving force. A thermal cycle containing a relatively slow heating/cooling rate with a long period of high temperature holding time was designed for APS-TBCs under isothermal furnace cycling test. The ERRs generated as consequence of CTE mismatch between layers and TGO growth were estimated. This work was fully described in Chapter 5. The failure

mechanism was evaluated qualitatively based on residual stress analysis for EB-PVD TBCs as a function of evolution of either localized or global interfacial roughness profile. The maximum residual stresses were identified with changes in interfacial roughness in both shape and size as a function of thermal cycles. Combined with failure theories from past studies, possible cracking scenarios at either peaks of the BC or valleys of the TC were described with the evolution of localized interfacial roughness, Chapter 3. The effect of the evolution of global interfacial roughness profile on the failure mechanism of EB-PVD coatings was discussed. The development of a transitional roughness model, where position-dependent maximum residual stress was identified provided an insight into possible cracking positions at post-failure of life cycle. With development of other interfacial roughness models describing interfacial roughness at different stage of thermal cycles, possible cracking routes were elaborated as a function of evolution of global interfacial roughness. This work was fully described in Chapter 4.

7.3. The development of solid particle erosion model based on EB-PVD TBCs——Research objective 3

The goal of the present study was to investigate the amount of erosion/erosion rate for EB-PVD TBCs under real engine service conditions. Factors determining the erosion behavior of the TC layer included the mechanical properties of target material (coatings) and erodent (silica particles in the present work), as well as parameters controlling the thermal environment of the TBCs. Based on past works which focused on temperature-dependent erosion rates and erosion rates affected by aging at different temperatures and time, the amount of erosion/ erosion rates was evaluated for EB-PVD TC impacted

by silica particles under thermal cycling conditions using modified analytical expressions and temperature-process-dependent model parameters. A stochastic approach was applied to simulate the erosion of TBCs under real service conditions, where the total number of impacts, the moment for impacting occurrence, the mass and angle for individual impacting were randomly selected within a thermal cycle. The total erosion was evaluated as a sum of cutting wear damage and deformation wear damage. The model parameters were calibrated by experimental data and the relationship between the amount of erosion/erosion rate and impact velocities, accumulated impact mass, pre-determined impact angles were investigated. In addition, the effect of parameters controlling the thermal cycling on the erosion rates was discussed. This work was described in Chapter 6.

8. Future works

Despite of a comprehensive study presented above, potentially some works could be done to further improve the performance of present analytical/numerical models. On the one hand, for the proposed numerical solutions, the functionality of current model is limited since it fails to integrate the dynamic evolution of interfacial roughness profile into FE simulation, Instead, the residual stresses are estimated by the static roughness profiles characterized from different stages of life cycles, and calculated stresses are used to qualitatively conduct the failure mechanism analysis. It is expected that a roughness-evolution dependent residual stress distribution could be obtained using the "in-situ" interfacial roughness profile as function of thermal cycles. In addition, a non-cracking model is applied for the present FE study where the crack nucleates as energy stored within layers exceeds the critical material toughness. For the future works, by introducing the dynamic cracking behavior (using either damage

model or cohesive zone theory), it is possible to conduct a quantitatively failure mechanism analysis that the energy release rates could be directly obtained from the numerical method based on FE analysis. On the other hand, the crack driving forces estimated from analytical models quantitatively are approximation of energy release rate through pure elastic energy functions. The energy stored from plastic deformation either during high temperature dwell time (creep effect) should be considered as a tremendous crack driving forces for crack nucleation. Simultaneously, the effect of external force generated within substrate layer on internal/residual stress distribution throughout the thickness of TBCs is significant factor determining the durability of TBC/engine components, specifically, the magnitude of centrifugal force reaches its maximum upon rotation of turbine blade in high velocity under high temperature service time. As the calculated results and conclusions from models needs to be validated, it is reasonable to consider the future research work combining with a proper designed experiments simulating the real engine service environments.

References

[1] A. G. Evans, D. R. Mumm, J. W. Hutchinson, G. H. Meier, and F. S. Pettit, "Mechanisms controlling the durability of thermal barrier coatings," *Prog. Mater. Sci.*, vol. 46, no. 5, pp. 505–553, 2001, doi: 10.1016/S0079-6425(00)00020-7.

[2] E. Tzimas, H. Müllejans, S. D. Peteves, J. Bressers, and W. Stamm, "Failure of thermal barrier coating systems under cyclic thermomechanical loading," *Acta Mater.*, vol. 48, no. 18–19, pp. 4699–4707, 2000, doi: 10.1016/S1359-6454(00)00260-3.

[3] S. Guo and Y. Kagawa, "Effect of loading rate and holding time on hardness and Young's modulus of EB-PVD thermal barrier coating," *Surf. Coat. Technol.*, vol. 182, no. 1, pp. 92–100, 2004, doi: 10.1016/S0257-8972(03)00861-2.

[4] U. Schulz, M. Menzebach, C. Leyens, and Y. Q. Yang, "Influence of substrate material on oxidation behavior and cyclic lifetime of EB-PVD TBC systems," *Surf. Coat. Technol.*, vol. 146–147, pp. 117–123, 2001, doi: 10.1016/S0257-8972(01)01481-5.

[5] N. P. Padture, M. Gell, and E. H. Jordan, "Thermal Barrier Coatings for Gas-Turbine Engine Applications," *Science*, vol. 296, no. 5566, pp. 280–284, Apr. 2002, doi: 10.1126/science.1068609.

[6] W. Beele, G. Marijnissen, and A. van Lieshout, "The evolution of thermal barrier coatings — status and upcoming solutions for today's key issues," *Surf. Coat. Technol.*, vol. 120–121, pp. 61–67, 1999, doi: 10.1016/S0257-8972(99)00342-4.

[7] G. Moskal, "The porosity assessment of thermal barrier coatings obtained by APS method," *J. Achiev. Mater. Manuf. Eng.*, vol. 20, no. 1–2, pp. 483–486, Jan. 2007.

[8] S. Guo and Y. Kagawa, "Effect of thermal exposure on hardness and Young's modulus of EB-PVD yttria-partially-stabilized zirconia thermal barrier coatings," *Ceram. Int.*, vol. 32, no. 3, pp. 263–270, 2006, doi: 10.1016/j.ceramint.2005.01.018.

[9] R. A. Miller, "Current status of thermal barrier coatings — An overview," *Surf. Coat. Technol.*, vol. 30, no. 1, pp. 1–11, Jan. 1987, doi: 10.1016/0257-8972(87)90003-X.

[10] R. Vaßen, M. O. Jarligo, T. Steinke, D. E. Mack, and D. Stöver, "Overview on advanced thermal barrier coatings," *Surf. Coat. Technol.*, vol. 205, no. 4, pp. 938–942, Nov. 2010, doi: 10.1016/j.surfcoat.2010.08.151.

[11] S. Bose and J. DeMasi-Marcin, "Thermal barrier coating experience in gas turbine engines at Pratt & Whitney," *J. Therm. Spray Technol.*, vol. 6, no. 1, pp. 99–104, Mar. 1997, doi: 10.1007/BF02646318.

[12] A. Feuerstein, J. Knapp, T. Taylor, A. Ashary, A. Bolcavage, and N. Hitchman, “Technical and Economical Aspects of Current Thermal Barrier Coating Systems for Gas Turbine Engines by Thermal Spray and EBPVD: A Review,” *J. Therm. Spray Technol.*, vol. 17, no. 2, pp. 199–213, Jun. 2008, doi: 10.1007/s11666-007-9148-y.

[13] R. Vassen, A. Stuke, and D. Stöver, “Recent Developments in the Field of Thermal Barrier Coatings,” *J. Therm. Spray Technol.*, vol. 18, no. 2, pp. 181–186, Jun. 2009, doi: 10.1007/s11666-009-9312-7.

[14] P. G. Lashmi, P. V. Ananthapadmanabhan, G. Unnikrishnan, and S. T. Aruna, “Present status and future prospects of plasma sprayed multilayered thermal barrier coating systems,” *J. Eur. Ceram. Soc.*, vol. 40, no. 8, pp. 2731–2745, Jul. 2020, doi: 10.1016/j.jeurceramsoc.2020.03.016.

[15] N. Schlegel, S. Ebert, G. Mauer, and R. Vaßen, “Columnar-Structured Mg-Al-Spinel Thermal Barrier Coatings (TBCs) by Suspension Plasma Spraying (SPS),” *J. Therm. Spray Technol.*, vol. 24, no. 1, pp. 144–151, Jan. 2015, doi: 10.1007/s11666-014-0138-6.

[16] H. Kassner, R. Siegert, D. Hathiramani, R. Vassen, and D. Stoever, “Application of Suspension Plasma Spraying (SPS) for Manufacture of Ceramic Coatings,” *J. Therm. Spray Technol.*, vol. 17, no. 1, pp. 115–123, Mar. 2008, doi: 10.1007/s11666-007-9144-2.

[17] R. S. Lima, B. M. H. Guerreiro, and M. Aghasibeig, “Microstructural Characterization and Room-Temperature Erosion Behavior of As-Deposited SPS, EB-PVD and APS YSZ-Based TBCs,” *J. Therm. Spray Technol.*, vol. 28, no. 1, pp. 223–232, Jan. 2019, doi: 10.1007/s11666-018-0763-6.

[18] N. Curry, Z. Tang, N. Markocsan, and P. Nylén, “Influence of bond coat surface roughness on the structure of axial suspension plasma spray thermal barrier coatings — Thermal and lifetime performance,” *Surf. Coat. Technol.*, vol. 268, pp. 15–23, Apr. 2015, doi: 10.1016/j.surfcoat.2014.08.067.

[19] A. Guignard, G. Mauer, R. Vaßen, and D. Stöver, “Deposition and Characteristics of Submicrometer-Structured Thermal Barrier Coatings by Suspension Plasma Spraying,” *J. Therm. Spray Technol.*, vol. 21, no. 3, pp. 416–424, Jun. 2012, doi: 10.1007/s11666-012-9762-1.

[20] Z. Zou *et al.*, “A comparative study on the performance of suspension plasma sprayed thermal barrier coatings with different bond coat systems,” *Surf. Coat. Technol.*, vol. 275, pp. 276–282, Aug. 2015, doi: 10.1016/j.surfcoat.2015.05.006.

[21] X. Ma and P. Ruggiero, “Practical Aspects of Suspension Plasma Spray for Thermal Barrier Coatings on Potential Gas Turbine Components,” *J. Therm. Spray Technol.*, vol. 27, no. 4, pp. 591–602, Apr. 2018, doi: 10.1007/s11666-018-0700-8.

[22] P. L. Ke, Y. N. Wu, Q. M. Wang, J. Gong, C. Sun, and L. S. Wen, “Study on thermal barrier coatings deposited by detonation gun spraying,” *Surf. Coat. Technol.*, vol. 200, no. 7, pp. 2271–2276, Dec. 2005, doi: 10.1016/j.surfcoat.2004.07.107.

[23] J. H. Kim, M. C. Kim, and C. G. Park, “Evaluation of functionally graded thermal barrier coatings fabricated by detonation gun spray technique,” *Surf. Coat. Technol.*, vol. 168, no. 2, pp. 275–280, May 2003, doi: 10.1016/S0257-8972(03)00011-2.

[24] P. L. Ke, Y. N. Wu, and C. Sun, “9 - Detonation gun sprayed thermal barrier coatings,” in *Thermal Barrier Coatings*, H. Xu and H. Guo, Eds. Woodhead Publishing, 2011, pp. 175–189. doi: 10.1533/9780857090829.2.175.

[25] J. H. Kim, M. C. Kim, and C. G. Park, “Effects of defects on the thermal fatigue behavior of detonation-gun sprayed thermal barrier coatings,” *Met. Mater. Int.*, vol. 7, no. 6, pp. 557–563, Nov. 2001, doi: 10.1007/BF03179254.

[26] P. L. Ke, Q. M. Wang, J. Gong, C. Sun, and Y. C. Zhou, “Progressive damage during thermal shock cycling of D-gun sprayed thermal barrier coatings with hollow spherical ZrO2–8Y2O3,” *Mater. Sci. Eng. A*, vol. 435–436, pp. 228–236, Nov. 2006, doi: 10.1016/j.msea.2006.07.133.

[27] T. A. Dobbins, R. Knight, and M. J. Mayo, “HVOF thermal spray deposited Y2O3-stabilized ZrO2 coatings for thermal barrier applications,” *J. Therm. Spray Technol.*, vol. 12, no. 2, pp. 214–225, Jun. 2003, doi: 10.1361/105996303770348320.

[28] H.-J. Rätzer-Scheibe and U. Schulz, “The effects of heat treatment and gas atmosphere on the thermal conductivity of APS and EB-PVD PYSZ thermal barrier coatings,” *Surf. Coat. Technol.*, vol. 201, no. 18, pp. 7880–7888, Jun. 2007, doi: 10.1016/j.surfcoat.2007.03.028.

[29] B. Bernard *et al.*, “Thermal insulation properties of YSZ coatings: Suspension Plasma Spraying (SPS) versus Electron Beam Physical Vapor Deposition (EB-PVD) and Atmospheric Plasma Spraying (APS),” *Surf. Coat. Technol.*, vol. 318, pp. 122–128, May 2017, doi: 10.1016/j.surfcoat.2016.06.010.

[30] P. Song, D. Naumenko, R. Vassen, L. Singheiser, and W. J. Quadakkers, “Effect of oxygen content in NiCoCrAlY bondcoat on the lifetimes of EB-PVD and APS thermal barrier coatings,” *Surf. Coat. Technol.*, vol. 221, pp. 207–213, Apr. 2013, doi: 10.1016/j.surfcoat.2013.01.054.

[31] G. Yang and C. Y. Zhao, “A Comparative Experimental Study on Radiative Properties of EB-PVD and Air Plasma Sprayed Thermal Barrier Coatings,” *J. Heat Transf.*, vol. 137, no. 9, Sep. 2015, doi: 10.1115/1.4030243.

[32] N. M. Yanar, M. Helminiak, G. H. Meier, and F. S. Pettit, “Comparison of the Failures during Cyclic Oxidation of Yttria-Stabilized (7 to 8 Weight Percent) Zirconia Thermal Barrier Coatings

Fabricated via Electron Beam Physical Vapor Deposition and Air Plasma Spray," *Metall. Mater. Trans. A*, vol. 42, no. 4, pp. 905–921, Nov. 2010, doi: 10.1007/s11661-010-0436-7.

[33] R. Herzog, P. Majerus, J. Mönch, R. W. Steinbrech, F. Schubert, and L. Singheiser, "Study of Crack Development in APS and EB-PVD TBCS with Bending Tests Using Acoustic Emission and In-Situ Visual Observation," in *27th Annual Cocoa Beach Conference on Advanced Ceramics and Composites: A: Ceramic Engineering and Science Proceedings*, John Wiley & Sons, Ltd, 2008, pp. 483–490. doi: 10.1002/9780470294802.ch69.

[34] J. R. Nicholls, M. J. Deakin, and D. S. Rickerby, "A comparison between the erosion behaviour of thermal spray and electron beam physical vapour deposition thermal barrier coatings," *Wear*, vol. 233–235, pp. 352–361, 1999, doi: 10.1016/S0043-1648(99)00214-8.

[35] T. E. Strangman, "Thermal Strain-Tolerant Abradable Thermal Barrier Coatings," *J. Eng. Gas Turbines Power*, vol. 114, no. 2, pp. 264–267, Apr. 1992, doi: 10.1115/1.2906582.

[36] Z. Zou *et al.*, "A highly strain and damage-tolerant thermal barrier coating fabricated by electro-sprayed zirconia hollow spheres," *J. Am. Ceram. Soc.*, vol. 101, no. 9, pp. 4375–4386, Sep. 2018, doi: 10.1111/jace.15697.

[37] K. Wada, Y. Ishiwata, N. Yamaguchi, and H. Matsubara, "Strain Tolerance and Microstructure of Thermal Barrier Coatings Produced by Electron Beam Physical Vapor Deposition Process," *Materials Science Forum*, 2006. /MSF.522-523.267 (accessed Jul. 14, 2020).

[38] B. K. Gupta, G. Farmer, and A. Walker, "Thick thermal barrier coating having grooves for enhanced strain tolerance," US5558922A, Sep. 24, 1996 Accessed: Jul. 14, 2020. [Online]. Available: https://patents.google.com/patent/US5558922A/en

[39] B. Lv, R. Mücke, X. Fan, T. J. Wang, O. Guillon, and R. Vaßen, "Sintering resistance of advanced plasma-sprayed thermal barrier coatings with strain-tolerant microstructures," *J. Eur. Ceram. Soc.*, vol. 38, no. 15, pp. 5092–5100, Dec. 2018, doi: 10.1016/j.jeurceramsoc.2018.07.013.

[40] L.-S. Wang *et al.*, "Gradient stiffening induced interfacial cracking and strain tolerant design in thermal barrier coatings," *Ceram. Int.*, vol. 46, no. 2, pp. 2355–2364, Feb. 2020, doi: 10.1016/j.ceramint.2019.09.226.

[41] M. Schaudinn, G. Witz, and H.-P. Bossmann, "Evolution of Thermal Barrier Coating Strain Tolerance During Engine Operation and its Application to Lifing Models," Jul. 2013, pp. 93–98. doi: 10.1115/GT2012-68123.

[42] M. A. Khan, M. Duraiselvam, S. S. Panwar, T. Jena, and S. R. Dhineshkumar, "Improvement of strain tolerance of functionally graded TBCs through laser surface micro-texturing," *J. Mater. Sci.*, vol. 52, no. 2, pp. 696–708, Jan. 2017, doi: 10.1007/s10853-016-0363-0.

[43] L. T. Wu, R. T. Wu, X. Zhao, and P. Xiao, “Microstructure parameters affecting interfacial adhesion of thermal barrier coatings by the EB-PVD method,” *Mater. Sci. Eng. A*, vol. 594, pp. 193–202, Jan. 2014, doi: 10.1016/j.msea.2013.11.054.

[44] R. Eriksson, S. Sjöström, H. Brodin, S. Johansson, L. Östergren, and X.-H. Li, “TBC bond coat–top coat interface roughness: Influence on fatigue life and modelling aspects,” *Surf. Coat. Technol.*, vol. 236, pp. 230–238, Dec. 2013, doi: 10.1016/j.surfcoat.2013.09.051.

[45] Y. Yamazaki, H. Fukanuma, and N. Ohno, “Effect of Interfacial Roughness of Bond Coat on the Residual Adhesion Strength of a Plasma Sprayed TBC System after Thermal Cycle Fatigue,” *J. Solid Mech. Mater. Eng.*, vol. 4, no. 2, pp. 196–207, 2010, doi: 10.1299/jmmp.4.196.

[46] C. R. C. Lima and J. M. Guilemany, “Adhesion improvements of Thermal Barrier Coatings with HVOF thermally sprayed bond coats,” *Surf. Coat. Technol.*, vol. 201, no. 8, pp. 4694–4701, Jan. 2007, doi: 10.1016/j.surfcoat.2006.10.005.

[47] B. A. Pint, I. G. Wright, W. Y. Lee, Y. Zhang, K. Prüßner, and K. B. Alexander, “Substrate and bond coat compositions: factors affecting alumina scale adhesion,” *Mater. Sci. Eng. A*, vol. 245, no. 2, pp. 201–211, May 1998, doi: 10.1016/S0921-5093(97)00851-4.

[48] D. Monceau, F. Crabos, A. Malié, and B. Pieraggi, “Effects of Bond-Coat Preoxidation and Surface Finish on Isothermal and Cyclic Oxidation, High Temperature Corrosion and Thermal Shock Resistance of TBC Systems,” *Materials Science Forum*, 2001. /MSF.369-372.607 (accessed Jul. 14, 2020).

[49] L. Chirivi and J. R. Nicholls, “Influence of Surface Finish on the Cyclic Oxidation Lifetime of an EB-PVD TBC, Deposited on PtAl and Pt-diffused Bondcoats,” *Oxid. Met.*, vol. 81, no. 1, pp. 17–31, Feb. 2014, doi: 10.1007/s11085-013-9429-4.

[50] J. A. Haynes, M. J. Lance, B. A. Pint, and I. G. Wright, “Characterization of commercial EB-PVD TBC systems with CVD (Ni,Pt)Al bond coatings,” *Surf. Coat. Technol.*, vol. 146–147, pp. 140–146, Sep. 2001, doi: 10.1016/S0257-8972(01)01483-9.

[51] N. M. Yanar, G. Kim, S. Hamano, F. S. Pettit, and G. H. Meier, “Microstructural characterization of the failures of thermal barrier coatings on Ni-base superalloys,” *Mater. High Temp.*, vol. 20, no. 4, pp. 495–506, Jan. 2003, doi: 10.1179/mht.2003.058.

[52] K. Vaidyanathan, E. H. Jordan, and M. Gell, “Surface geometry and strain energy effects in the failure of a (Ni, Pt)Al/EB-PVD thermal barrier coating,” *Acta Mater.*, vol. 52, no. 5, pp. 1107–1115, 2004, doi: 10.1016/j.actamat.2003.10.043.

[53] L. Xie, Y. Sohn, E. H. Jordan, and M. Gell, “The effect of bond coat grit blasting on the durability and thermally grown oxide stress in an electron beam physical vapor deposited thermal barrier

coating," *Surf. Coat. Technol.*, vol. 176, no. 1, pp. 57–66, 2003, doi: 10.1016/S0257-8972(03)00466-3.

[54] N. M. Yanar, F. S. Pettit, and G. H. Meier, "Failure characteristics during cyclic oxidation of yttria stabilized zirconia thermal barrier coatings deposited via electron beam physical vapor deposition on platinum aluminide and on NiCoCrAlY bond coats with processing modifications for improved performances," *Metall. Mater. Trans. A*, vol. 37, no. 5, pp. 1563–1580, May 2006, doi: 10.1007/s11661-006-0100-4.

[55] C. Che, G. Q. Wu, H. Y. Qi, Z. Huang, and X. G. Yang, "Effect of bond coat surface roughness on oxidation behaviour of air plasma sprayed thermal barrier coatings," *Surf. Eng.*, vol. 24, no. 4, pp. 276–279, Jul. 2008, doi: 10.1179/026708408X329470.

[56] J.-Y. Kwon, J.-H. Lee, Y.-G. Jung, and U. Paik, "Effect of bond coat nature and thickness on mechanical characteristic and contact damage of zirconia-based thermal barrier coatings," *Surf. Coat. Technol.*, vol. 201, no. 6, pp. 3483–3490, Dec. 2006, doi: 10.1016/j.surfcoat.2006.07.240.

[57] V. K. Tolpygo and D. R. Clarke, "The effect of oxidation pre-treatment on the cyclic life of EB-PVD thermal barrier coatings with platinum–aluminide bond coats," *Surf. Coat. Technol.*, vol. 200, no. 5–6, pp. 1276–1281, 2005, doi: 10.1016/j.surfcoat.2005.07.088.

[58] K. S. Murphy, K. L. More, and M. J. Lance, "As-deposited mixed zone in thermally grown oxide beneath a thermal barrier coating," *Surf. Coat. Technol.*, vol. 146–147, pp. 152–161, 2001, doi: 10.1016/S0257-8972(01)01371-8.

[59] H. Svensson, J. Angenete, and K. Stiller, "Microstructure of oxide scales on aluminide diffusion coatings after short time oxidation at 1050 °C," *Surf. Coat. Technol.*, vol. 177–178, pp. 152–157, 2004, doi: 10.1016/j.surfcoat.2003.09.002.

[60] S. Laxman, B. Franke, B. W. Kempshall, Y. H. Sohn, L. A. Giannuzzi, and K. S. Murphy, "Phase transformations of thermally grown oxide on (Ni,Pt)Al bondcoat during electron beam physical vapor deposition and subsequent oxidation," *Surf. Coat. Technol.*, vol. 177–178, pp. 121–130, 2004, doi: 10.1016/j.surfcoat.2003.08.072.

[61] Z. Xu, L. He, X. Zhong, R. Mu, S. He, and X. Cao, "Thermal barrier coating of lanthanum–zirconium–cerium composite oxide made by electron beam-physical vapor deposition," *J. Alloys Compd.*, vol. 478, no. 1–2, pp. 168–172, 2009, doi: 10.1016/j.jallcom.2008.11.073.

[62] H. Guo, S. Gong, K. Aik Khor, and H. Xu, "Effect of thermal exposure on the microstructure and properties of EB-PVD gradient thermal barrier coatings," *Surf. Coat. Technol.*, vol. 168, no. 1, pp. 23–29, 2003, doi: 10.1016/S0257-8972(02)00925-8.

[63] M. Martena, D. Botto, P. Fino, S. Sabbadini, M. M. Gola, and C. Badini, "Modelling of TBC system failure: Stress distribution as a function of TGO thickness and thermal expansion

mismatch," *Eng. Fail. Anal.*, vol. 13, no. 3, pp. 409–426, Apr. 2006, doi: 10.1016/j.engfailanal.2004.12.027.

[64] T. Tomimatsu, S. Zhu, and Y. Kagawa, "Effect of thermal exposure on stress distribution in TGO layer of EB-PVD TBC," *Acta Mater.*, vol. 51, no. 8, pp. 2397–2405, May 2003, doi: 10.1016/S1359-6454(03)00046-6.

[65] Y. C. Zhou and T. Hashida, "Coupled effects of temperature gradient and oxidation on thermal stress in thermal barrier coating system," *Int. J. Solids Struct.*, vol. 38, no. 24, pp. 4235–4264, Jun. 2001, doi: 10.1016/S0020-7683(00)00309-7.

[66] R. Kitazawa, H. Kakisawa, and Y. Kagawa, "Anisotropic TGO morphology and stress distribution in EB-PVD Y2O3-ZrO2 thermal barrier coating after in-phase thermo-mechanical test," *Surf. Coat. Technol.*, vol. 238, pp. 68–74, 2014, doi: 10.1016/j.surfcoat.2013.10.041.

[67] M. Ahrens, R. Vaßen, and D. Stöver, "Stress distributions in plasma-sprayed thermal barrier coatings as a function of interface roughness and oxide scale thickness," *Surf. Coat. Technol.*, vol. 161, no. 1, pp. 26–35, 2002, doi: 10.1016/S0257-8972(02)00359-6.

[68] J. Cheng, E. H. Jordan, B. Barber, and M. Gell, "Thermal/residual stress in an electron beam physical vapor deposited thermal barrier coating system," *Acta Mater.*, vol. 46, no. 16, pp. 5839–5850, Oct. 1998, doi: 10.1016/S1359-6454(98)00230-4.

[69] W. R. Chen, X. Wu, B. R. Marple, and P. C. Patnaik, "Oxidation and crack nucleation/growth in an air-plasma-sprayed thermal barrier coating with NiCrAlY bond coat," *Surf. Coat. Technol.*, vol. 197, no. 1, pp. 109–115, 2005, doi: 10.1016/j.surfcoat.2004.06.027.

[70] J. Kimmel, Z. Mutasim, and W. Brentnall, "Effects of Alloy Composition on the Performance of Yttria Stabilized Zirconia–Thermal Barrier Coatings," p. V004T02A014, 1999, doi: 10.1115/99-GT-350.

[71] W. Nowak *et al.*, "Effect of processing parameters on MCrAlY bondcoat roughness and lifetime of APS–TBC systems," *Surf. Coat. Technol.*, vol. 260, pp. 82–89, 2014, doi: 10.1016/j.surfcoat.2014.06.075.

[72] Y. Bai *et al.*, "Isothermal Oxidation Behavior of Supersonic Atmospheric Plasma-Sprayed Thermal Barrier Coating System," *J. Therm. Spray Technol.*, vol. 22, no. 7, pp. 1201–1209, Aug. 2013, doi: 10.1007/s11666-013-9979-7.

[73] M. Tanaka, M. Hasegawa, and Y. Kagawa, "Detection of Micro-Damage Evolution of Air Plasma-Sprayed Y₂O₃-ZrO₂ Thermal Barrier Coating through TGO Stress Measurement," *Mater. Trans.*, vol. 47, no. 10, pp. 2512–2517, 2006, doi: 10.2320/matertrans.47.2512.

[74] D. Liu, M. Seraffon, P. E. J. Flewitt, N. J. Simms, J. R. Nicholls, and D. S. Rickerby, “Effect of substrate curvature on residual stresses and failure modes of an air plasma sprayed thermal barrier coating system,” *J. Eur. Ceram. Soc.*, vol. 33, no. 15–16, pp. 3345–3357, 2013, doi: 10.1016/j.jeurceramsoc.2013.05.018.

[75] P. Song, *Influence of Material and Testing Parameters on the Lifetime of TBC Systems with MCrAlY and NiPtAl Bondcoats*. Forschungszentrum Jülich GmbH Zentralbibliothek Verlag, 2012.

[76] R. Eriksson, H. Brodin, S. Johansson, L. Östergren, and X.-H. Li, “Influence of isothermal and cyclic heat treatments on the adhesion of plasma sprayed thermal barrier coatings,” *Surf. Coat. Technol.*, vol. 205, no. 23–24, pp. 5422–5429, 2011, doi: 10.1016/j.surfcoat.2011.06.007.

[77] A. Fossati, M. D. Ferdinando, A. Lavacchi, A. Scrivani, C. Giolli, and U. Bardi, “Improvement of the Oxidation Resistance of CoNiCrAlY Bond Coats Sprayed by High Velocity Oxygen-Fuel onto Nickel Superalloy Substrate,” *Coatings*, vol. 1, no. 1, pp. 3–16, Nov. 2010, doi: 10.3390/coatings1010003.

[78] Y. Kim *et al.*, “TBC delamination life prediction by stress-based delamination map,” *Int. J. Precis. Eng. Manuf.-Green Technol.*, vol. 4, no. 1, pp. 67–72, Jan. 2017, doi: 10.1007/s40684-017-0009-y.

[79] H. Dong, G.-J. Yang, C.-X. Li, X.-T. Luo, and C.-J. Li, “Effect of TGO Thickness on Thermal Cyclic Lifetime and Failure Mode of Plasma-Sprayed TBCs,” *J. Am. Ceram. Soc.*, vol. 97, no. 4, pp. 1226–1232, 2014, doi: 10.1111/jace.12868.

[80] F. Traeger, M. Ahrens, R. Vaßen, and D. Stöver, “A life time model for ceramic thermal barrier coatings,” *Mater. Sci. Eng. A*, vol. 358, no. 1–2, pp. 255–265, 2003, doi: 10.1016/S0921-5093(03)00300-9.

[81] R. Vaßen, S. Giesen, and D. Stöver, “Lifetime of Plasma-Sprayed Thermal Barrier Coatings: Comparison of Numerical and Experimental Results,” *J. Therm. Spray Technol.*, vol. 18, no. 5–6, p. 835, Sep. 2009, doi: 10.1007/s11666-009-9389-z.

[82] C. Courcier, V. Maurel, L. Rémy, S. Quilici, I. Rouzou, and A. Phelippeau, “Interfacial damage based life model for EB-PVD thermal barrier coating,” *Surf. Coat. Technol.*, vol. 205, no. 13–14, pp. 3763–3773, 2011, doi: 10.1016/j.surfcoat.2011.01.008.

[83] J. L. Smialek, “Compiled furnace cyclic lives of EB-PVD thermal barrier coatings,” *Surf. Coat. Technol.*, vol. 276, pp. 31–38, 2015, doi: 10.1016/j.surfcoat.2015.06.018.

[84] S. M. Meier, D. M. Nissley, K. D. Sheffler, and T. A. Cruse, “Thermal Barrier Coating Life Prediction Model Development,” Jun. 1991, p. V005T13A003-V005T13A003. doi: 10.1115/91-GT-040.

[85] J. T. Demasi and M. Ortiz, “Thermal barrier coating life prediction model development, phase 1,” Dec. 1989, Accessed: Aug. 24, 2016. [Online]. Available: http://ntrs.nasa.gov/search.jsp?R=19900004072

[86] P. Kennard Wright, “Influence of cyclic strain on life of a PVD TBC,” *Mater. Sci. Eng. A*, vol. 245, no. 2, pp. 191–200, May 1998, doi: 10.1016/S0921-5093(97)00850-2.

[87] J. Rösler, M. Bäker, and K. Aufzug, “A parametric study of the stress state of thermal barrier coatings: Part I: creep relaxation,” *Acta Mater.*, vol. 52, no. 16, pp. 4809–4817, Sep. 2004, doi: 10.1016/j.actamat.2004.06.046.

[88] M. Białas, “Finite element analysis of stress distribution in thermal barrier coatings,” *Surf. Coat. Technol.*, vol. 202, no. 24, pp. 6002–6010, Aug. 2008, doi: 10.1016/j.surfcoat.2008.06.178.

[89] N. Nayebpashaee, S. H. Seyedein, M. R. Aboutalebi, H. Sarpoolaky, and S. M. M. Hadavi, “Finite element simulation of residual stress and failure mechanism in plasma sprayed thermal barrier coatings using actual microstructure as the representative volume,” *Surf. Coat. Technol.*, vol. 291, pp. 103–114, Apr. 2016, doi: 10.1016/j.surfcoat.2016.02.028.

[90] J. Rösler, M. Bäker, and M. Volgmann, “Stress state and failure mechanisms of thermal barrier coatings: role of creep in thermally grown oxide,” *Acta Mater.*, vol. 49, no. 18, pp. 3659–3670, Oct. 2001, doi: 10.1016/S1359-6454(01)00283-X.

[91] V. Maurel, E. P. Busso, J. Frachon, J. Besson, and F. N’Guyen, “A methodology to model the complex morphology of rough interfaces,” *Int. J. Solids Struct.*, vol. 51, no. 19, pp. 3293–3302, Oct. 2014, doi: 10.1016/j.ijsolstr.2014.04.015.

[92] M. Wen, E. H. Jordan, and M. Gell, “Effect of temperature on rumpling and thermally grown oxide stress in an EB-PVD thermal barrier coating,” *Surf. Coat. Technol.*, vol. 201, no. 6, pp. 3289–3298, 2006, doi: 10.1016/j.surfcoat.2006.07.212.

[93] D. Liu, C. Rinaldi, and P. E. J. Flewitt, “Effect of substrate curvature on the evolution of microstructure and residual stresses in EBPVD-TBC,” *J. Eur. Ceram. Soc.*, vol. 35, no. 9, pp. 2563–2575, Sep. 2015, doi: 10.1016/j.jeurceramsoc.2015.02.024.

[94] K. Sfar, J. Aktaa, and D. Munz, “Numerical investigation of residual stress fields and crack behavior in TBC systems,” *Mater. Sci. Eng. A*, vol. 333, no. 1, pp. 351–360, Aug. 2002, doi: 10.1016/S0921-5093(01)01859-7.

[95] E. P. Busso, Z. Q. Qian, M. P. Taylor, and H. E. Evans, “The influence of bondcoat and topcoat mechanical properties on stress development in thermal barrier coating systems,” *Acta Mater.*, vol. 57, no. 8, pp. 2349–2361, 2009, doi: 10.1016/j.actamat.2009.01.017.

[96] B. C. Zhang, K. Chen, N. Baddour, and P. C. Patnaik, “Failure and life evaluation of EB-PVD thermal barrier coatings using temperature-process-dependent model parameters,” *Corros. Sci.*, vol. 156, pp. 1–9, Aug. 2019, doi: 10.1016/j.corsci.2019.04.020.

[97] T. Strangman, D. Raybould, A. Jameel, and W. Baker, “Damage mechanisms, life prediction, and development of EB-PVD thermal barrier coatings for turbine airfoils,” *Surf. Coat. Technol.*, vol. 202, no. 4–7, pp. 658–664, 2007, doi: 10.1016/j.surfcoat.2007.06.067.

[98] R. G. Wellman and J. R. Nicholls, “Erosion, corrosion and erosion–corrosion of EB PVD thermal barrier coatings,” *Tribol. Int.*, vol. 41, no. 7, pp. 657–662, Jul. 2008, doi: 10.1016/j.triboint.2007.10.004.

[99] R. Wellman, G. Whitman, and J. R. Nicholls, “CMAS corrosion of EB PVD TBCs: Identifying the minimum level to initiate damage,” *Int. J. Refract. Met. Hard Mater.*, vol. 28, no. 1, pp. 124–132, Jan. 2010, doi: 10.1016/j.ijrmhm.2009.07.005.

[100] J. R. Nicholls, K. J. Lawson, A. Johnstone, and D. S. Rickerby, “Methods to reduce the thermal conductivity of EB-PVD TBCs,” *Surf. Coat. Technol.*, vol. 151–152, pp. 383–391, 2002, doi: 10.1016/S0257-8972(01)01651-6.

[101] R. A. Miller, “Thermal barrier coatings for aircraft engines: history and directions,” *J. Therm. Spray Technol.*, vol. 6, no. 1, p. 35, doi: 10.1007/BF02646310.

[102] P. Morrell and D. S. Rickerby, “Advantages/Disadvantages of Various TBC Systems as perceived by the Engine Manufacturer,” *ResearchGate*, Accessed: Aug. 24, 2016. [Online]. Available: https://www.researchgate.net/publication/268372243_AdvantagesDisadvantages_of_Various_TBC_Systems_as_perceived_by_the_Engine_Manufacturer

[103] C. H. Liebert, R. E. Jacobs, S. Stecura, and C. R. Morse, “Durability of zirconia thermal-barrier ceramic coatings on air-cooled turbine blades in cyclic jet engine operation,” Sep. 1976, Accessed: Aug. 24, 2016. [Online]. Available: http://ntrs.nasa.gov/search.jsp?R=19760025104

[104] S. Alperine, M. Derrien, Y. Jaslier, and R. Mevrel, “Thermal barrier coatings: The thermal conductivity challenge,” *NATO Workshop Therm. Barrier Coat.*, vol. AGARD-R-823, p. paper 1, 1998.

[105] T. E. Strangman and J. Schienle, “Tailoring Zirconia Coatings for Performance in a Marine Gas Turbine Environment,” p. V002T03A010, 1989, doi: 10.1115/89-GT-269.

[106] H. Xu, S. Gong, and L. Deng, “Preparation of thermal barrier coatings for gas turbine blades by EB-PVD,” *Thin Solid Films*, vol. 334, no. 1–2, pp. 98–102, 1998, doi: 10.1016/S0040-6090(98)01124-9.

[107] A. Hesnawi, H. Li, Z. Zhou, S. Gong, and H. Xu, “Isothermal oxidation behaviour of EB-PVD MCrAlY bond coat,” *Vacuum*, vol. 81, no. 8, pp. 947–952, 2007, doi: 10.1016/j.vacuum.2006.03.024.

[108] M. Movchan and Y. Rudoy, “Composition, structure and properties of gradient thermal barrier coatings (TBCs) produced by electron beam physical vapor deposition (EB-PVD).,” *Mater. Des.*, vol. 19, no. 5–6, pp. 253–258, 1998, doi: 10.1016/S0261-3069(98)00020-X.

[109] C. Leyens, B. A. Pint, U. Schulz, and I. G. Wright, “Influence of EB-PVD TBC Microstructure on Thermal Barrier Coating System Performance Under Cyclic Conditions,” Elsevier, ORNL/CP-103223, Apr. 1999. Accessed: Jul. 22, 2020. [Online]. Available: https://www.osti.gov/biblio/9211

[110] H. X. Zhu, N. A. Fleck, A. C. F. Cocks, and A. G. Evans, “Numerical simulations of crack formation from pegs in thermal barrier systems with NiCoCrAlY bond coats,” *Mater. Sci. Eng. A*, vol. 404, no. 1, pp. 26–32, Sep. 2005, doi: 10.1016/j.msea.2005.05.033.

[111] T. Xu, S. Faulhaber, C. Mercer, M. Maloney, and A. Evans, “Observations and analyses of failure mechanisms in thermal barrier systems with two phase bond coats based on NiCoCrAlY,” *Acta Mater.*, vol. 52, no. 6, pp. 1439–1450, Apr. 2004, doi: 10.1016/j.actamat.2003.11.025.

[112] R. D. Jackson, M. P. Taylor, H. E. Evans, and X.-H. Li, “Oxidation Study of an EB-PVD MCrAlY Thermal Barrier Coating System,” *Oxid. Met.*, vol. 76, no. 3, pp. 259–271, Oct. 2011, doi: 10.1007/s11085-011-9253-7.

[113] A. Vande Put, D. Oquab, and D. Monceau, “Characterization of TBC Systems with NiPtAl or NiCoCrAlYTa Bond Coatings after Thermal Cycling at 1100°C: A Comparative Study of Failure Mechanisms,” *Mater. Sci. Forum*, vol. 595–598, pp. 213–221, 2008, doi: 10.4028/www.scientific.net/MSF.595-598.213.

[114] J. A. Haynes, K. L. More, B. A. Pint, I. G. Wright, K. Cooley, and Y. Zhang, “Effects of Platinum Additions on the Adherence of Alumina Scales to CVD Aluminide Bond Coatings,” *Mater. Sci. Forum*, vol. 369–372, pp. 679–686, 2001, doi: 10.4028/www.scientific.net/MSF.369-372.679.

[115] R. Swadźba *et al.*, “Microstructure degradation of EB-PVD TBCs on Pd–Pt-modified aluminide coatings under cyclic oxidation conditions,” *Surf. Coat. Technol.*, vol. 237, pp. 16–22, Dec. 2013, doi: 10.1016/j.surfcoat.2013.09.022.

[116] J. A. Haynes, B. A. Pint, K. L. More, Y. Zhang, and I. G. Wright, “Influence of Sulfur, Platinum, and Hafnium on the Oxidation Behavior of CVD NiAl Bond Coatings,” *Oxid. Met.*, vol. 58, no. 5, pp. 513–544, Dec. 2002, doi: 10.1023/A:1020525123056.

[117] D. R. Clarke and W. Pompe, “Critical radius for interface separation of a compressively stressed film from a rough surface,” *Acta Mater.*, vol. 47, no. 6, pp. 1749–1756, 1999, doi: 10.1016/S1359-6454(99)00078-6.

[118] M. P. Schmitt, J. M. Schreiber, A. K. Rai, T. J. Eden, and D. E. Wolfe, “Development and Optimization of Tailored Composite TBC Design Architectures for Improved Erosion Durability,” *J. Therm. Spray Technol.*, vol. 26, no. 6, pp. 1062–1075, Aug. 2017, doi: 10.1007/s11666-017-0561-6.

[119] M. Gell, L. Xie, X. Ma, E. H. Jordan, and N. P. Padture, “Highly durable thermal barrier coatings made by the solution precursor plasma spray process,” *Surf. Coat. Technol.*, vol. 177–178, pp. 97–102, Jan. 2004, doi: 10.1016/j.surfcoat.2003.06.023.

[120] S. Rezanka, G. Mauer, and R. Vaßen, “Improved Thermal Cycling Durability of Thermal Barrier Coatings Manufactured by PS-PVD,” *J. Therm. Spray Technol.*, vol. 23, no. 1, pp. 182–189, Jan. 2014, doi: 10.1007/s11666-013-9971-2.

[121] X. Ma, K. Rivellini, P. Ruggiero, and G. Wildridge, “Toward Durable Thermal Barrier Coating with Composite Phases and Low Thermal Conductivity,” *J. Therm. Spray Technol.*, vol. 29, no. 3, pp. 423–432, Feb. 2020, doi: 10.1007/s11666-020-00979-x.

[122] S. Mahade, D. Zhou, N. Curry, N. Markocsan, P. Nylén, and R. Vaßen, “Tailored microstructures of gadolinium zirconate/YSZ multi-layered thermal barrier coatings produced by suspension plasma spray: Durability and erosion testing,” *J. Mater. Process. Technol.*, vol. 264, pp. 283–294, Feb. 2019, doi: 10.1016/j.jmatprotec.2018.09.016.

[123] T. Torigoe *et al.*, “Fundamental Coating Development Study to Improve the Isothermal Oxidation Resistance and Thermal Cycle Durability of Thermal Barrier Coatings,” *Mater. Sci. Forum*, vol. 522–523, pp. 247–254, 2006, doi: 10.4028/www.scientific.net/MSF.522-523.247.

[124] W. G. Mao, Y. C. Zhou, L. Yang, and X. H. Yu, “Modeling of residual stresses variation with thermal cycling in thermal barrier coatings,” *Mech. Mater.*, vol. 38, no. 12, pp. 1118–1127, Dec. 2006, doi: 10.1016/j.mechmat.2006.01.002.

[125] A. G. Evans, M. Y. He, and J. W. Hutchinson, “Mechanics-based scaling laws for the durability of thermal barrier coatings,” *Prog. Mater. Sci.*, vol. 46, no. 3–4, pp. 249–271, 2001, doi: 10.1016/S0079-6425(00)00007-4.

[126] J. D. Eshelby and R. E. Peierls, “The determination of the elastic field of an ellipsoidal inclusion, and related problems,” *Proc. R. Soc. Lond. Ser. Math. Phys. Sci.*, vol. 241, no. 1226, pp. 376–396, Aug. 1957, doi: 10.1098/rspa.1957.0133.

[127] K. W. Schlichting, N. P. Padture, E. H. Jordan, and M. Gell, “Failure modes in plasma-sprayed thermal barrier coatings,” *Mater. Sci. Eng. A*, vol. 342, no. 1–2, pp. 120–130, 2003, doi: 10.1016/S0921-5093(02)00251-4.

[128] J. W. Hutchinson and A. G. Evans, “On the delamination of thermal barrier coatings in a thermal gradient,” *Surf. Coat. Technol.*, vol. 149, no. 2, pp. 179–184, Jan. 2002, doi: 10.1016/S0257-8972(01)01451-7.

[129] S. R. Choi, J. W. Hutchinson, and A. G. Evans, “Delamination of multilayer thermal barrier coatings,” *Mech. Mater.*, vol. 31, no. 7, pp. 431–447, Jul. 1999, doi: 10.1016/S0167-6636(99)00016-2.

[130] B. Zhang, K. Chen, N. Baddour, and P. C. Patnaik, “Life Prediction of Atmospheric Plasma-Sprayed Thermal Barrier Coatings Using Temperature-Dependent Model Parameters,” *J. Therm. Spray Technol.*, vol. 26, no. 5, pp. 902–912, Jun. 2017, doi: 10.1007/s11666-017-0558-1.

[131] T. Beck, R. Herzog, O. Trunova, M. Offermann, R. W. Steinbrech, and L. Singheiser, “Damage mechanisms and lifetime behavior of plasma-sprayed thermal barrier coating systems for gas turbines — Part II: Modeling,” *Surf. Coat. Technol.*, vol. 202, no. 24, pp. 5901–5908, 2008, doi: 10.1016/j.surfcoat.2008.06.132.

[132] E. P. Busso, “Oxidation-induced stresses in ceramic-metal interfaces,” *J. Phys. IV*, vol. 09, no. PR9, pp. Pr9-287-Pr9-296, Sep. 1999, doi: 10.1051/jp4:1999929.

[133] D. S. Balint, S.-S. Kim, Y.-F. Liu, R. Kitazawa, Y. Kagawa, and A. G. Evans, “Anisotropic TGO rumpling in EB-PVD thermal barrier coatings under in-phase thermomechanical loading,” *Acta Mater.*, vol. 59, no. 6, pp. 2544–2555, 2011, doi: 10.1016/j.actamat.2011.01.004.

[134] X. Zhao and P. Xiao, “Residual stresses in thermal barrier coatings measured by photoluminescence piezospectroscopy and indentation technique,” *Surf. Coat. Technol.*, vol. 201, no. 3, pp. 1124–1131, Oct. 2006, doi: 10.1016/j.surfcoat.2006.01.035.

[135] E. P. Busso, J. Lin, S. Sakurai, and M. Nakayama, “A mechanistic study of oxidation-induced degradation in a plasma-sprayed thermal barrier coating system.: Part I: model formulation,” *Acta Mater.*, vol. 49, no. 9, pp. 1515–1528, May 2001, doi: 10.1016/S1359-6454(01)00060-X.

[136] A. M. Freborg, B. L. Ferguson, W. J. Brindley, and G. J. Petrus, “Modeling oxidation induced stresses in thermal barrier coatings,” *Mater. Sci. Eng. A*, vol. 245, no. 2, pp. 182–190, May 1998, doi: 10.1016/S0921-5093(97)00849-6.

[137] S. Kyaw, A. Jones, and T. Hyde, “Predicting failure within TBC system: Finite element simulation of stress within TBC system as affected by sintering of APS TBC, geometry of substrate and creep of TGO,” *Eng. Fail. Anal.*, vol. 27, pp. 150–164, 2013, doi: 10.1016/j.engfailanal.2012.07.005.

[138] M. Bäker, J. Rösler, and G. Heinze, “A parametric study of the stress state of thermal barrier coatings Part II: cooling stresses,” *Acta Mater.*, vol. 53, no. 2, pp. 469–476, Jan. 2005, doi: 10.1016/j.actamat.2004.10.004.

[139] E. P. Busso and Z. Q. Qian, “A mechanistic study of microcracking in transversely isotropic ceramic–metal systems,” *Acta Mater.*, vol. 54, no. 2, pp. 325–338, Jan. 2006, doi: 10.1016/j.actamat.2005.09.003.

[140] Z.-Z. Du and A. C. F. Cocks, “Constitutive models for the sintering of ceramic components—I. Material models,” *Acta Metall. Mater.*, vol. 40, no. 8, pp. 1969–1979, Aug. 1992, doi: 10.1016/0956-7151(92)90183-F.

[141] M. Tanaka, R. Kitazawa, T. Tomimatsu, Y. F. Liu, and Y. Kagawa, “Residual stress measurement of an EB-PVD Y2O3-ZrO2 thermal barrier coating by micro-Raman spectroscopy,” *Surf. Coat. Technol.*, vol. 204, no. 5, pp. 657–660, Dec. 2009, doi: 10.1016/j.surfcoat.2009.08.042.

[142] L. Zhou, S. Mukherjee, K. Huang, Y. W. Park, and Y. Sohn, “Failure characteristics and mechanisms of EB-PVD TBCs with Pt-modified NiAl bond coats,” *Mater. Sci. Eng. A*, vol. 637, pp. 98–106, 2015, doi: 10.1016/j.msea.2015.03.120.

[143] X. Zhao, X. Wang, and P. Xiao, “Sintering and failure behaviour of EB-PVD thermal barrier coating after isothermal treatment,” *Surf. Coat. Technol.*, vol. 200, no. 20, pp. 5946–5955, May 2006, doi: 10.1016/j.surfcoat.2005.09.006.

[144] A. G. Evans and J. W. Hutchinson, “The mechanics of coating delamination in thermal gradients,” *Surf. Coat. Technol.*, vol. 201, no. 18, pp. 7905–7916, Jun. 2007, doi: 10.1016/j.surfcoat.2007.03.029.

[145] N. A. Fleck, A. C. F. Cocks, and S. Lampenscherf, “Thermal shock resistance of air plasma sprayed thermal barrier coatings,” *J. Eur. Ceram. Soc.*, vol. 34, no. 11, pp. 2687–2694, Sep. 2014, doi: 10.1016/j.jeurceramsoc.2014.01.002.

[146] W. R. Chen, X. Wu, B. R. Marple, R. S. Lima, and P. C. Patnaik, “Pre-oxidation and TGO growth behaviour of an air-plasma-sprayed thermal barrier coating,” *Surf. Coat. Technol.*, vol. 202, no. 16, pp. 3787–3796, 2008, doi: 10.1016/j.surfcoat.2008.01.021.

[147] H. Dong, G.-J. Yang, H.-N. Cai, H. Ding, C.-X. Li, and C.-J. Li, “The influence of temperature gradient across YSZ on thermal cyclic lifetime of plasma-sprayed thermal barrier coatings,” *Ceram. Int.*, vol. 41, no. 9, Part A, pp. 11046–11056, Nov. 2015, doi: 10.1016/j.ceramint.2015.05.049.

[148] Y. Li, C.-J. Li, Q. Zhang, G.-J. Yang, and C.-X. Li, “Influence of TGO Composition on the Thermal Shock Lifetime of Thermal Barrier Coatings with Cold-sprayed MCrAlY Bond Coat,”

J. Therm. Spray Technol., vol. 19, no. 1, pp. 168–177, Jan. 2010, doi: 10.1007/s11666-009-9372-8.

[149] D. R. Mumm, A. G. Evans, and I. T. Spitsberg, "Characterization of a cyclic displacement instability for a thermally grown oxide in a thermal barrier system," *Acta Mater.*, vol. 49, no. 12, pp. 2329–2340, 2001, doi: 10.1016/S1359-6454(01)00071-4.

[150] V. K. Tolpygo, D. R. Clarke, and K. S. Murphy, "Evaluation of interface degradation during cyclic oxidation of EB-PVD thermal barrier coatings and correlation with TGO luminescence," *Surf. Coat. Technol.*, vol. 188–189, pp. 62–70, 2004, doi: 10.1016/j.surfcoat.2004.08.001.

[151] M. Li, X. Sun, W. Hu, and H. Guan, "Thermal shock behavior of EB-PVD thermal barrier coatings," *Surf. Coat. Technol.*, vol. 201, no. 16, pp. 7387–7391, May 2007, doi: 10.1016/j.surfcoat.2007.02.003.

[152] R. A. Miller, "Oxidation-Based Model for Thermal Barrier Coating Life," *J. Am. Ceram. Soc.*, vol. 67, no. 8, pp. 517–521, 1984, doi: 10.1111/j.1151-2916.1984.tb19162.x.

[153] E. P. Busso, J. Lin, and S. Sakurai, "A mechanistic study of oxidation-induced degradation in a plasma-sprayed thermal barrier coating system.: Part II: Life prediction model," *Acta Mater.*, vol. 49, no. 9, pp. 1529–1536, May 2001, doi: 10.1016/S1359-6454(01)00061-1.

[154] H. Lau, C. Leyens, U. Schulz, and C. Friedrich, "Influence of bondcoat pre-treatment and surface topology on the lifetime of EB-PVD TBCs," *Surf. Coat. Technol.*, vol. 165, no. 3, pp. 217–223, Feb. 2003, doi: 10.1016/S0257-8972(02)00726-0.

[155] Z. Shen, L. He, Z. Xu, R. Mu, and G. Huang, "LZC/YSZ DCL TBCs by EB-PVD: Microstructure, low thermal conductivity and high thermal cycling life," *J. Eur. Ceram. Soc.*, vol. 39, no. 4, pp. 1443–1450, Apr. 2019, doi: 10.1016/j.jeurceramsoc.2018.12.031.

[156] A. U. Munawar, U. Schulz, G. Cerri, and H. Lau, "Microstructure and cyclic lifetime of Gd and Dy-containing EB-PVD TBCs deposited as single and double-layer on various bond coats," *Surf. Coat. Technol.*, vol. 245, pp. 92–101, Apr. 2014, doi: 10.1016/j.surfcoat.2014.02.047.

[157] Z. Shen, L. He, Z. Xu, R. Mu, and G. Huang, "Rare earth oxides stabilized La2Zr2O7 TBCs: EB-PVD, thermal conductivity and thermal cycling life," *Surf. Coat. Technol.*, vol. 357, pp. 427–432, Jan. 2019, doi: 10.1016/j.surfcoat.2018.10.045.

[158] A. Ebach-Stahl, U. Schulz, R. Swadźba, and A. U. Munawar, "Lifetime improvement of EB-PVD 7YSZ TBCs by doping of Hf or Zr in NiCoCrAlY bond coats," *Corros. Sci.*, vol. 181, p. 109205, Apr. 2021, doi: 10.1016/j.corsci.2020.109205.

[159] E. P. Busso, H. E. Evans, L. Wright, L. N. McCartney, J. Nunn, and S. Osgerby, "A software tool for lifetime prediction of thermal barrier coating systems," *Mater. Corros.*, vol. 59, no. 7, pp. 556–565, 2008, doi: 10.1002/maco.200804138.

[160] Robert A.Miller, “Current status of thermal barrier coatings — An overview,” *Surf. Coat. Technol.*, vol. 30, no. 1, pp. 1–11, Jan. 1987, doi: 10.1016/0257-8972(87)90003-X.

[161] B. Gleeson, “Thermal Barrier Coatings for Aeroengine Applications,” *J. Propuls. Power*, vol. 22, no. 2, pp. 375–383, 2006, doi: 10.2514/1.20734.

[162] V. Viswanathan, G. Dwivedi, and S. Sampath, “Engineered Multilayer Thermal Barrier Coatings for Enhanced Durability and Functional Performance,” *J. Am. Ceram. Soc.*, vol. 97, no. 9, pp. 2770–2778, 2014, doi: 10.1111/jace.13033.

[163] A. Jadhav, N. P. Padture, F. Wu, E. H. Jordan, and M. Gell, “Thick ceramic thermal barrier coatings with high durability deposited using solution-precursor plasma spray,” *Mater. Sci. Eng. A*, vol. 405, no. 1, pp. 313–320, Sep. 2005, doi: 10.1016/j.msea.2005.06.023.

[164] B. Zhang, K. Chen, N. Baddour, and P. C. Patnaik, “Life Prediction of Atmospheric Plasma-Sprayed Thermal Barrier Coatings Using Temperature-Dependent Model Parameters,” *J. Therm. Spray Technol.*, vol. 26, no. 5, pp. 902–912, Jun. 2017, doi: 10.1007/s11666-017-0558-1.

[165] J. Frachon, “Multiscale approach to predict the lifetime of EB-PVD thermal barrier coatings,” phdthesis, École Nationale Supérieure des Mines de Paris, 2009. Accessed: Jan. 13, 2021. [Online]. Available: https://pastel.archives-ouvertes.fr/pastel-00869360

[166] S. M. Meier, D. M. Nissley, K. D. Sheffler, and T. A. Cruse, “Thermal Barrier Coating Life Prediction Model Development,” *J. Eng. Gas Turbines Power*, vol. 114, no. 2, pp. 258–263, Apr. 1992, doi: 10.1115/1.2906581.

[167] D. M. Nissley, “Thermal barrier coating life modeling in aircraft gas turbine engines,” *J. Therm. Spray Technol.*, vol. 6, no. 1, p. 91, Mar. 1997, doi: 10.1007/BF02646317.

[168] K. Chan, S. Cheruvu, and R. Viswanathan, “Development of a Thermal Barrier Coating Life Model,” Feb. 2009, pp. 591–595. doi: 10.1115/GT2003-38171.

[169] H.-T. Lin and P. F. Becher, “Creep Behavior of a SiC-Whisker-Reinforced Alumina,” *J. Am. Ceram. Soc.*, vol. 73, no. 5, pp. 1378–1381, 1990, doi: 10.1111/j.1151-2916.1990.tb05208.x.

[170] D. Pan, M. W. Chen, P. K. Wright, and K. J. Hemker, “Evolution of a diffusion aluminide bond coat for thermal barrier coatings during thermal cycling,” *Acta Mater.*, vol. 51, no. 8, pp. 2205–2217, May 2003, doi: 10.1016/S1359-6454(03)00014-4.

[171] E. Sánchez-González, P. Miranda, J. J. Meléndez-Martínez, F. Guiberteau, and A. Pajares, “Temperature dependence of mechanical properties of alumina up to the onset of creep,” *J. Eur. Ceram. Soc.*, vol. 27, no. 11, pp. 3345–3349, Jan. 2007, doi: 10.1016/j.jeurceramsoc.2007.02.191.

[172] B. Rajasekaran, G. Mauer, and R. Vaßen, “Enhanced Characteristics of HVOF-sprayed MCrAlY Bond Coats for TBC Applications,” *J. Therm. Spray Technol.*, vol. 20, no. 6, pp. 1209–1216, Dec. 2011, doi: 10.1007/s11666-011-9668-3.

[173] H. Abdeldaim and N. El Mahallawy, “The effect of sol-gel Al2O3 interlayer on oxidation behaviour of TBC system,” *Surf. Coat. Technol.*, vol. 350, pp. 469–479, Sep. 2018, doi: 10.1016/j.surfcoat.2018.07.035.

[174] A. Moridi, M. Azadi, and G. H. Farrahi, “Thermo-mechanical stress analysis of thermal barrier coating system considering thickness and roughness effects,” *Surf. Coat. Technol.*, vol. 243, pp. 91–99, Mar. 2014, doi: 10.1016/j.surfcoat.2012.02.019.

[175] W. X. Zhang, X. L. Fan, and T. J. Wang, “The surface cracking behavior in air plasma sprayed thermal barrier coating system incorporating interface roughness effect,” *Appl. Surf. Sci.*, vol. 258, no. 2, pp. 811–817, 2011, doi: 10.1016/j.apsusc.2011.08.103.

[176] K. Yuan, Y. Yu, and J.-F. Wen, “A study on the thermal cyclic behavior of thermal barrier coatings with different MCrAlY roughness,” *Vacuum*, vol. 137, pp. 72–80, Mar. 2017, doi: 10.1016/j.vacuum.2016.12.033.

[177] ABAQUS, “HKS Inc.,” *Provid. RI USA*, vol. 2019.

[178] T. S. Hille, T. J. Nijdam, A. S. J. Suiker, S. Turteltaub, and W. G. Sloof, “Damage growth triggered by interface irregularities in thermal barrier coatings,” *Acta Mater.*, vol. 57, no. 9, pp. 2624–2630, May 2009, doi: 10.1016/j.actamat.2009.01.022.

[179] W. R. Chen, R. Archer, X. Huang, and B. R. Marple, “TGO Growth and Crack Propagation in a Thermal Barrier Coating,” *J. Therm. Spray Technol.*, vol. 17, no. 5, p. 858, Oct. 2008, doi: 10.1007/s11666-008-9251-8.

[180] A. C. Karaoglanli, E. Altuncu, I. Ozdemir, A. Turk, and F. Ustel, “Structure and durability evaluation of YSZ+Al2O3 composite TBCs with APS and HVOF bond coats under thermal cycling conditions,” *Surf. Coat. Technol.*, vol. 205, pp. S369–S373, Jul. 2011, doi: 10.1016/j.surfcoat.2011.04.081.

[181] S. Mahade, N. Curry, S. Björklund, N. Markocsan, and S. Joshi, “Durability of Gadolinium Zirconate/YSZ Double-Layered Thermal Barrier Coatings under Different Thermal Cyclic Test Conditions,” *Materials*, vol. 12, no. 14, Art. no. 14, Jan. 2019, doi: 10.3390/ma12142238.

[182] R. Kromer, J. Cormier, S. Costil, D. Courapied, L. Berthe, and P. Peyre, “High temperature durability of a bond-coatless plasma-sprayed thermal barrier coating system with laser textured Ni-based single crystal substrate,” *Surf. Coat. Technol.*, vol. 337, pp. 168–176, Mar. 2018, doi: 10.1016/j.surfcoat.2018.01.006.

[183] J. Huang *et al.*, “Improve durability of plasma-splayed thermal barrier coatings by decreasing sintering-induced stiffening in ceramic coatings,” *J. Eur. Ceram. Soc.*, vol. 40, no. 4, pp. 1433–1442, Apr. 2020, doi: 10.1016/j.jeurceramsoc.2019.11.074.

[184] I. Spitsberg and K. More, “Effect of thermally grown oxide (TGO) microstructure on the durability of TBCs with PtNiAl diffusion bond coats,” *Mater. Sci. Eng. A*, vol. 417, no. 1, pp. 322–333, Feb. 2006, doi: 10.1016/j.msea.2005.11.014.

[185] C.-J. Li, H. Dong, H. Ding, G.-J. Yang, and C.-X. Li, “The Correlation of the TBC Lifetimes in Burner Cycling Test with Thermal Gradient and Furnace Isothermal Cycling Test by TGO Effects,” *J. Therm. Spray Technol.*, vol. 26, no. 3, pp. 378–387, Feb. 2017, doi: 10.1007/s11666-017-0530-0.

[186] Y. H. Sohn, J. H. Kim, E. H. Jordan, and M. Gell, “Thermal cycling of EB-PVD/MCrAlY thermal barrier coatings: I. Microstructural development and spallation mechanisms,” *Surf. Coat. Technol.*, vol. 146–147, pp. 70–78, 2001, doi: 10.1016/S0257-8972(01)01478-5.

[187] B. Cheng *et al.*, “Sintering-induced delamination of thermal barrier coatings by gradient thermal cyclic test,” *J. Am. Ceram. Soc.*, vol. 100, no. 5, pp. 1820–1830, 2017, doi: 10.1111/jace.14713.

[188] X. Xie, H. Guo, S. Gong, and H. Xu, “Thermal cycling behavior and failure mechanism of LaTi2Al9O19/YSZ thermal barrier coatings exposed to gas flame,” *Surf. Coat. Technol.*, vol. 205, no. 17, pp. 4291–4298, May 2011, doi: 10.1016/j.surfcoat.2011.03.047.

[189] S. Yang, H. Yuan, W. Zeng, and H. Guo, “Chemo-thermo-mechanical modeling of EB-PVD TBC failure subjected to isothermal and cyclic thermal exposures,” *Int. J. Fatigue*, vol. 141, p. 105817, Dec. 2020, doi: 10.1016/j.ijfatigue.2020.105817.

[190] C. Giolli, A. Scrivani, G. Rizzi, F. Borgioli, G. Bolelli, and L. Lusvarghi, “Failure Mechanism for Thermal Fatigue of Thermal Barrier Coating Systems,” *J. Therm. Spray Technol.*, vol. 18, no. 2, pp. 223–230, Jun. 2009, doi: 10.1007/s11666-009-9307-4.

[191] J. A. Ruud, A. Bartz, M. P. Borom, and C. A. Johnson, “Strength Degradation and Failure Mechanisms of Electron-Beam Physical-Vapor-Deposited Thermal Barrier Coatings,” *J. Am. Ceram. Soc.*, vol. 84, no. 7, pp. 1545–1552, 2001, doi: 10.1111/j.1151-2916.2001.tb00875.x.

[192] A. Bolcavage, A. Feuerstein, J. Foster, and P. Moore, “Thermal shock testing of thermal barrier coating/bondcoat systems,” *J. Mater. Eng. Perform.*, vol. 13, no. 4, pp. 389–397, Aug. 2004, doi: 10.1361/10599490419883.

[193] P. Ramaswamy, S. Seetharamu, K. J. Rao, and K. B. R. Varma, “Thermal shock characteristics of plasma sprayed mullite coatings,” *J. Therm. Spray Technol.*, vol. 7, no. 4, pp. 497–504, Dec. 1998, doi: 10.1361/105996398770350710.

[194] J. P. Feist, P. Y. Sollazzo, C. Pilgrim, and J. R. Nicholls, “Operation of a Burner Rig for Thermal Gradient Cycling of Thermal Barrier Coatings,” presented at the ASME Turbo Expo 2014: Turbine Technical Conference and Exposition, Sep. 2014. doi: 10.1115/GT2014-26325.

[195] D. E. Mack, T. Wobst, M. O. D. Jarligo, D. Sebold, and R. Vaßen, “Lifetime and failure modes of plasma sprayed thermal barrier coatings in thermal gradient rig tests with simultaneous CMAS injection,” *Surf. Coat. Technol.*, vol. 324, pp. 36–47, Sep. 2017, doi: 10.1016/j.surfcoat.2017.04.071.

[196] J. M. Drexler, A. Aygun, D. Li, R. Vaßen, T. Steinke, and N. P. Padture, “Thermal-gradient testing of thermal barrier coatings under simultaneous attack by molten glassy deposits and its mitigation,” *Surf. Coat. Technol.*, vol. 204, no. 16, pp. 2683–2688, May 2010, doi: 10.1016/j.surfcoat.2010.02.026.

[197] R. S. Lima, B. R. Marple, and P. Marcoux, “Thermal Gradient Behavior of TBCs Subjected to a Laser Gradient Test Rig: Simulating an Air-to-Air Combat Flight,” *J. Therm. Spray Technol.*, vol. 25, no. 1, pp. 282–290, Jan. 2016, doi: 10.1007/s11666-015-0311-6.

[198] N. J. Simms, P. J. Kilgallon, C. Roach, and J. E. Oakey, “Development of oxides at TBC – bond coat interfaces in burner rig exposures,” *Mater. High Temp.*, vol. 20, no. 4, pp. 519–526, Jan. 2003, doi: 10.1179/mht.2003.060.

[199] P. E. Hodge, S. Stecura, M. A. Gedwill, I. Zaplatynsky, and S. R. Levine, “Thermal barrier coatings: Burner rig hot corrosion test results,” *J. Mater. Energy Syst.*, vol. 1, no. 4, pp. 47–58, Mar. 1980, doi: 10.1007/BF02833361.

[200] T. Xu, M. Y. He, and A. G. Evans, “A numerical assessment of the durability of thermal barrier systems that fail by ratcheting of the thermally grown oxide,” *Acta Mater.*, vol. 51, no. 13, pp. 3807–3820, 2003, doi: 10.1016/S1359-6454(03)00194-0.

[201] A. C. Karaoglanli, A. Turk, I. Ozdemir, and F. Ustel, “Comparison of Oxidation and Thermal Shock Performance of Thermal Barrier Coatings,” *Mater. Manuf. Process.*, vol. 30, no. 6, pp. 717–723, Jun. 2015, doi: 10.1080/10426914.2014.952025.

[202] D. R. Mumm, M. Watanabe, A. G. Evans, and J. A. Pfaendtner, “The influence of test method on failure mechanisms and durability of a thermal barrier system,” *Acta Mater.*, vol. 52, no. 5, pp. 1123–1131, Mar. 2004, doi: 10.1016/j.actamat.2003.10.045.

[203] “Von Mises Criterion (Maximum Distortion Energy Criterion) - Strength (Mechanics) of Materials - Engineers Edge.” https://www.engineersedge.com/material_science/von_mises.htm (accessed Jan. 12, 2022).

[204] K. Tanaka, “Fatigue crack propagation from a crack inclined to the cyclic tensile axis,” *Eng. Fract. Mech.*, vol. 6, no. 3, pp. 493–507, Oct. 1974, doi: 10.1016/0013-7944(74)90007-1.

[205] H.-H. Yu and J. W. Hutchinson, “Influence of substrate compliance on buckling delamination of thin films,” *Int. J. Fract.*, vol. 113, no. 1, pp. 39–55, Jan. 2002, doi: 10.1023/A:1013790232359.

[206] Z.-G. Liu, W.-H. Zhang, J.-H. Ouyang, and Y. Zhou, “Novel thermal barrier coatings based on rare-earth zirconates/YSZ double-ceramic-layer system deposited by plasma spraying,” *J. Alloys Compd.*, vol. 647, pp. 438–444, Oct. 2015, doi: 10.1016/j.jallcom.2015.05.189.

[207] C. H. Hsueh *et al.*, “Effects of Bond Coat Surface-Roughness on Residual Stresses of Thermal Barrier Coating Systems,” May 2017, Accessed: Jul. 29, 2021. [Online]. Available: https://www.nist.gov/publications/effects-bond-coat-surface-roughness-residual-stresses-thermal-barrier-coating-systems

[208] P. F. Becher, C. Carter, J. Fuller, C. H. Hsueh, and S. A. Langer, “Surface-Roughness Induced Residual Stresses in Thermal Barrier Coatings: Computer Simulations,” Oak Ridge National Lab. (ORNL), Oak Ridge, TN (United States); Oak Ridge, TN, ORNL/CP-99990, Oct. 1998. Accessed: Jul. 29, 2021. [Online]. Available: https://www.osti.gov/biblio/1741

[209] S. M. Meier and D. K. Gupta, “The Evolution of Thermal Barrier Coatings in Gas Turbine Engine Applications,” *J. Eng. Gas Turbines Power*, vol. 116, no. 1, pp. 250–257, Jan. 1994, doi: 10.1115/1.2906801.

[210] Q. Xin, “2 - Durability and reliability in diesel engine system design,” in *Diesel Engine System Design*, Q. Xin, Ed. Woodhead Publishing, 2013, pp. 113–202. doi: 10.1533/9780857090836.1.113.

[211] V. K. Tolpygo, D. R. Clarke, and K. S. Murphy, “Oxidation-induced failure of EB-PVD thermal barrier coatings,” *Surf. Coat. Technol.*, vol. 146–147, pp. 124–131, 2001, doi: 10.1016/S0257-8972(01)01482-7.

[212] Y. Ozgurluk, K. M. Doleker, D. Ozkan, H. Ahlatci, and A. C. Karaoglanli, “Cyclic Hot Corrosion Failure Behaviors of EB-PVD TBC Systems in the Presence of Sulfate and Vanadate Molten Salts,” *Coatings*, vol. 9, no. 3, Art. no. 3, Mar. 2019, doi: 10.3390/coatings9030166.

[213] U. Schulz, K. Fritscher, and A. Ebach-Stahl, “Cyclic behavior of EB-PVD thermal barrier coating systems with modified bond coats,” *Surf. Coat. Technol.*, vol. 203, no. 5, pp. 449–455, Dec. 2008, doi: 10.1016/j.surfcoat.2008.08.056.

[214] H. Bhatnagar, S. Ghosh, and M. E. Walter, “Parametric studies of failure mechanisms in elastic EB-PVD thermal barrier coatings using FEM,” *Int. J. Solids Struct.*, vol. 43, no. 14, pp. 4384–4406, Jul. 2006, doi: 10.1016/j.ijsolstr.2005.07.037.

[215] R. G. Wellman and J. R. Nicholls, “Some observations on erosion mechanisms of EB PVD TBCS,” *Wear*, vol. 242, no. 1, pp. 89–96, Jul. 2000, doi: 10.1016/S0043-1648(00)00391-4.

[216] R. G. Wellman and J. R. Nicholls, “A Monte Carlo model for predicting the erosion rate of EB PVD TBCs,” *Wear*, vol. 256, no. 9, pp. 889–899, May 2004, doi: 10.1016/j.wear.2003.09.001.

[217] R. G. Wellman, M. J. Deakin, and J. R. Nicholls, “The effect of TBC morphology and aging on the erosion rate of EB-PVD TBCs,” *Tribol. Int.*, vol. 38, no. 9, pp. 798–804, Sep. 2005, doi: 10.1016/j.triboint.2005.02.008.

[218] J. Chen, B. D. Beake, R. G. Wellman, J. R. Nicholls, and H. Dong, “An investigation into the correlation between nano-impact resistance and erosion performance of EB-PVD thermal barrier coatings on thermal ageing,” *Surf. Coat. Technol.*, vol. 206, no. 23, pp. 4992–4998, Jul. 2012, doi: 10.1016/j.surfcoat.2012.06.011.

[219] R. G. Wellman and J. R. Nicholls, “On the effect of ageing on the erosion of EB-PVD TBCs,” *Surf. Coat. Technol.*, vol. 177–178, pp. 80–88, Jan. 2004, doi: 10.1016/j.surfcoat.2003.06.019.

[220] U. Schulz, B. Saruhan, K. Fritscher, and C. Leyens, “Review on Advanced EB-PVD Ceramic Topcoats for TBC Applications,” *Int. J. Appl. Ceram. Technol.*, vol. 1, no. 4, pp. 302–315, 2004, doi: 10.1111/j.1744-7402.2004.tb00182.x.

[221] M. Peters, C. Leyens, U. Schulz, and W. A. Kaysser, “EB-PVD Thermal Barrier Coatings for Aeroengines and Gas Turbines,” *Adv. Eng. Mater.*, vol. 3, no. 4, pp. 193–204, 2001.

[222] A. F. Renteria, B. Saruhan, U. Schulz, H.-J. Raetzer-Scheibe, J. Haug, and A. Wiedenmann, “Effect of morphology on thermal conductivity of EB-PVD PYSZ TBCs,” *Surf. Coat. Technol.*, vol. 201, no. 6, pp. 2611–2620, Dec. 2006, doi: 10.1016/j.surfcoat.2006.05.003.

[223] D. E. Wolfe, J. Singh, R. A. Miller, J. I. Eldridge, and D.-M. Zhu, “Tailored microstructure of EB-PVD 8YSZ thermal barrier coatings with low thermal conductivity and high thermal reflectivity for turbine applications,” *Surf. Coat. Technol.*, vol. 190, no. 1, pp. 132–149, Jan. 2005, doi: 10.1016/j.surfcoat.2004.04.071.

[224] J. R. Nicholls, R. G. Wellman, and M. J. Deakin, “Erosion of thermal barrier coatings,” *Mater. High Temp.*, vol. 20, no. 2, pp. 207–218, Jan. 2003, doi: 10.1179/mht.2003.024.

[225] J. R. Nicholls, Y. Jaslier, and D. S. Rickerby, “Erosion of EB-PVD thermal barrier coatings,” *Mater. High Temp.*, vol. 15, no. 1, pp. 15–22, Jan. 1998, doi: 10.1080/09603409.1998.11689572.

[226] Y. Liu, R. Ravichandran, K. Chen, and P. Patnaik, “Application of Machine Learning to Solid Particle Erosion of APS-TBC and EB-PVD TBC at Elevated Temperatures,” *Coatings*, vol. 11, no. 7, Art. no. 7, Jul. 2021, doi: 10.3390/coatings11070845.

[227] N. A. Fleck and Th. Zisis, “The erosion of EB-PVD thermal barrier coatings: The competition between mechanisms,” *Wear*, vol. 268, no. 11, pp. 1214–1224, May 2010, doi: 10.1016/j.wear.2009.12.020.

[228] S. M. Ning *et al.*, “Influence of particle shape on erosion behavior of EB-PVD thermal barrier coatings,” *Ceram. Int.*, vol. 48, no. 6, pp. 8627–8640, Mar. 2022, doi: 10.1016/j.ceramint.2021.12.074.

[229] J. H. Neilson and A. Gilchrist, “Erosion by a stream of solid particles,” *Wear*, vol. 11, no. 2, pp. 111–122, Feb. 1968, doi: 10.1016/0043-1648(68)90591-7.

[230] W. Tabakoff, “Investigation of coatings at high temperature for use in turbomachinery,” *Surf. Coat. Technol.*, vol. 39–40, pp. 97–115, Dec. 1989, doi: 10.1016/0257-8972(89)90045-5.

[231] S. Gokul Lakshmi, B. Malvi, D. S. Rao, D. K. Das, and M. Roy, “Comparison of erosion rate of EB-PVD and plasma sprayed TBC,” *Surf. Eng.*, vol. 37, no. 11, pp. 1396–1403, Nov. 2021, doi: 10.1080/02670844.2021.1997251.

[232] G. L. Sheldon and A. Kanhere, “An investigation of impingement erosion using single particles,” *Wear*, vol. 21, no. 1, pp. 195–209, Aug. 1972, doi: 10.1016/0043-1648(72)90257-8.

[233] J. G. A. Bitter, “A study of erosion phenomena part I,” *Wear*, vol. 6, no. 1, pp. 5–21, Jan. 1963, doi: 10.1016/0043-1648(63)90003-6.

[234] A. G. Evans, M. E. Gulden, M. Rosenblatt, and D. Tabor, “Impact damage in brittle materials in the elastic-plastic response régime,” *Proc. R. Soc. Lond. Math. Phys. Sci.*, vol. 361, no. 1706, pp. 343–365, Jun. 1978, doi: 10.1098/rspa.1978.0106.

[235] Slikkerveer, P.J., de With, G. (Bert), Field, J.E., and Materials and Interface Chemistry, “Mechanical etching of glass by powder blasting,” Technische Universiteit Eindhoven, 1999. doi: 10.6100/ir527360.

[236] E. Gregorová *et al.*, “Temperature dependence of Young′s modulus of silica refractories,” *Ceram. Int.*, vol. 41, no. 1, Part B, pp. 1129–1138, Jan. 2015, doi: 10.1016/j.ceramint.2014.09.039.

[237] J. Zhu and K. Ma, “Microstructural and mechanical properties of thermal barrier coating at 1400°C treatment,” *Theor. Appl. Mech. Lett.*, vol. 4, no. 2, p. 021008, Jan. 2014, doi: 10.1063/2.1402108.

[238] P. C. Twigg and T. F. Page, “The temperature-variant hardness response of duplex TBCs,” *Thin Solid Films*, vol. 236, no. 1, pp. 219–224, Dec. 1993, doi: 10.1016/0040-6090(93)90673-D.

[239] A. G. Evans, D. R. Clarke, and C. G. Levi, “The influence of oxides on the performance of advanced gas turbines,” *J. Eur. Ceram. Soc.*, vol. 28, no. 7, pp. 1405–1419, Jan. 2008, doi: 10.1016/j.jeurceramsoc.2007.12.023.

[240] *Handbook of Thermophysical Properties of Solid Materials*, vol. Vol. 3, Ceramics. Pergamon Press, 1961.

[241] B. Zhang, K. Chen, and N. Baddour, “Stress models for electron beam-physical vapor deposition thermal barrier coatings using temperature-process-dependent model parameters,” *J. Eur. Ceram. Soc.*, Apr. 2021, doi: 10.1016/j.jeurceramsoc.2021.04.046.

[242] B. Zhang, K. Chen, and N. Baddour, “The Effect of Interfacial Roughness on Residual Stresses in Electron Beam-Physical Vapor Deposition of Thermal Barrier Coatings,” *Coatings*, vol. 11, no. 3, Art. no. 3, Mar. 2021, doi: 10.3390/coatings11030341.

[243] A. Tsoga and P. Nikolopoulos, “Surface and grain-boundary energies in yttria-stabilized zirconia (YSZ-8 mol%),” *J. Mater. Sci.*, vol. 31, no. 20, pp. 5409–5413, Oct. 1996, doi: 10.1007/BF01159310.

Appendix A - Supporting document for journal paper 3 in chapter 5

A.1. Compilation of parameters and integration into analytical models using experimental data under thermal cycles

A.1.1. Characteristics of material properties affected by pre-heat treatment

As described in [185], APS-TBC specimen in both burner cycling and isothermal furnace test were pre-treated in a high temperature environment to obtain the uniform pre-oxide TGO layer with different thickness. This process also leads to the sintering behavior and possible delamination crack growth identified within TC under isothermal exposure [131]. The effect of the pre-heat treatment on APS-TBCs will be discussed in section A.1.1. The following different thermal cycling experiments applying to the TBCs yield various of life data which was found to be closely related to the pre-oxide thickness. The effect of the thermal cycling experiments on APS-TBCs will be discussed in A.1.2. The parameters affected by geometry of APS-TBCs will be discussed in A.1.3.

(a) Preheat treatment introduced pre-oxide TGO growth

All APS-TBC specimen undergoing the thermal cyclic experiments experienced first 4 hours pre-treatment at 1000℃, followed by another 4 hours pre-treatment at 1080℃ under Argon atmosphere. This procedure produces a uniform 1.3μm pre-oxide layer mainly containing α-alumina due to the

progressive oxidation of CoNiCrAlY (MCrAlY) BC layer for all TBCs. The further heat treatment includes 20, 50, 105, 225, 300, 350 hours isothermal heating at 1080℃, resulting in the TGO thickness of 2.7, 3.9, 5.0, 6.5, 7.0, 7.7μm for different APS-TBC specimen. Considering the initial TGO thickness of 1.3μm, the growth of pre-oxide TGO scale can be approximated using an exponential function as

$$d_{TGO}^{Pre} = k_p\left(T_{BC}\right)t^{n_{TGO}} + d_{TGO}^{ini} \tag{121}$$

where

$$k_p\left(T_{BC}\right) = C_{TGO} \times \exp\left(-\frac{Q_{TGO}}{RT}\right) \tag{122}$$

and where $k_p\left(T\right)$ is the temperature-dependent TGO growth rate. d_{TGO}^{ini} is the initial TGO thickness, $d_{TGO}^{ini} = 1.3\mu m$, C_{TGO}=33.56 μm$/s^{n_{TGO}}$, Q_{TGO}=94.117 KJ/mol and $n_{TGO} = 0.47687$ are TGO growth amplitude, TGO growth activation energy and TGO growth exponent, respectively. R is the gas constant and T_{BC} is temperature measured by a non-contact infrared thermometer [8] on the BC surface in Kelvin. The calculated TGO thickness as function of at preheat treatment time using equation (121) is plotted in Figure 106.

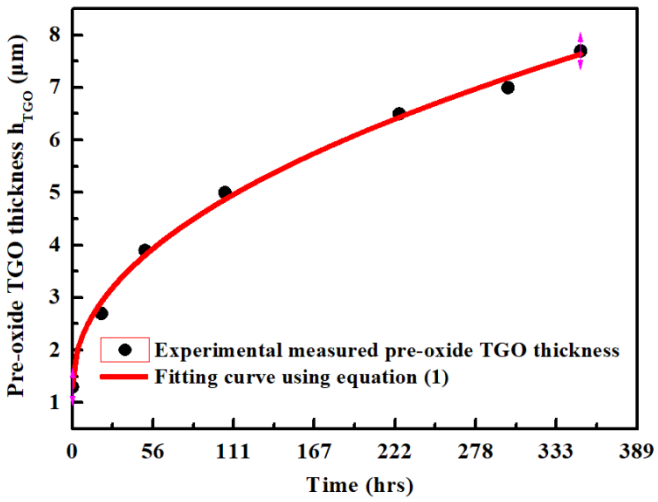

Figure 106 The thickness of pre-oxide TGO layer after isothermal pre-treatment at 1080℃

(b) Preheat treatment introduced sintering effect of TC

The isothermal preheat treatment of TBCs under high temperature also introduces the sintering effect on 7YSZ TC, where the corresponding increase of TC elastic modulus can be described through [81]

$$E_{TC}(t)=\frac{\beta E_{TBC}^{0}E_{TBC}^{\infty}}{\beta E_{TBC}^{0}+E_{TBC}^{\infty}-E_{TBC}^{0}} \tag{123}$$

where $\beta=1+A_{\sin t}\exp\left(-\frac{Q_{\sin t}}{\kappa_B T_{TC}\big|_y}\right)t^{n_{\sin t}}$. The E_{TBC}^{0} and E_{TBC}^{∞} are starting and bulk modulus of TC, the $A_{\sin t}=2\times10^{10}s^{m}$ $Q_{\sin t}=3eV$ and $n_{\sin t}=0.25$ are sintering amplitude, sintering activation energy and sintering exponent, respectively[81]. κ_B is the Boltzmann constant. t is time in seconds. $T_{TC}\big|_y$ is position-dependent temperature within TC layer. The β in equation (123) reveals the effect of parameters on the variation of relative density of TC. The shrinkage of porous 7YSZ TC leads to closure of pores within TC, which is reflected by the decrease of porosity and increase of elastic

modulus up to the bulk material. The difference in sintering rate for TC could be expected if various high temperatures are applied. The concept of equivalent sintering time t_{equiv}^{sint} should be used to describe the equivalent elastic modulus under different high temperature with its thermal history.

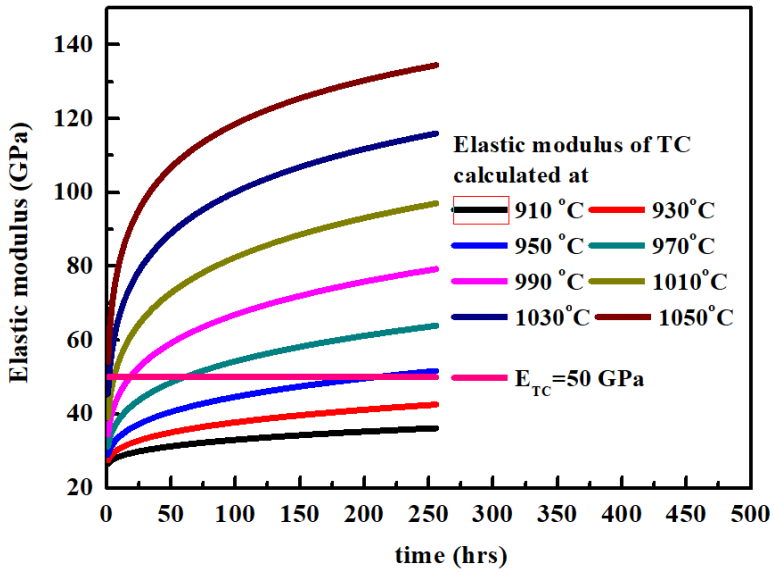

Figure 107 The increase of TC elastic modulus as function of sintering time under different temperatures

Figure 107 illustrates the increase of TC elastic modulus calculated by equation (123) as a function of sintering time at different depths of TC (with different temperatures when thermal gradient exists). It is evident that the same elastic modulus (e.g. 50Gpa) can be obtained by about 190 hours for TC sintering under 950℃, whereas it only requires 61 hours sintering under 970℃ and 6 hours sintering under 1010℃. This indicates that for the current study with respect to differences in preheat treatment temperatures and peak temperatures in the thermal cycling experiments, it is necessary to obtain an equivalent sintering time which bridges different thermal histories. It is assumed that the initial elastic modulus from the sintering process following thermal cycling experiments is $E_{TC}\left(t=1s, T_{TC}\big|_y = T_{cycle}\right)$, where the $t=1s$ indicates the time used to calculate the initial elastic

modulus at high temperature dwell time for the first thermal cycle is equal to 1s. $T_{TC}\big|_y = T_{cycle}$ suggests position-dependent peak temperatures are measured during dwell time of thermal cycles. Assuming the final elastic modulus from preheat treatment sintering process is $E_{TC}\left(t = t_F, T_{TC}\big|_y = T_{HT}\right)$ (where the $t = t_F$ indicates the time used to calculate the final elastic modulus at preheat treatment is equal to preheat treatment period described above (20-350 hours at 1080°C)), $T_{TC}\big|_y = T_{HT}$ suggests position-dependent temperatures are measured during preheat treatment. It is evident that the $E_{TC}\left(t = 1s, T_{TC}\big|_y = T_{cycle}\right)$ is a constant since maximum temperature (935-1150°C depends on the calculated depth of TC) and time (1s) used to calculate the initial elastic modulus in equation (123) is determined with respect to specific calculated depth *y*. However, for the preheat treatment, except for the difference of sintering temperature applied (1080°C) compared to the peak temperature of following thermal cycling conditions, there are seven sintering periods t_F which correspond to different final elastic modulus $E_{TC}\left(t = t_F, T_{TC}\big|_y = T_{HT}\right)$ at the end of preheat treatment. Due to the difference of sintering densification from preheat treatment, various sintering rates are reflected by the different rate of increase of elastic modulus of TC expected during high temperature dwell time. It is necessary to quantify the difference of sintering rates due to the difference of preheat treatment period by using the equivalent sintering time t_{equiv}^{sint} based on the criterion described below,

I. If the initial elastic modulus from the following sintering process during thermal cycling condition $E_{TC}\left(t = 1s, T_{TC}\big|_y = T_{cycle}\right)$ is smaller than the calculated final elastic modulus from the previous sintering process $E_{TC}\left(t = t_F, T_{TC}\big|_y = T_{HT}\right)$, then equation (123) is applied to obtain the equivalent sintering time t_{equiv}^{sint} for the following sintering process where the following elastic modulus is calculated starting from t_{equiv}^{sint}.

II. If the initial elastic modulus from the following sintering process $E_{TC}\left(t = 1s, T_{TC}\big|_y = T_{cycle}\right)$ is greater than the calculated final elastic modulus from the previous sintering process

$E_{TC}\left(t=t_F, T_{TC}\big|_y = T_{HT}\right)$, then $E_{TC}\left(t=t_F, T_{TC}\big|_y = T_{HT}\right)$ is applied as starting modulus E^0_{TBC} where the following elastic modulus is calculated starting from $t=1s$.

The calculated equivalent sintering time as a function of preheat treatment sintering time at 1μm above the TC/TGO interface is illustrated in Figure 108. The larger the equivalent time, the lower the rate of increase of the elastic modulus for high temperature dwell time during thermal cycling conditions.

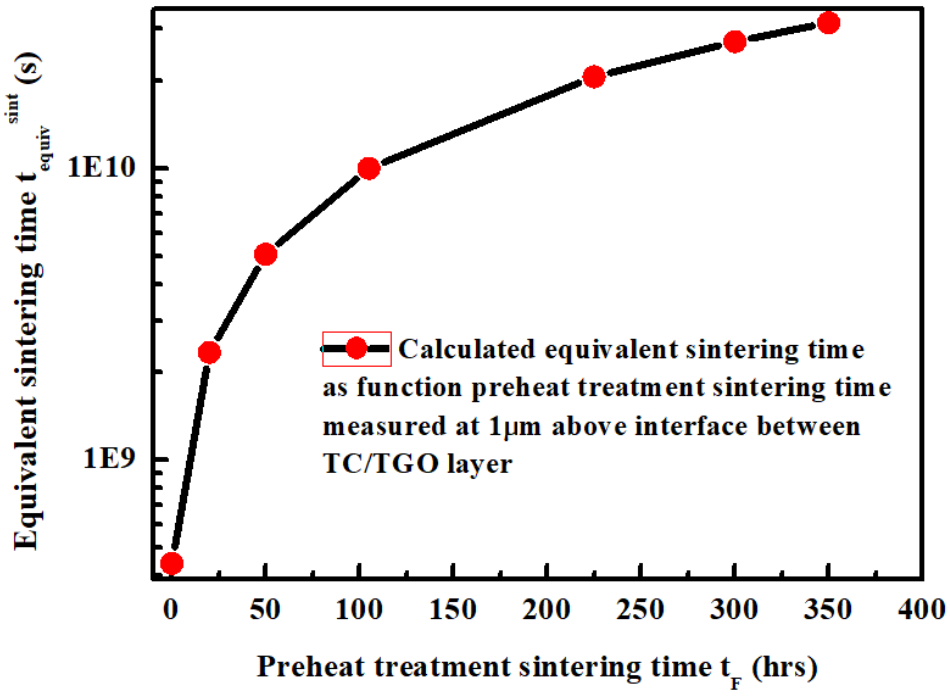

Figure 108 the calculated equivalent sintering time as function of preheat treatment sintering time

The method used to calculate equivalent sintering time can also be applied to the calculation of TGO growth under isothermal furnace test, where the equivalent TGO growth time t_{equiv}^{TGO} should be estimated to determine the initial TGO growth rate for the thermal cycling conditions.

A.1.2. Characteristics of material properties affected by thermal cycling experiments

(a) Life data for different pre-oxide TGO thickness

The life data based on different types of thermal cycling experiments are collected in [185] as a function of thickness of pre-oxide layer, Figure 109.

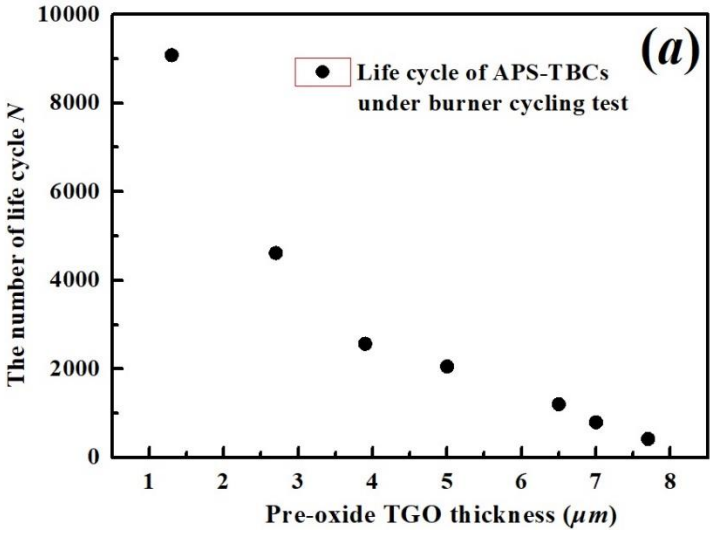

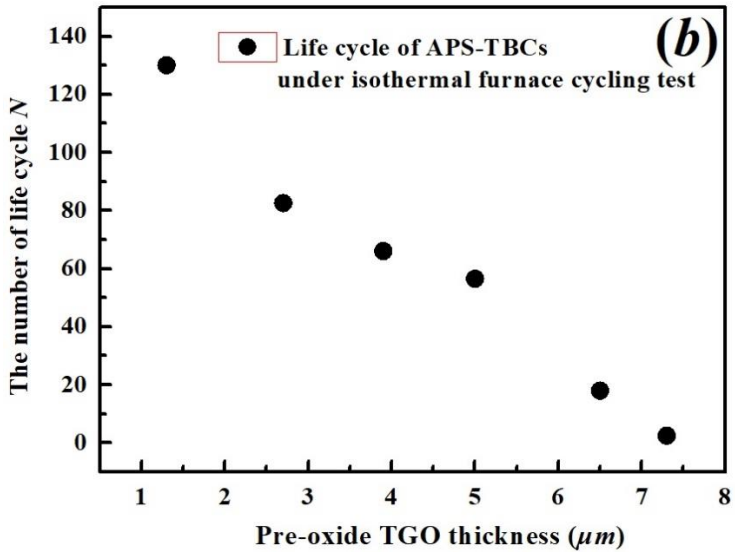

Figure 109 Life cycle of APS-TBCs under (a) burner cycling test (b) isothermal furnace cycling test with respect to different pre-oxide TGO thickness [185]

(b) TGO growth under thermal cycling experiments

The TGO growth under thermal cycling conditions is significantly affected by the temperature-dependent TGO growth rate, $k_p\left(T_{BC}\right)$ in equation (122). Several curves were illustrated in [131] according to experimentally measured TGO growth as a function of time based on different elevated temperatures. These data are used to fit the C_{TGO}, Q_{TGO} and n_{TGO} in equation (122) and shown in Figure 110(a). Since the total TGO growth rate varies depending on both temperature and time, equation (121) is rewritten in incremental form, which is then used to describe the growth of TGO thickness under thermal cycling conditions as

$$d_{TGO}\left(t_{equiv}^{TGO}\Big|_{t_0=t_{equiv}^{i}}+\Delta t\right)\approx d_{TGO}\left(t_{equiv}^{TGO}\Big|_{t_0=t_{equiv}^{i}}\right)+d\frac{\left(d_{TGO}\right)}{dt}\times\left[\left(t_{equiv}^{TGO}\Big|_{t_0=t_{equiv}^{i}}+\Delta t\right)-t_{equiv}^{TGO}\Big|_{t_0=t_{equiv}^{i}}\right]+d_{TGO}^{Pre} \quad (124)$$

where

$$d\frac{\left(d_{TGO}\right)}{dt}=n_{TGO}^{cycle}\times C_{TGO}^{cycle}\times\exp\left(-\frac{Q_{TGO}^{cycle}}{R\times T_{BC}}\right)\left(t_{equiv}^{TGO}\Big|_{t_0=t_{equiv}^{i}}\right)^{n_{TGO}^{cycle}-1} \quad (125)$$

Here, d_{TGO}^{pre} is the pre-oxide TGO thickness, varying from 1.3μm to 7.7μm as described in section A.1.1. t_{equiv}^{TGO} is the equivalent TGO growth time. Due to discrepancies between the elevated temperatures applied in isothermal preheat treatment and high temperature holding time thermal cycling conditions, it is necessary to obtain the equivalent TGO growth time t_{equiv}^{TGO} to bridge the two separate oxidation processes. By applying a similar method as used to obtain t_{equiv}^{sint}, the initial equivalent TGO growth time t_{equiv}^{i} are calculated to about 0.36, 3.72, 13.07, 31.64, 82.44, 154.71 hours for isothermal furnace cycling test at 1120℃ corresponding to 0, 20, 50, 105, 225, 350 hours further isothermal preheat treatment at 1080℃ with 1.3, 2.7, 3.9, 5, 6.5, 7.7μm pre-oxide thickness, Table 17.

Table 17 Equivalent initial TGO growth time for isothermal furnace cycling test

No	Preheat treatment time consumed t_{TGO}^{PRE} ① (hrs)	Pre-oxide thickness d_{TGO}^{Pre} ① (μm)	Equivalent initial TGO growth time t_{equiv}^{i} ② (hrs)	Calculated TGO thickness at failure life cycle (μm)

1	0	1.3	0.3656	6.21
2	20	2.7	3.7244	5.78
3	50	3.9	13.0667	5.49
4	105	5	31.6442	5.86
5	225	6.5	82.4361	6.62
6	350	7.7	154.7067	7.7

① The preheat treatment was conducted under isothermal heating at 1080℃

② The equivalent initial TGO growth time is calculated based on isothermal furnace cycling test where peak temperature during high temperature holding time is at 1120℃

The role of the TGO layer (considered to inhibit the further oxidation of BC layer) is evaluated by t_{equiv}^{i} in equation (124)-(125). The thicker the pre-oxide TGO layer, the longer the equivalent TGO growth time t_{equiv}^{i}, corresponding to lower TGO growth rate as n_{TGO}^{cycle} in equation (125) is smaller than unity. The calculated t_{equiv}^{i} is used as the initial time considering oxidation for actual isothermal furnace cycling tests, where the TGO thickness versus time is shown in Figure 110(b).

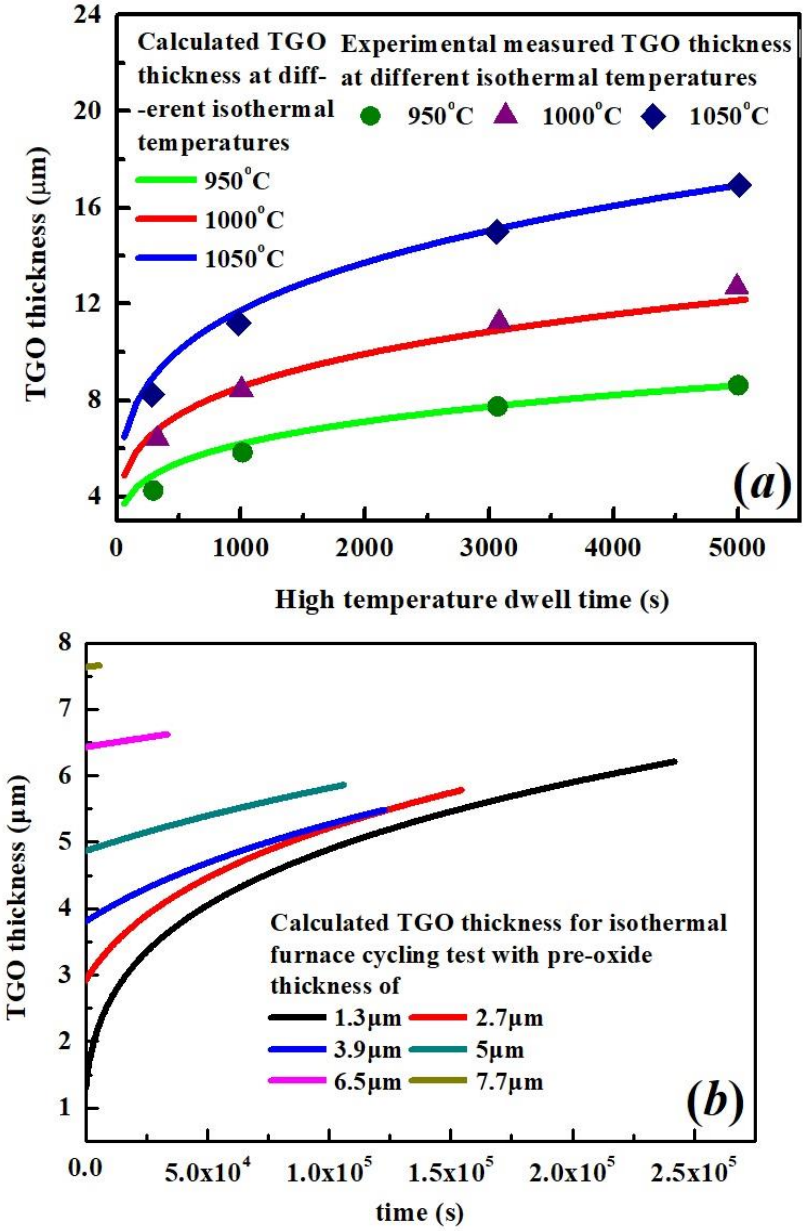

Figure 110 (a) Calculate TGO thickness using experimental data in [185] for parameter fitting (b) calculated TGO thickness for isothermal furnace cycling test with elevated temperature at 1120°C

However, for the burner cycling test, there exists a large temperature gradient during high temperature holding time, where the temperature calculated at the BC/TGO interface is approximately 935℃. Nevertheless, the relative short holding time (50s) further inhibits the growth of the TGO layer during the high temperature dwell period compared to that for the isothermal furnace test (26min).

Therefore, the calculated equivalent TGO growth time t_{equiv}^{TGO} is about 313.4 hours for the burner cycling test with elevated temperature at 935℃, corresponding to isothermal preheat treatment at 1080℃ with initial 1.3μm pre-oxide thickness. The growth of the TGO layer at 935℃ makes the final TGO thickness around 1.72μm at the end of burner cycling test. For the rest of sets, the calculated equivalent TGO growth time t_{equiv}^{TGO} are unrealistic high, which makes the TGO growth rate in equation (125) neglectable. This leads the calculated final TGO thickness to be essentially identical to the initial pre-oxide thickness. Considering the description above, the neglectable TGO growth under burner cycling test can be explained by the following:

1) The backside cooling applied on the BC/substrate surface decreases the temperature on the surface of the BC up to 935^{o}C during high temperature dwell time, which effectively inhibits the growth of the TGO layer compared to the isothermal furnace test (1120^{o}C uniformly throughout TBCs).

2) The relatively short dwell time (50s) further inhibits the growth of the TGO layer compared to the isothermal furnace test (24min).

3) Most importantly, the pre-oxide layer formed during preheat treatment at higher temperature (1080^{o}C) effectively inhibits the further growth of the TGO layer under the burner cycling test. Except for the specimen with 1.3μm oxide thickness, the TGO layers for the rest of the specimens are too thick to facilitate the growth of the TGO layer with the lower temperatures and less holding time of burner cycling tests.

The calculated results are in good agreement with experimental results [185] where limited TGO growth was found for all group sets under burner cycling tests.

(c) Variation of TC elastic modulus under thermal cycling experiments

The method describing the variation of TC elastic modulus during thermal cycling conditions [241] is adapted and used in the present work. That is, for the APS-TBCs of isotropic material for TBCs, there are three factors required to describe the temperature-position-process-dependent TC elastic modulus under burner cycling test. These are i) the elastic modulus which varies as a function of temperature during heating and cooling periods, ii) the increase of modulus due to the sintering effect during high temperature holding time, iii) the variation of i) and ii) considering the position-dependent temperature profile throughout the TC thickness. The temperature-dependent elastic modulus of TC is given by [147] and formulated and fitted by

$$E_{TC}\left(T_{TC}\big|_{y}\right)=\gamma\exp\left(-\frac{T_{TC}\big|_{y}}{\tau}\right)+E_{TC}^{f}\left(t\right) \tag{126}$$

where γ and τ are fitting parameters, $E_{TC}^{f}\left(t\right)$ is the process-dependent modulus of the TC estimated from isothermal sintering at the end of high-temperature thermal cycles using equation (123) where the equivalent sintering time t_{equiv}^{sint} is substituted as starting time to calculate $E_{TC}\left(t\right)$.

The elastic modulus of TC $E_{TC}\left(T_{TC}\big|_{y},t\right)$ calculated from equation (123) and equation (126) as a function of time and position is shown in Figure 111(a)(b). With the existence of the thermal gradient, there are large discrepancies for elastic modulus measured at different positions. That is, higher elastic modulus is calculated close to the TC/TGO interface due to the lower temperature during high temperature dwell time at initial stage of thermal cycling experiments, Figure 111(a). Nevertheless, there is an obvious sintering effect which leads to a dramatically increase of elastic modulus at surface of TC, Figure 111(b). This might be explained by the thermal gradient that exists throughout the

thickness of the TC layer, where the surface of the TC material experiences higher temperatures than close to the TC/TGO interface, Figure 111(b).

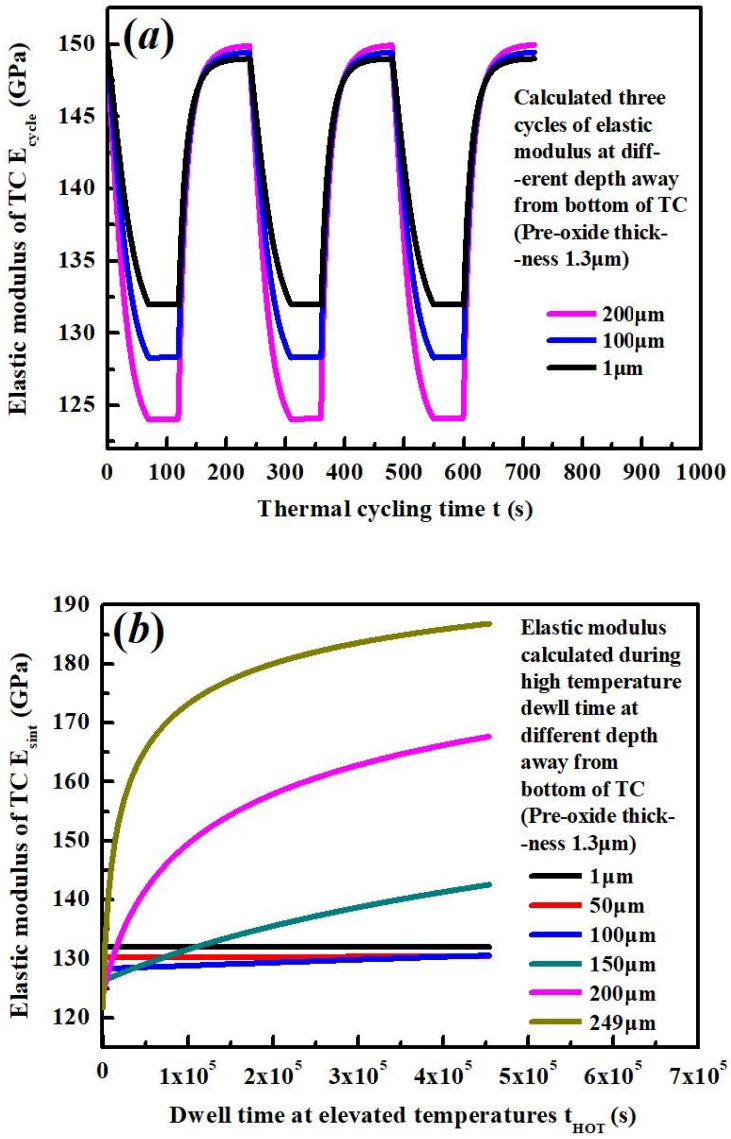

Figure 111 The elastic modulus of TC calculated at different positions with pre-oxide thickness of 1.3µm (a) for first three cycles (b) during high temperature dwell period

The same equations are used to calculate the elastic modulus of the TC based on the isothermal furnace cycling test. Since thermal cycling loading is applied uniformly throughout the TBCs, the effect of a thermal gradient is eliminated. With the longer high temperature holding time, the effect of sintering is more evident for specimens with short-time preheat treatment history (black curve), Figure 112.

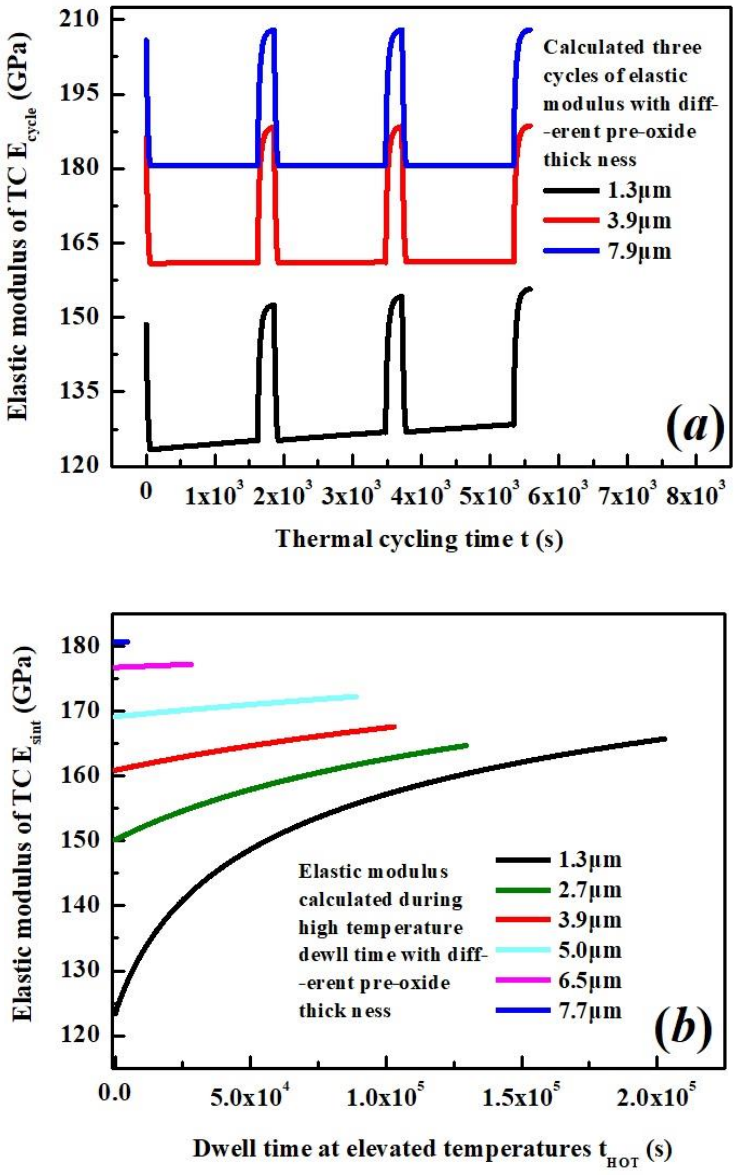

Figure 112 The elastic modulus of TC calculated at different positions with different pre-oxide thickness under isothermal furnace test (a) for first three cycles (b) during high temperature dwell period

(d) Other temperature-dependent thermal and mechanical properties of APS-TBCs

Except for the aforementioned temperature-process dependent model parameters, the temperature-dependent model parameters used in the current study are fitted based on experimental data provided in [147]. The elastic modulus of TGO and BC are described by equation (127)-(128) as

$$E_{TGO}\left(T_{BC}\right) = -26.91925 \times \exp(T_{BC}/786.82282) + 426.29843 \quad \left(GPa\right) \tag{127}$$

$$E_{BC}\left(T_{BC}\right) = -49.52802 \times \exp(T_{BC}/1215.93266) + 262.72012 \quad \left(GPa\right) \tag{128}$$

The elastic modulus E_{TGO} of TGO involved in the calculations of ERR correlate to crack generation as a consequence of dilatational expansion due to TGO growth, accompanied with phase transformation strain. The elastic modulus E_{BC} of the BC is used to calculate ERR correlated to thermal gradient during high temperature holding time under burner cycling test, where the first Dundur's elastic mismatch parameter is expressed by [128]

$$\alpha_D = \frac{\bar{E}_{TC}\left(T_{TC}\big|_y, t\right) - \bar{E}_{BC}\left(T_{BC}\right)}{\bar{E}_{TC}\left(T_{TC}\big|_y, t\right) + \bar{E}_{BC}\left(T_{BC}\right)} \tag{129}$$

Here, the plain strain modulus of the TC and BC are described by $\bar{E}_{TC}\left(T_{TC}\big|_y, t\right) = \dfrac{E_{TC}\left(T_{TC}\big|_y, t\right)}{1-\nu_{TC}}$ and $\bar{E}_{BC} = \dfrac{E_{BC}\left(T_{BC}\right)}{1-\nu_{BC}}$, respectively. $E_{TC}\left(T_{TC}\big|_y, t\right)$ is the temperature-process-position dependent TC elastic modulus, Figure 111. The coefficients of thermal expansion (CTE) for all three layers are described by equation (130)-(132) [147] as

$$\alpha_{TC}\left(T_{TC}\big|_{y}\right)=(4.04124\times10^{-4}\times T_{TC}^{y}+9.56961)\times10^{-6}\quad(1/K)\qquad(130)$$

$$\alpha_{TGO}\left(T_{BC}\right)=(1.32\times10^{-3}\times T_{BC}+7.58748)\times10^{-6}\quad(1/K)\qquad(131)$$

$$\alpha_{BC}\left(T_{BC}\right)=(5.06\times10^{-3}\times T_{BC}+10.79679)\times10^{-6}\quad(1/K)\qquad(132)$$

The CTE for the three layers are used to calculate the thermal stresses generated as a consequence of CTE mismatch upon cooling, where the yield strength of the TC is involved. This accounts for the inelastic behavior of the TC material, considering that creep behavior is no longer effective at low temperature. The yield strength for bulk 7YSZ is illustrated in Figure 113 [239].

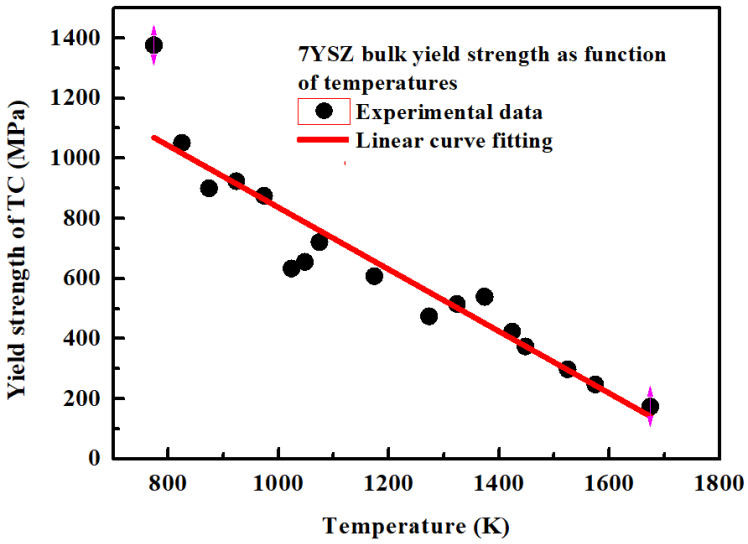

Figure 113 Yield strength of bulk 7YSZ material [239]

Considering the porosity of TC in TBCs, it is expected that the porosity decreases as the sintering effect proceeds at elevated temperature, which in turn, strengthens the TC material and increases the yield strength of TC. The effect of sintering is incorporated into the expression of yield strength of TC by

$$\sigma_Y = \frac{E_{TC}\left(T_{TC}\big|_y, t\right)}{K_{TC}} \times \left(k_Y\, T_{TC}\big|_y + \sigma_{Y0}\right) \tag{133}$$

where K_{TC} is the bulk modulus of 7YSZ TC, k_Y and σ_{Y0} is a fitting parameter.

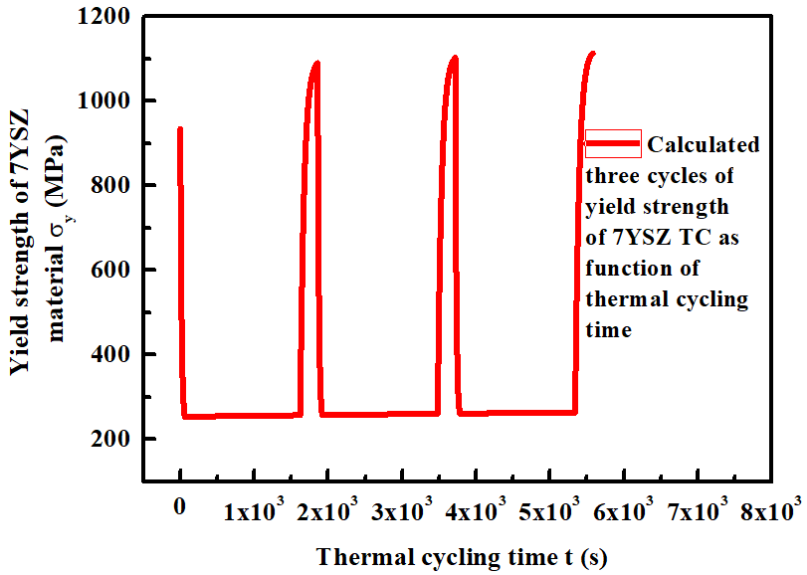

Figure 114 The calculated yield strength of 7YSZ TC as function of thermal cycling time

A.1.3. Characteristics of parameters affected by geometry of APS-TBCs

The development of cracks under isothermal high temperature loading was experimentally measured and elaborated in [131]. It was pointed out that the ratio of crack length over TC thickness might be directly correlated to the ERR generated as a consequence of the thermal gradient developing at holding time [128]. The development of delamination cracks in APS-TBCs can be separated into two phases [131], namely incubation and propagation phases. The growth of microcracks is relatively stable during the incubation phase and the crack length *b* is described as a function of TGO thickness and interfacial geometrical parameters as

$$b_{stable} = \frac{1}{2} W \times \frac{4 d_{TGO}}{A} \tag{134}$$

With the increase of TGO thickness, the damage mechanism changes from microscopic cracks propagation and coalescences to meso-macroscopic cracks, where there exists a large increase of maximum crack length. According to the statistical analysis [185], this is accompanied by a decrease of number of cracks identified within the TC of TBCs. The transition of crack path from the ceramic YSZ layer to the interface between TC/TGO leads to the uncontrolled rapid crack propagation, where the critical TGO thickness was identified to be within 5-6μm [185]. We take 5.5μm as the critical TGO thickness and use equation (135) to describe the crack length *b* as a function of high temperature exposure time for crack propagation phase as

$$b_{prop} = A_{crack} \exp\left(-\frac{t_{high}}{Q_{crack}} \right) + y_{crack} \tag{135}$$

Here, $A_{crack} = 16071.65$, $Q_{crack} = \text{-}7140.27$, $y_{crack} = \text{-}22155$ are temperature dependent crack growth parameters and t_{high} is the high temperature exposure time. The process-dependent isothermal crack length for the burner cycling test is calculated using equations (134)-(135) and illustrated in Figure 115 with different pre-oxide TGO thicknesses. The horizontal coordinate indicates time, including both isothermal preheat treatment and thermal cycling test. As described in the proceeding sections, for the burner cycling test, the growth of the TGO layer occurs mainly within the preheat treatment, where limited oxide is formed during thermal cycling experiments due to the low temperature at the BC surface and short duration of high temperature holding time. Therefore, except when pre-oxide TGO thickness equals 1.3μm, there is no delamination crack growth for the experimental set where the pre-oxide TGO layer is thinner than the critical TGO thickness, Figure 115(a).

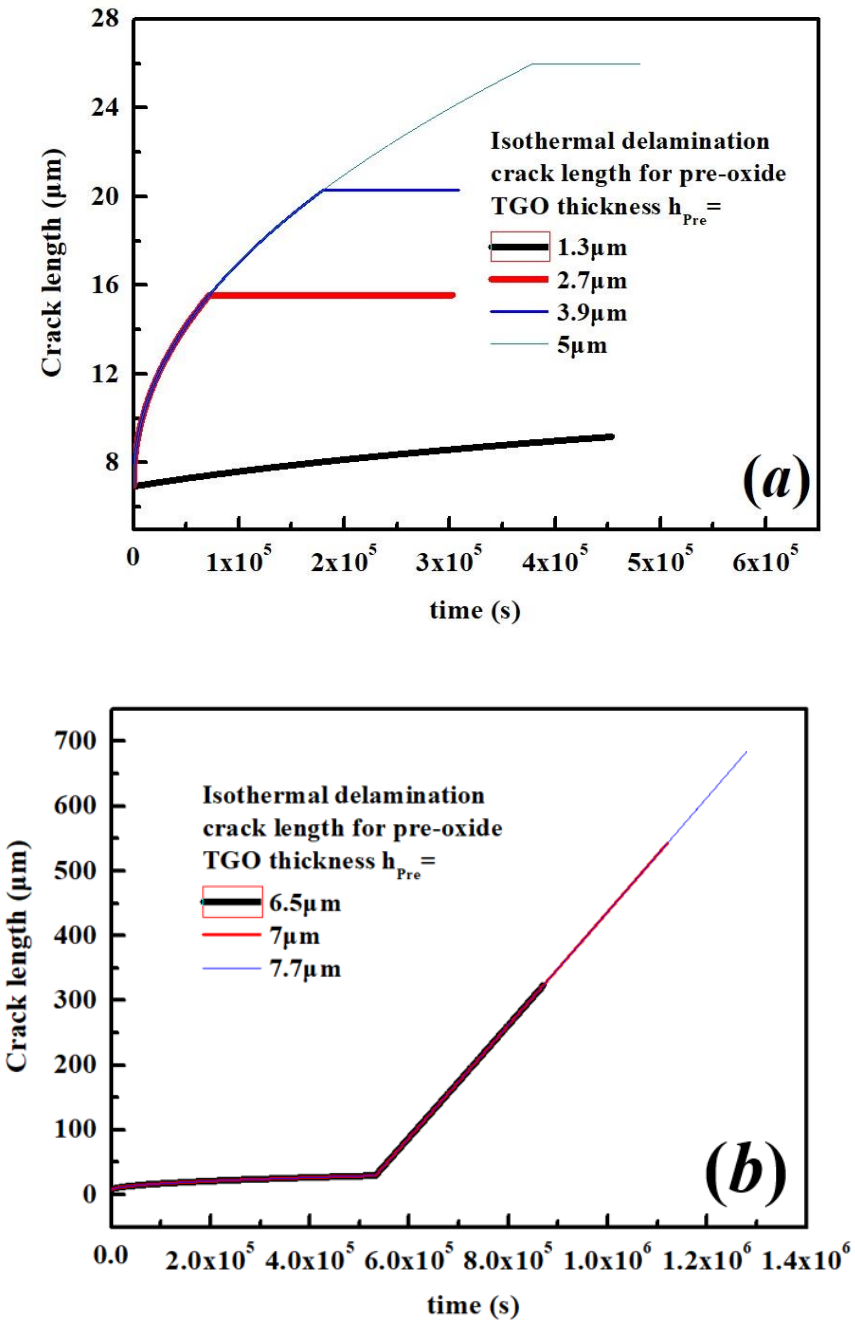

Figure 115 The process-dependent isothermal crack length as a function of time (a) Pre-oxide TGO thickness less than critical TGO thickness (5.5μm) (b) Pre-oxide TGO thickness more than critical TGO thickness (5.5μm)

For the pre-oxide layer thicker than critical TGO thickness, the propagation of a delamination crack becomes independent of TGO growth and follows linear elastic fracture mechanics, Figure 115(b). The crack growth rate for pre-oxide TGO thickness of 1.3μm is much slower than for the rest of the sets. This can be explained by the TGO growth rate for the burner cycling test being evidently lower than for the preheat treatment, since a lower BC surface temperature is applied due to the thermal gradient. This limits the TGO growth rate and results in a lower crack growth rate compared to the rest of the sets.

A.2. Analytical models for evaluating the energy release rate under different thermal cycling experiments

A.2.1. Analytical models for TGO ERR generated due to TGO growth

As described in sections A.1.1 and A.1.2, all specimens experience isothermal preheat treatment at elevated temperature, with various periods to produce pre-oxide TGO of different thickness. These specimens are then designed to undergo either isothermal furnace cycling testing or burner cycling testing. The progressive oxidation of the BC is generally considered to have two effects on the durability of TBCs. On one hand, the pre-oxide layer, specifically the preferred dense, continuous α-alumina layer, is relatively impermeable to oxygen, which retards the further oxidation of metallic BC [135]. On the other hand, the growth of TGO layer leads to the dilatational strain generated as a consequence of phase transformation from β-NiAl to γ-Ni or γ'-Ni_3Al with α-Al_2O_3. The strains generated during TGO growth are unable to be fully accommodated by the limited inelastic behavior (creep) of the TGO itself, which triggers the nucleation of internal cracks and facilitates the propagation of cracks at neighboring TC layers. Therefore, to evaluate the crack driving force and the TGO growth stress generated due to BC

oxidation, it is necessary to calculate the volume of total TGO thickness and rate of TGO growth, as well as the accompanying volumetric strain due to phase transformation. The growth of the TGO layer under thermal cycling loading is deliberately described using an incremental form, which precisely estimates the accumulated TGO thickness under the temperature fluctuations of thermal cycling conditions. The normalized fraction of oxidizing phase which has chemically reacted with oxygen is defined as $f(t)$ and is given by

$$f(t) = \frac{d_{TGO}}{d_{TGO}^{max}} \tag{136}$$

The value of $f(t)$ varies from 0, before oxidation begins, to 1 when primary oxidation is complete [132] and the TGO growth rate is evaluated through the first derivative of equation (136). The evaluation of volumetric strain generated due to phase transformation involves the analysis of the chemical reaction of progressive oxidation of the aforementioned MCrAlY BC system. The phase transformation from β-NiAl to γ-Ni or γ'-Ni_3Al with α-Al_2O_3 is described by

$$\frac{2}{3}NiAl + \frac{1}{2}O_2 \rightarrow \frac{1}{3}Al_2O_3 + \frac{2}{3}Ni \tag{137}$$

The Pilling-Bedworth ratio Π is introduced to quantitatively estimate the true mean volumetric strain e_V^T from phase transformation described by equation(138)-(139) as

$$\Pi = \frac{V}{V_0} = \frac{\Omega_{Al_2O_3} + 2\Omega_{Ni}}{2\Omega_{NiAl}} \tag{138}$$

$$e_V^T = \frac{1}{3}\ln\Pi \tag{139}$$

Here, Ω_i represents the atomic volumes in equation (138) found in [135], which in turn yields $e_V^T \approx 0.122$. With the first derivative of equation (136) and equation (139), the non-recoverable deformation rate $\dot{\varepsilon}_{TGO}(t)$ induced by the oxidation of metallic phases can be calculated through equation (140) [132] as

$$\dot{\varepsilon}_{TGO}(t) = f_2^{ini}\dot{f}(t)\left(P\frac{S'}{\tilde{S}} + e_V^T\mathbf{1}\right) \tag{140}$$

Here, f_2^{ini} is the initial volume fraction of metallic phase β-NiAl, which has not been oxidized, where $f_2^{ini} \approx 0.526$ according to [135]. $\tilde{S}$ and S' are the norm and deviatoric components of the aggregate stress tensor, respectively. *P* is a coefficient depending on the shape of the oxide particles. It is considered that isotropic volumetric expansion occurs during phase transformation for APS-TBCs and gives *P*=0 for the current study. Therefore, the stress generated due to TGO growth is simplified into a scalar and described by equation (141) where $\varepsilon_{TGO}(t)$ is obtained by integrating the equation (140) with respect to time from

$$\sigma_{TGO}(T_{BC},t) = \frac{E_{TGO}(T_{BC})\times\varepsilon_{TGO}(t)}{1-\nu_{TGO}} \tag{141}$$

where $E_{TGO}(T_{BC})$ and ν_{TGO} are temperature-dependent elastic modulus and Poisson's ratio of the TGO layer. Similar to the form of the crack driving force due to CTE mismatch, the ERR for crack triggered by TGO growth stress is described as [131]

$$G_{TGO}^{GR} = \frac{\left(1-\nu_{TGO}^2\right)}{2E_{TGO}(T_{BC})}\times\sigma_{TGO}^2(T_{BC},t)\times d_{TGO}\times Y^2 \tag{142}$$

As mentioned in the section A.1.2, there exists a large discrepancy between the TGO growth behavior under two types of thermal cycling tests. The growth of TGO layer under burner cycling test is limited due to moderate temperatures at the surface of the BC and inadequate elevated exposure time. For the isothermal cycling test, the growth of the TGO layer is more evident for the specimens with a thinner pre-oxide TGO layer.

A.2.2. Analytical models for TC ERR generated due to thermal gradient

The introduction of back side cooling during the high temperature holding time and rapid heating/cooling process leads to a large thermal gradient under burner cycling testing. This temperature difference within the TC between the surface and positions close to the interface of the TC/TGO is a critical factor for the formation of cracks. Cracks may form in different ways. For example, an isolated crack can form and propagate parallel to the interface. Alternatively, the crack is connected to the free edges of the TC [128], Figure 75.

The methods to calculate the ERR depend on the thermal gradient developed either during high temperature holding time or upon rapid cooling. Two different analytical methods are demonstrated in the following sections.

(a) The ERR generated due to thermal gradient developed at high temperature holding time

The analytical solutions to calculate the crack driving force due to the high heat flux developed for isothermal high temperature environment can be found in [128]. As shown in Figure 75, two possible crack routes are given and corresponding ERR are proposed.

For an isolated interface crack developed within the TC parallel to the interface, Figure 75, the thermal gradient is assumed between the upper and lower faces. The crack is insulated where this temperature difference facilitates crack propagation and might further lead to the spallation of the TC. A moment $M_{0TC\_insul}^{TH\_GR}$ and force $F_{0TC\_insul}^{TH\_GR}$ are imposed on the spalled TC to fit the gap, these are given by [128]

$$\begin{aligned} F_{0TC\_insul}^{TH\_GR} &= \frac{1}{2}\bar{E}_{TC}\left(T_{TC}\big|_y, t\right)\alpha_{TC}\left(T_{TC}\big|_y\right)\Delta T_{TC/interface} H \\ M_{0TC\_insul}^{TH\_GR} &= -\frac{1}{12}\bar{E}_{TC}\left(T_{TC}\big|_y, t\right)\alpha_{TC}\left(T_{TC}\big|_y\right)\Delta T_{TC/interface} H^2 \end{aligned} \tag{143}$$

where $\Delta T_{TC/interface}$ is the difference between the temperature measured at a position within the TC, $T_{TC}\big|_y$, and the temperature measured at the interface, T_{BC}. By restoring the edge of the spalled TC to the remaining section of the TBCs and imposing the continuity of moment, force, displacement and rotation, the analytical final moment $M_{TC\_insul}^{TH\_GR}$ and force $F_{TC\_insul}^{TH\_GR}$ can be obtained from [128]

$$\begin{aligned} F_{TC\_insul}^{TH\_GR} &= \frac{(b/H)(a_{22}+12b/H)F_{0TC\_insul}^{TH\_GR} - 12(b/H)a_{12}M_{0TC\_insul}^{TH\_GR}/H}{\aleph} \\ \frac{M_{TC\_insul}^{TH\_GR}}{H} &= \frac{12(b/H)(a_{11}+b/H)M_{0TC\_insul}^{TH\_GR}/H - (b/H)a_{12}F_{0TC\_insul}^{TH\_GR}}{\aleph} \end{aligned} \tag{144}$$

Here, $\aleph = \left(a_{11} + b/H\right)\left(a_{22} + 12\,b/H\right) - a_{12}^2$. The value of compliance coefficient a_{ij} depends on the ratio of the TC crack length over TC thickness $\frac{b}{H}$ and first Dundurs' elastic mismatch parameters, equation (129) tabulated in [205]. It is evident that the sintering effect of the TC plays a significant role in determining the calculated compliance coefficients a_{ij} for the current study, as can be seen for a_{11} calculated for different sintering periods and pre-oxide thickness, Figure 116. In Figure 116, the effect of crack length on compliance coefficients is shown for specimens with pre-oxide thickness of 6.5, 7.3 and 7.7μm. These groups of specimens are considered to undergo rapid crack propagation (specimens where pre-oxide thickness is larger than the critical TGO thickness), which is further reflected by an increase of a_{11} in Figure 116.

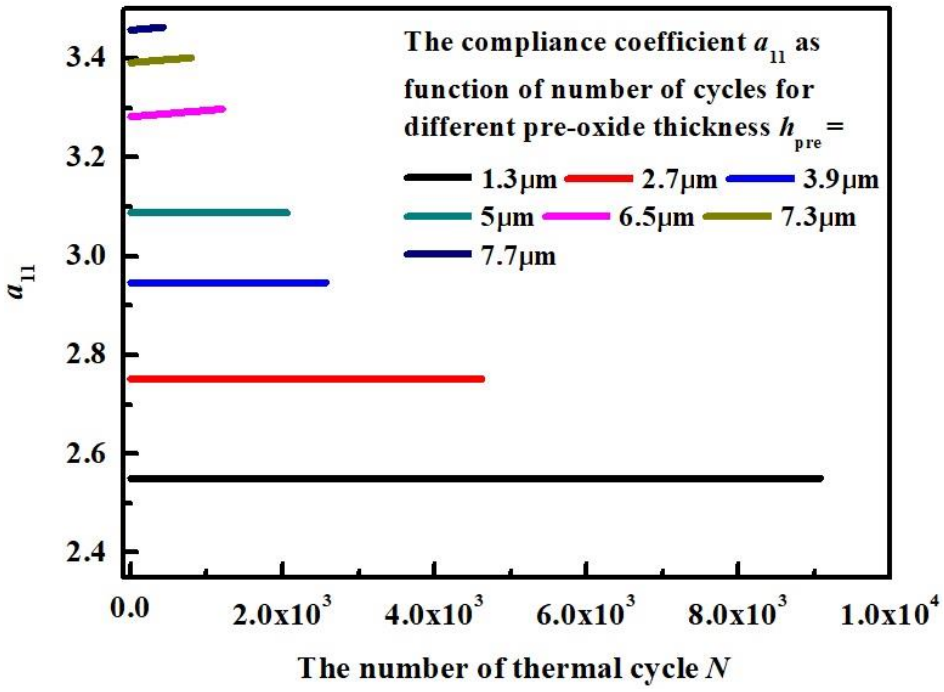

Figure 116 the calculated compliance coefficient a_{11} as function of thermal cycles for different pre-oxide thickness

Except for constant value of $a_{12}=a_{21}=1.7$ [205], the average value for a_{11} and a_{22} are presented in Figure 117 as a function of pre-oxide thickness.

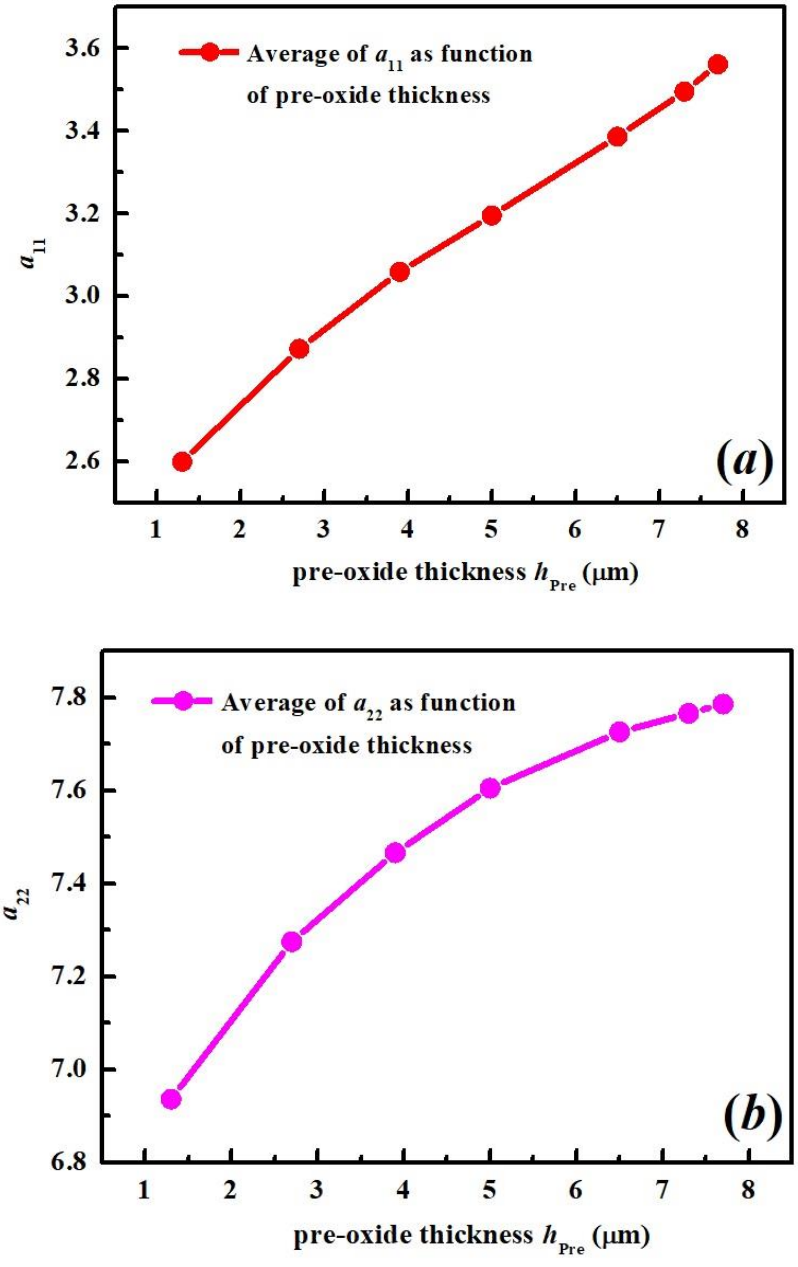

Figure 117 Calculated average a_{ij} as function of pre-oxide thickness (a) a_{11} (b) a_{22}

Accordingly, the stress intensity factors for mode I and mode II are given by

$$K_I^{ISOTHEM} = c_{21} F_{TC\_insul}^{TH\_GR} \Big/ \sqrt{H} + 2\sqrt{3} c_{22} M_{TC\_insul}^{TH\_GR} \Big/ H^{3/2}$$
$$K_{II}^{ISOTHEM} = c_{11} F_{TC\_insul}^{TH\_GR} \Big/ \sqrt{H} + 2\sqrt{3} c_{12} M_{TC\_insul}^{TH\_GR} \Big/ H^{3/2} \quad (145)$$

Similar to the compliance coefficient a_{ij}, the stress intensity coefficients c_{ij} also depends on the ratio of TC crack length to TC thickness $\frac{b}{H}$ and first Dundurs' elastic mismatch parameters tabulated in [205]. Similar to Figure 116 and Figure 117, the calculated c_{12} as a function of cycle numbers, as well as average value for c_{ij} as a function of pre-oxide thickness are illustrated in Figure 118 and Figure 119.

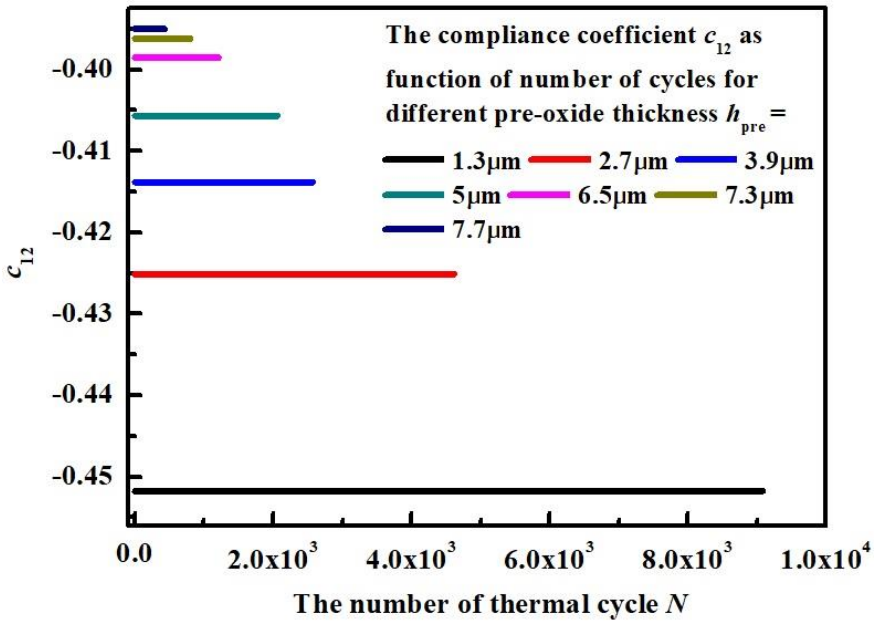

Figure 118 the calculated compliance coefficient c_{12} as function of thermal cycles for different pre-oxide thickness

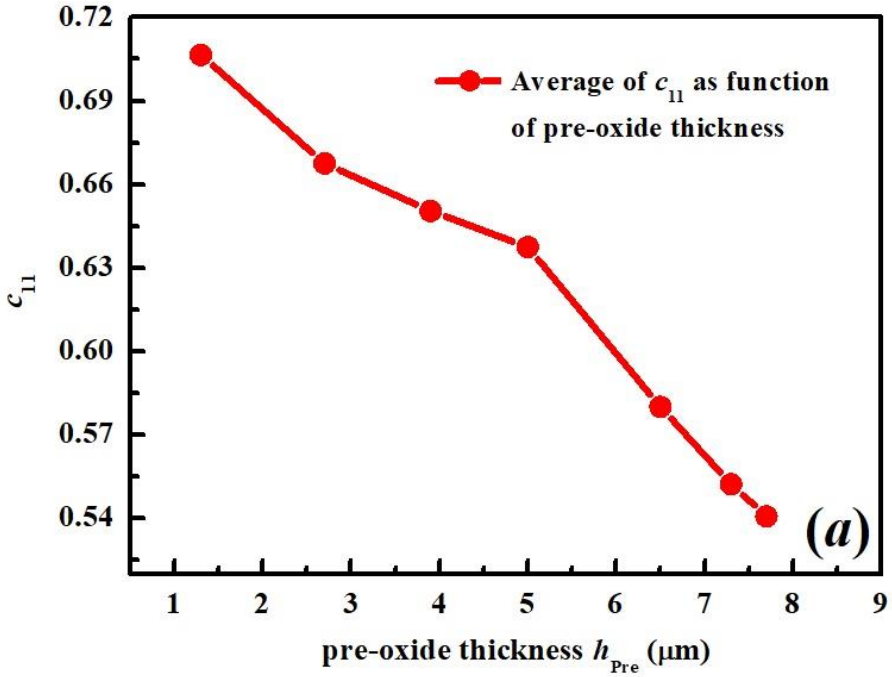
0.72
0.69
0.66
0.63
0.60
0.57
0.54
c_{11}
Average of c_{11} as function
of pre-oxide thickness
(a)
1
2
3
4
5
6
7
8
9
pre-oxide thickness h_{Pre} (μm)

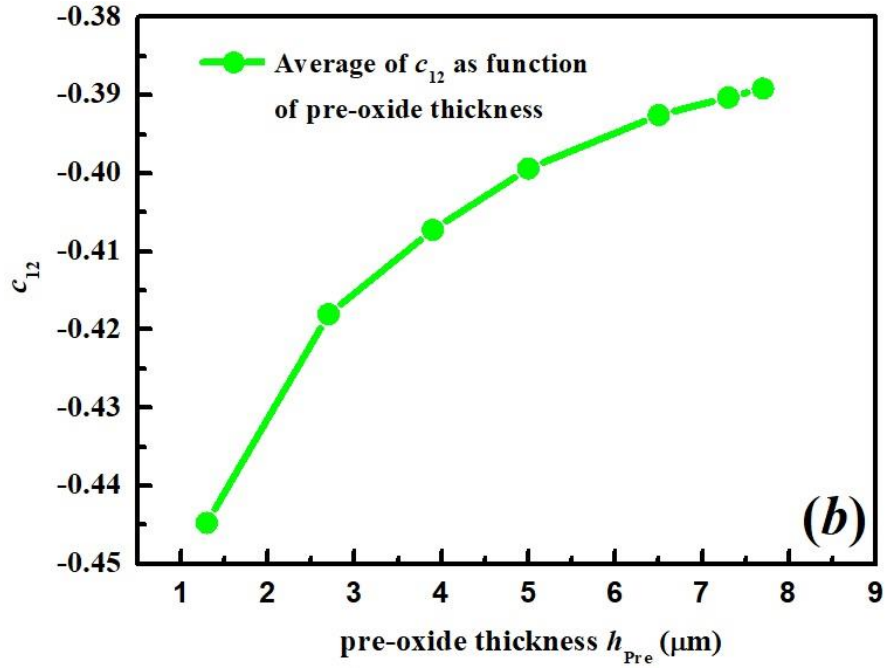
-0.38
-0.39
-0.40
-0.41
-0.42
-0.43
-0.44
-0.45
c_{12}
Average of c_{12} as function
of pre-oxide thickness
(b)
1
2
3
4
5
6
7
8
9
pre-oxide thickness h_{Pre} (μm)

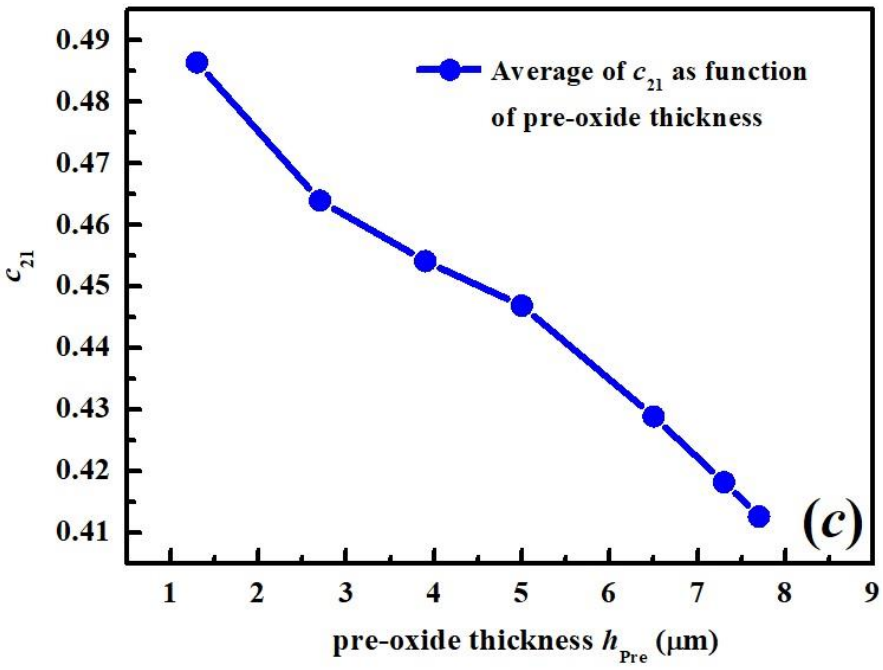

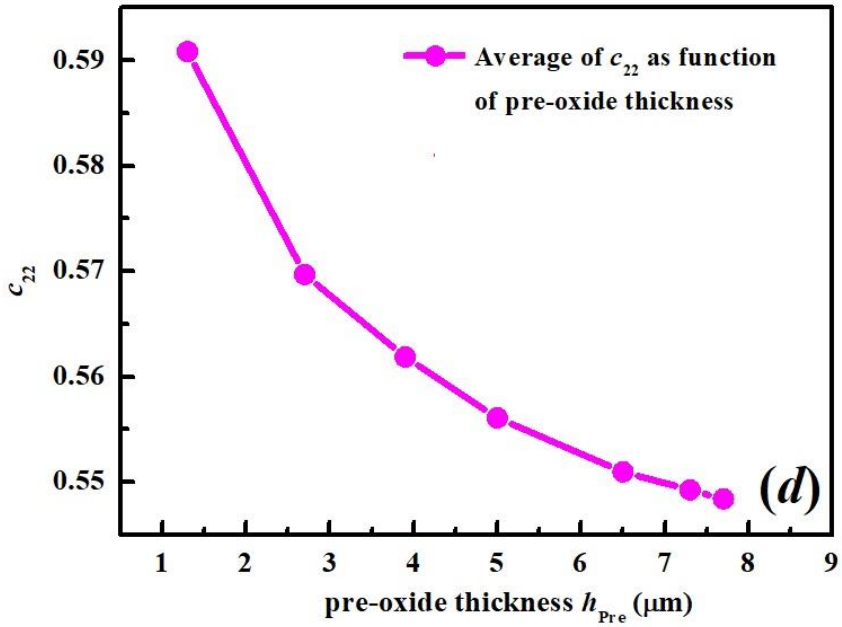

Figure 119 Calculated average c_{ij} as function of pre-oxide thickness (a) c_{11} (b) c_{12} (c) c_{21} (d) c_{22}

The corresponding ERR and mode mixture for an isolated interface crack developed under isothermal heat flux environment is described by [128]

$$G_{TC}^{ISOTHEM\_insulated}=\frac{1}{2}\left(\frac{1}{\bar{E}_{TC}\left(T_{TC}\big|_{y},t\right)}+\frac{1}{\bar{E}_{BC}\left(T_{BC}\right)}\right)\left[\left(K_{I}^{ISOTHEM}\right)^{2}+\left(K_{II}^{ISOTHEM}\right)^{2}\right] \quad (146)$$

$$\psi=\tan^{-1}\left(\frac{K_{II}^{ISOTHEM}}{K_{I}^{ISOTHEM}}\right)$$

For the crack connecting to the free edge of the TC, there are two factors to be considered including i) the effect of thermal gradient that induces the bending moment into the TBCs and ii) heating of the TBC above the stress-free temperature T_{dep}, which induces a CTE mismatch between TC and BC during high temperature holding time, resulting in residual compression within the TC. Corresponding analytical expressions are given to describe the stress as a consequence CTE mismatch $\bar{\sigma}_{TC\_edge}^{TH\_GR}$ and thermal gradient $\Delta\sigma_{TC\_edge}^{TH\_GR}$ developed within TC [128], as

$$\Delta\sigma_{TC\_edge}^{TH\_GR}=\bar{E}_{TC}\left(T_{TC}\big|_{y},t\right)\alpha_{TC}\left(T_{TC}\big|_{y}\right)\left(T_{TC}\big|_{y}-T_{TC}\big|_{surf}\right) \quad (147)$$

$$\bar{\sigma}_{TC\_edge}^{TH\_GR}=2\bar{E}_{TC}\left(T_{TC}\big|_{y},t\right)\left\{\alpha_{BC}\left(T_{BC}\right)\left(T_{BC}-T_{dep}\right)-\alpha_{TC}\left(T_{TC}\big|_{y}\right)\left(\frac{T_{TC}\big|_{y}+T_{TC}\big|_{surf}}{2}-T_{dep}\right)\right\} \quad (148)$$

where $T_{TC}\big|_{surf}$ is the TC surface temperature. The corresponding steady-state ERR for an edge delamination crack developed under isothermal heat flux is described by

$$G_{TC}^{ISOTHEM\_edge}=\frac{\left(\bar{\sigma}_{TC\_edge}^{TH\_GR}\right)^{2}H}{2\bar{E}_{TC}\left(T_{TC}\big|_{y},t\right)}+\frac{\left(\Delta\sigma_{TC\_edge}^{TH\_GR}\right)^{2}H}{24\bar{E}_{TC}\left(T_{TC}\big|_{y},t\right)} \quad (149)$$

(b) The ERR generated due to thermal gradient developed upon cooling

Analytical solutions have been proposed to calculate the crack driving force due to the thermal gradient generated from rapid temperature change upon cooling [144]. Similar to the method described in the isothermal case, an in-plane stress $\sigma_{TC\_Cool}^{TH\_GR}(y)$ is assumed at a given depth within the uncracked coating, where the corresponding unit force $P_{TC\_Cool}^{TH\_GR}$ (force/length) and unit moment $M_{TC\_Cool}^{TH\_GR}$ (moment/length) are given by [144]

$$\begin{aligned} P_{TC\_Cool}^{TH\_GR} &= \int_{-d}^{0} \sigma_{TC\_Cool}^{TH\_GR}(y)dy \\ M_{TC\_Cool}^{TH\_GR} &= \int_{-d}^{0} \sigma_{TC\_Cool}^{TH\_GR}(y)(D+y)dy \end{aligned} \tag{150}$$

Here, d is the crack depth and D is the location of the neutral bending axis, Figure 120.

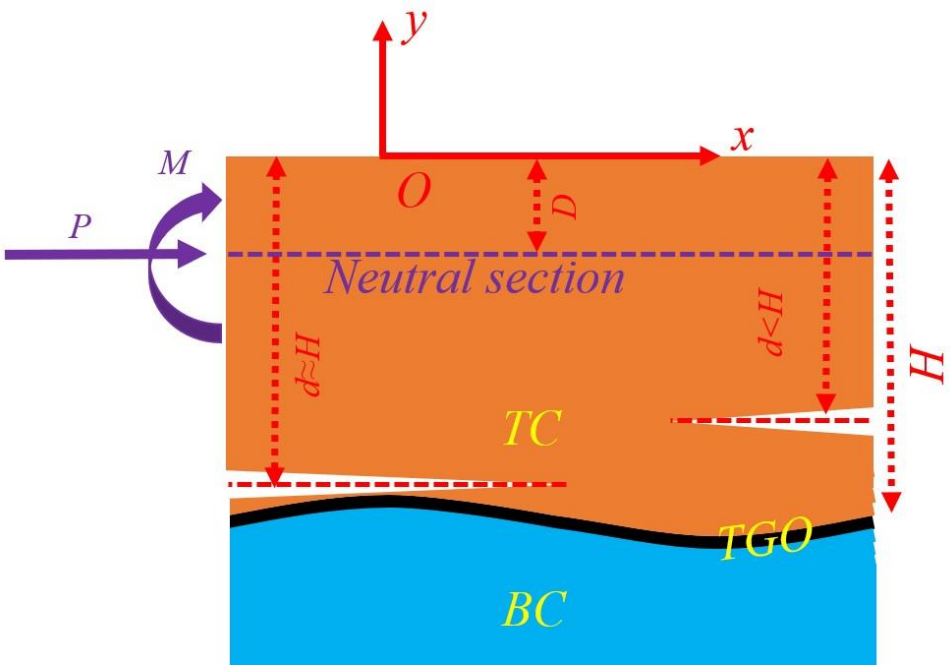

Figure 120 A schematic of the tri-layer coating system identifying the parameters used

in the analysis

Considering the entire TC is affected by the sintering effect, Evans et al [144] suggested that there is linear distribution for residual stress within the TC layer. The form of in-plane stress can be expressed by [144]

$$\sigma_{TC\_Cool}^{TH\_GR}\left(y\right)=\bar{\sigma}_{TC\_Cool}^{TH\_GR}+\sigma_{0TC\_Cool}^{TH\_GR}\left(1+2\frac{y}{H}\right) \tag{151}$$

where

$$\begin{aligned}\bar{\sigma}_{TC\_Cool}^{TH\_GR}&=E_{TC}\left(T_{TC}\big|_{y},t\right)\alpha_{TC}\left(T_{TC}\big|_{y}\right)\Delta T\big|_{surf/interf}\left(0.5-\Phi\right)\Big/\left(1-\upsilon_{TC}\right)\\ \sigma_{0TC\_Cool}^{TH\_GR}&=E_{TC}\left(T_{TC}\big|_{y},t\right)\alpha_{TC}\left(T_{TC}\big|_{y}\right)\Delta T\big|_{surf/interf}\Big/2\left(1-\upsilon_{TC}\right)\end{aligned} \tag{152}$$

The temperature $\Delta T\big|_{surf/interf}$ is given by $\Delta T\big|_{surf/interf}=\Delta T\big|_{surf}-\Delta T\big|_{interf}$, which indicates the instantaneous difference between temperature drop at the surface $\Delta T\big|_{surf}$ and at the TC/BC interface $\Delta T\big|_{interf}$, provided the temperatures from the BC and TGO layer are identical. The dimensionless ratio of mismatch strains Φ is described through [144]

$$\Phi=\frac{\left[\alpha_{BC}\left(T_{BC}\right)-\alpha_{TC}\left(T_{TC}\big|_{y}\right)\right]\Delta T\big|_{interf}}{\alpha_{TC}\left(T_{TC}\big|_{y}\right)\Delta T\big|_{surf/interf}} \tag{153}$$

Substituting equation (151)-(153) into equation (150), the unit force and unit moment can be re-written as

$$P_{TC\_Cool}^{TH\_GR} = \left(\bar{\sigma}_{TC\_Cool}^{TH\_GR} + \sigma_{0TC\_Cool}^{TH\_GR}\right) d - \sigma_{0TC\_Cool}^{TH\_GR}\, d^2 / H$$
$$M_{TC\_Cool}^{TH\_GR} = \sigma_{0TC\_Cool}^{TH\_GR}\, d^3 / (6H) \tag{154}$$

The expressions for crack driving forces were proposed by Evans et al [144], depending on the position where the crack was identified. The mix mode ERR $G_{TC\_interf}^{TEMPVARY}$ and mode mixture $\phi_{TC\_interf}^{TEMPVARY}$ are determined when the crack is close to the interface, $d \approx H$ in Figure 120 as

$$G_{TC\_interf}^{TEMPVARY} = \frac{H}{6\bar{E}_{TC}\left(T_{TC}\big|_y, t\right)}\left[3\left(\bar{\sigma}_{TC\_Cool}^{TH\_GR}\right)^2 + \left(\sigma_{0TC\_Cool}^{TH\_GR}\right)^2\right] \tag{155}$$

or

$$G_{TC\_interf}^{TEMPVARY} = \frac{\left(1 - 3\Phi + 3\Phi^2\right)}{6} \times \left[(1+\upsilon_{TC})/(1-\upsilon_{TC})\right] E_{TC}\left(T_{TC}\big|_y, t\right) H\left(\alpha_{TC}\left(T_{TC}\big|_y\right)\Delta T\big|_{surf/interf}\right) \tag{156}$$

$$\phi_{TC\_interf}^{TEMPVARY} = \tan^{-1}\left(\frac{\sqrt{3}\bar{\sigma}_{TC\_Cool}^{TH\_GR}\tan\omega - \sigma_{0TC\_Cool}^{TH\_GR}}{\sqrt{3}\bar{\sigma}_{TC\_Cool}^{TH\_GR} + \sigma_{0TC\_Cool}^{TH\_GR}\tan\omega}\right) \tag{157}$$

For plane strain conditions, the ω=52.1°.

For cracks located above the interface $d < H$ in Figure 120, the mode I $K_{I\_TC\_above}^{TEMPVARY}$ stress intensity factor and ERR $G_{I\_TC\_above}^{TEMPVARY}$ are described by

$$K_{I\_TC\_above}^{TEMPVARY} = \frac{P_{TC\_Cool}^{TH\_GR}\sqrt{d}}{\sqrt{2\cos\omega}} \tag{158}$$

$$G_{I\_TC\_above}^{TEMPVARY} = \frac{\left(K_{I\_TC\_above}^{TEMPVARY}\right)^2}{\bar{E}_{TC}\left(T_{TC}\big|_y, t\right)} \tag{159}$$

The crack driving force $G_{TC}^{TEMPVARY}$ is determined using different equations depending on whether the crack nucleated at the interface $G_{TC\_interf}^{TEMPVARY}$ or above the interface $G_{I\_TC\_above}^{TEMPVARY}$.

A.2.3. Analytical models for TC ERR generated due to Thermal shock

Due to the rapid heating/cooling process under burner cycling test, the effect of thermal shock on the nucleation of a delamination crack should be considered and included into the total ERR. The cracking driving force for thermal shock with thermal gradient was evaluated by Fleck et al [145]. The elastic thermal strain is generated due to CTE mismatch upon heating and cooling, where the in-plane residual stress calculated at a given position $y = y_0$ for a flat interface is described by

$$\sigma_{TC}^{TH\_SH} = \frac{E_{TC}\left(T_{TC}\big|_y, t\right)}{1-\upsilon_{TC}} \times \Delta\varepsilon_{CTE}^{TC}\Big|_{y=y_0}^{gradient} \tag{160}$$

Similar to the abovementioned methods in section A.2.2, the corresponding unit force $P_{TC}^{TH\_SH}$ and unit moment $M_{TC}^{TH\_SH}$ for thermal shock are obtained by substituting equation (160) into equation (150). Neglecting the effect of the first and second Dundurs' elastic mismatch parameters for simplicity, the stress intensity factors for mode I and mode II are obtained by equation (161) which has a similar form to equation (145), [145].

$$K_{I\_TC}^{TH\_SH} = 0.434\frac{P_{TC}^{TH\_SH}}{\sqrt{\hat{A}H}} + 0.558\frac{M_{TC}^{TH\_SH}}{\sqrt{\hat{I}H^3}}$$
$$K_{II\_TC}^{TH\_SH} = 0.558\frac{P_{TC}^{TH\_SH}}{\sqrt{\hat{A}H}} - 0.434\frac{M_{TC}^{TH\_SH}}{\sqrt{\hat{I}H^3}} \quad (161)$$

Here, dimensionless units $\hat{A}$ and $\hat{I}$ are used to characterize the equivalent area and moment of inertia of the TC materials. For isotropic APS TC with homogeneous temperature distribution, $\hat{A}=1$ and $\hat{I}=\frac{1}{12}$ are assumed for rectangular 2D TBCs.

Nevertheless, due to the existence of a thermal gradient and sintering effect, the value of $\hat{A}$ and $\hat{I}$ vary as function of $E_{TC}\left(T_{TC}\big|_y, t\right)$, which depends on the sintering time and temperature at different calculated depth, as described by equation (162)-(163)

$$\hat{A} = \int_{-H}^{0} \frac{E_{TC}\left(T_{TC}\big|_y, t\right)}{E_{TC}\left(T_{TC}\big|_{interf}, t\right)} \frac{dy}{H} \quad (162)$$

$$\hat{I} = \frac{1}{H^3}\int_{-H}^{0} \frac{E_{TC}\left(T_{TC}\big|_y, t\right)}{E_{TC}\left(T_{TC}\big|_{interf}, t\right)} \left(y-D\right)^2 dy \quad (163)$$

The value of $\hat{A}$ and $\hat{I}$ are calculated upon heating/cooling as functions of time and described in Figure 121 together with the value for homogeneous TC materials.

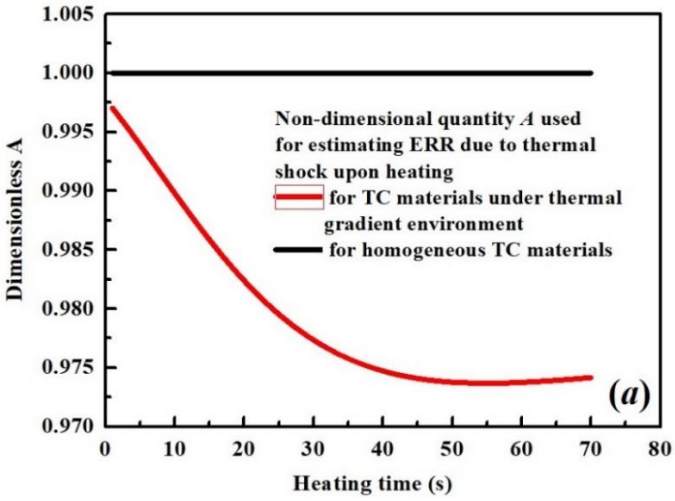
1.005
1.000
0.995
0.990
0.985
0.980
0.975
0.970
Dimensionless A
Non-dimensional quantity A used
for estimating ERR due to thermal
shock upon heating
for TC materials under thermal
gradient environment
for homogeneous TC materials
(a)
0
10
20
30
40
50
60
70
80
Heating time (s)

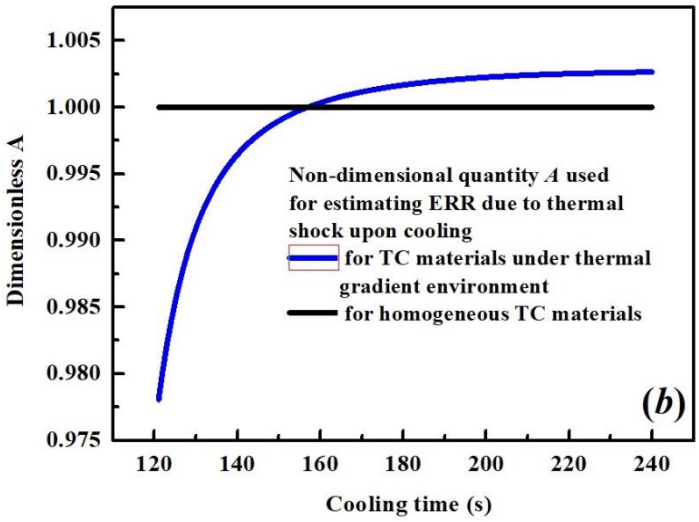
1.005
1.000
0.995
0.990
0.985
0.980
0.975
Dimensionless A
Non-dimensional quantity A used
for estimating ERR due to thermal
shock upon cooling
for TC materials under thermal
gradient environment
for homogeneous TC materials
(b)
120
140
160
180
200
220
240
Cooling time (s)

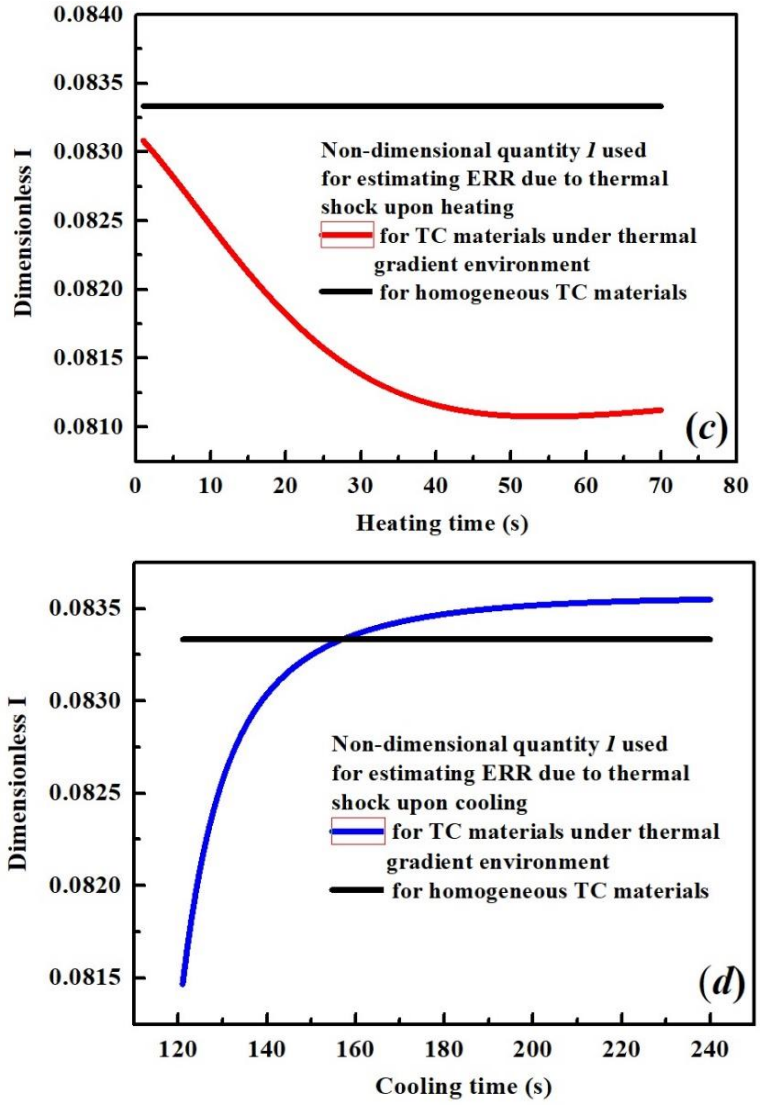

Figure 121 The dimensionless quantity that used as parameters characterizing the inhomogeneity in TC as function of time: for $\hat{A}$ upon (a) heating (b) cooling and for $\hat{I}$ upon (c) heating (d) cooling

The abovementioned location of the neutral bending axis *D* is given by

$$D = \frac{H}{\hat{A}} \int_{-H}^{0} \frac{E_{TC}\left(T_{TC}\big|_{y}, t\right)}{E_{TC}\left(T_{TC}\big|_{interf}, t\right)} \frac{y}{H} \frac{dy}{H} \tag{164}$$

The mode I and mode II stress intensity factors are used to calculate the mix mode ERR and mode mixture for thermal shock developed under burner cycling test, described by

$$G_{TC}^{TH\_SH} = \frac{1-\upsilon_{TC}^2}{E_{TC}\left(T_{TC}\big|_y, t\right)}\left[\left(K_{I\_TC}^{TH\_SH}\right)^2 + \left(K_{II\_TC}^{TH\_SH}\right)^2\right] \tag{165}$$

Appendix B - Supporting document for journal paper 4 in chapter 6

B.1. Parameters $\alpha_0, n, \varepsilon, \phi$ characterizing the erosion behavior of EB-PVD TC

In the present section, parameters $\alpha_0, n, \varepsilon, \phi$ characterizing the erosion behavior of EB-PVD TC are determined through the method described in [229] using the experimentally measured erosion rates with respect to different temperatures [224], [230] tabulated in Table 18.

Table 18 The experimentally measured erosion rate of EB-PVD TBCs [224], [230]

Temperature (℃)	Impact velocity(m/s)	Erodent	Impact angles (°)	Erosion rates (g/kg)
Room Temperature (RT)	170	60μm SiO_2	30	9.58
			60	15.44
			75	17.39
			90	18.3
540℃	122	40μm Al_2O_3	15	2.06
			20	3.98

			25	5.09
			36	7.62
			53	10.76
			83	14.33
			90	14.7
910℃	300	60μm SiO_2	30	27
			45	25.2
			60	16.7
			75	8.9
			90	5.4

B.1.1. Erosion curves and parameters characterizing the erosion behavior of EB-PVD TC at RT and 540℃

Typically, a brittle erosion is found according to erosion data measured for EB-PVD TC with silica erodent at RT and with alumina erodent at 540℃, where the maximum erosion rate is identified at an impact angle of 90°. The procedure to estimate the parameters characterizing the erosion behavior of brittle material is used and described in following steps.

(1) Considering the negligible critical impact velocity *K* for brittle material (see section B.2), the deformation wear kinetic energy ε can be estimated using equation (166) with the experimentally measured erosion rate at 90° $W_t\big|_{\alpha=90^o}$ and accumulated impact mass *M* as well as impact velocity *V*.

$$\varepsilon = \frac{\frac{1}{2}MV^2}{W_t\big|_{\alpha=90^o}} \tag{166}$$

(2) Once the ε is determined, the deformation wear $W_d(\alpha)$ can be estimated at different angles using equation (167). The corresponding cutting wear $W_t(\alpha)$ can be calculated by subtracting the deformation wear $W_d(\alpha)$ from experimentally measured total erosion rate $W_c(\alpha)$ using equation (168).

$$W_d(\alpha) = \frac{\frac{1}{2}M\left(V\sin\alpha\right)^2}{\varepsilon} \tag{167}$$

$$W_c(\alpha) = W_t(\alpha) - W_d(\alpha) \tag{168}$$

(3) The maximum cutting wear therefore can be identified at specific maximum angle of cutting wear

$\alpha_{c\max}$, from which the erosion parameter n can be estimated by solving equation (169). The critical angle α_0 is calculated by substituting n into equation (94).

$$\sin n\alpha_{c\max} - \frac{n}{2}\frac{\cos n\alpha_{c\max}}{\tan n\alpha_{c\max}} = 0 \tag{169}$$

(4) For brittle erosion, there is no "turning point" at which maximum erosion rate is found at specific impact angle. According to [229], the cutting wear kinetic energy ϕ is evaluated based on the comparison between angle giving half the erosion experienced at 90° ($\alpha_{\frac{1}{2}}$) and the critical angle α_0, equation (170)

$$\phi = \begin{cases} \varepsilon \times \left(\dfrac{\cos^2 \alpha_{\frac{1}{2}}}{\frac{1}{2} - \sin^2 \alpha_{\frac{1}{2}}} \right) & \alpha_{\frac{1}{2}} > \alpha_0 \\ \varepsilon \times \left(\dfrac{\cos^2 \alpha_{\frac{1}{2}} \sin n\alpha_{\frac{1}{2}}}{\frac{1}{2} - \sin^2 \alpha_{\frac{1}{2}}} \right) & \alpha_{\frac{1}{2}} < \alpha_0 \end{cases} \tag{170}$$

Substituting the experimentally measured erosion rates from RT and 540℃ into equation (166)-(170), parameters characterizing the erosion behavior of EB-PVD TC are identified and tabulated in Table 19. The erosion rates are calculated as function of impact angles and illustrated in Figure 122-Figure 123, together with experimentally measured erosion rates.

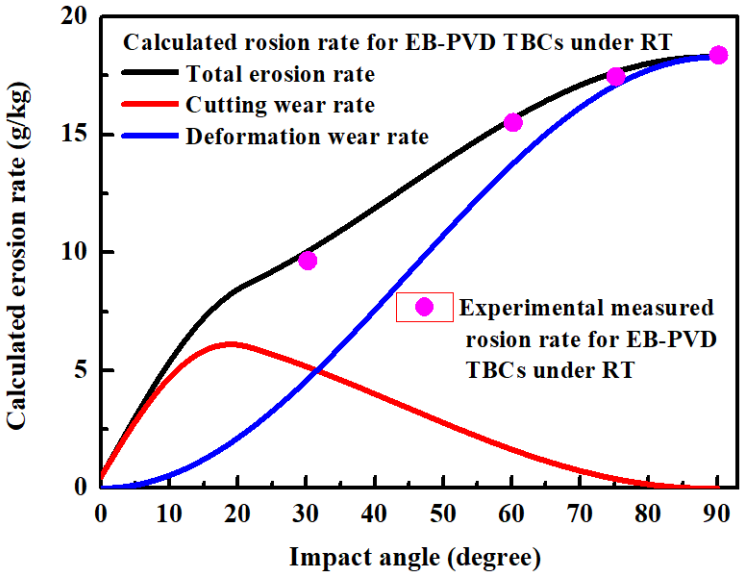

Figure 122 the calculated erosion rate of EB-PVD TC under impact of silica particles at RT temperature

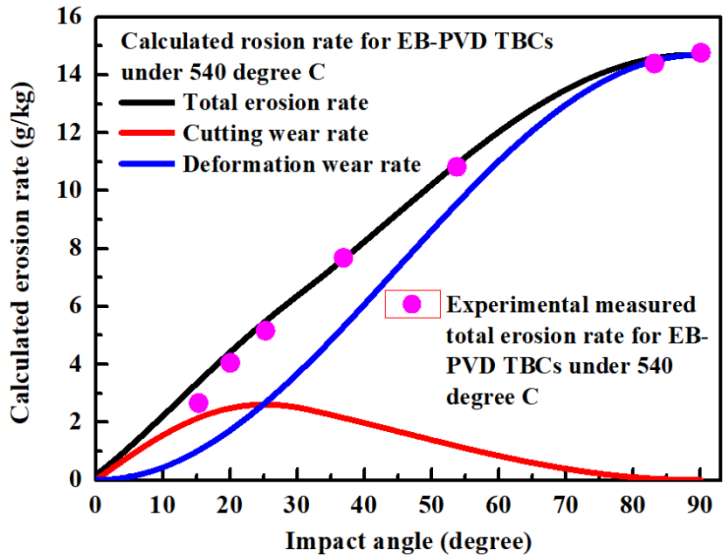

Figure 123 the calculated erosion rate of EB-PVD TC under impact of alumina particles at 540℃

B.1.2. Erosion curves and parameters characterizing the erosion behavior of EB-PVD TC at 910℃

Ductile erosion is found for EB-PVD TC with silica erodent at 910℃, where the maximum erosion rate (estimated at turning point) is identified at impact angle of $\alpha_{\max} = 30°$. The method to evaluate the parameters characterizing the erosion behavior are identical to step (1)-(3) in section B.1.1 except for the cutting wear kinetic energy ϕ that is estimated by equation (171),

$$\phi = \varepsilon \times \left(\sin n\alpha_{\max} - \frac{n}{2} \frac{\cos n\alpha_{\max}}{\tan n\alpha_{\max}} \right) \tag{171}$$

However, due to the limited experimental data (none of erosion data provided for $\alpha < \alpha_{\max}$), it is impossible to identify the maximum angle of cutting wear $\alpha_{c\max}$ following the regular sequence of steps from (1)-(4). In the present study, assuming the a part of experimentally measured erosion data falls into a range of $\alpha \geq \alpha_0$, cutting wear kinetic energy ϕ is obtained by fitting experimentally measured total erosion rates into expression 1B in equation (93) considering the deformation wear kinetic energy ε can be estimated following step(1)-(2) in section B.1.1, Figure 124.

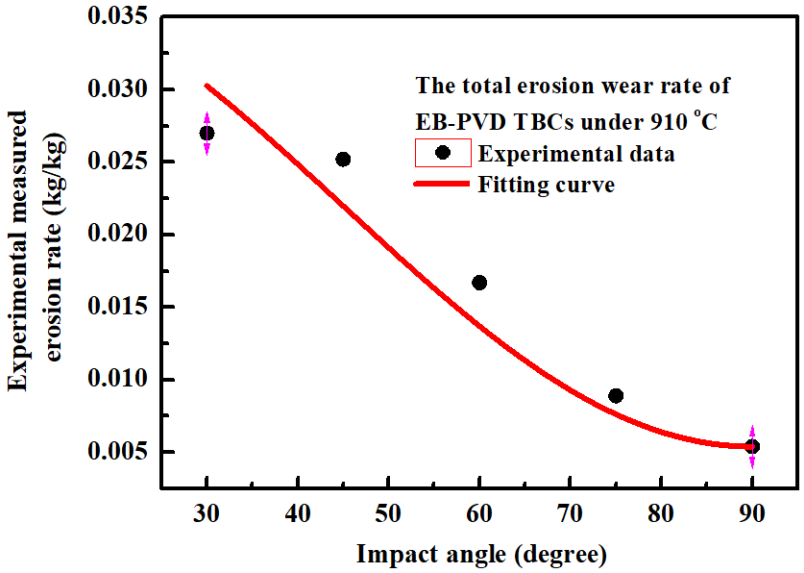

Figure 124 the experimentally measured erosion rates at 910℃ with fitting curve used to obtain the cutting wear kinetic energy ϕ

Therefore, the parameter *n* is obtained by substituting ϕ and solving equation (171) whereas α_0 is estimated by equation (94). The maximum angle of cutting wear can be estimated by substituting *n* into equation (169) ($\alpha_{c\max} \approx 28.82^o$ for erosion curve at 910℃). Parameters characterizing the erosion behavior of EB-PVD TC at 910℃ are tabulated in Table 19. The erosion rates are calculated as function of impact angles and illustrated in Figure 125, together with experimentally measured erosion rates.

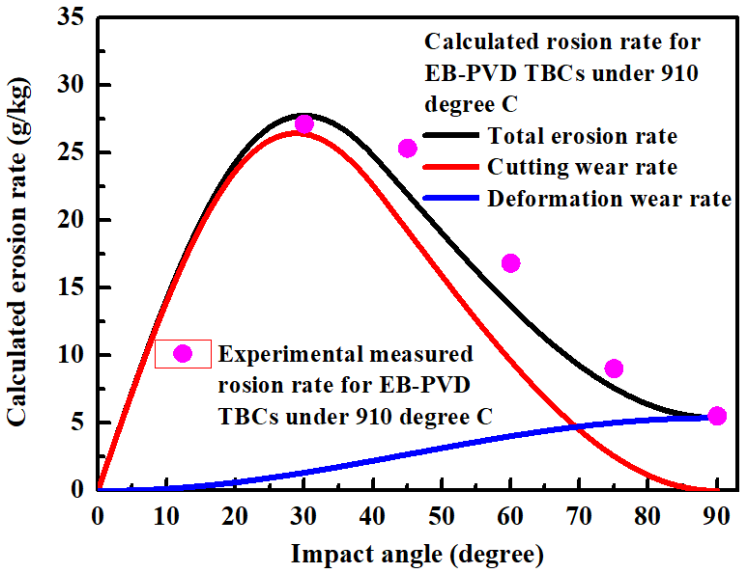

Figure 125 the calculated erosion rate of EB-PVD TC under impact of silica particles at 910℃

Table 19 Parameters characterizing the erosion behavior of EB-PVD TC at different temperatures

Temperatures (℃)	Impact velocity (m/s)	Erodent	cutting wear kinetic energy ϕ (m^2/s^2)	deformation wear kinetic energy ε (m^2/s^2)	n	α_0 (°)
20	170	60μm SiO_2	2.05×10^6	7.90×10^5	3.982	22.60
540	122	40μm Al_2O_3	2.21×10^6	5.06×10^5	2.841	31.68

910	300	60μm SiO_2	1.17×10^6	8.33×10^6	2.202	40.87

B.2. Determining the critical velocity and the effect of sintering of TC on the kinetic energies

In the present section, the effect of critical velocity on the deformation wear kinetic energy is evaluated. The critical impact velocity K is evaluated by substituting the temperature-dependent yield strength and the out-of-plane elastic modulus into equation (100) and the results are illustrated in Figure 126.

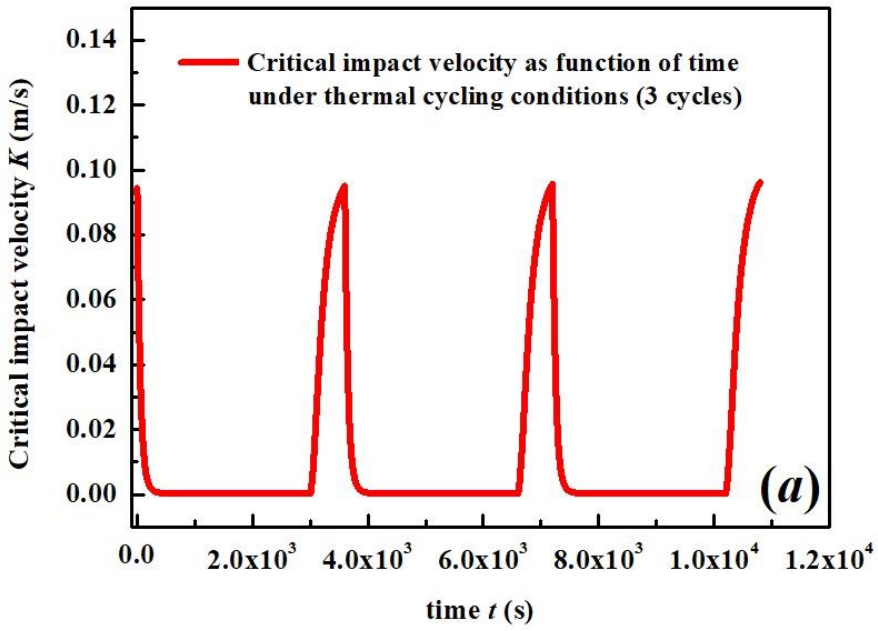

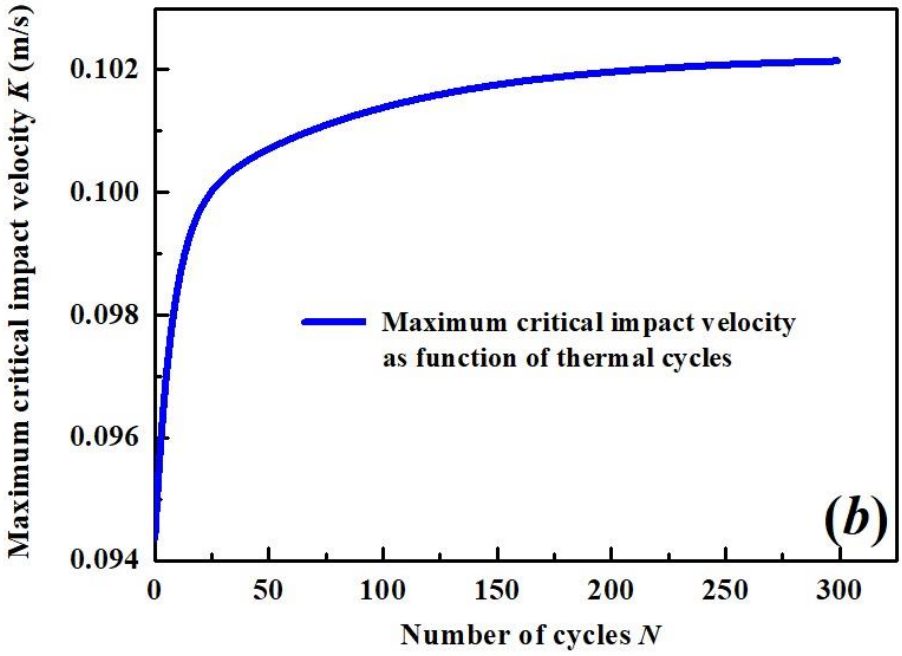

Figure 126 The calculated critical impact velocity of EB-PVD TC (a) as function of time for three cycles (b) as function of number of cycles

It is evident that the value of critical impact velocity is much less than the impact velocity applied for present study at either RT (170m/s) or 910℃ (300m/s). This indicates that the contribution of deformation wear generated from vertical impact of erodent can't be neglected throughout the thermal cycles. For simplification, the critical impact velocity is neglected from analytical expression of deformation wear kinetic energy in equation (105).

In the present section, the effect of sintering of TC on the kinetic energies are evaluated. Hutchinson et at [128] proposed an analytical model that is used to evaluate the energy release rate generated due to the sintering cracks as top surface of coating is at a sufficiently high temperature. The sintering crack propagate perpendicular to the surface of TC (within columns) initially. The crack could reorient into a delamination at depth a when the sintering stress σ_s, developed over a depth H, is sufficiently large. The schematic diagram of development of sintering crack is illustrated in Figure 127. The expression of sintering energy release rate G_{sint} is given by [128]

$$G_{sint} = \frac{4}{\pi}\left(\frac{\sigma_s^2 H}{\bar{E}_{TC}}\right)\left(\frac{a}{H}\right)\left[\left(1.3-0.18\frac{H}{a}\right)\sin^{-1}\left(\frac{H}{a}\right)\right]^2 \qquad (172)$$

where $\bar{E}_{TC}$ is TC effective elastic modulus. In equation (172), *a* defines the depth of crack developing from the surface of TC to the position where the crack reorient into delamination crack that propagate laterally. In other words, the length of sintering cracks determines the position of potential damage which might be exerted by external erosion process.

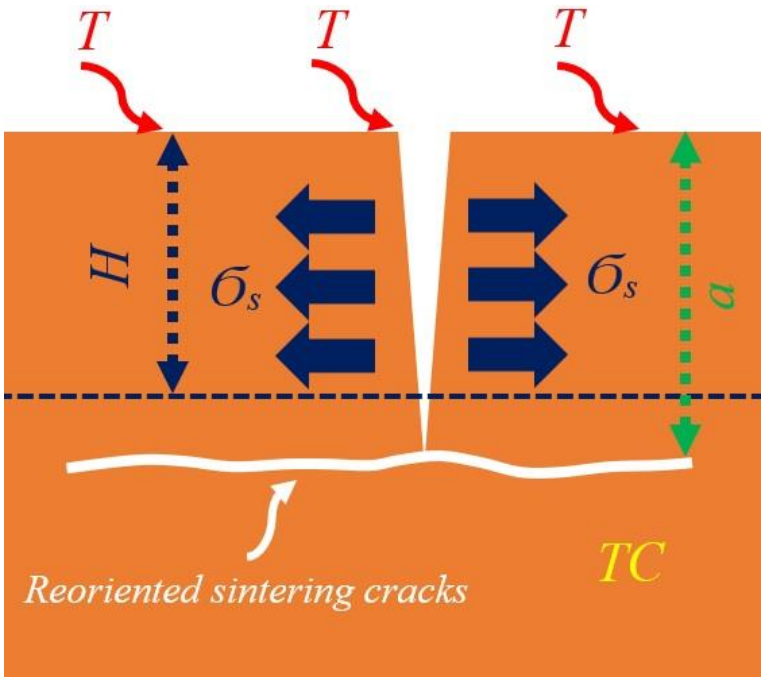

Figure 127 the schematic diagram of sintering crack developed within TC [128]

The cutting wear and deformation wear kinetic energy indicate the erosion resistance of TC layer. Therefore, it is assumed that temperature-time-dependent behavior can be described by incorporating a function inversely proportional to sintering crack length generated during high temperature dwell time, equation (119).

The abovementioned parameter *H* in equation (172) indicates the depth of sintering stress generated within TC layer. In the present study, the value of *H* is assumed to be the maximum depth of

penetration $Z_{\max}$ that is able to be reached and eroded for spherical particles, equation (101). The sintering stress is given by [140],

$$\sigma_s = \frac{2\gamma}{r_p} \tag{173}$$

where γ is the surface free energy per unit area given by [243],

$$\gamma = 1.927 - 0.428\times10^{3}T \tag{174}$$

γ is a constant during sintering crack growth during high temperature dwell time. r_p in equation (173) is the mean pore radius given by [140],

$$r_p = \frac{\left[\left(1-\rho_{rl}\right)/6\right]^{1/3} L}{2} \tag{175}$$

L is the average size of isotropic grains composing YSZ columns given by [139],

$$\dot{L} = \dot{L}_0 \exp\left(-\frac{Q}{RT}\right)\left(\frac{L_0}{L}\right)^{\beta-1}\left(1-\rho_i\right)^{-\frac{\beta-1}{2}} \tag{176}$$

where $\dot{L}_0 = 2\times10^{-3}\,\mu m/s$, $Q = 192\,kJ/mol$, $R = 8.314$, $\beta = 5$ [139]. The average grain size L as function of time can be solved by four-order Runge-Kutta method. It is assumed that the propagation of crack within TC occurs as the energy release rate reaches the critical through-thickness fracture toughness which is given by [81] and modified into equation (177).

$$G_{sint} = \left\{\alpha - \beta\left[1-\exp\left(\gamma\frac{a}{Z_{\max}}\right)\right]^2\right\}G_{crit}^{0} \tag{177}$$

where the value of fitting parameters $\alpha = 1$, $\beta = 0.9$, $\gamma = 0.693$ are determined by assumption in [81],

$$\begin{cases} G_{sint} = G_{crit}^{0} & for \quad a = 0 \\ G_{sint} = 0.1G_{crit}^{0} & for \quad a \to \infty \end{cases} \tag{178}$$

G_{crit}^{0} is the theoretical through-thickness toughness of TC and given by value of $1J/m^2$ [187]. The calculated critical through-thickness fracture toughness is illustrated in Figure 128 as function of crack length *a*.

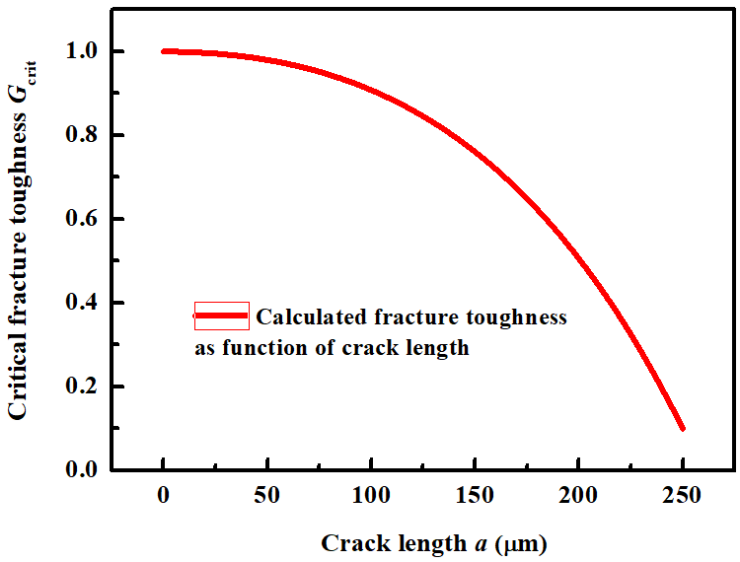

Figure 128 Calculated critical through-thickness fracture toughness as function of crack length

The equation (172) could be rewritten as equation (179) in order to use the 4th Runge-Kutta method to derive the correlation between sintering crack length *a* to high temperature dwell time t_{HIGH},

$$F(t,a) = G_{sint} - \frac{4}{\pi}\left(\frac{\sigma_s^2 Z_{\max}}{\bar{E}_{TC}}\right)\left(\frac{a}{Z_{\max}}\right)\left[\left(1.3 - 0.18\frac{Z_{\max}}{a}\right)\sin^{-1}\left(\frac{Z_{\max}}{a}\right)\right]^2 \tag{179}$$

where

$$\frac{da}{dt} = -\frac{F_t(t,a)}{F_a(t,a)} \tag{180}$$

The sintering crack length *a* is obtained by integrating the equation (180) with respect to time and calculated results is illustrated in Figure 129 as function of high temperature dwell time t_{HIGH}.

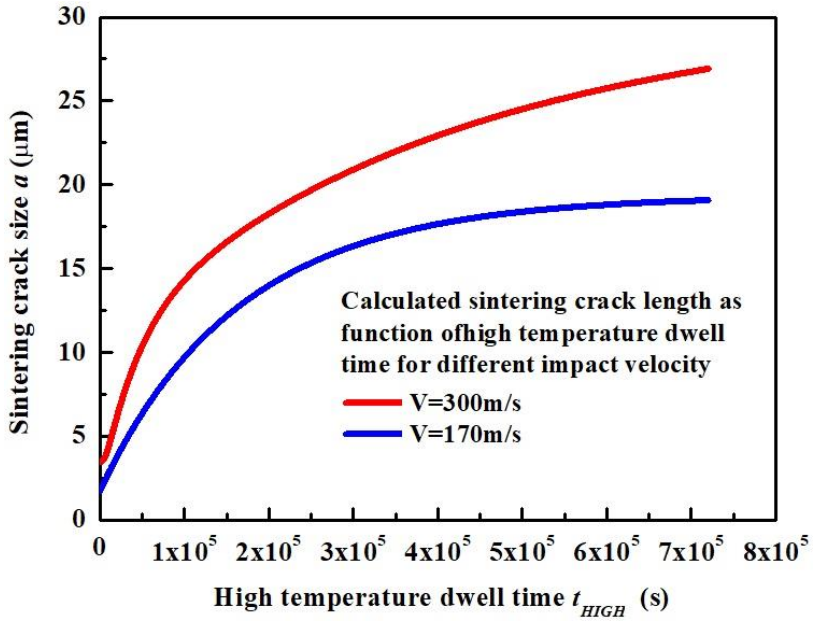

Figure 129 Sintering crack length as function of high temperature dwell time

The calculated crack length in Figure 129 indicates the depth of sintering crack reaches and position of plane where the crack reorientation occurs. It is evident that the crack length increases rapidly at beginning of dwell time. This can be explained by the significant sintering effect at early stage of high temperature dwell time, where elevated temperature at surface of TC leads to a high magnitude of sintering crack driving force that initiates the vertical crack propagating and reorienting at given crack length *a*. The crack growth rate decreases at later stage of high temperature dwell time. This corresponds to the decrease of sintering stress (r_p increase in equation (173) results in decrease of σ_s in equation (172)) and increase of elastic modulus equation $\bar{E}_{TC}$ in equation (172) which generally lower the sintering crack driving force. This might also indicate that at later of dwell time, the erosion rates are higher due to the extend of sintering cracks at deeper positions within TC where the sintering cracks reorient. However, the erosion rate decreases as a function of sintering time.

B.3. Model validation

In the present section, the validation of temperature-process-dependent erosion model is described. The calculated results are illustrated and compared with erosion rates measured experimentally. The model parameters η'' and ξ'' in equation (117) and equation (118) are fitted using erosion rate measured experimentally at RT and 910°C with impact velocity 170m/s and 300m/s, respectively. The sintering parameters $f(a)$ and $\mathrm{g}(a)$ in equation (120) are fitted using erosion rate measured experimentally with different sintering temperatures and time [217], [219].

B.3.1. Validation of temperature dependent erosion behavior

To calibrate the temperature-dependent model parameters $\eta''(T)$ and $\xi''(T)$ in equation (117) and equation (118), the erosion rate is calculated by equation (93) at first cycle to minimize the effect of time-dependent sintering behavior on the estimated cutting wear and deformation wear kinetic energy. The temperature is selected ranging from RT-1400°C where parameters of erodent including impact angles, impact mass and impact velocity (170,300m/s) are designed and tabulated in Table 20 based on experimentally measured erosion rates [225].

Table 20 Parameters used to calculate temperature-dependent fitting parameters

No# of Cycle	Temperatures (°C)	Impact angles (°)	Impact mass (kg)	Impact velocity (m/s)
Determined cycle number N: 1	Determined T ranging from [RT, 1400]	Determined α ranging from [5-90]	Determined accumulated mass M=1	Determined V: 170,300

Figure 130 illustrates the calculated erosion rates at first thermal cycle for different temperatures. Figure 130 (a) shows erosion rates measured experimentally at RT with impact velocity 170m/s, and Figure 130 (b) shows erosion rates at 910°C with impact velocity 300m/s. Figure 130 indicates that the erosion rate decreases as temperature increase for silica particle - EB-PVD TC erosion system, i.e., there exists a significant drop of erosion rate at large angles as temperature increase. This in turn corresponds to increase of deformation wear kinetic energy at elevated temperatures, Figure 98(d). The decrease of erosion rate at elevated temperatures is also experimentally measured in [231] for EB-PVD TC with silica particles. In addition, it is evident that apart from the erosion rates calculated at RT, the rest of erosion curves indicates that the coating might be eroded in a pseudo-ductile manner at intermediate to elevated temperatures. This is related to thermal property of silica erodent at elevated temperatures which softens, as mentioned above, at about 500°C [240]. The half-melted silica particles pull out the fractured columns at glancing angles, increasing the cutting wear and is attached to fractured column at high angles. This decreases the deformation wear at elevated temperatures, leading to a pseudo-ductile erosion curves calculated for most of temperatures in Figure 130.

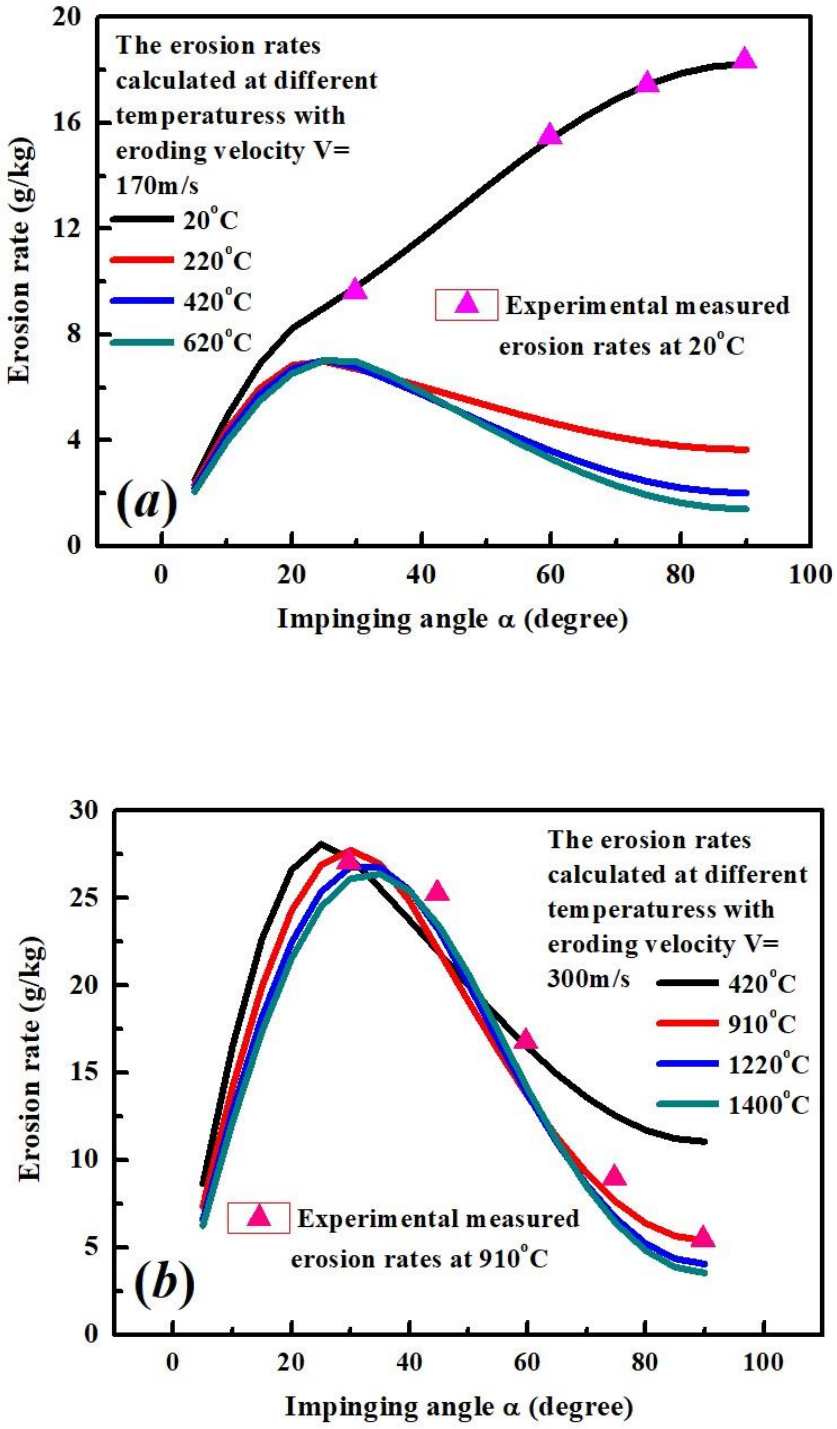

Figure 130 Calculated erosion rates as function of impact angles at first thermal cycle for different temperatures with erosion rates measured experimentally [225] using (a) impact velocity 170m/s (b) impact velocity 300m/s

In addition, the ratio of cutting wear (estimated by section (A) and (C) in equation (93)) over deformation wear (estimated by section (B) in equation (93)) is calculated and evaluated as function of different impinging angles for various of temperatures, Figure 131.

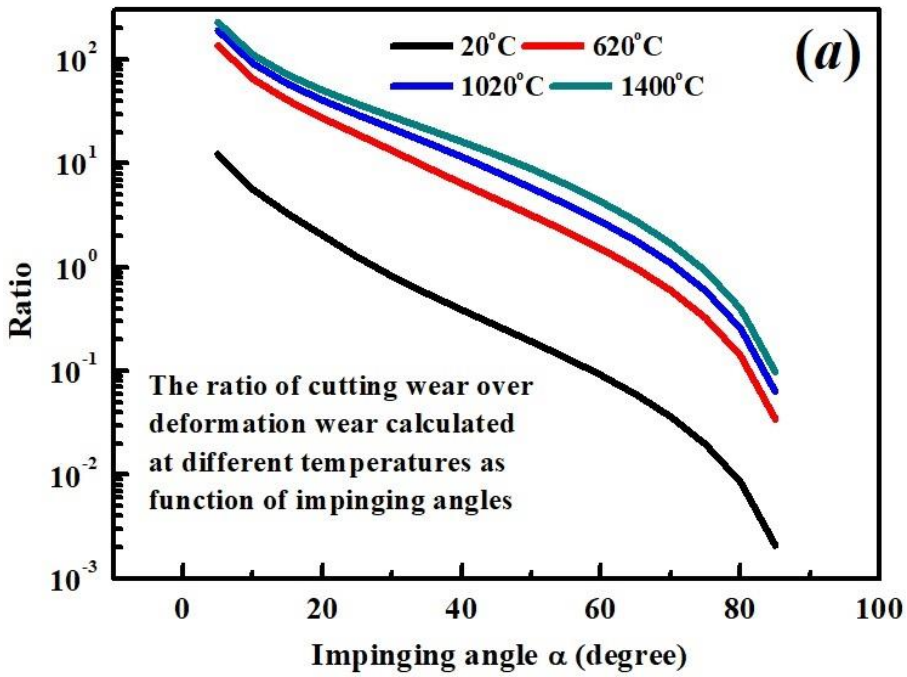

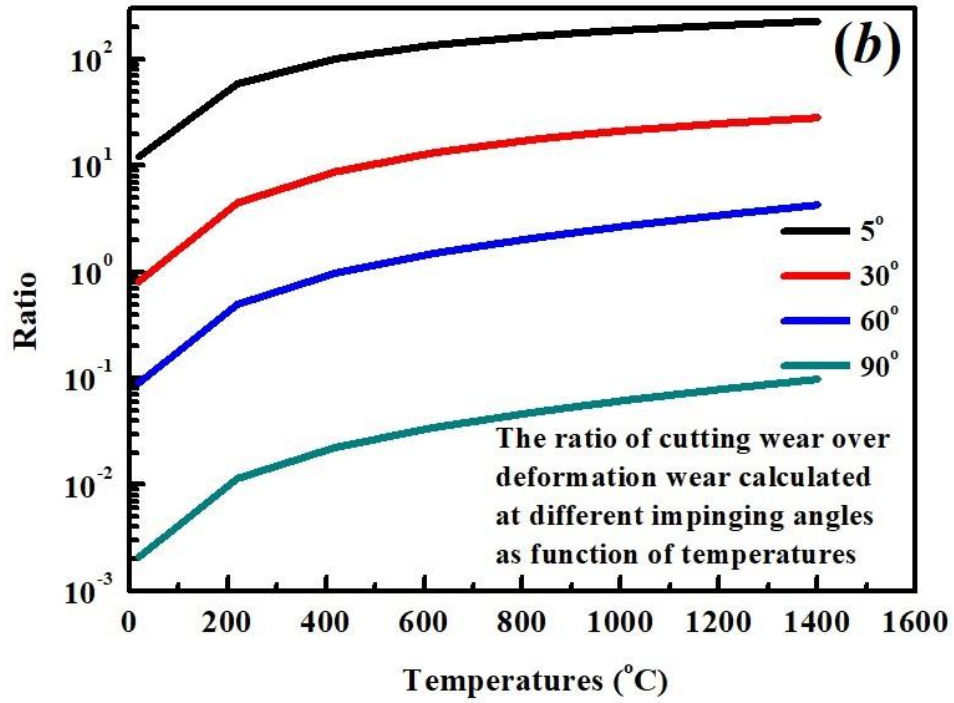

Figure 131 The calculated ratio of cutting wear over deformation wear as function of (a) different impinging angles (b) various of temperatures

It is evident that the ratio drops dramatically as the calculated impinging angles increase from 0-90°. This corresponds to the fact that the erosion is dominated by cutting wear at shallow angles with an increase of deformation wear as the impact angles increase, Figure 131(a). It should be noted that the ratio of cutting wear over deformation wear is higher at elevated temperature compared to that at lower temperature, Figure 131 (b), especially for the ratio at shallow angles. This significant increase of cutting wear is explained by softening/partially melting/pasty of silica erodent that is capable to pull out fracture section of coatings that otherwise not be removed at relative shallow angle [216], [218], [224].

B.3.2. Validation of sintering time-dependent erosion behavior

To calibrate the $f(a)$ and $g(a)$ in equation (120), the erosion is calculated by equation (107) based on erosion test conducted for EB-PVD TC at three different sintering stages [217], [219]. The details of experimental preparations (including the TC pre-sintering time and temperatures, parameters used for erosion test including the impact angles, impact velocities and particle mass) are tabulated in Table 21. Note that the mass of erodent for individual particles described in [217], [219] were determined by size of them, ranging from 20-1000μm. For the present work, the erosions are calculated using random parameter $m_i = \rho_p \times \frac{4}{3}\pi R^3$ where the radius R is assumed to be randomly vary between 20-1000μm.

Table 21 Parameters of experimental settings in [219] used to calculate sintering-dependent fitting parameters

TC pre-sintering time (hours	TC pre-sintering temperatures (°C)	Particle impact angles (°)	Particle impact mass (g)	Particle impact velocity (m/s)
0 (As received)	RT	Randomly selected α ranging from [30, 90]	Randomly selected m_i where R ranging from [20, 1000]	Randomly selected V ranging from [50, 400]
24	1500			
100	1100			

Figure 132 illustrates the calculated erosion rates for EB-PVD TC under various of pre-sintering treatments under different temperatures, together with erosion measured experimentally [217].

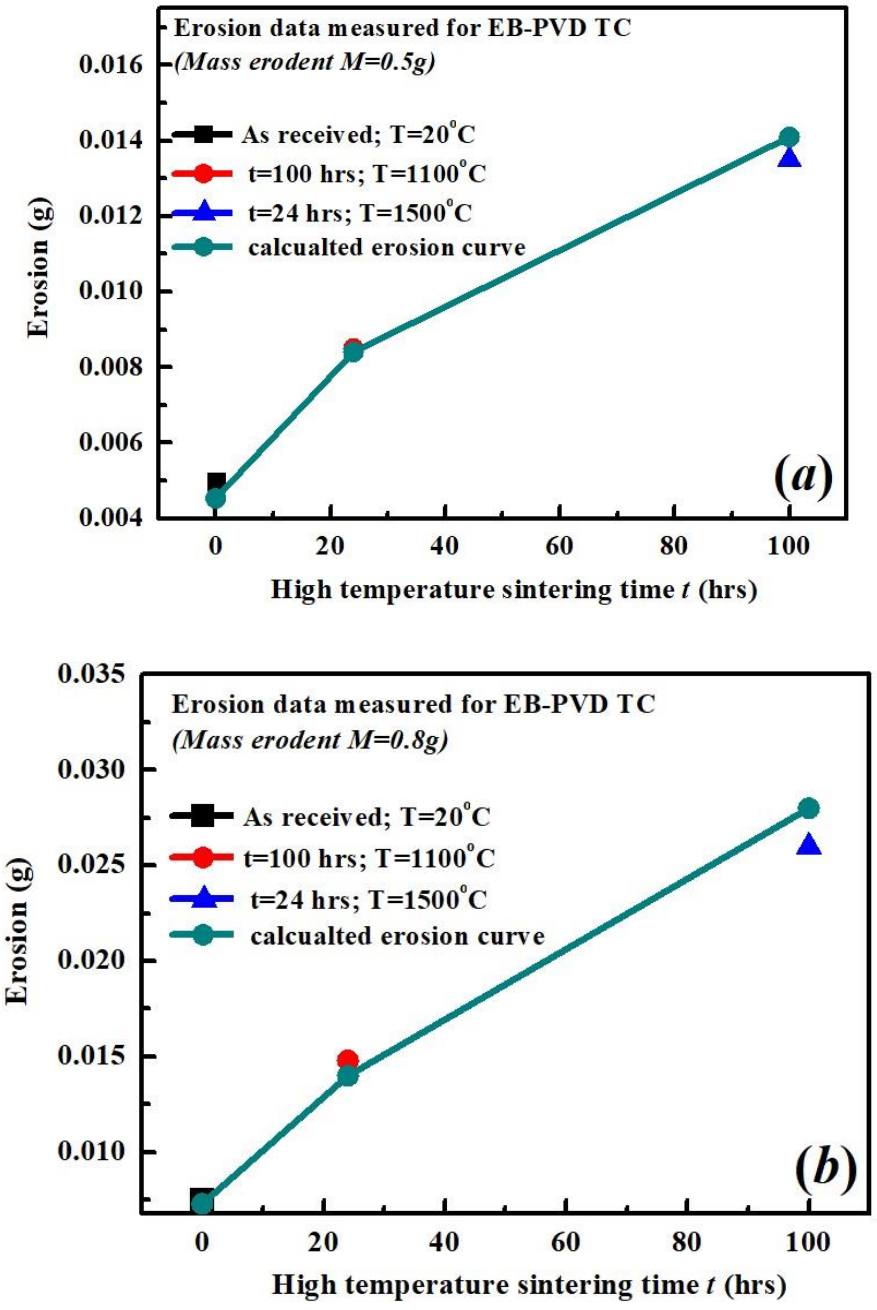

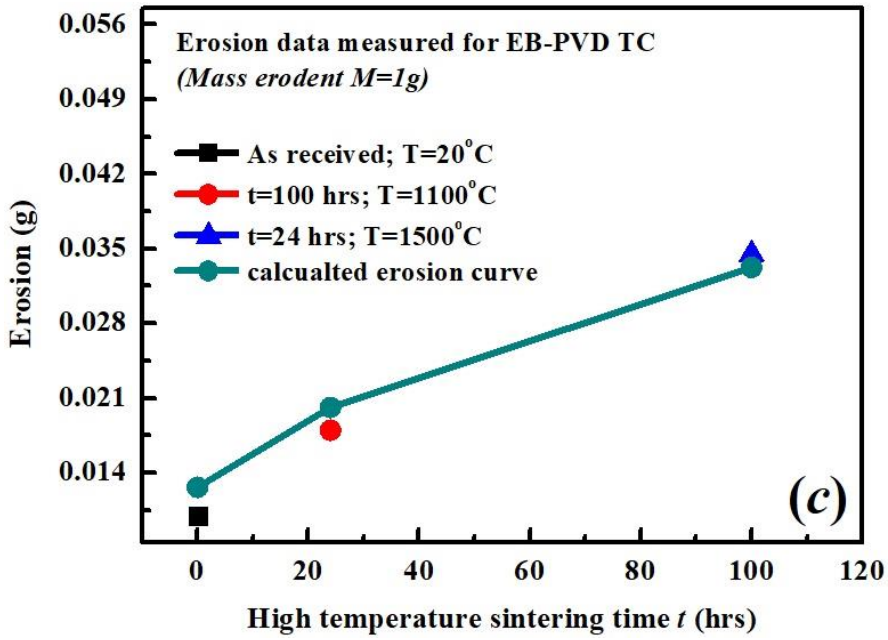

Figure 132 Calculated erosion as function of high temperature sintering time with erosion measured experimentally [217] for different accumulated mass (a) M=0.5g (b) M=0.8g (c) M=1g

The fitting parameters in equation (120) (calibrated by experimental measured erosions) can be used to indicate the general trend of kinetic energies affected by sintering behavior of TC. This follows since the erodent used from sintering erosion experiments is selected to be alumina particles with impact velocity in a range of 50-400m/s, instead, for the present study with analytical model, the material property of silica particle is selected with defined velocities (V=170 and 300m/s), which are then used to obtain the fitting parameters. In addition, unlike the procedures of estimating the temperature-dependent fitting parameters using deterministic functions, the sintering parameters is fitted by stochastic approach described in section 6.2.3, where the impact angles and impact mass during high temperature dwell time are randomly selected.